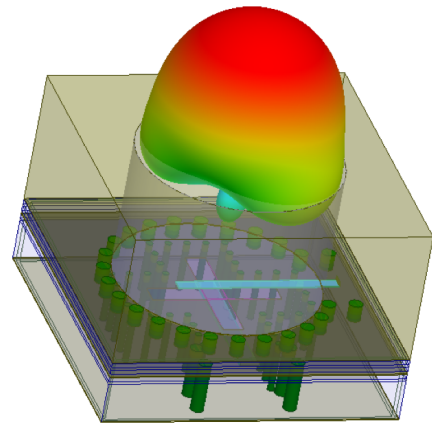
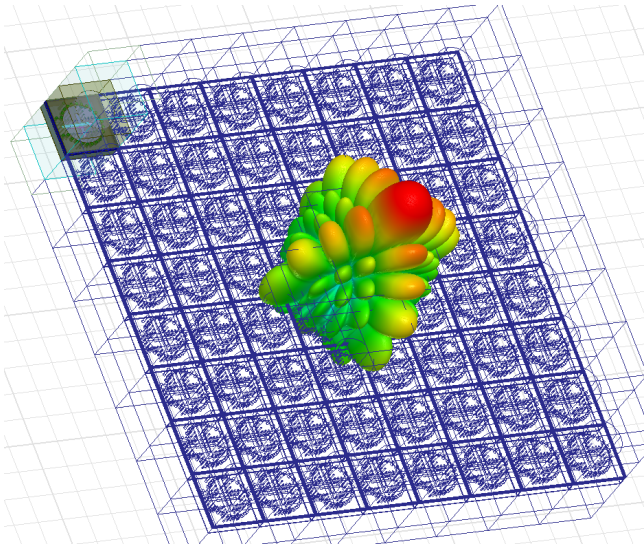




CHALMERS
UNIVERSITY OF TECHNOLOGY



Dual Polarized Circular Waveguide Aperture Antenna Element in PCB and Hardback Technology

Design of a Single Element and Analysis of Phased Array Performance

Master thesis in master program Wireless, Photonics and Space Engineering

TRA LUNDGREN

Dual Polarized Circular Waveguide Aperture Antenna Element in PCB and Hardback Technology

Design of a Single Element and Analysis of Phased Array
Performance

TRA LUNDGREN



Department of Signals and Systems
Division of Antenna Systems
Antenna Research Group
CHALMERS UNIVERSITY OF TECHNOLOGY
Gothenburg, Sweden 2017

Dual Polarized Circular Waveguide Aperture Antenna Element in PCB and
Hardback Technology
Design of a Single Element and Analysis of Phased Array Performance
TRA LUNDGREN

© TRA LUNDGREN, 2017.

Supervisor: Ingolf Larsson, Ericsson AB
Examiner: Marianna Ivashina, Signals and Systems

Department of Signals and Systems
Division of Antenna Systems
Antenna Research Group
Chalmers University of Technology
SE-412 96 Gothenburg
Telephone +46 31 772 1000

Cover: Dual polarized circular waveguide in Printed Circuit Board (PCB) with hardback technology. The final element using a cavity backed slot feeding and its radiation pattern in 3D created by the software HFSS. The image to the right is the single element with both ports excited at 15 GHz. The left side image shows the single element in an 8·8 phased array setup with all elements excited at 15 GHz and its radiated pattern in 3D.

Typeset in L^AT_EX
Gothenburg, Sweden 2017

Dual Polarized Circular Waveguide Aperture Antenna Element in PCB and
Hardback Technology
Design of a Single Element and Analysis of Phased Array Performance
TRA LUNDGREN
Department of Signals and Systems
Chalmers University of Technology

Abstract

This MSc thesis investigates the use of Printed Circuit Board (PCB) hardback technology as a method to manufacture a dual polarized circular aperture antenna element for use in phased arrays operating at mm-wave frequencies. The manufacturing idea is to drill hole(s) in a post-bonded hardback of a PCB, i.e. a 5 mm thick sheet of copper, to create the radiating aperture. The design requirements include:

- i A vertical sub-array should have a co-polar gain larger than 2 dBi at $\pm 60^\circ$ in the azimuth cut.
- ii The reflection- and mutual coupling coefficients of the antenna element should both be lower than -13 dB over a frequency band of at least 6% given the center frequency
- iii The diameter of the radiating aperture should be sufficiently small to allow for an inter-element spacing in the array grid of 0.53λ

In order to achieve the inter-element spacing of 0.53λ the waveguide needs to be loaded. Both dielectric filling and ridges are investigated in this MSc thesis. The element feeding network (i.e. either a stripline feed or a cavity backed slot feed) is included in the element design by using a multilayer stack-up approach. Extensive parametric studies were carried out by using the ANSYS High Frequency Electromagnetic Field Simulation (HFSS) software. The dielectric filled waveguide aperture design, fed with the cavity-backed cross-slot, was found the most promising. It was capable of fulfilling almost all performance requirements, both for the single element and the array.

Keywords: aperture antenna, dual polarized, phased array, hardback PCB, circular waveguide

Acknowledgements

This project would not have been possible without the help and input from a lot of people. First off I'd like to express my gratitude to Marianna Ivashina, my examiner. You have been more than an examiner, helping and supporting me throughout this project. Without you, this project would not have become what it is today. I'd want to thank Ingolf Larsson, my supervisor at Ericsson, for the master thesis idea, design ideas and answering all of my questions. Along with Stefan Johansson, thank you both for giving me this opportunity, enabling me to delve deeper into the world of antennas and for asking great questions!

Livia Cerullo, without you I would've been lost. I can't express my gratitude for your patience and support throughout problems with HFSS, clusters, antennas and life. I'll say it one more time: you're the best. Lars Manholm, I'm really glad you got involved in this master thesis, your input and experience have helped me a lot. Thank you for always being there to help me out, I've appreciated it a ton. Hawal Rashid, you've also helped me out with ideas and new perspectives when I needed it, I look forward to sharing workspace with you again!

Many more people have helped me out with this project, either with ideas, experience, knowledge, support or encouragement, to name a few: Mark Whale, Henrik Boklund, Erik Nilsson, Olle Nyström, Tomas Bergsten, Anders Ek and everyone else; thanks for being a part of this. Last but not least I want to thank all my family and friends for everything.

This is for you grandpa, I'm finally getting the diploma.

Tra Lundgren, Gothenburg, April 2017

Contents

1	Introduction	1
1.1	Purpose	2
1.2	Scope	2
1.3	Objective	2
1.4	Outline of report	3
2	Theory	5
2.1	PCB Hardback Technology	5
2.2	Aperture Antenna Elements	6
2.2.1	Waveguide Elements	8
2.2.1.1	Characterization of Circular Apertures	9
2.2.1.2	Dielectrically Loaded Circular Apertures	11
2.2.1.3	Ridged Circular Apertures	13
2.3	Earlier Designs of Circular Apertures in Phased Arrays	16
2.3.1	Circular Waveguides in Phased Arrays by C. C. Chen	16
2.3.1.1	Dielectric Filled Waveguide Design	18
2.3.1.2	Ridged Waveguide Design	19
2.3.2	Lee's Dielectric Groove Design	21
2.4	Feeding of Circular Apertures	23
2.4.1	E-field Probes	24
2.4.1.1	Striplines	24
2.4.2	Bandwidth Enhanced Slot	25
2.4.2.1	Paryani's Cavity Backed Crossed Slot	26
2.5	Phased Antenna Arrays	30
2.5.1	Element Placement	31
2.5.1.1	Grating Lobes and Beam Steering	33
3	Design Methods	37
3.1	Overview of Workflow	37
3.2	Designs	39
3.2.1	Drilled Ridged Waveguide	39
3.2.1.1	Parametric Study of Ridged Drilled Element	44
3.2.1.1.1	Inner Radius r_1	44
3.2.1.1.2	Outer Radius r_2	44
3.2.1.1.3	Total Radius a	44

3.2.1.2	Conclusions of Parametric Study of Drilled Ridged Element	44
3.2.2	Stripline Fed Dielectric Filled Waveguide	51
3.2.2.1	Stripline Feeding	51
3.2.2.2	Cavity height	53
3.2.2.3	Starting Point	54
3.2.2.3.1	Waveguide Radius: r_{wg}	55
3.2.2.3.2	PCB Substrates: h_1, h_2	56
3.2.2.3.3	Stripline and Vias	56
3.2.2.3.4	Wave Port Setup	57
3.2.2.4	Parametric Study of Stripline Fed Dielectric Element	57
3.2.2.4.1	Isolation Between Polarizations	58
3.2.2.4.2	Stripline Length: L_s	58
3.2.2.4.3	Stripline Width: W_s	59
3.2.2.4.4	Upper Substrate Height: h_2	59
3.2.2.4.5	Lower Substrate Height: h_1	60
3.2.2.4.6	Cavity Size	60
3.2.2.4.7	Waveguide Radius	60
3.2.2.4.8	Waveguide Height	60
3.2.2.5	Conclusions of Parametric Study	61
3.2.3	Slot Coupled Fed Dielectric Filled Waveguide	69
3.2.3.1	Starting Parameters	69
3.2.3.1.1	Slot Length: L	73
3.2.3.1.2	Slot Width: W	73
3.2.3.1.3	Substrate Heights: h_1, h_2, h_3, h_4	74
3.2.3.1.4	Cavity Size: d_{cavity}	74
3.2.3.1.5	Stripline Position and Stub: L_s, L_m	74
3.2.3.2	Parametric Study	74
3.2.3.2.1	Height of Substrate 1: h_1	74
3.2.3.2.2	Height of Substrate 2: h_2	74
3.2.3.2.3	Height of Substrate 3: h_3	75
3.2.3.2.4	Height of Substrate 4: h_4	75
3.2.3.2.5	Slot Length: L	75
3.2.3.2.6	Slot Width: W	75
3.2.3.2.7	Stripline Placement in Slot: L_s	75
3.2.3.2.8	Stripline Width: W_s	76
3.2.3.2.9	Stripline Stub Length: L_m	76
3.2.3.2.10	Cavity Size: d_{cavity}	76
3.2.3.2.11	Waveguide Height	76
3.2.3.2.12	Conclusions of Parametric Study	95
3.2.3.3	Evaluation of Slot Coupled Design	103
3.2.3.4	Stripline in Middle of Slot	104
3.2.3.4.1	Waveguide Radius	107
3.2.3.4.2	Unit Cell Design	108

3.2.3.4.3	Final Parameters	110
4	Results and Discussion	115
4.1	Single Element Performance	115
4.1.1	Sub-array	115
4.1.2	S-parameters	117
4.1.3	Radiation Patterns	118
4.1.4	Losses	122
4.2	Array Performance	124
4.2.1	Mutual Coupling	124
4.2.2	Embedded Patterns	127
4.2.3	Beam Steering	127
5	Conclusions and Recommendations for Future Work	139
5.1	Ridged Element Design	139
5.2	Dielectric Filled Design	139
	References	141
A	Knapsack Problem: Matlab code	I
B	Parametric Study of Stripline Fed Dielectric Element: Impedance	III
C	Parametric Study of Slot Coupled Dielectric Element: Impedance	XI

1

Introduction

In today's society the continuous development of technology goes toward a networked society where everything is connected. The increasing demand for higher data rates, increasing number of devices being connected and a desire to decrease the energy consumption drives the development forward. All these demands are taken into account with the coming of the next generation of mobile networks, the fifth generation: 5G. [1, pp. xxxiii]

One part of the 5G evolution is the use of antenna arrays. [1, 2] At the moment, the base stations in the cellular network mainly use antennas with broad beams to cover the cell. This makes the energy efficiency low since the main part of the energy does not reach the user. Furthermore, the different base stations together with user equipment can cause interference [1, 2], lowering the efficiency of the system and affecting the experience for the end user. The use of antenna arrays could overcome these problems and it is the reason for them being viewed as the next generation of antennas in cellular networks. Antenna arrays present several advantages [3, pp. 330 - 331]:

- Large transmitting planar array antennas have a high directivity which results in a high gain when low-loss materials are used [4].
- In contrast to reflector antennas, which also are highly directional and thus could have a high gain, antenna arrays can have a low profile and thereby occupy less volume.
- The direction and the shape of the beam can be controlled by changing the phase and amplitude of the antenna element excitations, also known as electrically steered beam.

With the beam-forming capability, the energy efficiency will increase since the energy can be concentrated towards the user equipment (UE), e.g. a cell phone. This will also decrease the risk of interference since the signals will be concentrated to smaller areas with less overall transmitted power. [1, pp. 75]

When an antenna element is considered for a 5G phased array the scanning area is relatively large. This means that the antenna element needs to be able to handle a large scan angle and still have a decent bandwidth. Some common element types are: [5]

- Waveguide aperture elements: small bandwidth but handling wide scan angles well.
- Fragmented aperture antenna: large bandwidth but handles wide scan angles bad.
- Tapered-slot antenna: large bandwidth, handles wide scan angles well but is harder to manufacture and has a large physical volume.

Ericsson AB is currently developing 5G technology where the Antenna System and Network Performance department is researching low-cost and high efficiency antenna arrays for 5G.

1.1 Purpose

The purpose of the MSc thesis is to investigate possible aperture antenna element designs with a future use in 5G phased arrays in mind. The aim is to see if it is possible to use a Printed Circuit Board (PCB) with a hardback (see section 2.1) to create a radiating aperture.

1.2 Scope

The project is limited to antenna elements of aperture type and a manufacturing method using PCB hardback technology. Different design concepts are to be investigated and the most suitable antenna element design will be studied in more detail. The investigation is limited to simulations, the aim of the project is to demonstrate the feasibility of the element type and a full optimization of the design is not intended.

1.3 Objective

The antenna designs investigated should fulfill certain requirements in order to determine their performance. The first requirement is that the antenna element shall be implementable into a vertical sub-array. For this MSc thesis, the following design goals for the sub-array design were set:

1. The sub-array shall be a vertical two element sub-array
2. The antenna element diameter shall be $\leq 0.53\lambda$
3. The antenna elements in the sub-array shall be dual polarized
4. The reflection coefficient S_{nn} of the sub-array shall be less than -13 dB
5. The bandwidth shall be more than 5% of the center frequency ($\frac{\Delta f}{f_c} > 0.05$) given the above return loss criteria. Furthermore, the bandwidth should have an added margin of 20% to allow for e.g. impedance bandwidth. This gives a bandwidth criteria of: $0.05 \cdot 1.2 = 0.06 \Rightarrow 6\%$

6. Minimum gain of +2 dBi at $\pm 60^\circ$ in azimuth for a sub-array (-1 dBi for a single element)
7. The difference in the co-polar gains between the two orthogonal polarizations shall at maximum be 3 dB
8. Sub-array loss < 1.0 dB (e.g. difference between directivity and gain < 1.0 dB)
9. Inband isolation between the orthogonally-polarized ports should be below -15 dB
10. The cross-polar decoupling (XPD) [3, pp. 28] should be above 20 dB over the entire operating area: $20 < 10 \log_{10}(\frac{G_{co}(\theta, \phi)}{G_{xp}(\theta, \phi)})$
11. The magnitude of the coupling coefficients to adjacent unit cells (not sub-arrays) in a 0.53λ array grid should be less than -13 dB

The frequency range of the antenna element was not specified in the requirements. For the MSc thesis a center frequency of 15 GHz was chosen, see section 3.2. The operating area of the array was set to $\pm 60^\circ$ in azimuth and $\pm 15^\circ$ in elevation for this MSc thesis.

1.4 Outline of report

First the report start with an introduction to the PCB hardback manufacturing technique in section 2.1 In section 2.2 the basic theory concerning circular waveguide elements is presented. The theory chapter then proceeds to present some of the previous designs of circular apertures in phased arrays that are documented in the literature, see section 2.3. Two of the excitation methods used in this project are also documented in section 2.4. The theory section then concludes with the theory of phased arrays in section 2.5

Chapter 3 deals with the different design concepts investigated in this project. The structure is chronological and summarized accordingly. Here the main focus is on the parametric studies made of each design concept. Finally, the design closest to fulfill the requirements is optimized (section 3.2.3.4) and it is afterwards analyzed in a finite array environment.

The resulting performance of the optimized isolated element and the finite array is presented in chapter 4, where the fulfillment of the requirements stated in section 1.3 is the main focus. In chapter 5 a summary of the conclusions made during the MSc thesis are presented, along with possible future work and questions that could be researched further.

2

Theory

In this chapter the theory of aperture type antenna elements and antenna arrays is presented. The chapter starts with an introduction to the PCB hardback manufacturing technique.

2.1 PCB Hardback Technology

PCBs consists of dielectric material with copper foil on one or both sides, this copper foil is etched and thus used to create circuits. A common problem when designing PCBs is the generated heat during operation. One method of handling the excessive heat is to use a metal hardback as a heatsink, e.g. one of the copper foils is made thicker to dissipate heat. The metal hardback is usually made from copper or aluminum with a thickness ranging from 1 - 10 mm, where thinner hardbacks are easier to manufacture.

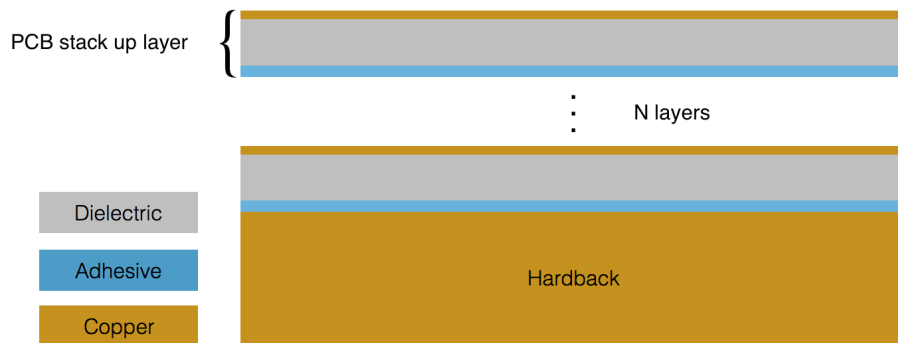


Figure 2.1: Generic overview of a PCB stack up with a post-bonded metal hardback using an adhesive.

There are two types of hardbacks: pre- or post-bonded, relating to the when the hardback is added to the PCB design. The pre-bonded method is limited to a lower thickness range as the hardback then is included in the etching and manufacturing process of the PCB. The post-bonding alternative enables a thicker hardback since it is applied after the etching process. This can be done either by soldering or using an adhesive which can be conductive or non-conductive. In figure 2.1 a generic overview of a PCB with a post-bonding

hardback can be seen. [6–12]

In this MSc thesis a new usage of the metal hardback will be investigated; the possibility of creating a radiating antenna aperture with the hardback, opposed to the original thermal management purpose. To create a radiating aperture, a hole could be drilled in the hardback during the PCB manufacturing process. An advantage of this approach is the simplicity of creating the aperture and the possibility of using the PCB layers underneath the hardback to create the feeding network. In figure 2.2 the general design idea is shown where the feeding and aperture parts of the PCB stack up are marked.

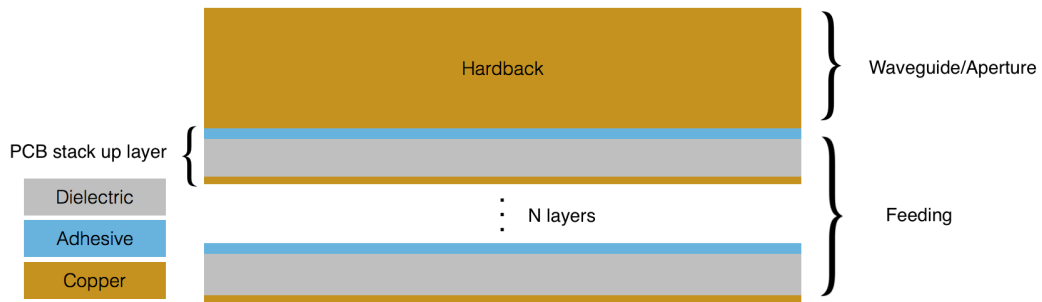


Figure 2.2: A generic PCB stack up showing the design idea of the feeding and aperture placement.

2.2 Aperture Antenna Elements

An aperture antenna element is an element which radiates through an opening in a metal surface [3]. The following elements belong to the aperture antenna family:

1. Waveguides
 - (a) Radiating through the aperture at the end of the waveguide (the cross-section area), see figure 2.3a
 - (b) Radiating slots in a waveguide wall, see figure 2.3b
2. Horn antennas, see figure 2.3c

All of these element types were reviewed at the start of the project. However, both the horn (item 2) and the slots (item 1b) were discarded as possible solutions.

The horn was not considered further due to the requirement of an element diameter smaller than 0.53λ . The element diameter of a horn is too large to be able to fulfill this requirement. [13] Furthermore, a horn is harder to manufacture because of the tapering of the walls. This implies higher production costs and a possible increase in sensitivity due to tolerance issues, when compared

to the other alternatives.

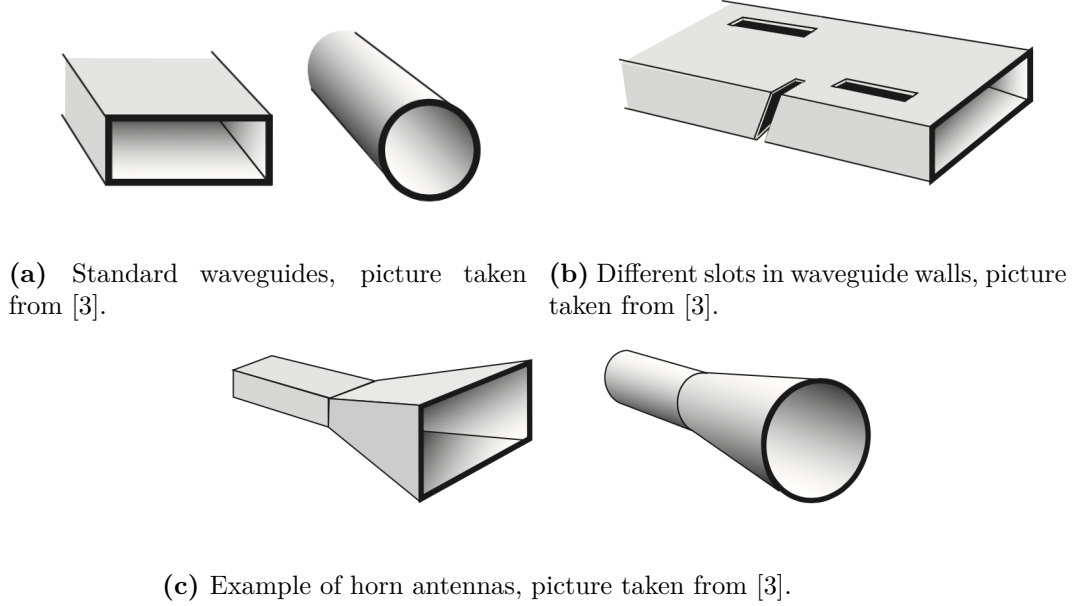


Figure 2.3: Antennas belonging to the aperture family of antennas, pictures taken from [3].

Radiating slots in the waveguide walls (item 1b) was not considered further due to the requirement of a future implementation of the sub-array into a phased array. This requirement requires individual excitation of each element in order to enable beam steering (see section 2.5.1.1). This is a problem with the slots in a waveguide wall due to the difficulty to individual excitation of the slots which in practice would require a complex feeding network. To accomplish an individual excitation, the design would have to be altered and the resulting element would be more alike a rectangular waveguide radiating through their main opening than slots in a waveguide wall.

When both the horns and slots in a waveguide wall are dismissed, the only remaining element is (1a), waveguides radiating through their aperture. This element type is therefore the element type further considered in this MSc thesis.

Another requirement that limits the available design options is the requirement of dual polarization. This requirement infers a constraint on a symmetrical antenna element design, since the resonant frequency needs to be present in two perpendicular dimensions. If the element is not symmetric the different dimensions of the waveguide will result in two different resonant frequencies. Therefore, the waveguide needs to have a symmetric cross-section e.g. circular or square. The usual rectangular design can not be used without a heavy impact on matching conditions for the different polarizations. [14] [15] [16]

2.2.1 Waveguide Elements

Waveguides are a well established RF component invented in the late 19th century [17]. Since then they have been used in different applications, especially where their ability to handle high power is an important factor, e.g. in radars. Waveguides guide the EM-field through encapsulation by metal walls, forcing the field to propagate between the walls.

Waveguides can be seen as a cavity where different discrete solutions exist for a propagating field, called modes. The first mode to propagate has a λ_g of which half fits in the largest diameter of the waveguide ($d_{wg} = \lambda_g/2$). In figure 2.4 the first mode for a rectangular and a circular waveguide is shown where a half λ_g fits over the largest dimension. The corresponding frequency, the cutoff frequency f_c , is the lowest frequency to propagate in the waveguide without being significantly attenuated. However, the attenuation still has a large impact close to f_c .

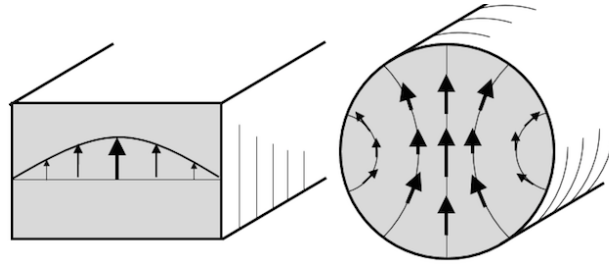


Figure 2.4: The first mode for a rectangular and a circular waveguide, TE_{10} and TE_{11} respectively. Picture taken from [18].

A waveguide can have two different types of modes propagating; Transverse Electric- (TE) and Transverse Magnetic-modes (TM). The difference between these two types is which of the E_z - and H_z -components equals zero (\hat{z} oriented in the propagating direction). When the electric field component in the propagating direction is zero ($E_z = 0$) the mode is of TE type and when the magnetic component is zero in the propagating direction ($H_z = 0$) the mode is a TM-mode. These two types of modes have different solutions to Helmholtz equation which result in different cutoff frequencies. [19, p. 100-101]

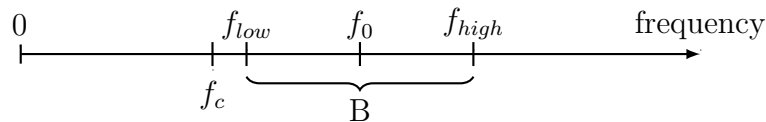


Figure 2.5: Overview of the frequencies involved when designing a waveguide. f_c is the cutoff frequency of the waveguide, f_{low} and f_{high} are the lower respectively higher frequencies of the operating bandwidth (B). f_0 is the center frequency of the bandwidth. Between f_c and f_{low} there should be a margin of 10-20%, $f_{low} = m \cdot f_c$.

In order to not operate too close to the cutoff frequency a rule of thumb is to add between 10-20% margin to the lowest operating frequency, e.g. $f_{low} = m \cdot f_c = 1.1f_c$. A generic overview of the design frequencies when designing an aperture antenna are shown in figure 2.5. The cutoff frequency can be expressed in terms of the center frequency, f_0 , the bandwidth B (in percent of f_0) and the chosen margin m from the cutoff frequency according to

$$\begin{aligned} f_{low} = f_0 \left(1 - \frac{B}{2}\right) &\Rightarrow m f_c = f_0 \left(1 - \frac{B}{2}\right) \Rightarrow \\ &\Rightarrow f_c = f_0 \left(\frac{1 - \frac{B}{2}}{m}\right). \end{aligned} \quad (2.1)$$

Equation (2.1) will prove useful later on.

As mentioned in section 2.1 the design idea is to create the aperture by drilling into the hardback. The most common drills create circular holes, but there exist drills that make squared holes. However, these drills are not as common as the circular ones and information about them is scarce, especially concerning PCB manufacturing techniques. Therefore, with this uncertainty in mind, the MSc thesis was limited to circular apertures, since circular drills are readily available in the PCB manufacturing process.

2.2.1.1 Characterization of Circular Apertures

When designing a circular waveguide the radius, a , is the main design parameter since it determines the cutoff frequency, f_c . The cutoff frequency can be calculated through [19, pp. 121-130]

$$f_c = \frac{q_{nm}}{2\pi a \sqrt{\mu\epsilon}} = \frac{k_c}{2\pi \sqrt{\mu\epsilon}} \quad \text{with} \quad k_c = \frac{q_{nm}}{a} \quad (2.2)$$

where q_{nm} is the m th root to the Bessel function of order n for TM-modes and the m th root to the derivative of the Bessel function of order n for TE-modes, μ is the permeability, ϵ is the permittivity and k_c is the cutoff wave number. In table 2.1 the first TE and TM modes' q_{nm} are listed. [19, pp. 121-130] As can be seen, the first mode to propagate is the TE₁₁-mode since its Bessel constant is the lowest one.

Table 2.1: The Bessel constant, q_{nm} for the first TE and TM modes for a circular waveguide. The lowest constant is for the TE₁₁-mode meaning it has the lowest cutoff frequency and it is therefore the first mode to propagate. [19]

n	TE _{$n1$}	TE _{$n2$}	TE _{$n3$}	TM _{$n1$}	TM _{$n2$}	TM _{$n3$}
0	3.832	7.016	10.174	2.405	5.520	8.654
1	1.841	5.331	8.536	3.832	7.016	10.174
2	3.054	6.706	9.970	5.135	8.417	11.620

The size of the antenna element is important and an upper limit is set by the requirement stating that the element diameter should be smaller than $0.53\lambda_0$ (requirement 2). If equations (2.1) and (2.2) are combined and the radius is expressed in terms of wavelengths ($a = a_c \cdot \lambda_0$), the aperture radius can be expressed as a function of the bandwidth and margin as specified in equation (2.1).

$$\left. \begin{aligned} f_c &= f_0 \left(\frac{1 - \frac{B}{2}}{m} \right) \\ f_c &= \frac{q_{nm}}{2\pi a \sqrt{\mu\epsilon}} \end{aligned} \right\} \Rightarrow \frac{q_{nm}}{2\pi a \sqrt{\mu\epsilon}} = f_0 \left(\frac{1 - \frac{B}{2}}{m} \right) \Rightarrow \quad (2.3)$$

$$\left[a \text{ [m]} \Rightarrow a_c \text{ } [\lambda_0] \right] \Rightarrow a_c = \frac{q_{nm}}{2\pi \sqrt{\mu_r \epsilon_r}} \cdot \frac{m}{(1 - B/2)} \quad (2.4)$$

If only the first fundamental mode is assumed to propagate, the margin from the cutoff frequency is chosen to be 15% and the bandwidth is set to 6% (from requirement 5); equation (2.3) reduces to

$$a_c = \frac{1.871}{2\pi \sqrt{\mu_r \epsilon_r}} \cdot \frac{1.15}{(1 - 0.06/2)} = \frac{0.3530}{\sqrt{\mu_r \epsilon_r}} \text{ } [\lambda_0] \Rightarrow \quad (2.5)$$

$$d_c = \frac{0.695}{\sqrt{\mu_r \epsilon_r}} \text{ } [\lambda_0] \left[q_{nm} = q_{TE11} = 1.871, m = 1.15, B = 0.06 \right]. \quad (2.6)$$

As can be seen, the diameter of the aperture, d_c , is too large when the requirement of an element diameter below $0.53\lambda_0$ (requirement 2) is considered, if no alteration of the relative permeability or permittivity is made. The conclusion is that a circular aperture element needs to be loaded in order to fulfill requirement 2. The two main methods of loading a waveguide is to fill the element with dielectric material or to use ridges. Both of these two methods enables a smaller physical size whilst keeping the electrical size of the waveguide the same [20].

The aperture radius also affects the radiation pattern, for example the beamwidth in the E- and H-planes. [21] If the field distribution in the circular waveguide corresponds to a TE_{11} -mode, which is valid for a circular waveguide operating with the first fundamental mode, the E- and H-fields expressed in a spherical coordinate system are [22, pp. 688]

$$\begin{aligned} E_r &= 0 & H_r &= 0 \\ E_\theta &= C_2 \sin(\phi) \frac{J_1(Z)}{Z} & H_\theta &= -\frac{E_\phi}{\eta} \\ E_\phi &= C_2 \cos(\theta) \cos(\phi) \frac{J'_1(Z)}{1 - (Z/q_{TE11})^2} & H_\phi &= \frac{E_\theta}{\eta}, \end{aligned} \quad (2.7)$$

where $J_n(x)$ is the Bessel function of order n of the value x , r is the distance from the aperture and

$$\begin{aligned}
Z &= ka \sin(\theta), & J'_1(Z) &= J_0(Z) - J_1(Z)/Z, & k &= \omega \sqrt{\mu \epsilon}, \\
\eta &= \sqrt{\mu/\epsilon} & \text{and} & & C_2 &= \frac{jka E_0 J_1(q_{TE11}) e^{-jkr}}{r}.
\end{aligned} \tag{2.8}$$

Both E-field components (E_θ and E_ϕ) are proportional to a , the radius of the aperture.

In figure 2.6 these two field components are shown for different values of the aperture radius, a (equation (2.7)). E_θ and E_ϕ corresponds to the E-field in the E- and H-plane respectively. From the specifications listed in section 1.3 the difference in co-polar gain between the two polarizations in any plane should be less than 3 dB (requirement 7). The E- and H-plane cuts are orthogonal and thus a comparison between them can be used as a first control of this requirement (the E- and H-planes would correspond to the two polarizations given a symmetric antenna).

From figure 2.6 it can be seen that a larger aperture size narrows the pattern of the E-plane co-polar gain, making it more similar to the H-plane cut. The edge of the operating area is at $\pm 60^\circ$ and at this point the difference between the E- and H-plane cuts are the largest. As can be seen the difference at $\pm 60^\circ$ decreases with increasing aperture radius and at $a = 0.22\lambda_0$ the difference between the co-polar gains is $\Delta E_{60^\circ} = 3.0369$ dB.

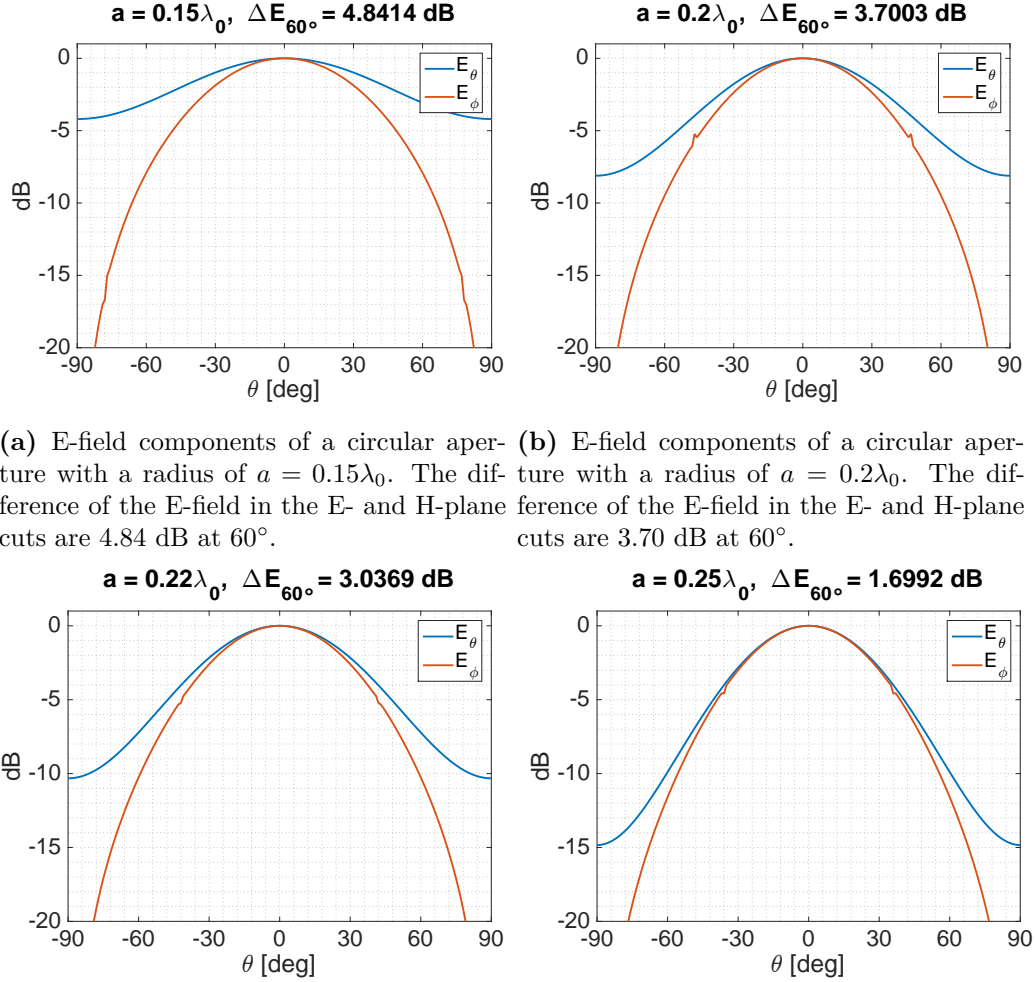
The conclusion is therefore that the aperture radius needs to be slightly larger than $0.22\lambda_0$ in order to fulfill requirement 7. When using equations (2.7) and (2.8) the relative permittivity was set to $\epsilon_r = 4$ since this dielectric filling is available in the PCB manufacturing process (see section 3.2). The radius of the aperture was rescaled to free space wavelengths to remove the frequency dependency and make it easier to assess the unit cell size requirement (requirement 2).

2.2.1.2 Dielectrically Loaded Circular Apertures

One method commonly used to load a waveguide is the use of dielectric filling inside the waveguide, meaning that a material with a higher permittivity than unity is used ($\epsilon_r > 1$). [5, 20, 23] When the relative permittivity, ϵ_r , is increased the physical size of the waveguide can be smaller while keeping the electrical size of the waveguide the same, see equation (2.5). The wavelength of a specified frequency scales proportionally with the square-root of ϵ_r according to [19, pp. 16-17]

$$\lambda_g = \frac{\lambda_0}{\sqrt{\epsilon_r}}. \tag{2.9}$$

This can also be seen in equation (2.2) where an increase in permittivity decreases the cutoff frequency, meaning a larger wavelength now fit in the wave-



(a) E-field components of a circular aperture with a radius of $a = 0.15\lambda_0$. The difference of the E-field in the E- and H-plane cuts are 4.84 dB at 60° . (b) E-field components of a circular aperture with a radius of $a = 0.2\lambda_0$. The difference of the E-field in the E- and H-plane cuts are 3.70 dB at 60° .

(c) E-field components of a circular aperture with a radius of $a = 0.22\lambda_0$. The difference of the E-field in the E- and H-plane cuts are 3.04 dB at 60° . (d) E-field components of a circular aperture with a radius of $a = 0.25\lambda_0$. The difference of the E-field in the E- and H-plane cuts are 1.70 dB at 60° .

Figure 2.6: The E_θ and E_ϕ components of the E-field of a circular aperture for different radii, obtained using equations (2.7) and (2.8). The fields have been normalized to 0. The specifications requires a maximum difference in the co-polar gain between the two polarizations to be below 3 dB (requirement 7). ΔE_{60° is the difference between the two E-field cuts at 60° which can be used as an indication of whether or not requirement 7 can be fulfilled. To fulfill this requirement a radius of at least $0.22\lambda_0$ is needed.

uide even though the physical size remains the same. Equation (2.3) can be rewritten to express the permittivity instead

$$\epsilon_r = \left[\frac{q_{nm}}{2\pi a \sqrt{\mu\epsilon_0}} \cdot \left(\frac{f_0(1 - \frac{B}{2})}{m} \right)^{-1} \right]^2 \quad (2.10)$$

By expressing the aperture radius a in terms of free space wavelengths, $a = a_c \cdot \lambda_0$, equation (2.10) can be rewritten as

$$\begin{aligned} \epsilon_r &= \left[\frac{q_{nm}}{2\pi a_c \lambda_0 \sqrt{\mu\epsilon_0}} \cdot \frac{m}{f_0(1 - \frac{B}{2})} \right]^2 = \left\{ f_0 = \frac{c_0}{\lambda_0} \right\} = \\ &= \left[\frac{q_{nm}}{2\pi a_c \lambda_0 \sqrt{\mu\epsilon_0}} \cdot \frac{\lambda_0 m}{c_0(1 - \frac{B}{2})} \right]^2 = \left\{ c_0 = \frac{1}{\sqrt{\mu_0\epsilon_0}} \right\} = \\ &= \left[\frac{q_{nm}}{2\pi a_c \sqrt{\mu\epsilon_0}} \cdot \frac{m \sqrt{\mu_0\epsilon_0}}{(1 - \frac{B}{2})} \right]^2 = \left[\frac{q_{nm}}{2\pi a_c \sqrt{\mu_r}} \cdot \frac{m}{(1 - \frac{B}{2})} \right]^2 \end{aligned} \quad (2.11)$$

to make it frequency independent.

In figure 2.7 this relationship is graphically shown for the first propagating mode (TE₁₁) in a circular waveguide with different values of B and m , the relative permeability μ_r is set to one. From the graph one can see that in order to get an element diameter smaller than 0.5λ (i.e. a radius $< 0.25\lambda_0$) an $\epsilon_r > 2$ is needed, for a bandwidth percentage $> 5\%$.

2.2.1.3 Ridged Circular Apertures

The other method used to reduce the physical size of a waveguide is to alter the geometry of the waveguide cross-section by using ridges. In order to have the two polarizations of the antenna element to have similar characteristics the cross-section of the waveguide needs to be symmetric in two planes, meaning that the waveguide needs to be of the four ridged type. In figure 2.8 a quad ridge circular waveguide cross-section can be seen. [5, 20, 23]

The cutoff frequency of a quad ridge waveguide can be calculated through [24]

$$2\pi\mathbf{H}(\rho) = \oint_c \mathbf{J}(\rho') \times \nabla'_t G dl' \quad (2.12)$$

which gives for a TE-mode (only circumferential component)

$$2J_t(\rho) - jk_c \oint_c J_t(\rho') \sin\left(\hat{r}, \frac{\rho' - \rho}{|\rho - \rho'|}\right) \times H_1^{(2)}(k_c|\rho - \rho'|) dl' = 0 \quad (2.13)$$

and for a TM-mode (only axial component)

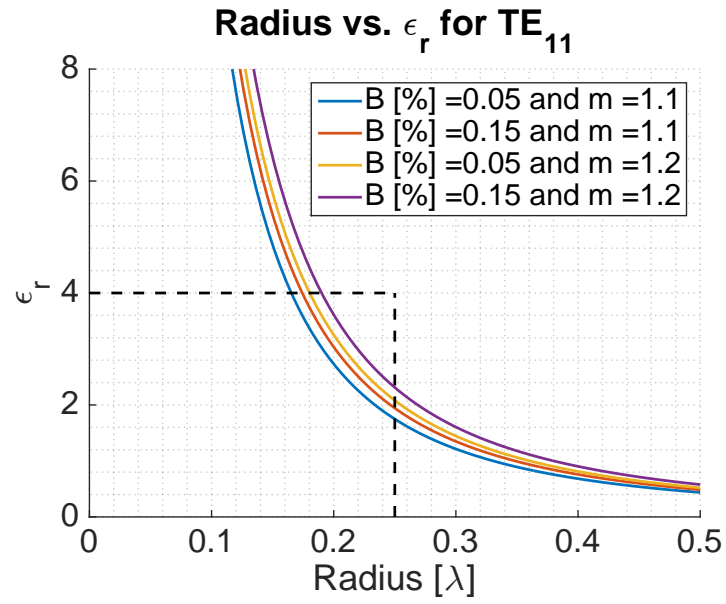


Figure 2.7: Graph of equation (2.11) for the first propagating mode in a circular waveguide, TE₁₁. The available dielectric filling ($\epsilon_r = 4$) in the PCB manufacturing process and a radius of $0.25\lambda_0$ are marked in the graph.

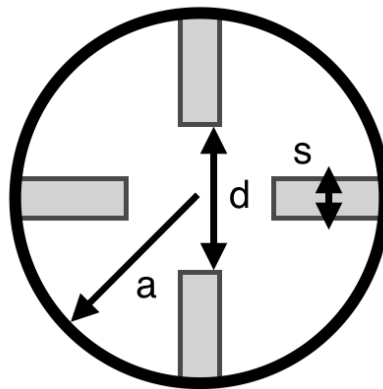


Figure 2.8: A generic layout of a quad ridged circular waveguide's cross-section.

$$2J_z(\rho) - jk_c \oint_c J_z(\rho') \sin\left(\hat{t}', \frac{\rho' - \rho}{|\rho - \rho'|}\right) \times H_1^{(2)}(k_c|\rho - \rho'|) dl' = 0 \quad (2.14)$$

where the sine-function is the angle between two unit vectors, \hat{t}' is the tangential unit vector and ρ is the position vector. Through these equations Balanis and Sun [24] created a graph showing the cutoff frequencies for different geometries, see figure 2.9.

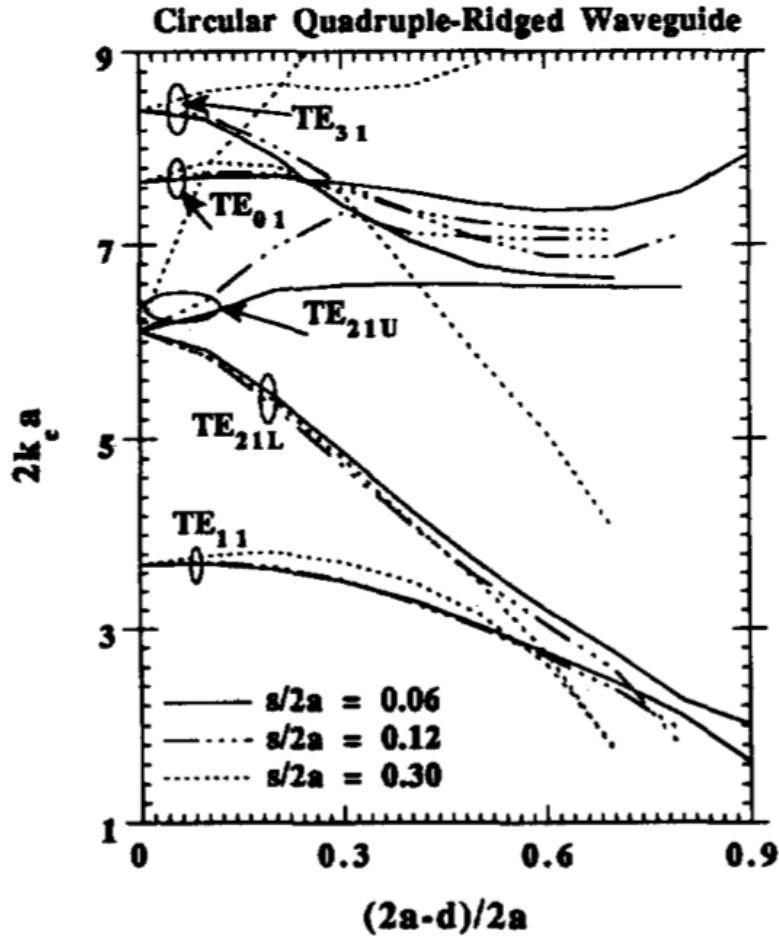


Figure 2.9: Cutoff frequencies for a circular quad ridged waveguide, see figure 2.8 for notations. Graph is taken from [24].

Waveguides with four ridges suffer from mode splitting which can be seen in figure 2.9 where TE_{21} has an upper and a lower version of its original form. These are created by two different excitations of the TE_{21} . The lower version, TE_{21L} , is created by two in-phase TE_{21} whilst the upper version, TE_{21U} , is created by two anti-phase TE_{21} . [24] [25]

As can be seen in figure 2.9 the second mode to propagate is TE_{21L} . This mode has a closer cutoff frequency to the fundamental mode than in a waveguide without ridges. Therefore, the available bandwidth for a ridge waveguide, in this regard, is smaller. The TE_{21L} needs to be suppressed in order for a quad ridge circular waveguide to be able to fulfill the bandwidth requirement. Another characteristic seen in figure 2.9 is that the ridge height is the main parameter affecting the cutoff frequency.

2.3 Earlier Designs of Circular Apertures in Phased Arrays

At the start of the MSc thesis a thorough investigation of previous work concerning circular apertures in phased arrays was made. In this section a short summary of the relevant articles from this study is presented.

The use of waveguide aperture antennas as elements in phased arrays was mainly investigated during the 1960's to the 80s. Using PCB to create the aperture elements was not an established manufacturing method during this time period. The most common approach was to use standard waveguides with either ridges, dielectric filling or a combination of both and assemble these into an array. The specifications for these early designs differs from the specifications for this project. The main differences are a larger bandwidth with a lower requirement of S_{nn} (e.g. $|S_{11}| < -10$ dB compared to $|S_{11}| < -13$ dB for this project).

As mentioned, most of the work was done 50-30 years ago, where a handful of persons wrote a major part of the available material. Three of the main design concepts (ridges, dielectric filling and disks/grooves) are described in more detail below by two of the main authors, C. C. Chen and J. J. Lee. Other relevant material found are listed in table 2.2.

2.3.1 Circular Waveguides in Phased Arrays by C. C. Chen

Chen investigated different methods to implement waveguides as antenna elements in phased arrays and compared the performance of these designs. In particular, he presented two designs for squared and circular waveguides respectively. However, only the circular designs implements a dual-polarization. The circular waveguide designs comprise one using dielectric filling and one using ridges to reduce the element size. [20]

Table 2.2: Short summary of relevant articles related to circular aperture antenna elements in phased arrays.

Ref. no.	Short summary
[13]	Ridged square and circular waveguides and their performance given the geometry of the ridges.
[14]	Three geometries of rectangular waveguides in phased arrays and their performance.
[25]	Theoretical expressions and analysis of ridged waveguides.
[26]	Resonances, surface waves and reflection at aperture of circular waveguides in phased array. Numerical analysis of the theoretical boundary value problem of triangular grid.
[27]	Shorter version of [26].
[28]	Matching of circular waveguide element with dielectric disks.
[29]	Design of dielectric sheet above array of circular waveguides to avoid reflections when scanning. Dielectric disks for loading.
[30]	Design of element using dielectric filling, metallic disks, ridges and foam.
[31]	Mode degeneracy and impact on bandwidth when using ridges (dual, quad, octo).
[32]	Bandwidth and cutoff frequency of quad ridged waveguides.
[33]	Modes, cutoff frequencies and other characteristics of quad ridged waveguides.
[34]	Quad ridged waveguide with hollow ridges as feed. Dual frequency bands.
[35]	Quad ridged square waveguide with dielectric slab in middle to create circular polarization.
[36]	Wide-angle, wide-band phased array elements; waveguides investigated but discarded in favor of a tapered slot.
[37]	Characteristics of squared dual and quad ridged waveguides in a phased array environment.
[38]	Square and circular ridged waveguides: attenuation, power handling and cutoff frequency of first fundamental mode.

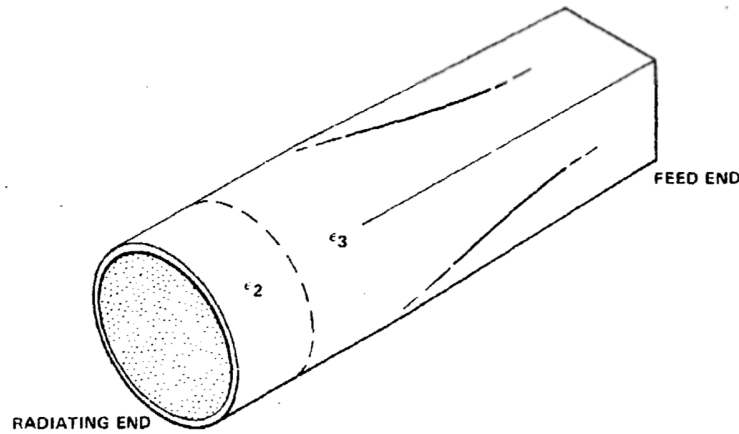


Figure 2.10: Chen’s circular waveguide aperture element design using a dielectric filling. The element has a square waveguide section at the feeding point which then smoothly transitions to a circular waveguide in order to suppress the circular TM_{01} -mode. The drawing and design were taken from [20].

2.3.1.1 Dielectric Filled Waveguide Design

In figure 2.10 the dielectric filled element can be seen. The dielectric material numbered 2 at the radiating end is chosen so that its permittivity, ϵ_2 , prevents the TM_{01} -mode. This means that ϵ_2 should be low enough to only admit the first circular mode TE_{11} . Prevention of the circular TM_{01} -mode from propagating is also the purpose of the square feed. By suppressing the TM_{01} , which is the next propagating mode for a circular aperture after the first fundamental mode TE_{11} , the bandwidth of the element is increased. The other dielectric material (number 3), with the permittivity ϵ_3 , together with the physical dimensions of the different parts of the element is chosen so as to impedance match the element. [20]

The reason for the TM_{01} prevention at both the radiating and feeding end of the element is to make sure that the mutual coupling between the elements in the array does not excite the TM_{01} -mode in either end. The resulting bandwidth is shown in figure 2.11 where a bandwidth of $\sim 30\%$ is achieved with a VSWR of 2 ($RL = -9.5$ dB).

Problems with this design according to Chen ([20] p. 5-1) is:

“...fabrication of this array is very cumbersome from the standpoint of weight, cooling, packaging, efficiency and cost effectiveness.”

Those are all troublesome points with the requirements of this MSc thesis in mind. Furthermore, using two different dielectric materials adds complexity to the manufacturing process. The continuous transition between a squared feed and a circular aperture is also hard to accomplish if a simple drilled hole is the considered manufacturing technique. A discrete step solution could be

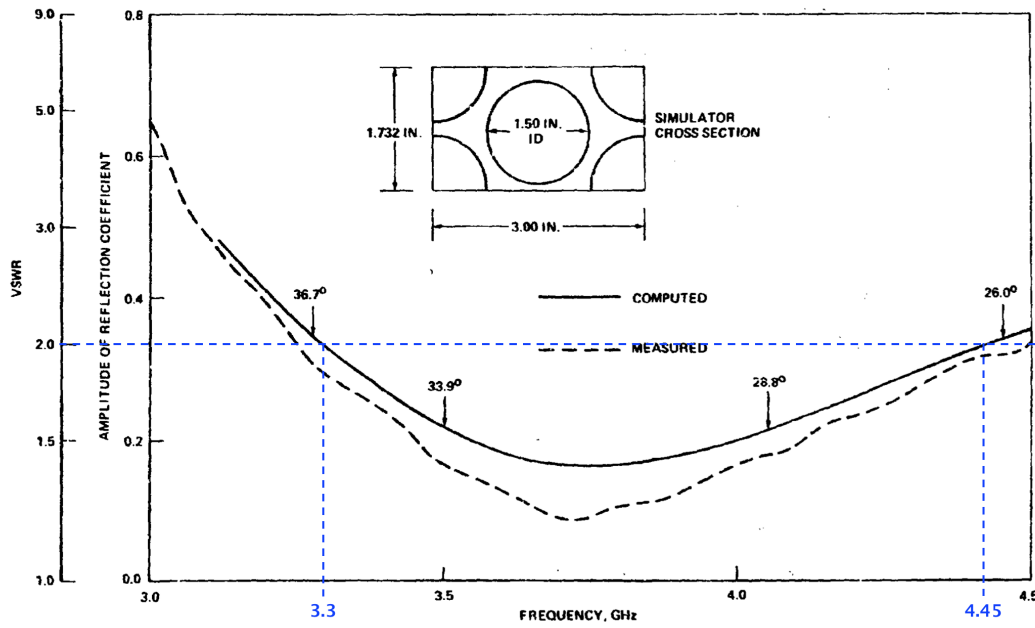


Figure 2.11: Graph of reflection coefficient and VSWR versus frequency of Chen's dielectric design in a phased array implementation. With a VSWR of 2 the corresponding bandwidth between frequencies 3.3 and 4.45 GHz is $\sim 30\%$ with a center frequency of 3.875 GHz. Figure is taken from [20] with modifications in blue.

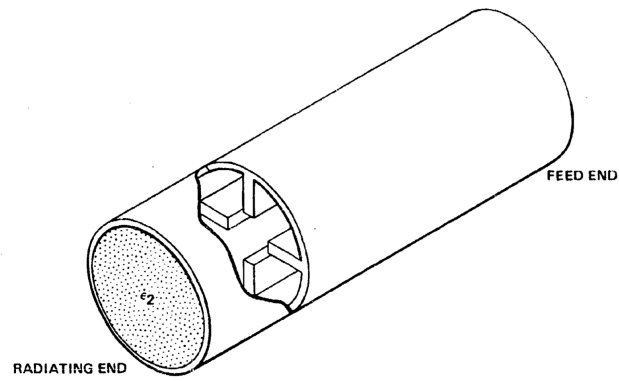
possible by using drills of different sizes and layouts. However, this is outside of the scope since only circular drills are to be used.

2.3.1.2 Ridged Waveguide Design

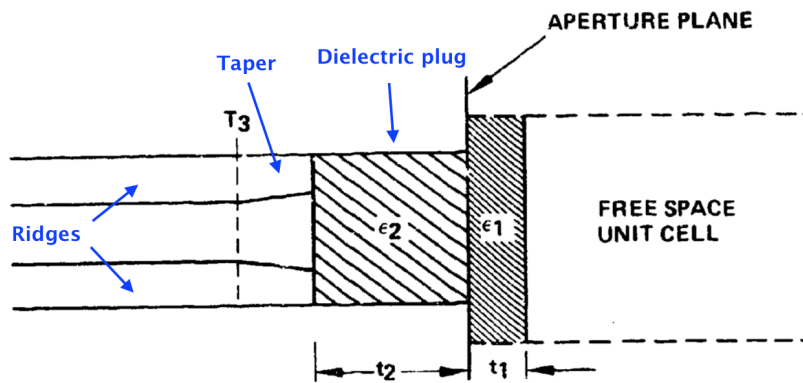
In figure 2.12 the ridged design by Chen can be seen. The waveguide has four ridges in order to facilitate a dual polarization. The ridges are slightly tapered as can be seen in figure 2.12b and its radiating end has a dielectric plug before the ridges. According to Chen, the ridges increase the available bandwidth between TE_{11} and TM_{01} and give rise to a lower attenuation of the field than the dielectric filled design. In Chen's design the TM_{01} -mode is evanescent in the ridged part of the waveguide and the dielectric part suppresses the TE_{21} -mode. [20]

The return loss of the design implemented in an array is seen in figure 2.13 where a VSWR of 2 (corresponding to a return loss of 9.5 dB) gives a bandwidth of $\sim 20\%$ with 3.85GHz as the center frequency. [20]

Ridges of the common type, rectangular thick metal sheets protruding into the waveguide, is hard to create by drilling into a PCB hardback. Especially when they are tapered and a dielectric plug is used as well, as was the case in Chen's design. The problem with a dielectric plug is that the dielectric filling created during the PCB manufacturing process is in liquid form at first and then solidifies.



(a) Overview of ridged waveguide, design and picture taken from [20].



(b) Sideview of ridged waveguide, worth noting is the taper of the ridges and the dielectric filling close to the aperture. Design and picture taken from [20].

Figure 2.12: Ridged circular waveguide element for phased array use. Picture taken from [20].

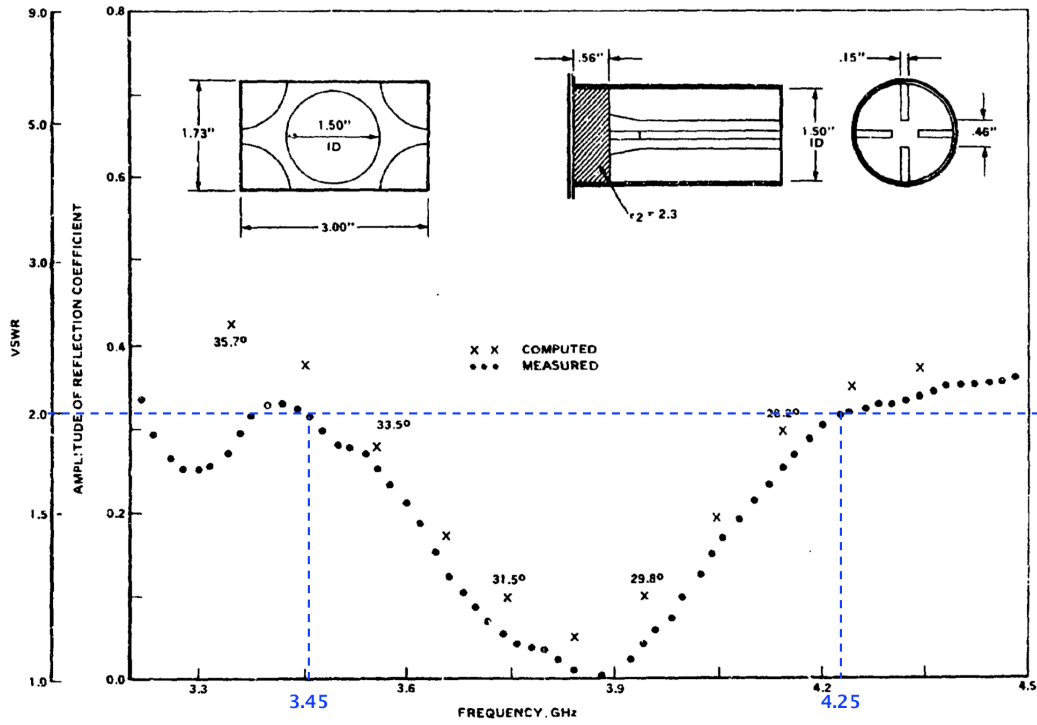


Figure 2.13: Graph of reflection coefficient and VSWR versus frequency of Chen's ridged design in a phased array implementation. With a VSWR of 2 the corresponding bandwidth between frequencies 3.45 and 4.25 GHz is ~20% with a center frequency of 3.85 GHz. Picture is taken from [20] with modifications in blue.

2.3.2 Lee's Dielectric Groove Design

Lee presents in [39] a design where a circular groove in the dielectric filling of a circular waveguide is used for impedance matching. The starting idea for Lee was his conclusion that an infinitely thin metal iris would create a good matching for a waveguide element. Lee deduced that manufacturing an infinitely thin iris was too complex and he investigated a different realization, i.e. a dielectric groove. In figures 2.14 and 2.15 the first design idea is presented as well as the realization where the iris is exchanged for a thinner dielectric slab of a lower permittivity than the dielectric filling material. [39]

However, Lee found the manufacturing of two different dielectric materials too complex and therefore changed the design once more. Lee exchanged the dielectric slab with an H-shaped plug of the same dielectric constant as the filling which can be seen in figure 2.16 where the final design is shown. Lee combined simulations and measurements to find the best design of the dielectric plug. [39]

The return loss of Lee's final design using a dielectric plug in an array can be seen in figure 2.17 for vertical polarization in the H-plane when scanning to

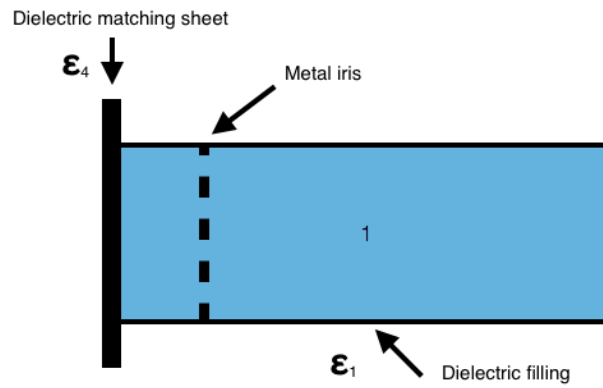


Figure 2.14: Sideview of Lee's design, a waveguide with dielectric filling and an infinitely thin metal iris, the starting idea.

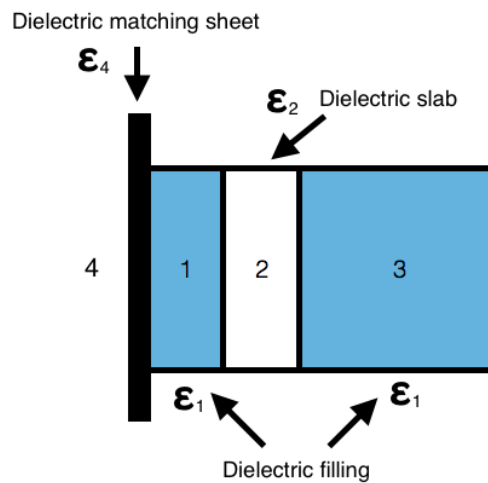


Figure 2.15: Sideview of Lee's design, a waveguide with a thin dielectric slab (2) with lower permittivity than the dielectric filling ($\epsilon_2 < \epsilon_1$) used as a substitute for an infinitely thin metal iris.

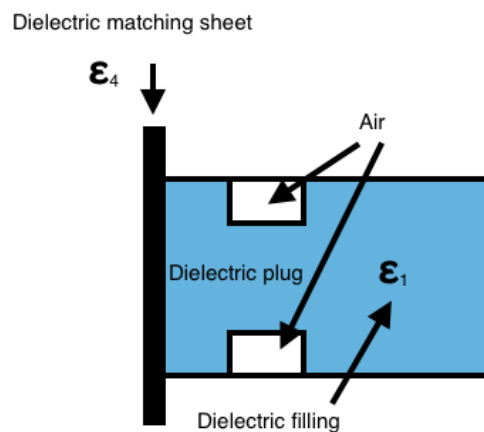


Figure 2.16: Lee's final design of the replacement of the thin metal iris using a dielectric plug in the waveguide instead. The plug is created by removing some of the dielectric material, shown in the figure as the white portion in the waveguide filled with air.

32° with the array. For a return loss value of 10 dB a relative bandwidth of $\sim 6\%$ is achieved for a center frequency of 9.325 GHz. [39]

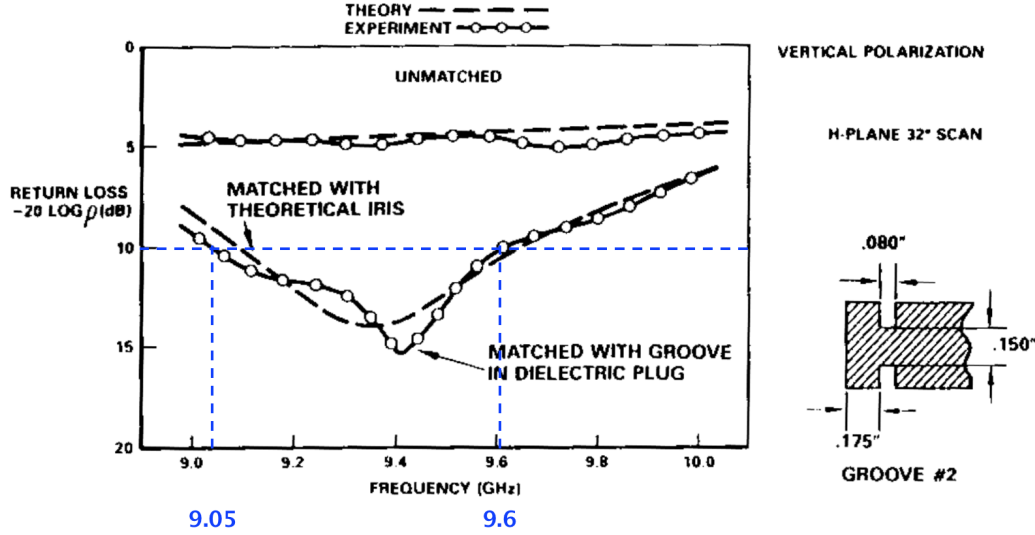


Figure 2.17: The return loss versus frequency of Lee's final design with a dielectric plug as well as an unmatched element. Both simulations and measurements are presented for both designs. With a return loss of 10 dB the corresponding bandwidth between frequencies 9.05 and 9.6 GHz is $\sim 6\%$ with a center frequency of 9.325 GHz. Picture is taken from [39] with modifications in blue.

This design approach is hard to implement given the PCB hardback manufacturing technique, since the considered dielectric filling is made by filling the drilled hole with a liquid dielectric material which later harden and becomes solid. This is not compatible with the creation of the groove shown in Lee's design.

The same is not entirely true for the metal iris which was the starting point. The drilled hole could be partially filled with dielectric filling, a metal iris added when the filling has solidified and then another layer of dielectric filling could be added. This would add complexity to the manufacturing process but it could be done.

2.4 Feeding of Circular Apertures

In order for an antenna to function it has to be excited. The signal comes from the receiver or transmitter circuit and the impedance of these parts needs to be transformed to the antenna impedance. In this section different feeding concepts are presented which will be used later in the project.

2.4.1 E-field Probes

One common feeding method when feeding a waveguide is to use an E-field probe, e.g. a stripline, inserted a distance of approximately $\lambda_g/4$ from the end wall. The probe should be inserted along the E-field lines of the mode(s) that is excited. It acts as a current source which excites the E-field where the intensity depends on where in the E-field it is inserted. If the probe is at the point where the E-field has its maximum amplitude (e.g. the middle of the waveguide for the first mode) the coupling between the probe and the waveguide is maximized. The probe excites higher order modes as well which are evanescent, they alter the impedance of the probe and as such the distance to the end wall is not exactly $\lambda_g/4$. In figure 2.18 a cross-section of the probe is seen, using the distance from the end wall and the length of the probe the performance of the excitation can be optimized. [40, pp. 276-281]

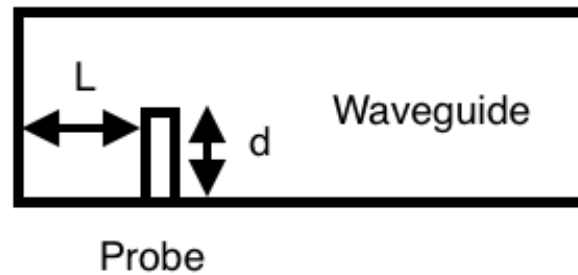


Figure 2.18: Generic cross-section of a waveguide fed with an E-field probe.

An E-field probe is often made by using a coax transition where the center pin is inserted into the waveguide through a slit. Another possibility is to make the probe from a stripline. Since this project is limited to a PCB hardback design technique, a stripline approach is likely.

2.4.1.1 Striplines

A stripline consists of a conductor in between two dielectric substrates, a cross-section view is seen in figure 2.19 for an asymmetric stripline. It is considered asymmetric since the two substrate heights are different. To calculate the impedance of an asymmetric stripline is somewhat tedious, but can be done by using [41, pp. 126-133]

$$Z_0 = \frac{1}{\sqrt{\epsilon_r}} \left[Z_{0,ctr}(1, W, b, t) - \Delta Z_{0,air} \right] \quad \text{with} \quad (2.15)$$

$$Z_{0,ctr}(1, W, b, t) = \frac{\eta_0}{2\pi\sqrt{\epsilon_r}} \ln \left(1 + 0.5 \frac{8b}{\pi w'} \left[\frac{8b}{\pi w'} + \sqrt{\left(\frac{8b}{\pi w'} \right)^2 + 6.27} \right] \right), \quad (2.16)$$

$$Z_{0,air} = 2 \left[\frac{Z_{0,ctr}(1, W, h_1, t) \cdot Z_{0,ctr}(1, W, h_2, t)}{Z_{0,ctr}(1, W, h_1, t) + Z_{0,ctr}(1, W, h_2, t)} \right], \quad (2.17)$$

$$\Delta Z_{0,air} = \frac{0.26\pi}{8} Z_{0,air}^2 \left(0.5 - \frac{h_1 + t/2}{h_1 + h_2 + t} \right)^{2.2} \left(\frac{t + W}{h_1 + h_2 + t} \right)^{2.9}, \quad (2.18)$$

$$w' = W + \frac{\Delta w}{t} t, \quad (2.19)$$

$$\frac{\Delta w}{t} = \frac{1}{\pi} \left[1 - 0.5 \ln \left(\frac{1}{(2b/t + 1)^2} + \left[\frac{1/4\pi}{W/t + 1.1} \right]^m \right) \right], \quad (2.20)$$

$$\text{and } m = \frac{6}{3 + 2t/b}. \quad (2.21)$$

When the width of the stripline is increased the resistance is decreased and vice versa.

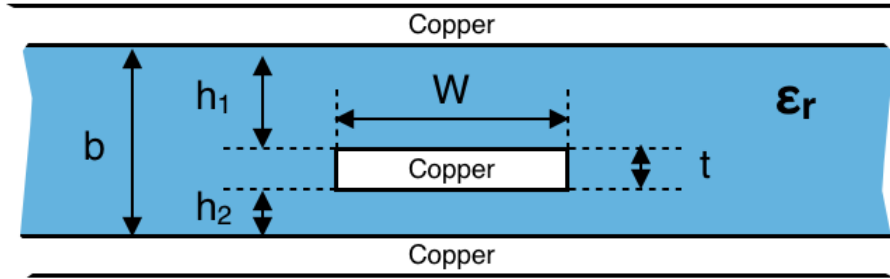


Figure 2.19: Cross-section of an asymmetric stripline with notation.

2.4.2 Bandwidth Enhanced Slot

A waveguide can also be excited by a slot which in turn is excited by e.g. a probe or a stripline. A slot can be seen as a waveguide aperture where the waveguide is very short in the propagation dimension. The first resonant frequency of a slot is the frequency with a wavelength corresponding to the slot length of $L = \lambda_g/2$ [3, 22, 42, 43] (the same as for a rectangular waveguide, see section 2.2.1).

In [42] a way to improve the bandwidth of a slot excited by a microstrip is presented by creating a dual resonance. The microstrip creates a fictitious short circuit when the microstrip feeds the slot close to the edge, see figure 2.20. As

a result the slot exhibits two resonances since it, from an electric field view-point, has two effective lengths. The first resonant frequency is the standard frequency corresponding to a slot length of $L = \lambda_g/2$. The second resonant frequency is higher since the length of the slot has become shorter, as the fictitious short circuit is seen as the slot edge.

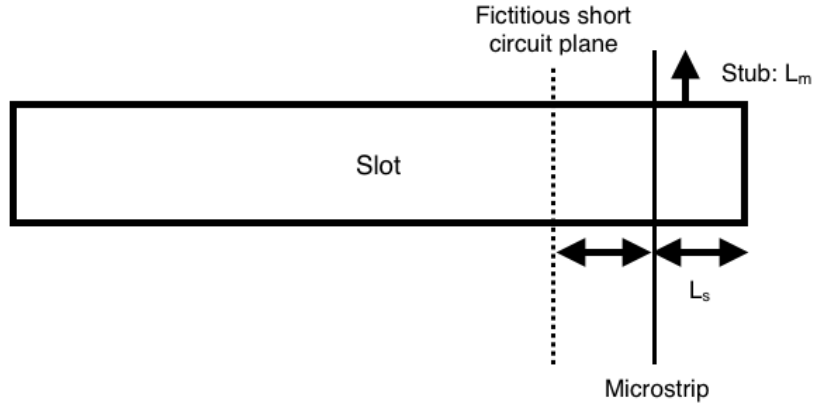


Figure 2.20: Schematic view of a double resonant slot fed by a microstrip line creating a fictitious short circuit.

The idea can be seen in figure 2.21 where the simulated electric field of the slot is seen for the two resonances, in figure 2.22 an overview is seen. In figure 2.22 (a) the lower resonance is seen without the fictitious short circuit. The higher resonance's E-field is seen in figure 2.22 (b) where the slot length is shorter. The distance from the slot edge to the microstrip, L_s , is the main design parameter which determines the second resonant frequency. The stub length, L_m and width of the slot, W , are then used to create a matched case for both resonances. [42], [43]

2.4.2.1 Paryani's Cavity Backed Crossed Slot

In [44] Paryani describes a cavity backed cross slot designed created with PCB. The usage of PCB makes the design interesting since a hardback PCB is to be used in this project. Unfortunately, there are some inconsistencies in the given parametric values in the report with regards to the pictures, tables and text. Therefore, no exact values are given here, only the general conclusions made by Paryani et. al. [44, 45]

The PCB stack up consists of a square cavity created by vias in the PCB, a cross slot to achieve a dual polarization and a feeding layer with microstrip lines connected with vias to feeding ports on the bottom. In figures 2.23 and 2.24 the design and stackup can be seen. [44, 45]

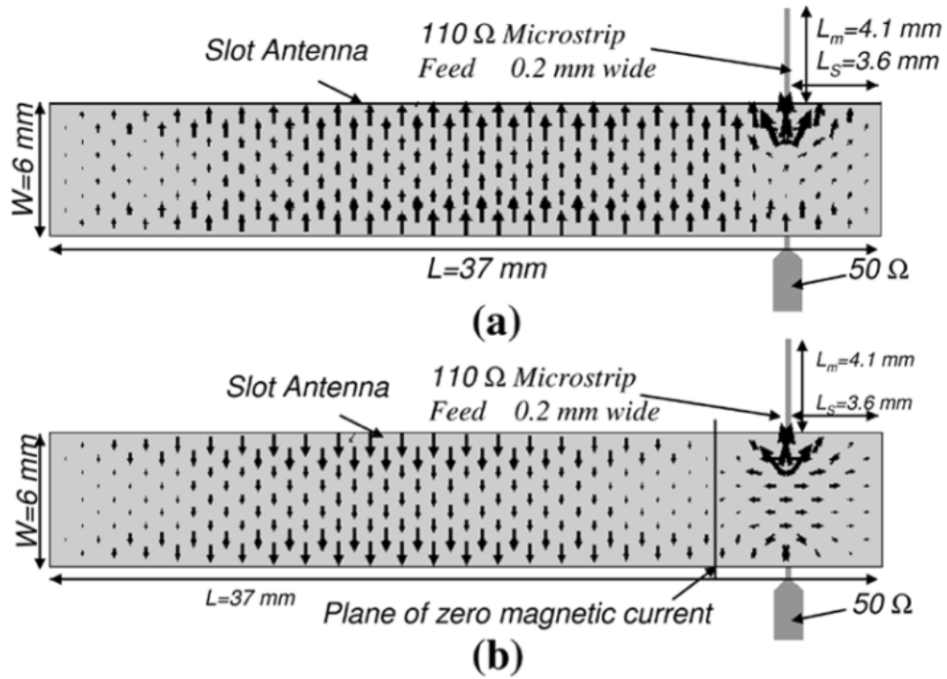


Figure 2.21: Field distribution of the slot showing the two resonances. In figure (a) the standard excitation is seen where the whole slot is excited. In figure (b) the field distribution with the fictitious short circuit is seen. For the excitation case when the microstrip creates a fictitious short circuit the resulting effective resonant length of the slot is shorter than in the ordinary case, creating a resonance at a higher frequency. Picture taken from [43].

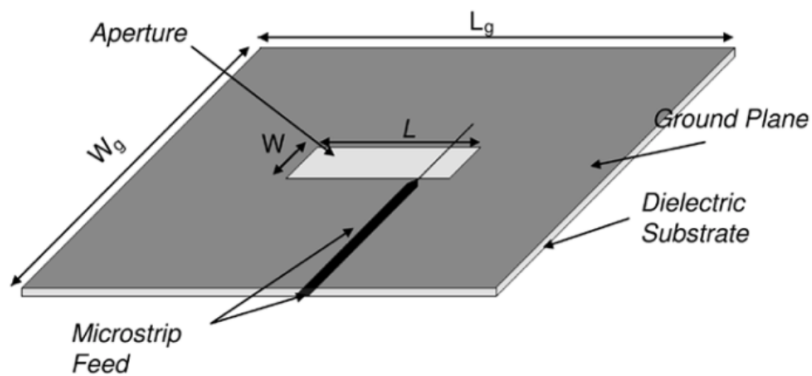


Figure 2.22: Perspective view of the double resonant slot with its ground plane. Picture taken from [43].

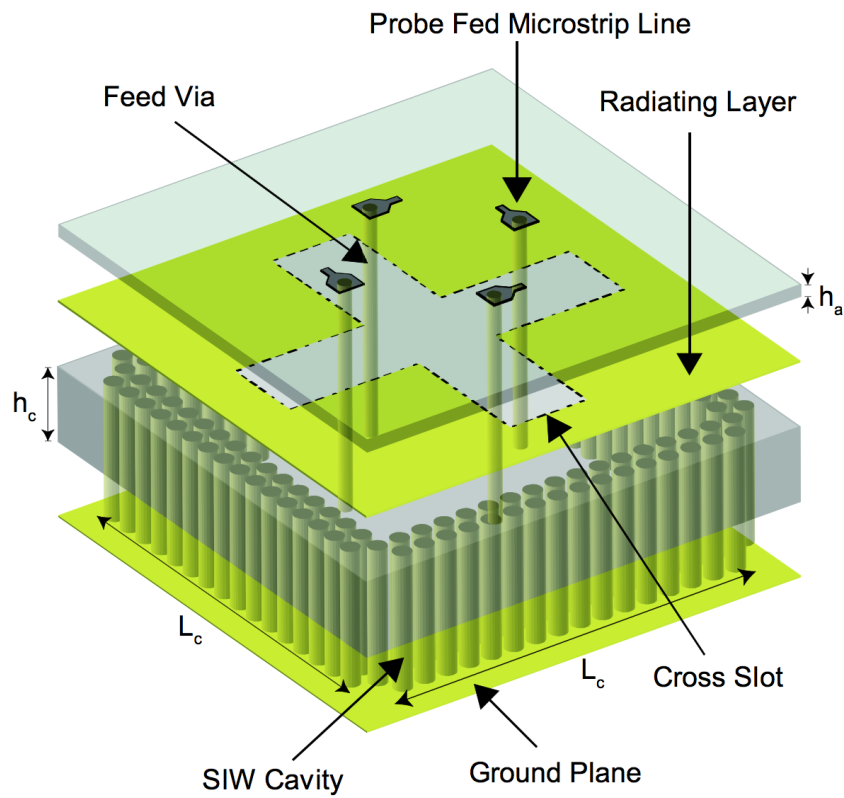
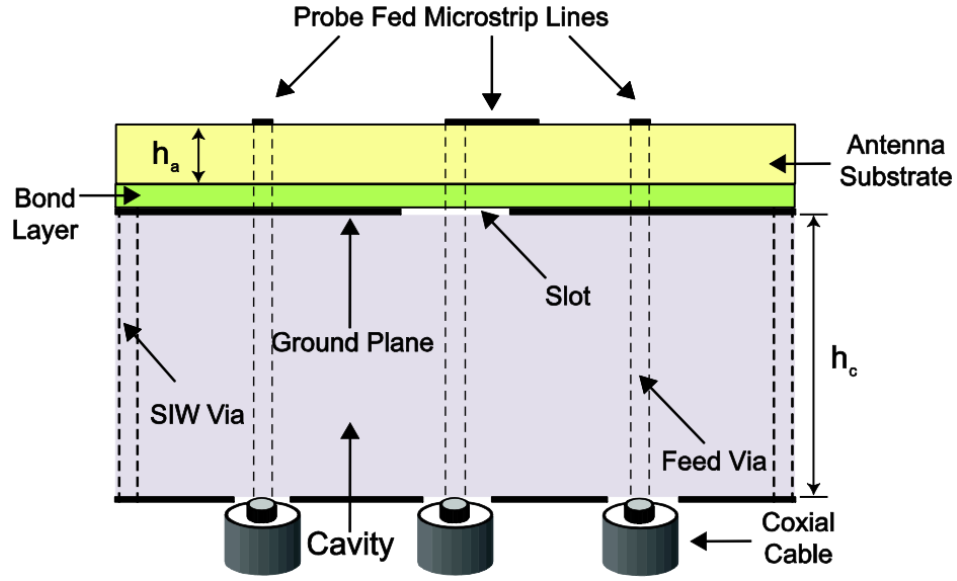
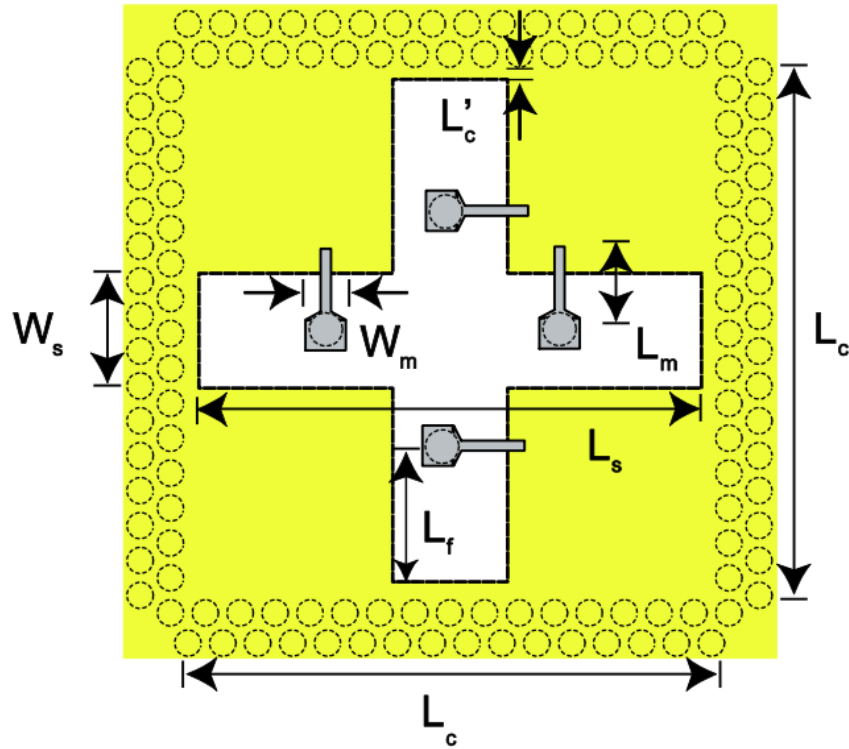


Figure 2.23: Perspective view of the design made by Paryani. The stackup can be seen with the cavity, cross slot and feeds shown. Picture taken from [44].



(a) Cross section view of the design made by Paryani where the layers of the antenna is seen. At the bottom there are coax connectors connected to vias which in turn connect to microstrips on top of the PCB stack up. Picture taken from [44].



(b) Topview of the design made by Paryani where several of the parameters important for the performance of the antenna are defined; L_m , L_s and L_f . Picture taken from [44].

Figure 2.24: Paryani's design viewed from the top and side, where several parameters are seen. Pictures are taken from [44].

Paryani uses the theory from section 2.4.2 to create a double resonance in the slot which increases the bandwidth. The report further describes the different parameters and their effect on the performance. As mentioned in section 2.4.2 the main design parameters are the placement of the microstrips, the stub lengths of the microstrips and the width of the slot. Furthermore, the cavity height is important in order to optimize the excitation of the slot. When the placement of the feeding microstrips move closer to the middle of the slot, the difference between the two resonant frequencies increases.

2.5 Phased Antenna Arrays

A common design goal for antenna arrays is a high directivity. One of the basic relationships in antenna engineering is equation (2.22) where the relation between maximum directivity and the aperture area of the antenna is clearly seen. [3, 22, 46]

$$D_{max} = \frac{4\pi}{\lambda^2} A \quad (2.22)$$

Therefore, when an antenna with a high directivity is needed there exists two different solutions

- Designing an antenna with a large aperture area, e.g. a reflector antenna, and realizing a uniform aperture field distribution.
- Designing an array consisting of many small antenna elements that synthesize a large aperture area.

The last item is an antenna array, where many small antenna elements together simulate a large antenna. Antenna arrays have several advantages. First, the excitation of the antenna elements in the array can be used to alter the constructive and destructive interference between the elements in order to control the radiating pattern. This means that a beam can be electrically steered instead of rotating the antenna mechanically, which is the case for a reflector antenna with a single feed. [3, 22, 46] One exception is a reflector antenna where beam steering is realized by using different array elements to excite the reflector, a phased array-fed (PA-fed) reflector antenna. [47, 48]

Second, the array design is more flexible with regard to the volume it occupies, often an array is planar whilst a reflector antenna has a curvature and thus it occupies a larger volume. This distinction is seen in figure 2.25 where a generic planar array and a reflector antenna is seen both from the side and top. The disadvantages of an array is a more complex design where the critical effect of mutual coupling between the elements needs to be handled and a higher production cost. [3, 22, 46]

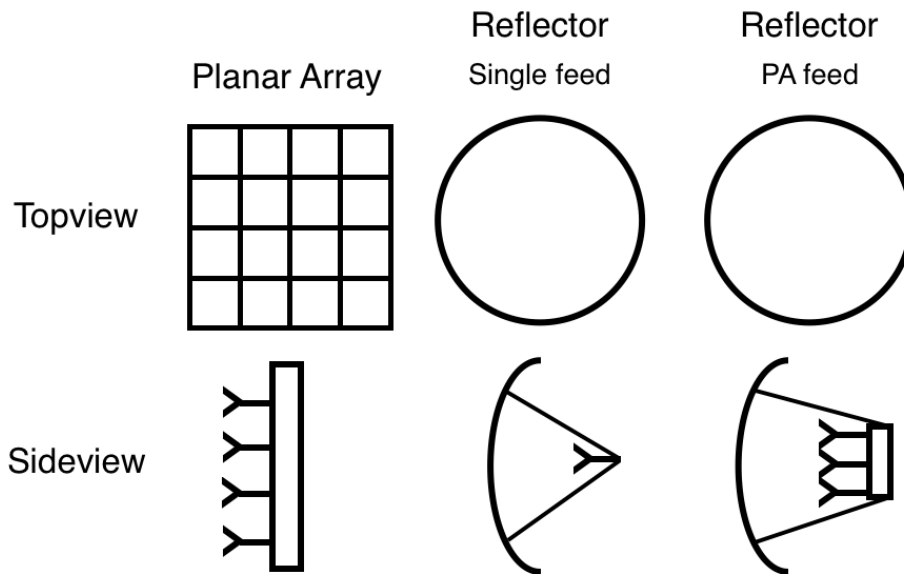


Figure 2.25: Generic layout of a planar array and reflector antennas with two feeding concepts; single feed and PA-fed, viewed from the top and from the side. Note the difference in size in the sideview, where the reflector antennas occupy more volume.

There are many different design parameters available when creating an antenna array. First and foremost are the antenna elements with their radiation characteristics. An antenna array is not limited to using only one type of element. Different element types can be used in an antenna array to e.g. create a desired radiation pattern or an array with two operating frequency bands.

The other design parameters of an array are the spacing, placement and number of radiating elements and excitations of the elements. In figure 2.25 a simple rectangular uniform array grid is shown for the planar array. Other alternatives are a triangular grid or more complex layouts with irregular element positioning. [3, 22, 46, 49, 50]

The placement of the elements and the radiation characteristics will be covered in this section. The theory will be limited to planar arrays consisting of one element type as well as conventional rectangular array grid layouts since that is the scope of the project.

2.5.1 Element Placement

As mentioned earlier, the placement of the elements is one of the main design parameters for an array. The radiated fields from the individual elements interact through destructive and constructive interference, thus the placement of the elements alters the resulting radiated field from the array. This can be expressed in several ways, here only one will be covered.

The array analysis method explained here neglects any mutual coupling between the elements, e.g. the elements are seen as isolated elements whose radiated fields together create the array pattern. In order to obtain the field from the array, the sum of the radiating patterns of each element is needed, where the field is expressed in vector form including the phase. [3, 22, 46]

$$\begin{aligned} \mathbf{E}_{tot} &= \mathbf{E}_1 + \mathbf{E}_2 + \dots + \mathbf{E}_P = \sum_{i=1}^P \mathbf{E}_i = \sum_{i=1}^P C_i \frac{e^{-j(k\mathbf{R}_i + \Phi_i)}}{\mathbf{R}_i} = \\ &= C_1 \frac{e^{-j(k\mathbf{R}_1 + \Phi_1)}}{\mathbf{R}_1} + C_2 \frac{e^{-j(k\mathbf{R}_2 + \Phi_2)}}{\mathbf{R}_2} + \dots + C_N \frac{e^{-j(k\mathbf{R}_P + \Phi_P)}}{\mathbf{R}_P} \end{aligned} \quad (2.23)$$

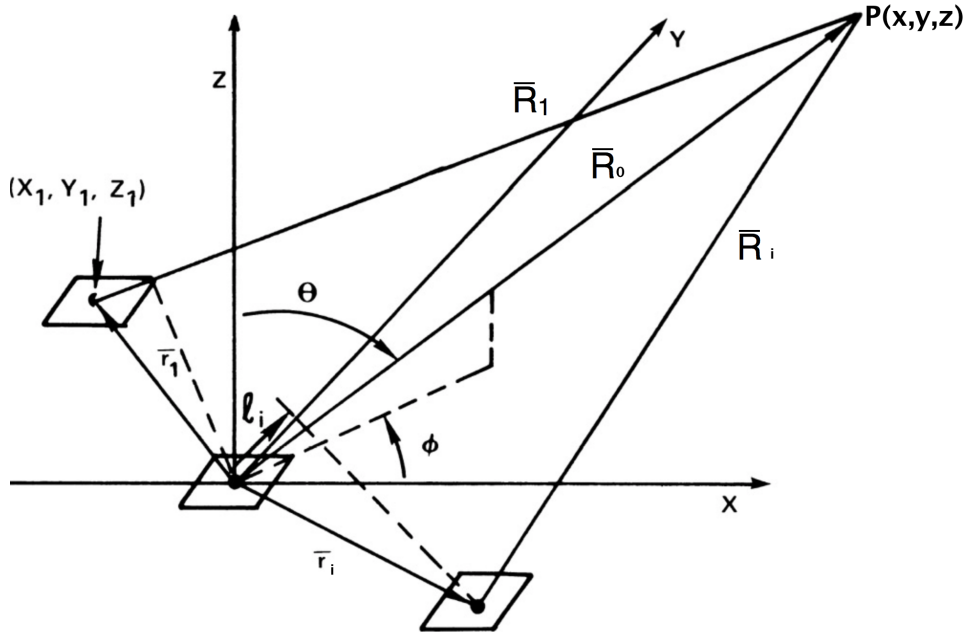


Figure 2.26: Three elements in an array where the vector notations are shown. \vec{R}_i is the vector to the far field point for element i , \vec{r}_i is the vector in the array plane between the center element and element i . Picture taken from [46] with some modifications.

The constant C_i is the far-field amplitude of antenna element i , \mathbf{R}_i is the spatial vector to the far field point $P(x, y, z)$ where the field is being summed and Φ_i is the phase excitation of element i . A general overview of an array configuration illustrating the notation can be seen in figure 2.26 with three elements. Using figure 2.26 the following relationships can be established for a planar array in the xy -plane with element spacing d_x and d_y (in wavelengths) in the x - and y -direction respectively [3, 22, 46]

$$\mathbf{r}_i = k(md_x\hat{x} + nd_y\hat{y} + 0\hat{z}) \quad (2.24)$$

$$\mathbf{R}_0 = \mathbf{r}_i + \mathbf{R}_i = \{\mathbf{R}_i \gg \mathbf{r}_i\} \Rightarrow \mathbf{R}_0 \approx \mathbf{R}_i \text{ for amplitudes.} \quad (2.25)$$

The last approximation is called the Fraunhofer approximation and it is valid since the element spacing is usually small compared to the far field point where

the array is designed to operate. [3] By using equations (2.24) and (2.25) the summation of the resulting electric field, from equation (2.23), can be rewritten as [22]

$$\begin{aligned} \mathbf{E}_{tot} &= \sum_{i=1}^P \mathbf{E}_i = \sum_{i=1}^P C_i \frac{e^{-j(k\mathbf{R}_i + \Phi_i)}}{\mathbf{R}_0} = [\text{uniform excitation}] = \\ &= \underbrace{\frac{C_0}{\mathbf{R}_0}}_{\text{Element factor}} \underbrace{\sum_{i=1}^P e^{-j(k\mathbf{R}_i + \Phi_i)}}_{\text{Array factor}} = EF \cdot AF(\hat{\mathbf{r}}). \end{aligned} \quad (2.26)$$

As can be seen the total E-field of a uniformly excited array can be written as a product of the element factor (EF) and the array factor (AF).

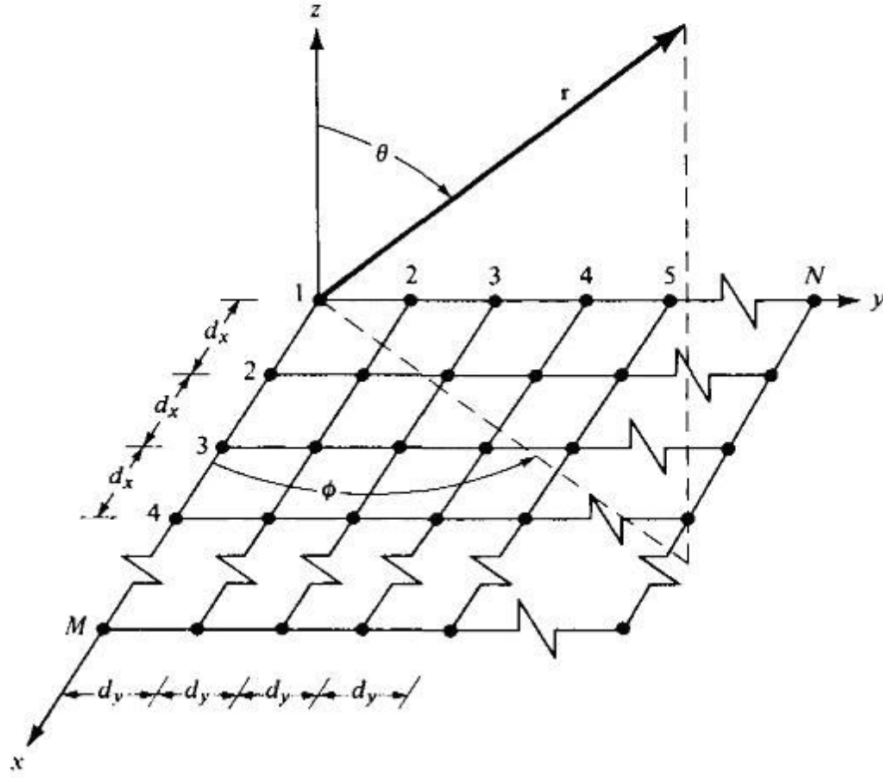


Figure 2.27: A layout of a planar array antenna where the element spacing in the x- and y-directions are uniform and the definitions of d_x , d_y , ϕ and θ are shown. Picture taken from [22].

2.5.1.1 Grating Lobes and Beam Steering

A closer analysis of equation 2.26 shows that the AF function has multiple maxima, since $e^{jx} = \cos(x) + j \sin(x)$. These other maxima are called grating lobes and are an unwanted effect in an antenna array since the grating lobes lowers the field intensity in the desired direction (main beam). Given a planar

array with M elements in the x-direction and N elements in the y-direction the AF can be rewritten (see figure 2.27 for notation)

$$\begin{aligned} u_0 &= \sin(\theta_0) \cos(\phi_0) & \mathbf{R}_0 &= u_0 \hat{x} + v_0 \hat{y} + \cos(\theta_0) \hat{z} \\ v_0 &= \sin(\theta_0) \sin(\phi_0) & \mathbf{r}_i &= nd_x \hat{x} + md_y \hat{y} + pd_z \hat{z} \end{aligned} \quad (2.27)$$

$$\begin{aligned} AF(\hat{\mathbf{r}}) &= \sum_{i=1}^P e^{-j(k\mathbf{R}_i + \Phi_i)} = \sum_{i=1}^P e^{-j(k(\mathbf{R}_0 - \mathbf{r}_i) + \Phi_i)} = \\ &= e^{-jk\mathbf{R}_0} \sum_{i=1}^P e^{-j(-k\mathbf{r}_i + \Phi_i)} = e^{-jk\mathbf{R}_0} \sum_{m=1}^M \sum_{n=1}^N e^{-j(-k(md_x \hat{x} + nd_y \hat{y}) + \Phi_{mn})} = \\ &= e^{-jk\mathbf{R}_0} \sum_{m=1}^M e^{j(kmd_x \sin(\theta) \cos(\phi) - \Phi_{xmn})} \sum_{n=1}^N e^{j(knd_y \sin(\theta) \sin(\phi) - \Phi_{ymn})}. \end{aligned} \quad (2.28)$$

When the phase is a multiple of 2π the AF has a maxima according to

$$\begin{aligned} kd_x \sin(\theta) \cos(\phi) - \Phi_{xmn} &= \pm 2m\pi, & m &= 0, 1, 2, \dots \\ kd_y \sin(\theta) \sin(\phi) - \Phi_{ymn} &= \pm 2n\pi, & n &= 0, 1, 2, \dots \end{aligned} \quad (2.29)$$

By altering the phase excitation, Φ_{mn} , between the elements, the interference can be used to form a beam in a specific direction. In order to steer a beam to (ϕ_0, θ_0) the phase excitation should be

$$\begin{aligned} \Phi_{mnx} &= k\mathbf{r}_{ix} \cdot \mathbf{R}_{0x} = kmd_x u_0 \hat{x} = kmd_x \sin(\theta_0) \cos(\phi_0) \hat{x} \\ \Phi_{mny} &= k\mathbf{r}_{iy} \cdot \mathbf{R}_{0y} = knd_y v_0 \hat{y} = knd_y \sin(\theta_0) \sin(\phi_0) \hat{y} \\ \Phi_{mnz} &= k\mathbf{r}_{iz} \cdot \mathbf{R}_{0z} = kpd_z \cos(\theta_0) \hat{z} \\ \Phi_{mnp} &= k \left(md_x \sin(\theta_0) \cos(\phi_0) \hat{x} + nd_y \sin(\theta_0) \sin(\phi_0) \hat{y} + pd_z \cos(\theta_0) \hat{z} \right) \end{aligned} \quad (2.30)$$

This resulting Φ_{mnp} is the phase steering inserted in the array factor in equation (2.28). The phase steering is here expressed in all three dimensions, for a planar array in the xy-plane the element spacing in \hat{z} ($d_z = 0$) is zero. If equations (2.29) and (2.30) are combined, an expression for the grating lobe locations is achieved.

$$\begin{aligned} kd_x \sin(\theta) \cos(\phi) - kd_x \sin(\theta_0) \cos(\phi_0) &= \pm 2m\pi, & m &= 0, 1, 2, \dots \\ kd_y \sin(\theta) \sin(\phi) - kd_y \sin(\theta_0) \sin(\phi_0) &= \pm 2n\pi, & n &= 0, 1, 2, \dots \\ kd_x \left(\sin(\theta) \cos(\phi) - \sin(\theta_0) \cos(\phi_0) \right) &= \pm 2m\pi \\ kd_y \left(\sin(\theta) \sin(\phi) - \sin(\theta_0) \sin(\phi_0) \right) &= \pm 2n\pi \\ \sin(\theta) \cos(\phi) - \sin(\theta_0) \cos(\phi_0) &= \pm \frac{m\lambda}{d_x} \\ \sin(\theta) \sin(\phi) - \sin(\theta_0) \sin(\phi_0) &= \pm \frac{n\lambda}{d_y} \end{aligned} \quad (2.31)$$

If equation (2.31) is solved for θ and ϕ

$$\begin{aligned}\phi &= \tan^{-1} \left(\frac{\sin(\theta_0) \sin(\phi_0) \pm m\lambda/d_x}{\sin(\theta_0) \cos(\phi_0) \pm n\lambda/d_y} \right) \\ \theta &= \sin^{-1} \left(\frac{\sin(\theta_0) \cos(\phi_0) \pm m\lambda/d_x}{\cos(\phi)} \right) = \sin^{-1} \left(\frac{\sin(\theta_0) \sin(\phi_0) \pm n\lambda/d_y}{\sin(\phi)} \right).\end{aligned}\tag{2.32}$$

The main maxima is when $m = n = 0$, and the grating lobes have $m \neq 0 \vee n \neq 0$. It can now be seen, in equation (2.32), that the element spacing needs to be $d_x < \lambda/2$ and $d_y < \lambda/2$ in order to avoid grating lobes.

3

Design Methods

This chapter first describes the workflow during the project and the tools used. Secondly, it describes the design process chronologically, enabling the reader to follow the ideas and decisions taken during the work as it unfolded.

3.1 Overview of Workflow

The design and optimization of the element were done using ANSYS High Frequency Electromagnetic Field Simulation (HFSS), an EM-field simulation software. By parametrizing the model the different parameters were altered in order to find a good match. The starting point for each design, i.e. the starting values of the design parameters, was chosen through a combination of theory and previous work.

A first investigation of the performance was done with the starting parameters and then a parametric study was performed. Using the conclusions from the parametric study the appropriate parameters were then altered in order to achieve a better performance. In figure 3.1 the general method of the simulations is shown in a flow chart.

At the start, the feeding network was not taken into consideration in order to lower simulation time and design complexity. This stage helped to identify inherent problems with the chosen aperture design and gave a basic understanding of the performance of the aperture. The distinction between the feeding and aperture parts of the PCB stack up is shown in figure 3.2, from the figure it is seen that the first simulation stage only considered the metal hardback.

A parameter can affect the impedance (resistance and reactance) and resonant frequency(ies) of the design. Since these are a limited set of responses several parameters affected the performance in similar ways. The choice of which parameter to alter in these cases was often determined by manufacturing limitations and considerations (low-cost, tolerances etc.).

The results of the parametric studies are presented by S-parameters in dB-scale together with Smith charts. By combining these two graphs the frequencies

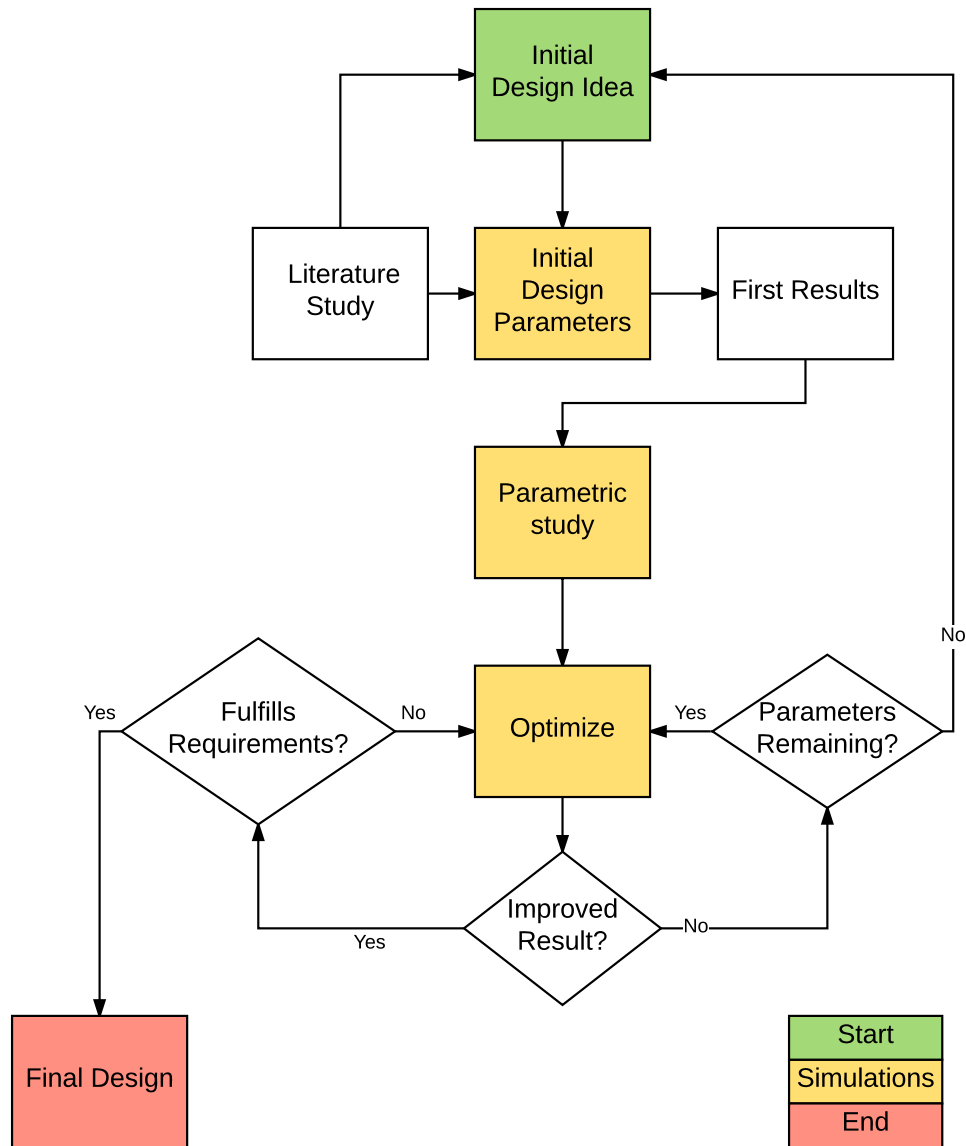


Figure 3.1: Flowchart of the simulation workflow for the designs.

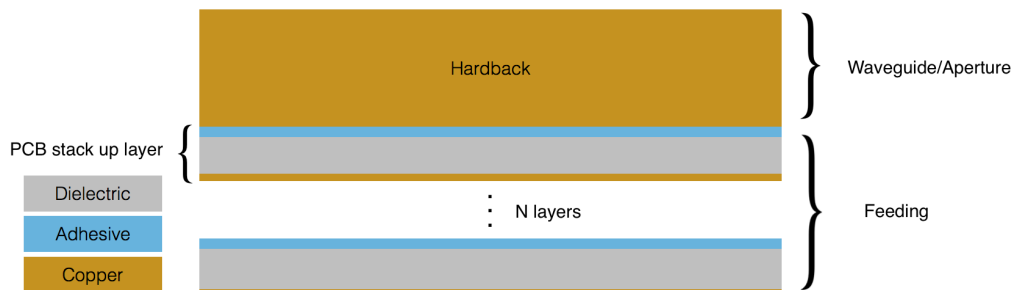


Figure 3.2: The PCB stack up for a generic design where the location of the feeding and the aperture is shown.

of the Smith chart can be mapped since a dip in the S-parameter plot corresponds to a point close to the middle in the Smith chart. The resonance (the loop in the Smith chart) determines the available bandwidth, the resonance should not be too large since then the S-parameter requirement is not fulfilled. It should neither be too narrow since the bandwidth requirement then is not fulfilled.

The parametric studies were made with the overall behavior of all of the parameters in mind. Specific numbers and performance were not the focus. As such, the results presented in the parametric studies are not detailed, instead the trends are documented. These were later used to optimize the element and the details of this iterative process are not covered in this report, the end result will instead be presented.

3.2 Designs

The designs investigated in this project had the goal of fulfilling the specifications listed in section 1.3. However, the exact frequency was left unspecified in the requirements and a decision of designing frequency had to be made. A frequency of 15 GHz was chosen since Ericsson AB has made designs for that frequency earlier. Furthermore, PCB manufacturing restrictions are not as limiting around 15 GHz compared to higher frequencies given the longer wavelength. The choice of 15 GHz gives a starting point for the waveguide radius using equation (2.1). This gives the cutoff frequency

$$f_c = f_0 \left(\frac{1 - \frac{B}{2}}{m} \right) = 15 \left(\frac{1 - \frac{0.06}{2}}{1.15} \right) \text{ GHz} = 12.65 \text{ GHz} \quad (3.1)$$

when a 6% bandwidth and a 15% margin from the cutoff frequency, m , is used, see section 2.2.1.1 for details.

Additionally, there are manufacturing restrictions which need to be taken into consideration when investigating possible design ideas. The following tolerances, material choices and manufacturing techniques impose restrictions to the design:

- Standard radius of vias are 0.25 mm
- The dielectric filling available for the waveguide has an $\epsilon_r \sim 4 - 4.5$
- A copper thickness of 0.0347 mm was used for the striplines and ground planes. This corresponds to a PCB standard of 1 oz/ft² copper (1 oz of copper evenly spread over ft² gives a thickness of 0.0347 mm).

3.2.1 Drilled Ridged Waveguide

The first design concept was to use ridges to load the waveguide aperture. The idea was to create the ridges by drilling holes into the PCB hardback. A top

view of the design can be seen in figure 3.3 and a perspective view of the HFSS model in figure 3.4.

The main design parameters are the radii of the drilled holes, r_1 and r_2 , together with the placement of the smaller holes, p , as shown in figure 3.3. The placement can be expressed through the total radius of the waveguide.

$$a = r_1 + 2r_2 + (p - r_2 - r_1) = p + r_2 \quad \Rightarrow \quad p = a - r_2 \quad (3.2)$$

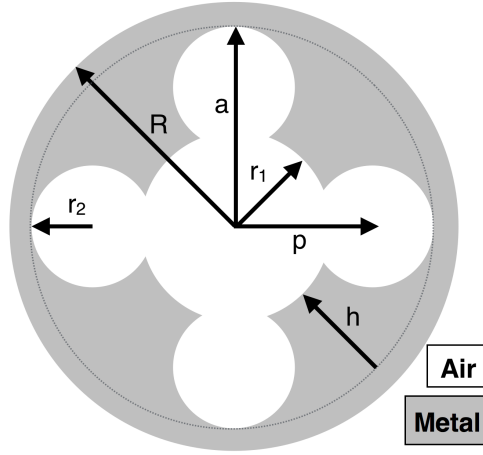


Figure 3.3: Top view of a ridged circular aperture created by drilling five holes in a metal block.

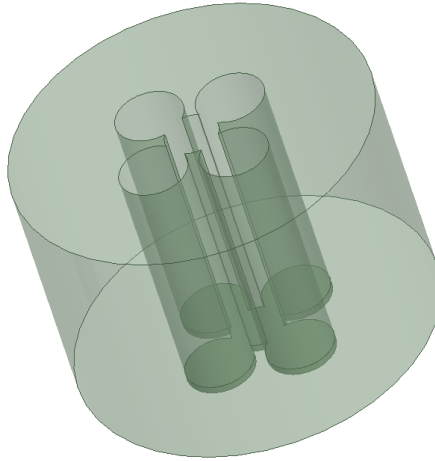


Figure 3.4: Perspective view of the HFSS model of the drilled ridged design.

The excitation of the model was done with a *wave port* in HFSS with the same shape as the drilled holes united together. The aim of the first parametric sweep was to find a correct starting point with a cutoff frequency corresponding to 12.65 GHz from equation (3.1). As previously mentioned, only the

hardback part was studied in the beginning to evaluate the basic aperture design.

The starting values of the parameters were chosen to be close to the design described in section 2.3.1.2, which meant $a = 0.252\lambda_h$, $r_1 = 0.3a$ and $r_2 = 0.38a$. In table 3.1 the values of the parameters are presented.

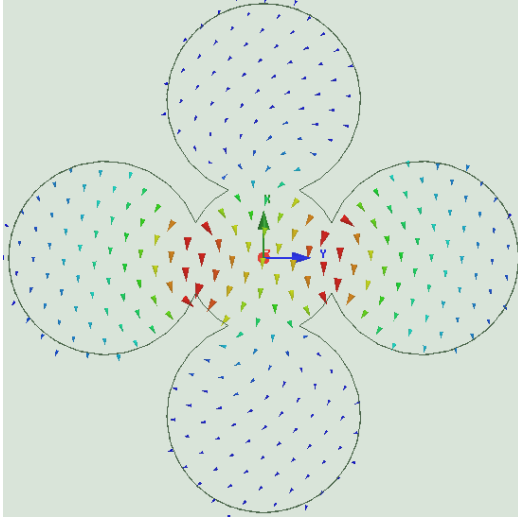
Table 3.1: Summary of the design parameters and their values investigated during the design process of the drilled ridged waveguide. See figure 3.3 for the definitions of the parameters.

	[mm]	Start	Sweep
Inner Radius r_1		1.5	0.5-3.5
Outer Radius r_2		1.9	1.7-2.25
Total Radius a		5	4-6
Height		14	-
Total Radius R		10	-

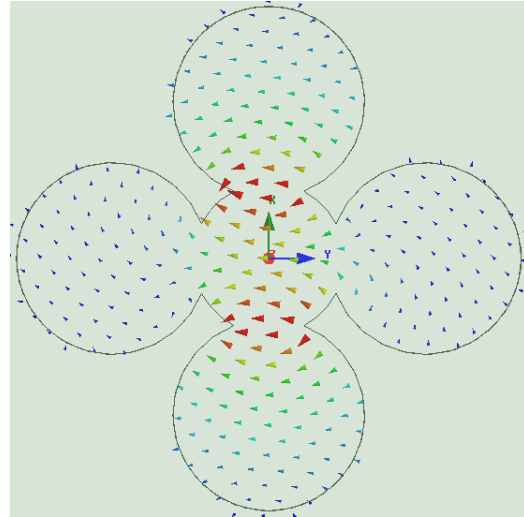
The different modes excited by HFSS are seen in figure 3.5 where the first two modes are the same mode but rotated 90° . As can be seen the modes have a major part of their power close to the ridges except for the fourth mode. This implies that a change of the ridge size will greatly affect the performance and the mode characteristics, e.g. the cutoff frequency for each mode.

The cutoff frequencies for the four first modes are shown in figures 3.6 and 3.7, here it is seen that the two first modes have the same cutoff frequency which is to be expected since they are the same mode. Furthermore, the third mode is very close to the first and second mode, this is problematic when the bandwidth requirement is taken into account. There has to be enough difference between the cutoff frequencies to allow the fundamental mode to propagate alone inband, otherwise the polarization purity and the radiation pattern will deteriorate. This problem was described in section 2.2.1.3 where the TE_{21L} -mode needs to be suppressed in order to get a higher available bandwidth between the modes compared to a standard waveguide. Chen (in his ridged design, see section 2.3.1.2), accomplished this by using dielectric filling and a taper of the ridges. Those methods were deemed to be hard to incorporate in the manufacturing process and were thus not investigated.

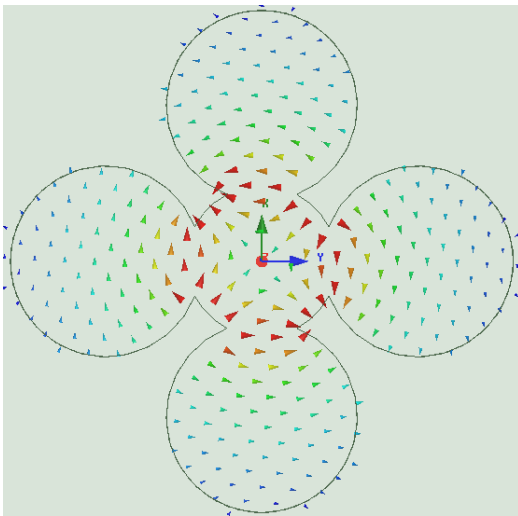
Furthermore, the cutoff frequency of the design was very sensitive to a change of either of the radii (r_1, r_2). This could prove problematic with regard to the manufacturing tolerances where the position and size of the drilled holes may not be exact.



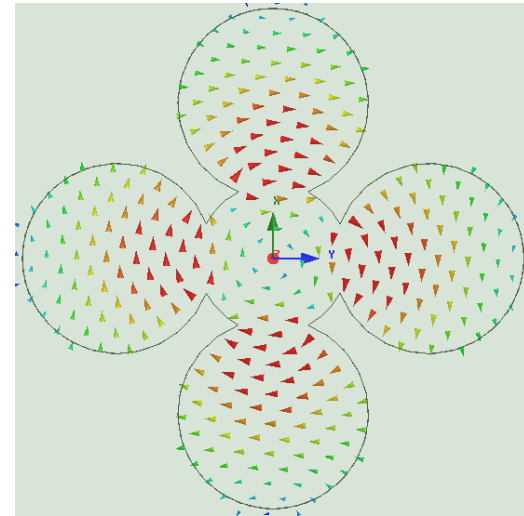
(a) The first mode excited by HFSS, it is perpendicular to the second mode seen in figure 3.5b.



(b) The second mode excited by HFSS, it is perpendicular to the first mode seen in figure 3.5a.



(c) The third mode excited by HFSS.



(d) The fourth mode excited by HFSS.

Figure 3.5: The first four modes excited by HFSS in the ridged design.

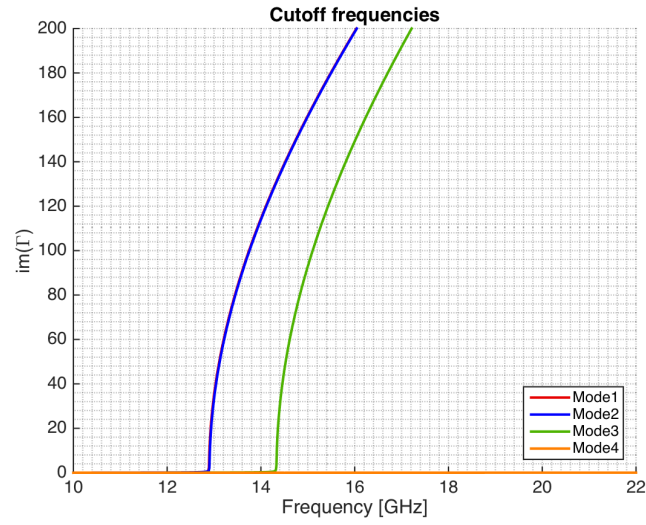


Figure 3.6: The cutoff frequencies for the four modes excited in HFSS. Since the first two modes are the same mode, only rotated, their cutoff frequency is the same. The next mode, mode 3, has a cutoff frequency fairly close to the first fundamental mode.

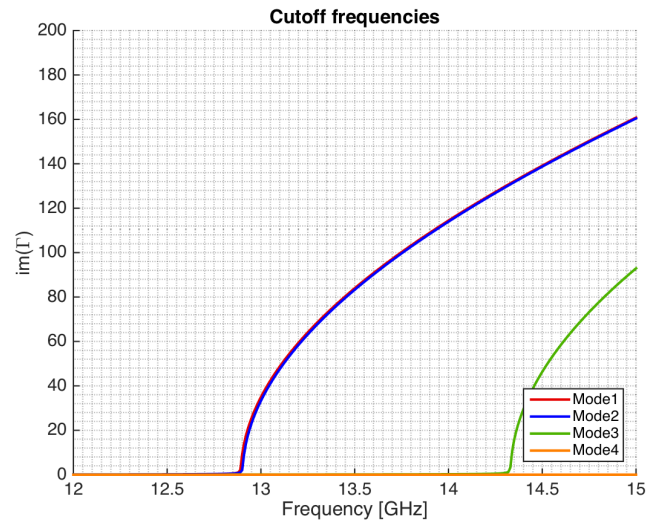


Figure 3.7: A closer figure of the cutoff frequencies for the four modes excited in HFSS, the fundamental mode has $f_c = 12.9$ GHz and mode 3 has $f_c = 14.3$ GHz. Since the first two modes are the same mode, only rotated, their cutoff frequency is the same. The next mode, mode 3, has a cutoff frequency fairly close to the first fundamental mode.

3.2.1.1 Parametric Study of Ridged Drilled Element

The parameters shown in figure 3.3 were altered to see how they affected the antenna performance. There are artifacts in all of the results from the parameter sweeps which probably are due to problems with the meshing since the parameters affected the port size. The overall behavior is presented here in Smith chart and $|S_{nn}|$ form for the first and the third mode. The second mode is not shown since it has the same behavior as the first mode and the fourth mode does not propagate in the design in the given frequency interval. The port re-normalization impedance in HFSS was set to 50Ω .

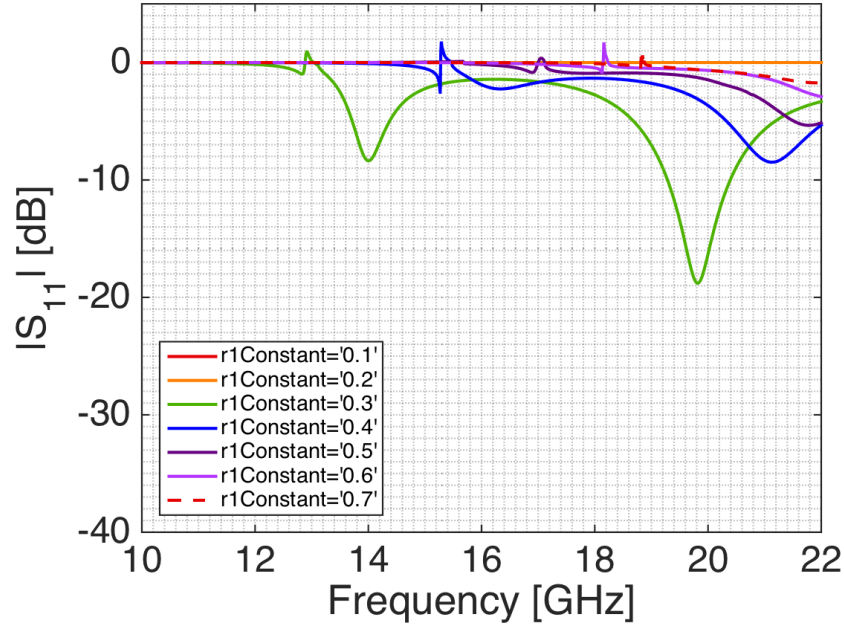
3.2.1.1.1 Inner Radius r_1 The performance of the antenna when the inner drilled hole's radius is changed can be seen in figure 3.8 for mode 1 and figure 3.9 for mode 3. The sweep was done with the parameter 'r1Constant' which was defined as a constant times the value of a which was 5 mm. This parametric sweep shows severe problematic behavior, e.g. the S-parameters have positive values on several occasions, which makes it hard to draw any conclusions.

3.2.1.1.2 Outer Radius r_2 The performance of the antenna when the outer drilled holes' radius is changed can be seen in figure 3.10 for mode 1 and figure 3.11 for mode 3. The sweep was done with the parameter 'r2Constant' which was defined as a constant times the value of a which was 5 mm. This parametric sweep shows problematic behavior, e.g. the S-parameters have positive values on several occasions, which makes it hard to draw any conclusions.

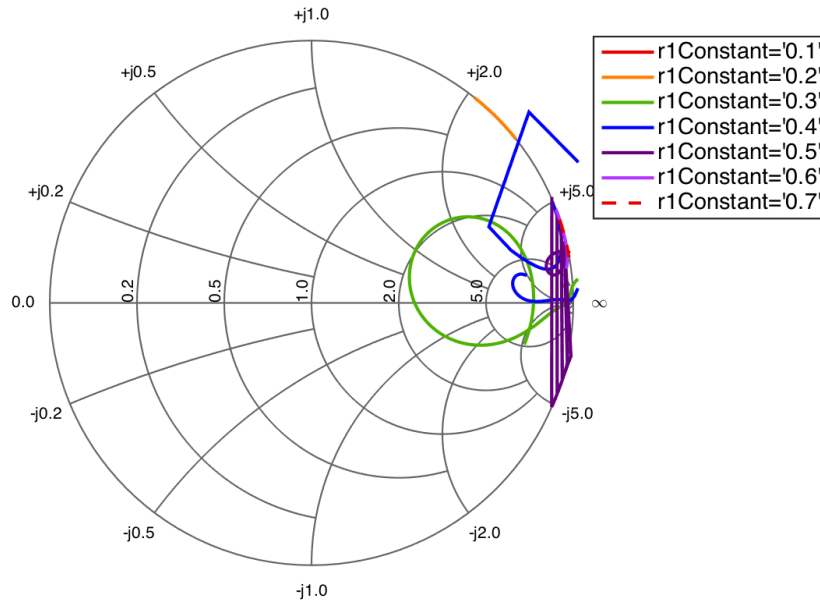
3.2.1.1.3 Total Radius a The performance of the antenna when the total radius of the waveguide, a , is changed can be seen in figure 3.12 for mode 1 and figure 3.13 for mode 3. The sweep was done with the parameter 'aConstant' which was defined as a constant times the wavelength of 15 GHz which is 20 mm. a determines the placement, p , of the outer drilled holes by the expression $p = a - r_2$. This parametric sweep shows problematic behavior, e.g. the S-parameters have positive values on several occasions, which makes it hard to draw any conclusions.

3.2.1.2 Conclusions of Parametric Study of Drilled Ridged Element

As can clearly be seen all of the parametric sweeps have some odd behavior and the results of this study is therefore hard to analyze. Efforts were made to identify the source of these problems by checking the parameters and the meshing of the model but the source could not be identified. However, what can be seen is that small changes of the radii r_1 and r_2 result in large frequency shifts. This, together with the difficulties of analyzing the model properly and the issue of the cutoff frequencies being close together, indicated that the design

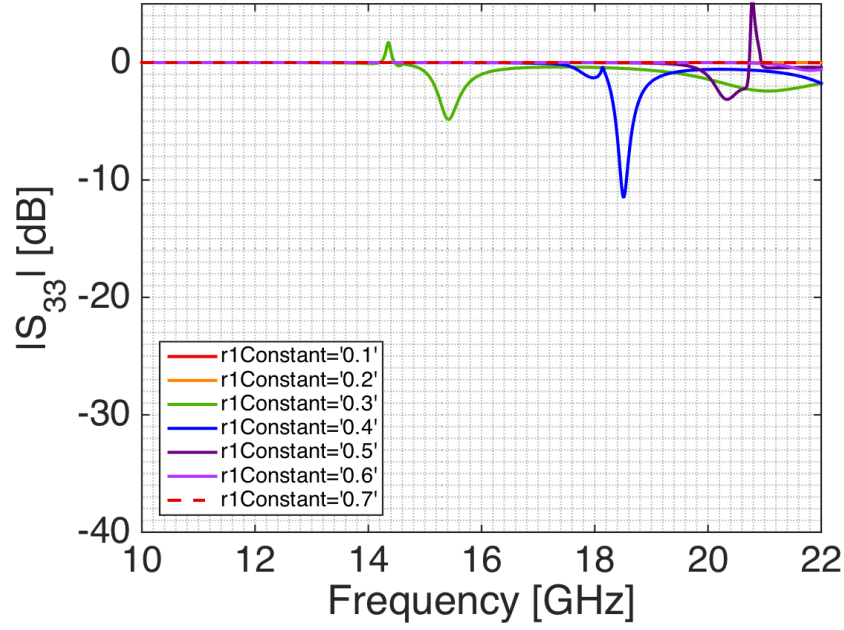


(a) $|S_{11}|$ in dB-scale for different radii of the inner drilled hole, r_1 , for mode 1. The other parameters were fixed and had the starting values as stated in table 3.1.

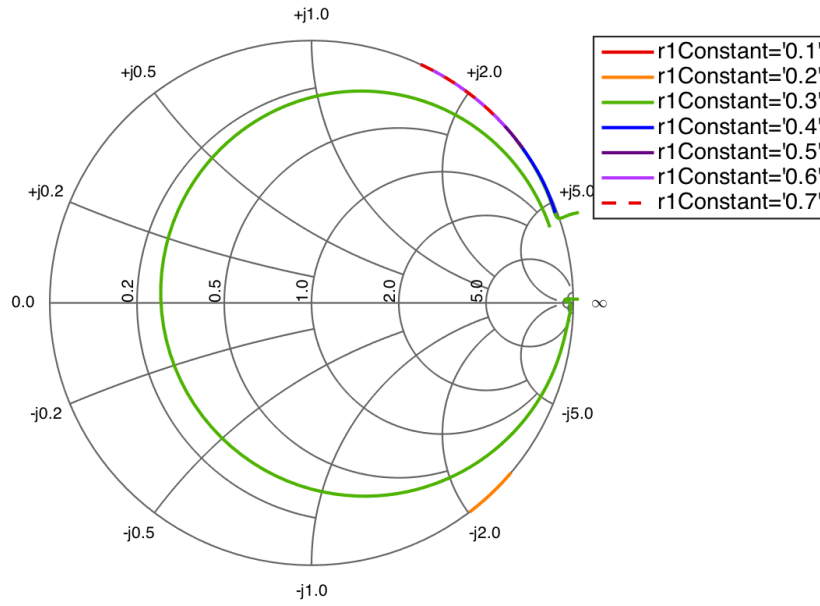


(b) Smith chart of S_{11} for different radii of the inner drilled hole, r_1 , for mode 1. The other parameters were fixed and had the starting values as stated in table 3.1.

Figure 3.8: Parametric study of S_{11} for different radii of the inner drilled hole, r_1 , for mode 1. The other parameters were fixed and had the starting values as stated in table 3.1.

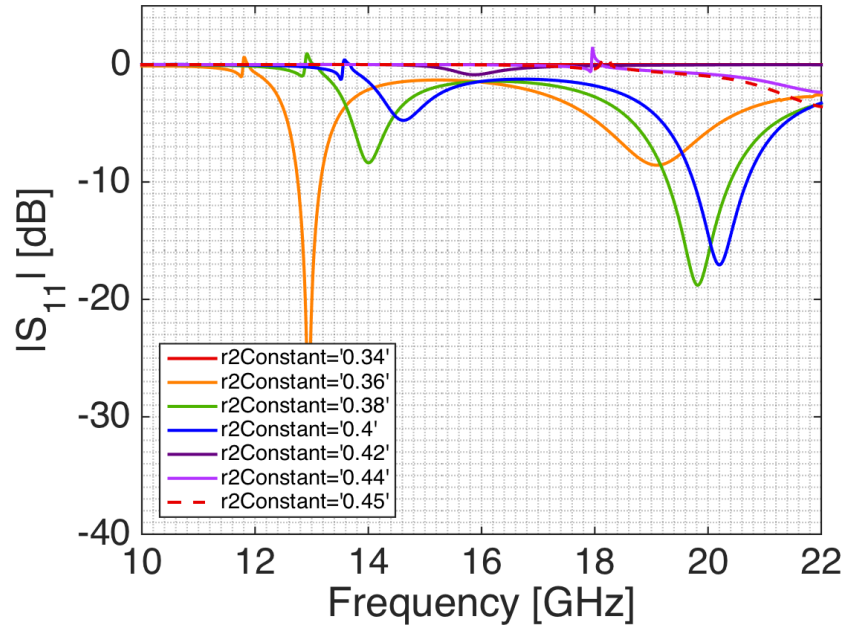


(a) $|S_{33}|$ in dB-scale for different radii of the inner drilled hole, r_1 , for mode 3. The other parameters were fixed and had the starting values as stated in table 3.1.

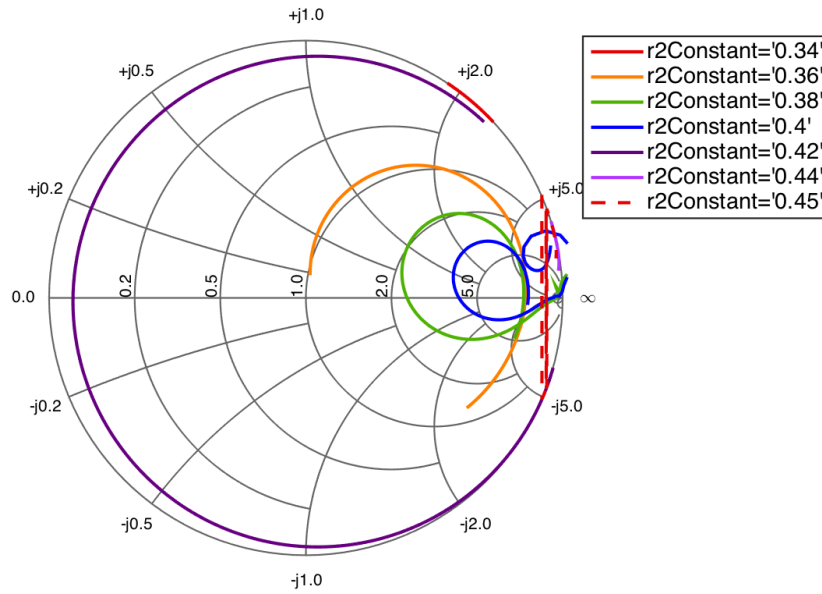


(b) Smith chart of S_{33} for different radii of the inner drilled hole, r_1 , for mode 3. The other parameters were fixed and had the starting values as stated in table 3.1.

Figure 3.9: Parametric study of S_{33} for different radii of the inner drilled hole, r_1 , for mode 3. The other parameters were fixed and had the starting values as stated in table 3.1.

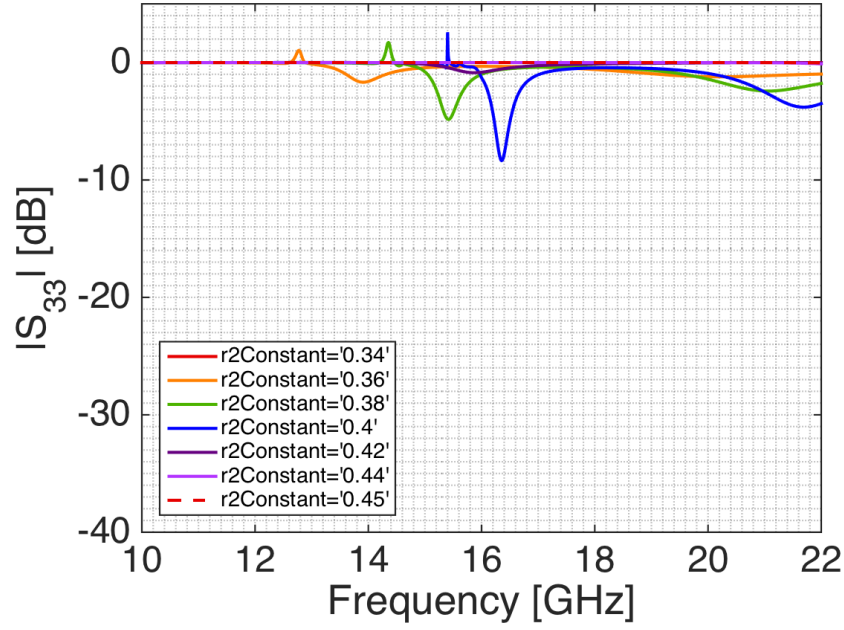


(a) $|S_{11}|$ in dB-scale for different radii of the outer drilled hole, r_2 , for mode 1. The other parameters were fixed and had the starting values as stated in table 3.1.

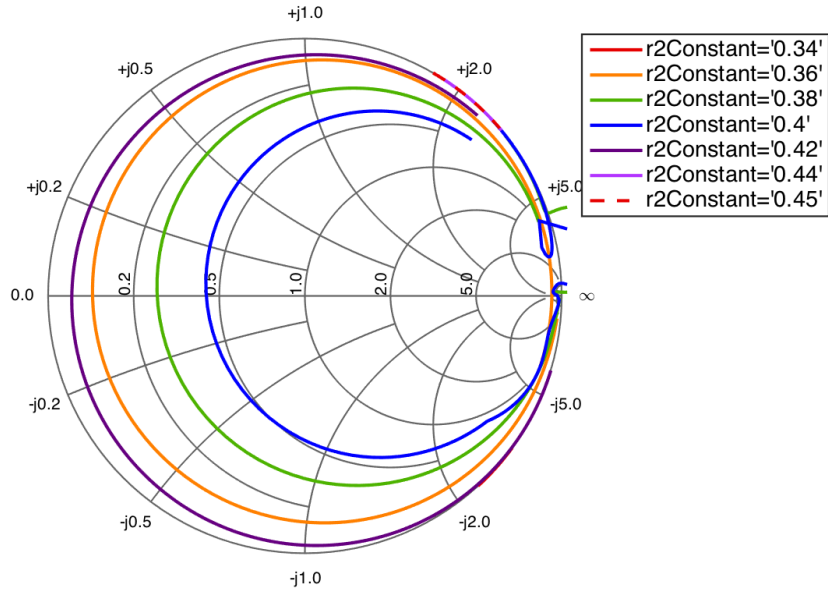


(b) Smith chart of S_{11} for different radii of the outer drilled hole, r_2 , for mode 1. The other parameters were fixed and had the starting values as stated in table 3.1.

Figure 3.10: Parametric study of S_{11} for different radii of the outer drilled hole, r_2 , for mode 1. The other parameters were fixed and had the starting values as stated in table 3.1.

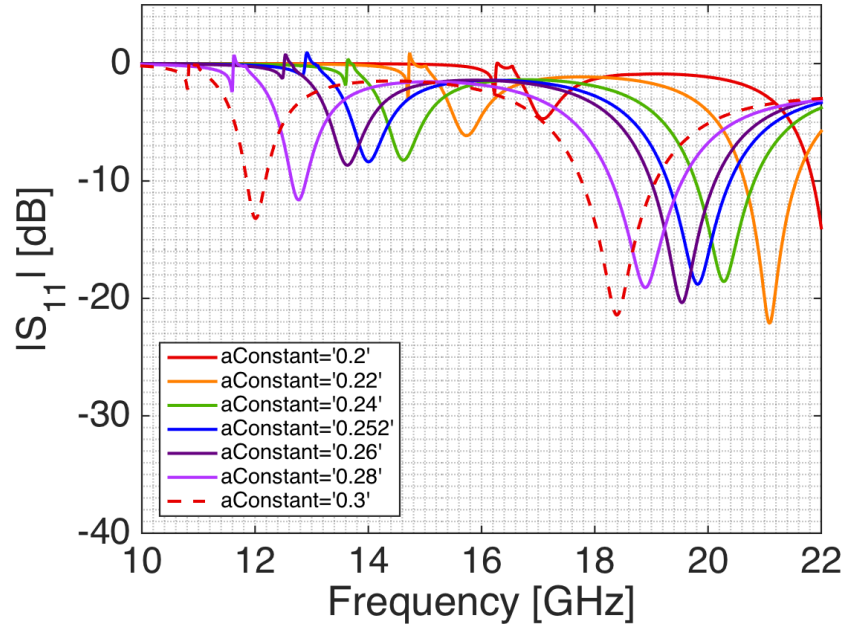


(a) $|S_{33}|$ in dB-scale for different radii of the outer drilled hole, r_2 , for mode 3. The other parameters were fixed and had the starting values as stated in table 3.1.

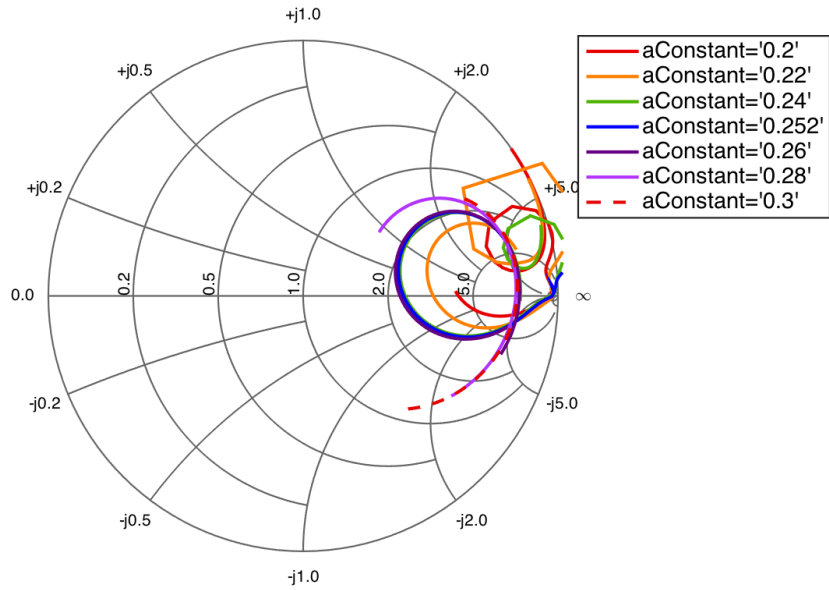


(b) Smith chart of S_{33} for different radii of the outer drilled hole, r_2 , for mode 3. The other parameters were fixed and had the starting values as stated in table 3.1.

Figure 3.11: Parametric study of S_{33} for different radii of the outer drilled hole, r_2 , for mode 3. The other parameters were fixed and had the starting values as stated in table 3.1.

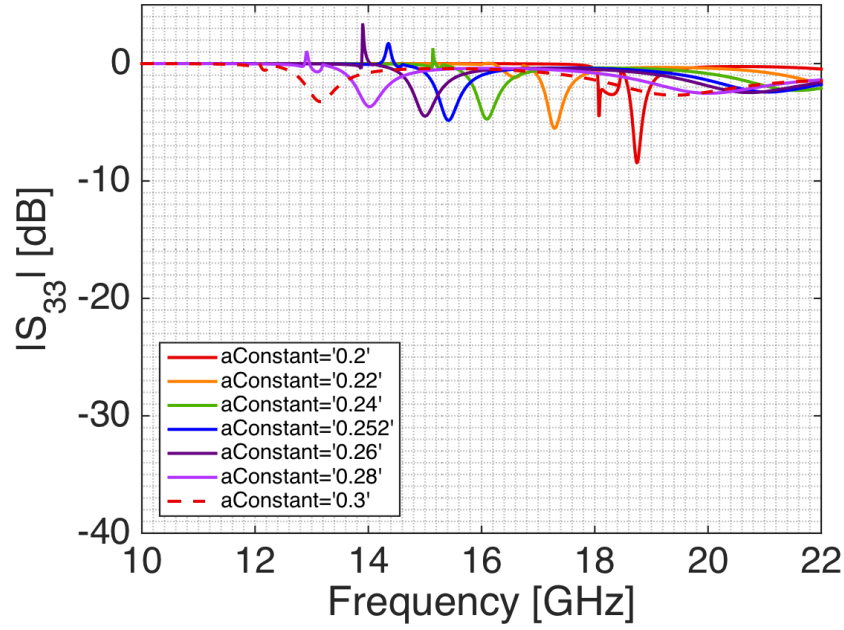


(a) $|S_{11}|$ in dB-scale for different total radii, a , for mode 1. The other parameters were fixed and had the starting values as stated in table 3.1.

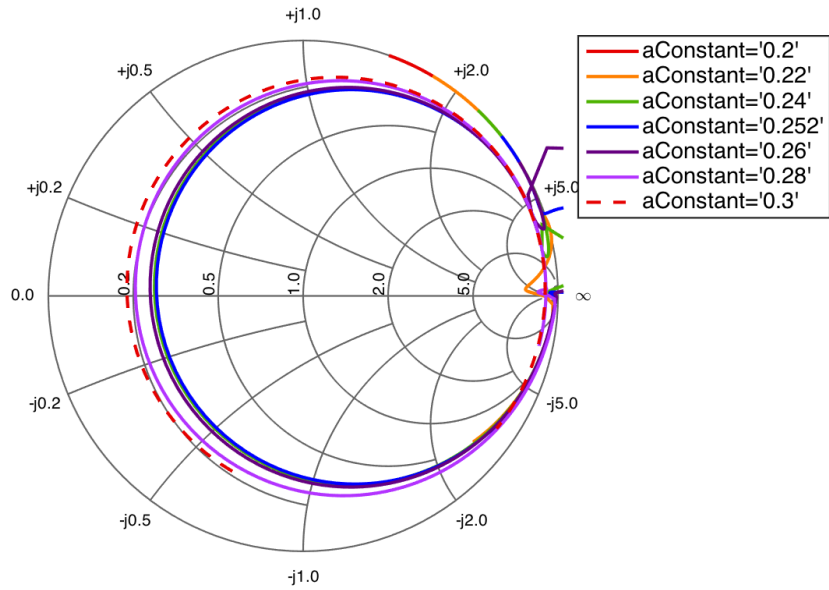


(b) Smith chart of S_{11} for different total radii, a , for mode 1. The other parameters were fixed and had the starting values as stated in table 3.1.

Figure 3.12: Parametric study of S_{11} for different total radii, a , for mode 1. The other parameters were fixed and had the starting values as stated in table 3.1.



(a) $|S_{33}|$ in dB-scale for different total radii, a , for mode 3. The other parameters were fixed and had the starting values as stated in table 3.1.



(b) Smith chart of S_{33} for different total radii, a , for mode 3. The other parameters were fixed and had the starting values as stated in table 3.1.

Figure 3.13: Parametric study of S_{33} for different total radii, a , for mode 3. The other parameters were fixed and had the starting values as stated in table 3.1.

idea would have troubles fulfilling the requirements and functioning properly. Therefore, another design idea was investigated, using dielectric loading which does not suffer from the cutoff frequency problem.

3.2.2 Stripline Fed Dielectric Filled Waveguide

The next design idea was to use the other waveguide loading method; using dielectric material to fill a drilled hole in the metal hardback. The first question investigated was whether or not the available dielectric filling could fulfill the requirement of a maximum aperture diameter of 0.53λ . As shown in section 2.2.1.2 and in figure 2.7 a relative permittivity of 4 can fulfill an aperture diameter smaller than 0.5λ . After this control, the next step was to investigate the feeding of the element.

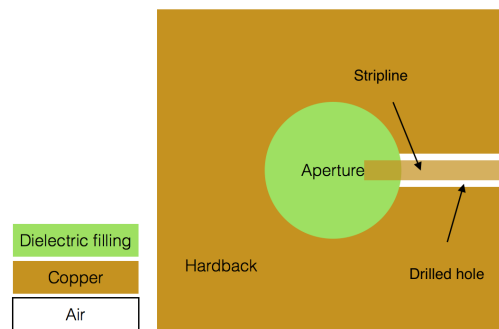
3.2.2.1 Stripline Feeding

The first excitation method investigated was the use of E-field probes. Since the element should be dual polarized, two probes orthogonal to each other were needed. At this moment in the design process, the element only consisted of a metal block with a drilled hole filled with dielectric material. If a stripline were to be inserted into the waveguide, a hole had to be made extending from the side of the metal block into the waveguide. The hole in the sidewall can be seen in figure 3.14.

Since the main idea with the drilled design was the simplicity of manufacturing, a hole made into the sidewall of the waveguide did not seem like a good solution. Furthermore, the design should be implemented in a subarray where at least two elements may share the same hardback. This would be problematic if holes would be drilled in the side of the hardback. It would be hard to implement and the insertion and suspension of a stripline into the hole would be complicated. Therefore, this excitation idea was not considered further.

A new excitation idea was to implement the striplines into the PCB stack up underneath the hardback. The waveguide would then need to be extended into the PCB, a transition from the aperture in the hardback to the PCB. This was done by creating a *substrate integrated waveguide* (SIW) by vias emulating a metal wall inside the substrate. In order for the vias to behave as a solid metal wall for the design frequency the distance between the vias needs to be $< \lambda_g/10$. [51]

The stripline can not be inserted directly beneath the metal hardback since that would short circuit it, therefore a substrate is needed between the hardback and the stripline. This can be seen in figure 3.15 if the substrate labeled 2 is removed. Furthermore, the SIW under the stripline should be of a height close to $\lambda_g/4$, see section 2.4.1. The cavity created under the stripline need to be closed on the bottom and therefore a ground plane is needed. A summary



(a) Schematic top view of the proposed drilled hole into the hardback for the stripline feeding of the waveguide, not to scale.



(b) Schematic sideview of the proposed drilled hole into the hardback for the stripline feeding of the waveguide, not to scale.

Figure 3.14: Schematic top and cross section of a stripline feeding where the stripline is inserted through a drilled hole into the hardback.

of these deductions are shown in figure 3.15 where the substrate numbered 1 should have a thickness of $\lambda_g/4$.

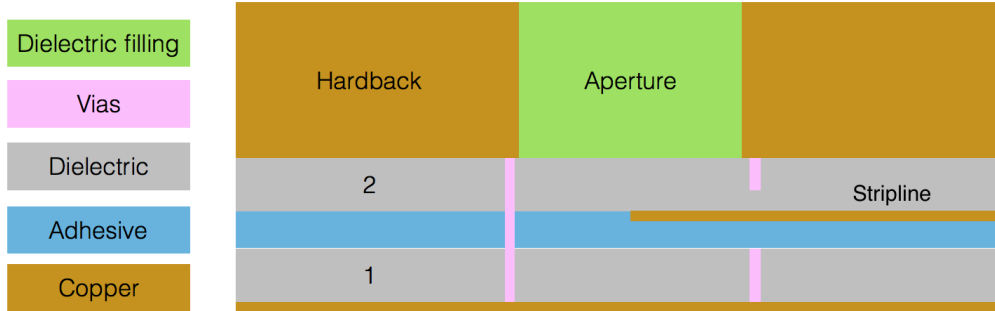


Figure 3.15: Schematic cross section of a dielectric filled aperture with an excitation beneath the hardback in the PCB. The distance between the stripline and the ground plane should be close to $\lambda_g/4$ to create a resonance. The vias create a SIW inside the PCB stack up.

3.2.2.2 Cavity height

As mentioned, the substrate underneath the striplines needs to have a height of $\lambda_g/4$. The available heights of the substrate are limited and the cavity therefore needs to be built up by a combination of discrete substrate slabs. The substrates need to be put together using an adhesive which have a discrete height and another dielectric constant than the substrate. The available heights for the substrate RO4350B (a substrate commonly used for these frequencies) are listed in table 3.2 together with the thickness of the adhesive, RO4450F Bondply, used to create a stack up. Additionally, the production cost of extra layers as well as impurities due to the adhesive process need to be taken into account. With this in mind fewer layers are better.

Table 3.2: Available substrate thicknesses of the dielectric material RO4350B and the adhesive RO4450F, data from data sheets provided by Rogers Corporation [52, 53].

Material	ϵ_r	Available thicknesses [mm]						
RO4350B	3.66	0.168	0.254	0.338	0.422	0.508	0.762	1.524
RO4450F	3.52 ± 0.05	0.101						

To conclude, there are a discrete number of available heights which should be combined to get as close as possible to a specified height. This problem belongs to the Knapsack problem family [54, pp.3]. An algorithm to find possible combinations was written in Matlab (see appendix A) and the result is presented in table 3.3.

The found combinations were compared to a stack up using three layers of 0.726 mm thick substrates, only solutions better than that are presented. Com-

binations using more than four layers were discarded because of the previously mentioned drawbacks. The permittivity difference between the substrate and the Bondply was not taken into account in the algorithm. The reasoning being that the permittivities of the two materials are so similar (3.66 and 3.52 respectively) and the impurities of the Bondply already contributes to an uncertainty.

As can be seen in table 3.3, the only combination using three substrates is the $3 \cdot 0.762$ stack up. The best results are achieved with combinations of four substrates, however the height difference of 0.02 mm when using the three combination stack up was deemed good enough. Especially when considering the increased cost, complexity and impurities of the stack up with added layers. Thus the $3 \cdot 0.762$ combination was used, resulting in a total height of 2.589 mm including the Bondply.

Table 3.3: Found combinations of layers which adds up closely enough to a cavity height of $\lambda_g/4$. h_{tot} is the total height of the stack up, the sum of the Bondply and substrates.

The number of layers of specific thickness [mm]							$\lambda_g/4 - h_{tot}$
0.168	0.254	0.338	0.422	0.508	0.762	1.524	[mm]
-	-	-	1	2	1	-	0.00773
-	-	2	-	-	2	-	0.00773
-	1	-	1	-	2	-	0.00773
1	-	-	-	1	2	-	0.00773
1	2	-	-	-	-	1	0.00773
2	-	1	-	-	-	1	0.00973
-	-	-	-	-	3	-	0.02273

3.2.2.3 Starting Point

The CAD model of the design from HFSS can be seen in figures 3.16 and 3.17. From the design a set of parameters can be identified which were studied. They are listed below with their notation:

- Stripline:
 - Length: L_s
 - Width: w_s
- Waveguide:
 - Radius: r_{wg}
 - Length (height of PCB hardback): h_{metal}
- PCB substrates:
 - Heights: h_1, h_2
- Vias:
 - Size: d_{via}
 - Placement and distance between vias: $d_{via-via}, d_{via-s}$

A summary of these parameters with their starting, end and investigated values are presented in table 3.4.

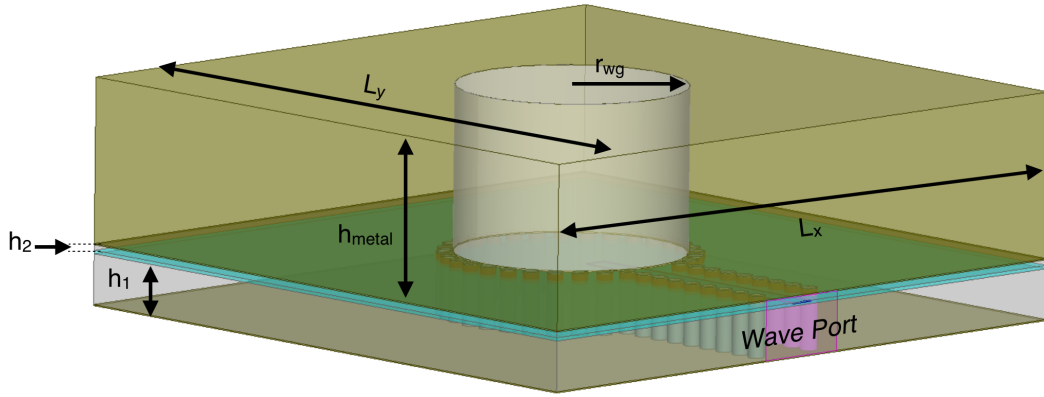


Figure 3.16: Perspective view of the stripline fed waveguide filled with dielectric with some of the parameter definitions.

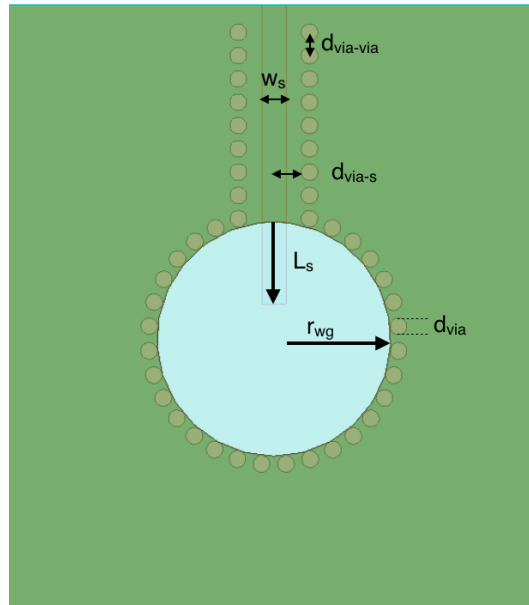


Figure 3.17: Top view of the stripline fed waveguide filled with dielectric with some of the parameter definitions.

3.2.2.3.1 Waveguide Radius: r_{wg} The first parameter to be determined was the waveguide radius. The permittivity of the dielectric material was given and with equation (2.2) and the calculated cutoff frequency from equation (3.1) (using a 6% bandwidth and 15% margin from cutoff) a waveguide radius of

Table 3.4: Summary of the design parameters and their values investigated during the design process of the stripline fed dielectric filled waveguide.

	Start	Sweep	End
Waveguide Radius	3.5 mm	2.5 - 4.5 mm	3.5 mm
Waveguide Length	5 mm	3-9 mm	5 mm
Stripline Length in waveguide	$0.5 \cdot r$	$[0.1, 0.9] \cdot r$	$0.5 \cdot r$
Stripline Width	0.5 mm	0.3-0.7	0.5
Substrate 1	$3 \cdot 0.704 \text{ mm} / 1.524 \text{ mm}$	0.254-1.524 mm	1.524 mm
Substrate 2	0.168 mm	0.168-0.762 mm	0.168 mm
Via Radius	0.25 mm	-	0.25 mm
Via Distance parts of λ_g	10	-	10

$$\begin{aligned}
 f_c &= \frac{q_{nm}}{2\pi a \sqrt{\mu\epsilon}} \Rightarrow 12.65 \cdot 10^9 \text{ Hz} = \frac{1.841}{2\pi a \sqrt{\mu_0 \cdot 4 \cdot \epsilon_0}} \Rightarrow \\
 \Rightarrow r_{wg} = a &= \frac{1}{12.65 \cdot 10^9} \cdot \frac{1.841}{2\pi \sqrt{\mu_0 \cdot 4 \cdot \epsilon_0}} = 0.0035 \text{ m} = 3.5 \text{ mm}
 \end{aligned} \tag{3.3}$$

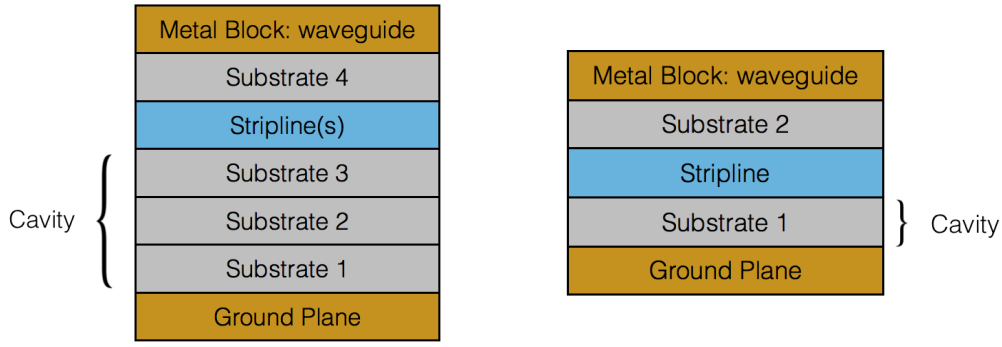
was calculated. With this size and dielectric filling the next mode to propagate is TM_{01} with a cutoff frequency of $f_{\text{TM}_{01c}} = 16.39 \text{ GHz}$.

3.2.2.3.2 PCB Substrates: h_1, h_2 The starting point for the upper substrate, h_2 , between the PCB hardback and the stripline, was chosen to be the thinnest available substrate since it would be the cheapest. As previously mentioned, the starting point of the cavity height were chosen to be three slabs of 0.762 mm glued together with Bondply with a thickness of 0.101 mm.

However, when doing a coarse parametric study of the cavity height, e.g. the lower substrate h_1 , it was discovered that the highest available substrate (1.524 mm, see table 3.2) could give a resonance at the correct frequency. Therefore, it was decided that the benefit of a cavity height close to $\lambda_g/4$ was neglect-able in comparison to a simpler and cheaper model. The change can be seen in figure 3.18.

3.2.2.3.3 Stripline and Vias A value of 0.5 mm was chosen as a starting point since it seemed reasonable given the other dimensions in the model. Another approach would have been to choose the width of the stripline to get a specific impedance. The width would then have to either be calculated or simulated. This would be time consuming and since the stripline width would in either way be studied and altered, a chosen starting point given the model's parameters was deemed to be good enough.

The length of the stripline was set to $0.5r_{wg}$ as it was in the middle of the parameter span, this parameter definition can be seen in figure 3.19. The radius of the vias was set to the standard 0.25 mm with a spacing of $\sim \lambda_g/10$.



(a) Schematic view of the stack up for the design with a cavity created with three substrates. Heights are not to scale.

(b) Schematic view of the stack up for the design with a cavity using only one substrate. Heights are not to scale.

Figure 3.18: Schematic overview of the stack up for the two different cavity configurations, heights are not to scale.

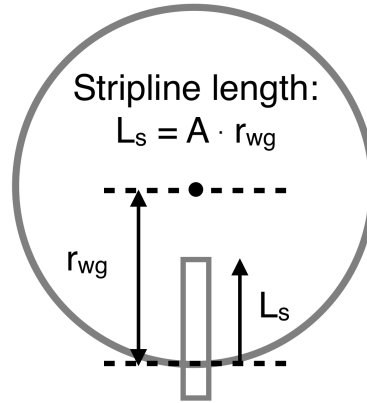


Figure 3.19: The definition of the stripline length, where it is expressed in parts of the waveguide radius $L = A \cdot r$, e.g. if $A = 1$ the stripline is extending into the middle of the waveguide and if $A = 0$ the stripline ends at the start of the aperture.

3.2.2.3.4 Wave Port Setup The wave port used in HFSS was set to a width of ten times the stripline width, according to standard procedure when simulating striplines from the HFSS documentation. In order to check if the wave port width was correct a simple model of only the stripline and the vias inside the PCB was simulated. The port width should not contribute to excitation of extra modes in the stripline. This was however the case when the width was set to ten times the stripline width and the width was decreased until higher modes were not a problem anymore. The port was normalized to $50 \, \Omega$ since the feeding network would have that impedance.

3.2.2.4 Parametric Study of Stripline Fed Dielectric Element

The following parametric studies were made using the design presented in figures 3.16 and 3.17. The size of the hardback and PCB was set to $L_x = 1.3\lambda_0$

and $L_y = 1\lambda_0$. In hindsight, these chosen dimensions were not optimal since a periodic ground plane can give rise to resonances ($L_y = 1\lambda_0$ is especially troublesome). The waveguide was placed in the middle of the design.

The design had only one stripline exciting the aperture in order to reduce complexity and simulation time, and if the element was promising the other polarization would be added. One test was made in the beginning with two striplines to verify that the isolation between the polarizations was good enough.

3.2.2.4.1 Isolation Between Polarizations The first test made was with two striplines inserted into the waveguide to see if a good enough isolation was possible to achieve. The element was not optimized, i.e. impedance matched, at this test and the result was only used as a first control of the isolation. The result can be seen in figure 3.21 where S_{11} and S_{22} are approximately 5 dB whereas S_{12} is of the order of -20 dB.

The parameters in the design are mainly the same as in the starting parameter column in table 3.4. The only changes are a stripline width of 0.323 mm and the use of three substrates of 0.704 mm height to create the cavity. The design can be seen in figure 3.20 and a stack up of the design is shown in figure 3.18a. The distance between the center of the vias and the stripline center is the same distance as between the vias, $\lambda_g/10$.

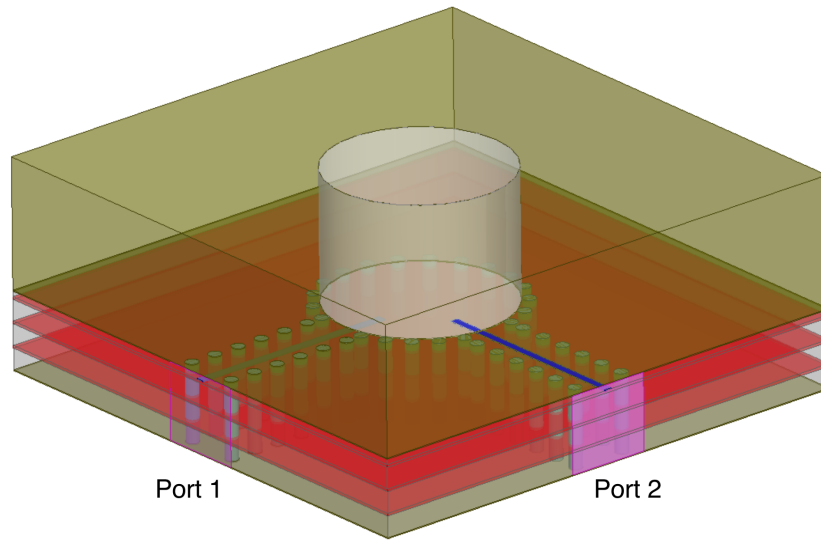


Figure 3.20: Overview of the dielectric design excited by two striplines to verify the possibility of an acceptable isolation between the two orthogonal polarizations.

3.2.2.4.2 Stripline Length: L_s The length of the stripline protruding into the waveguide was altered. The definition of the 'StripLengthConstant' parameter used can be seen in figure 3.19. The result of this parametric sweep

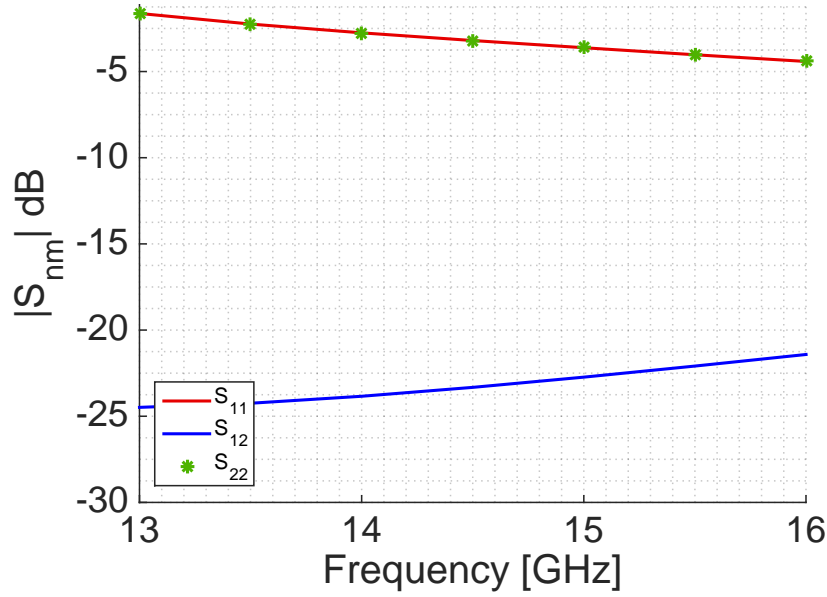


Figure 3.21: Graph of the S-parameters for a dual polarized dielectric filled element excited by two striplines. The element is not optimized and this was only used to confirm that a good enough isolation could be achieved.

is shown in figure 3.22.

As can be seen in the Smith chart in figure 3.22b a longer stripline rotates the resonance in the Smith chart. This is due to an impedance change where the reactance part is the one mostly affected.

The frequency span of the resonance also changes and has a maximum around a stripline length of 0.7 of the waveguide radius. A shorter and a longer length decreases the frequency span and the resonance is also rotated further away from the center of the Smith chart, see figure 3.22b. This implies a change in both resistance and reactance due to the length of the stripline. From the results, a stripline length of 0.5 waveguide radius inside the aperture gives a good resonance, since its resonant frequency span is not as large as the other lengths.

3.2.2.4.3 Stripline Width: W_s The width of the stripline exciting the waveguide affects the impedance, as expected. For the result of the parametric study, see figure 3.23. An increased width of the stripline decreases the resistance in accordance to theory, see section 2.4.1. A change of the width also affects the reactance, an increased width gives a more inductive behavior. This parameter is easy to change and does not give a shift in frequency, it is thus a good parameter for tuning.

3.2.2.4.4 Upper Substrate Height: h_2 The height of the upper substrate, the substrate between the stripline and the metal block, was studied.

The result is presented in figure 3.24. A change of the upper substrate height gives a change in impedance, mainly in reactance. A higher upper substrate decreases the reactance, which is clearly seen in figure 3.24b. The resonant frequency and the bandwidth are more or less unaltered.

3.2.2.4.5 Lower Substrate Height: h_1 The height of the lower substrate, the substrate between the stripline and the ground plane, was studied. The results can be seen in figure 3.25. The resonance and matching is very affected by this parameter as can be seen in the Smith chart. A higher substrate gives a larger resonant frequency span whilst a too thin substrate fails to give any resonant behavior for the design frequency. From the results the reasonable lower substrate heights are deemed to be 1.524 or 0.762 mm. This parameter would probably benefit from more available substrate heights.

3.2.2.4.6 Cavity Size Another parameter studied was the size of the cavity, meaning the radius of the via placement inside the substrates creating the cavity or the SIW. The parameter was chosen relative to the waveguide radius, so a 'cavitySizeChange' of -1 mm means a cavity with a radius 1 mm smaller than the waveguide radius. The results can be seen in figure 3.26. It is seen that a smaller cavity gives a smaller resonant frequency span, but the difference between the performance of different cavity sizes are not that large compared to the other parameters. It was concluded that a cavity size the same as the waveguide radius gave a good behavior.

3.2.2.4.7 Waveguide Radius The waveguide radius was also studied, even though it had been theoretically calculated. The results can be seen in figure 3.27. As can be seen, the best matching is achieved for 3.5 mm. A change of the radius results in a shift in frequency of the resonance, as expected, since the radius determines the operating frequency of the waveguide. Since the design frequency was chosen to be 15 GHz the waveguide radius of 3.5 mm gives the correct frequency response. The result for 4 mm shows some problematic behavior around 16.5 GHz, and a likely reason is a numerical artifact in the software.

3.2.2.4.8 Waveguide Height The waveguide height was also studied, the results can be seen in figure 3.28. A shorter length gives a smaller resonant frequency span. Furthermore, an alteration of the length gives a rotation in the Smith chart. This is expected, since the distance between generator and load is changed. One oddity is the frequency shift of the resonance where two possible explanations were identified.

The first is the existence of higher order modes in the waveguide. If the waveguide is not long enough the higher modes are not attenuated and may shift the resonant frequency or create other resonances. With a longer waveguide these resonances should disappear as the higher modes are attenuated. Some of this

behavior is seen when the waveguide length is increased considerably. The frequency shift gets smaller and smaller with increasing height which suggest the higher modes are attenuated.

The second possible explanation is the reflection from the waveguide and air interface. When the waveguide length is changed the phase shift of the reflection is also altered, corresponding to a certain wavelength. If destructive interference from the reflection is a parameter used for tuning of the element, the correct phase length for this interference is fixed. Therefore, when the length is changed, the frequency being subject to the interference also changes, corresponding to the wavelength giving the 'correct' phase shift of the reflection.

Further studies of the waveguide need to be done in order to conclude which of these phenomenon are responsible for the frequency shift behavior. This investigation was not made during the thesis but is recommended for future studies.

3.2.2.5 Conclusions of Parametric Study

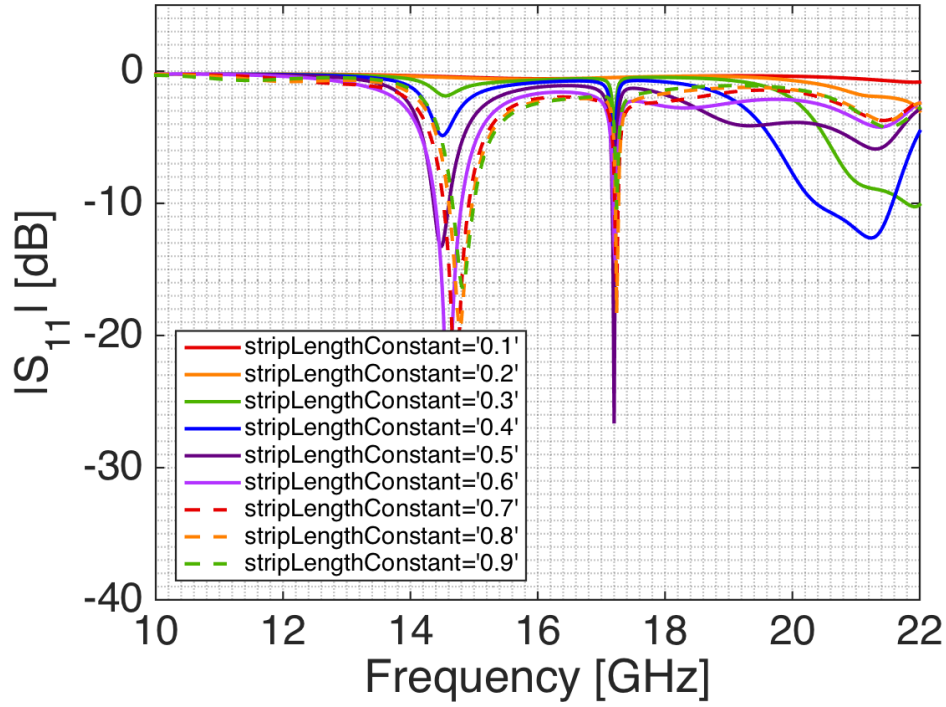
The parameters with the largest effect on the resonance for the stripline fed dielectric filled waveguide are:

- The stripline length, L_s
- The lower substrate height, h_1

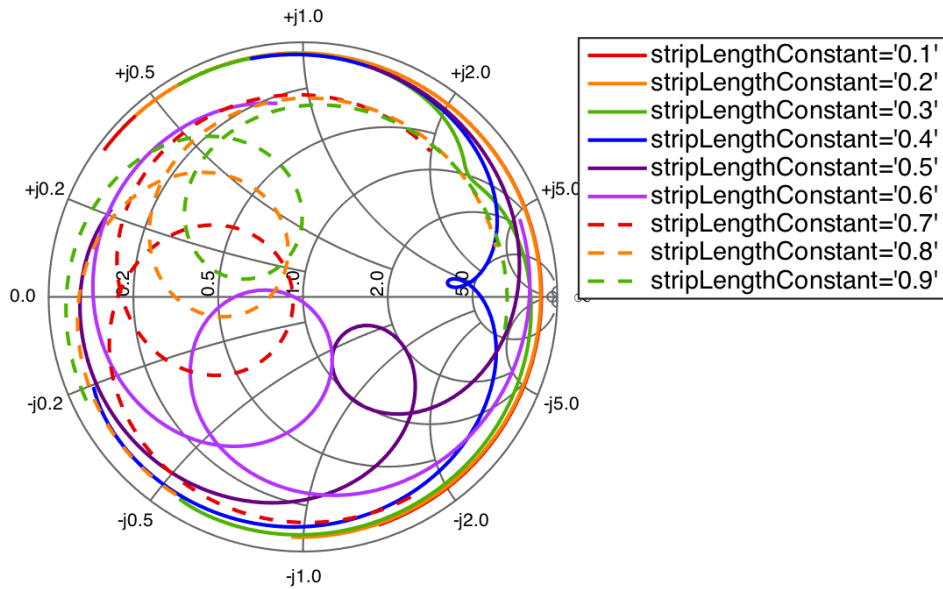
These should be chosen so the resonance is in the proper frequency span and the other parameters should then be used to improve the performance. One problem with the available parameters is the lack of centered resonances in the Smith charts in figures 3.22 to 3.28. This results in a too narrow bandwidth and the return loss requirement is not fulfilled. The not centered resonance implies a mismatch in impedance with regard to the characteristic impedance, a different value than $50\ \Omega$ for normalization in the HFSS settings could help with this issue. However, the design will be fed using a $50\ \Omega$ -feeding network and the design should be compatible with this feeding network at a later stage.

Using the conclusions from the parametric study the parameters were altered in order to further optimize the element. This process was iterative and a detailed description will not be presented. After extensive trials the available parameters were deemed to be insufficient in order to achieve a resonance in the middle of the Smith chart with regard to the characteristic impedance of $50\ \Omega$.

The HFSS tool of normalizing and de-embedding the wave port was used to show that the phase offset inherent to the design posed some problems (the problem discussed in the parametric study of the waveguide height, sec-

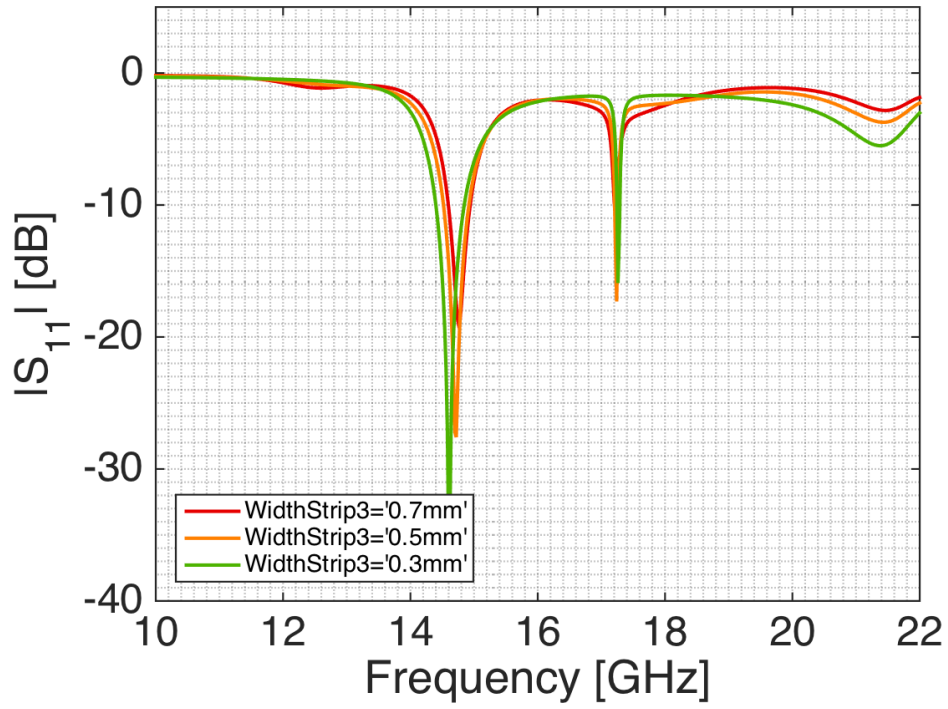


(a) $|S_{11}|$ in dB-scale for different lengths of the stripline into the waveguide in parts of the waveguide radius. The other design parameters had the starting values listed in table 3.4.

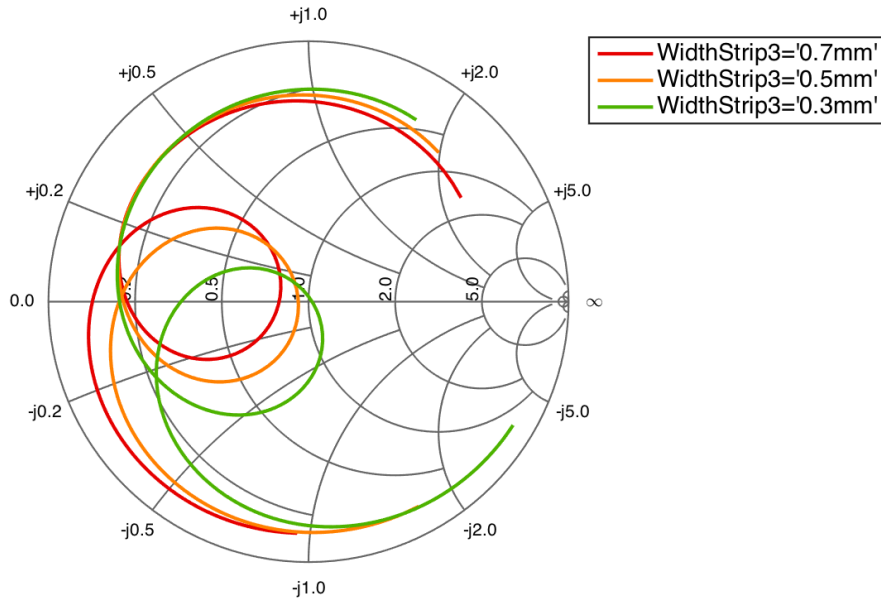


(b) Smith chart of S_{11} for different lengths of the stripline into the waveguide in parts of the waveguide radius for frequencies between 13-17 GHz. The other design parameters had the starting values listed in table 3.4.

Figure 3.22: Parametric study of the stripline length into the waveguide, the other design parameters had the starting values listed in table 3.4.

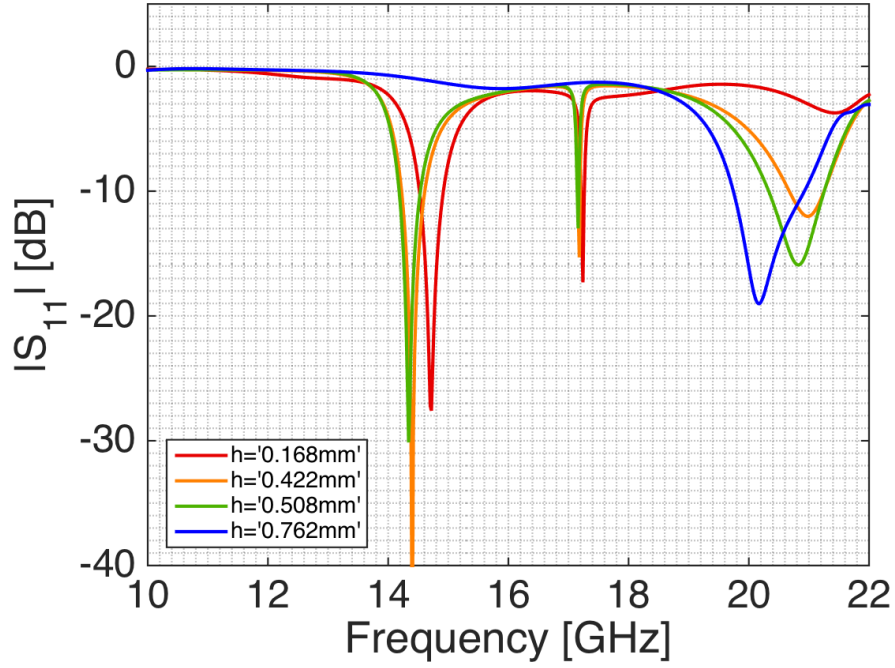


(a) $|S_{11}|$ in dB-scale for different stripline widths. The other design parameters had the starting values listed in table 3.4.

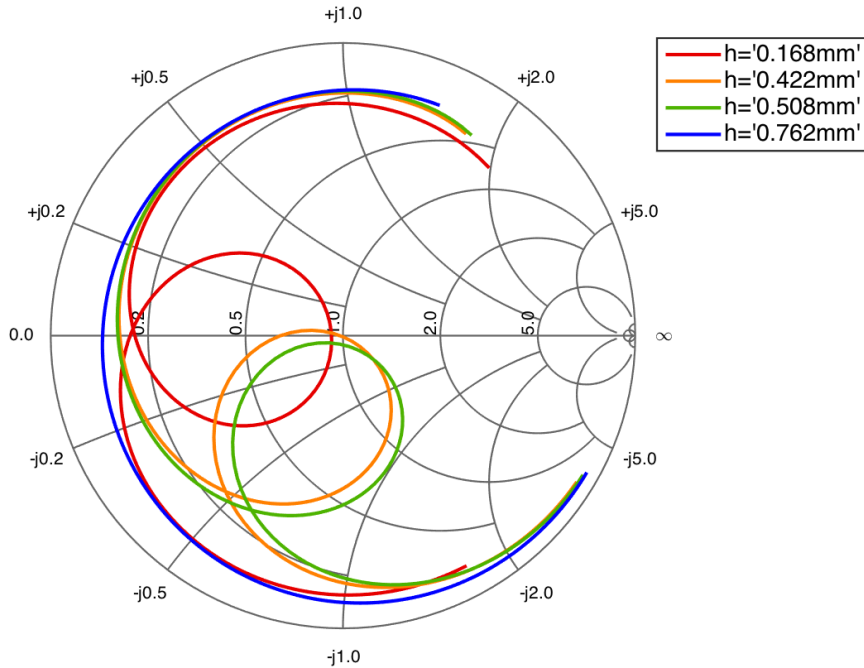


(b) Smith chart of S_{11} for different stripline widths for frequencies between 13-17 GHz. The other design parameters had the starting values listed in table 3.4.

Figure 3.23: Parametric study of the stripline width. The other design parameters had the starting values listed in table 3.4.

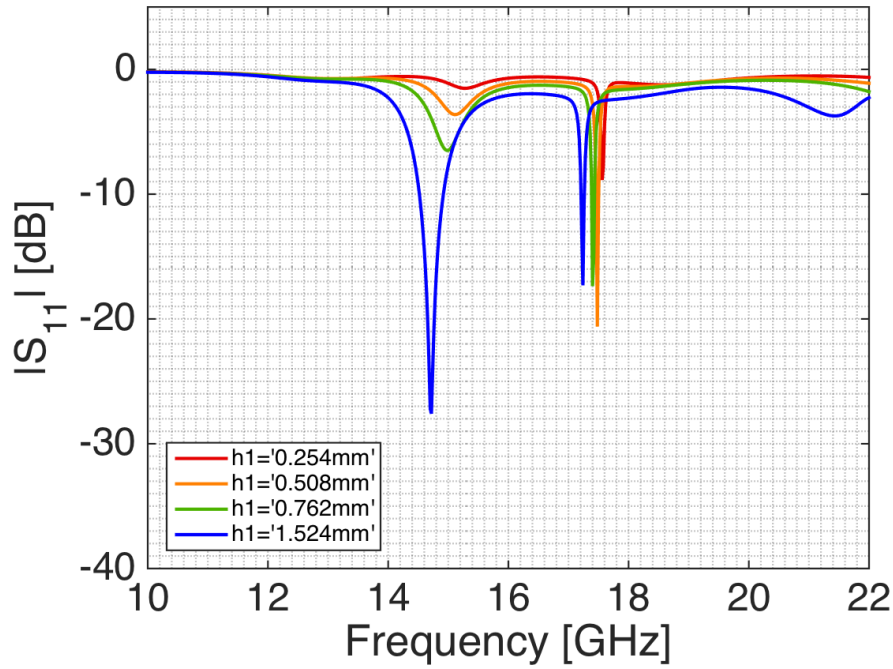


(a) $|S_{11}|$ in dB-scale for different heights of the upper substrate, the substrate between the stripline and the metal block. The other design parameters had the starting values listed in table 3.4.

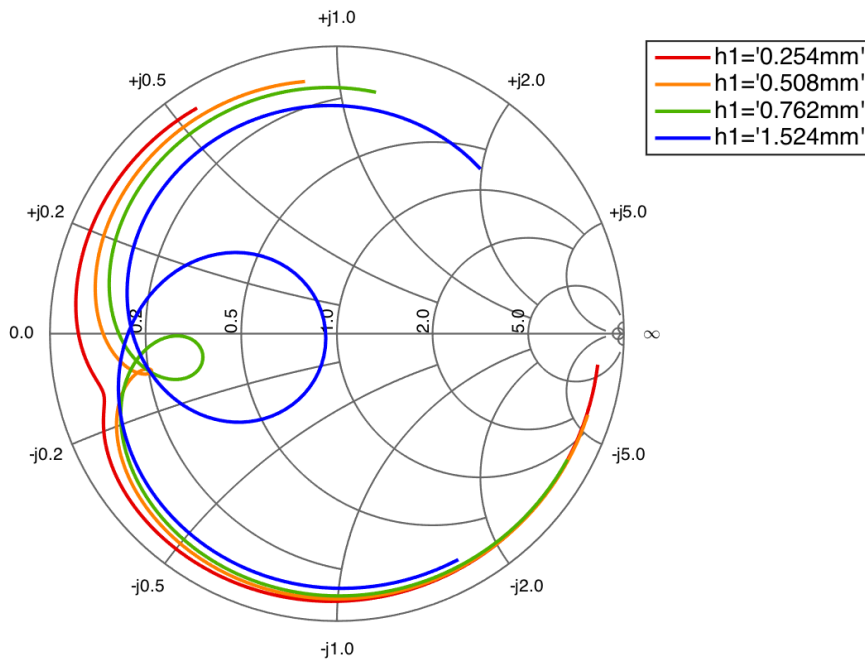


(b) Smith chart of S_{11} for different heights of the upper substrate, the substrate between the stripline and the metal block for frequencies between 13-17 GHz. The other design parameters had the starting values listed in table 3.4.

Figure 3.24: Parametric study of the upper substrate height. The other design parameters had the starting values listed in table 3.4.

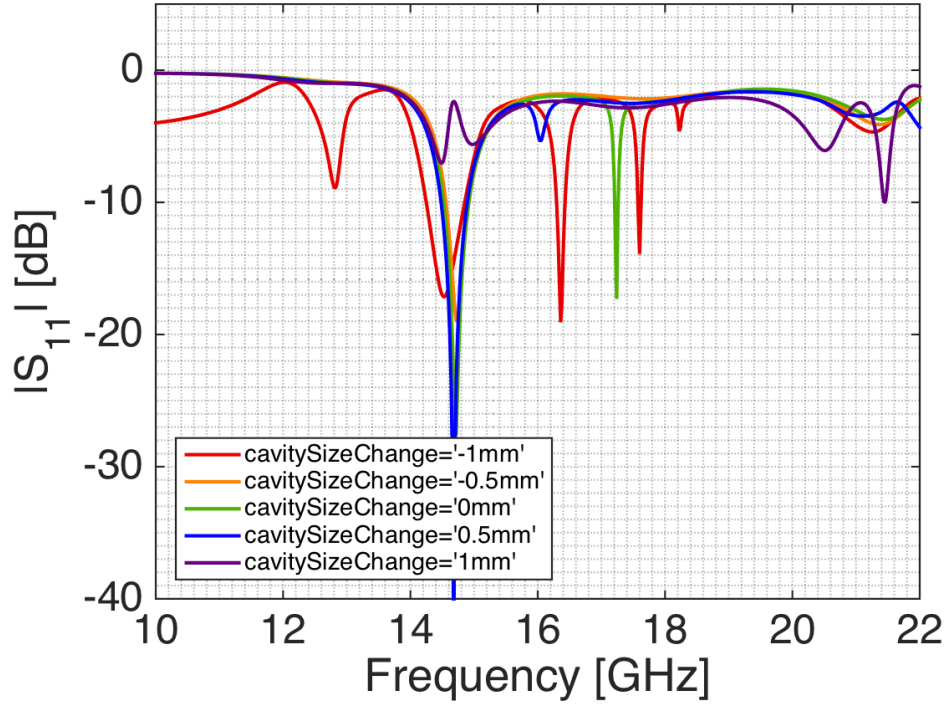


(a) $|S_{11}|$ in dB-scale for different heights of the lower substrate, the substrate between the stripline and the ground plane. The other design parameters had the starting values listed in table 3.4.

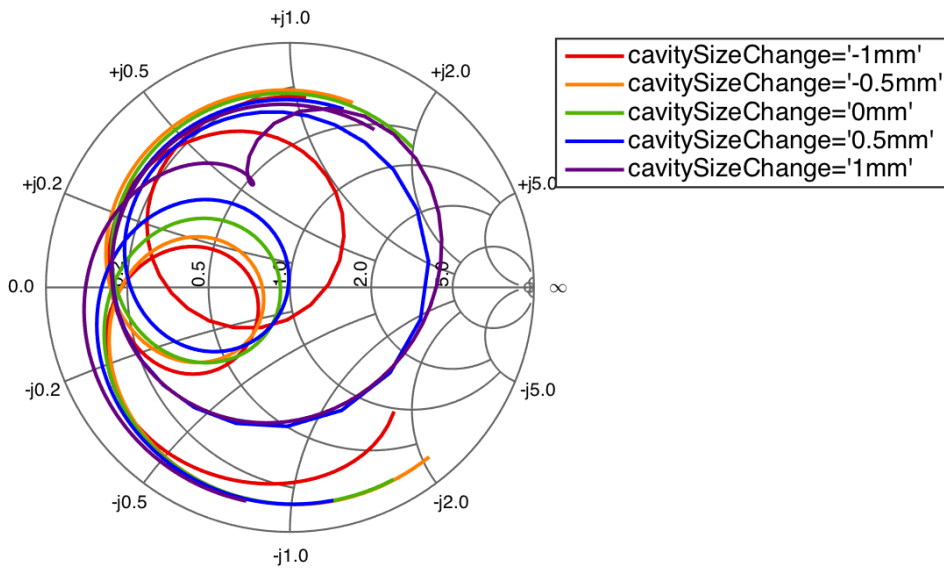


(b) Smith chart of S_{11} for different heights of the upper substrate, the substrate between the stripline and the ground plane for frequencies between 13-17 GHz. The other design parameters had the starting values listed in table 3.4.

Figure 3.25: Parametric study of the lower substrate height. The other design parameters had the starting values listed in table 3.4.

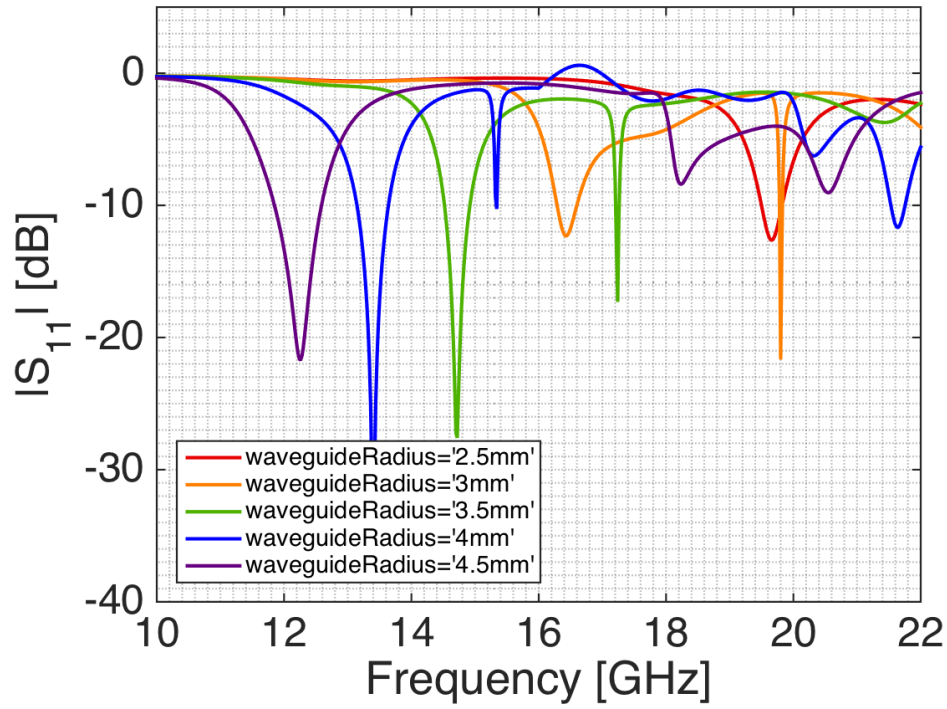


(a) $|S_{11}|$ in dB-scale for different radii of the cavity, the circle created by the vias inside the substrates. The other design parameters had the starting values listed in table 3.4.

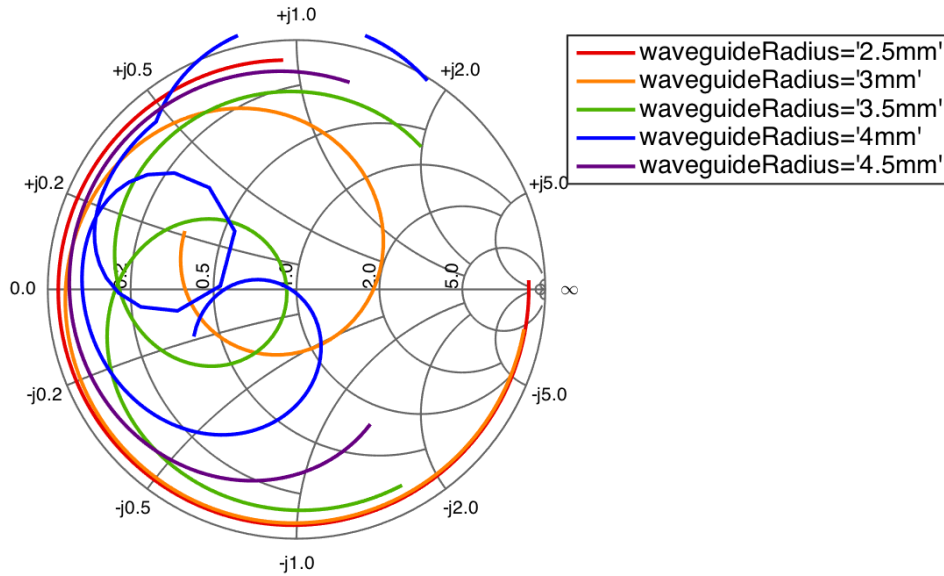


(b) Smith chart of S_{11} for different radii of the cavity, the circle created by the vias inside the substrates for frequencies between 13-17 GHz. The other design parameters had the starting values listed in table 3.4.

Figure 3.26: Parametric study of the cavity radius. The other design parameters had the starting values listed in table 3.4.

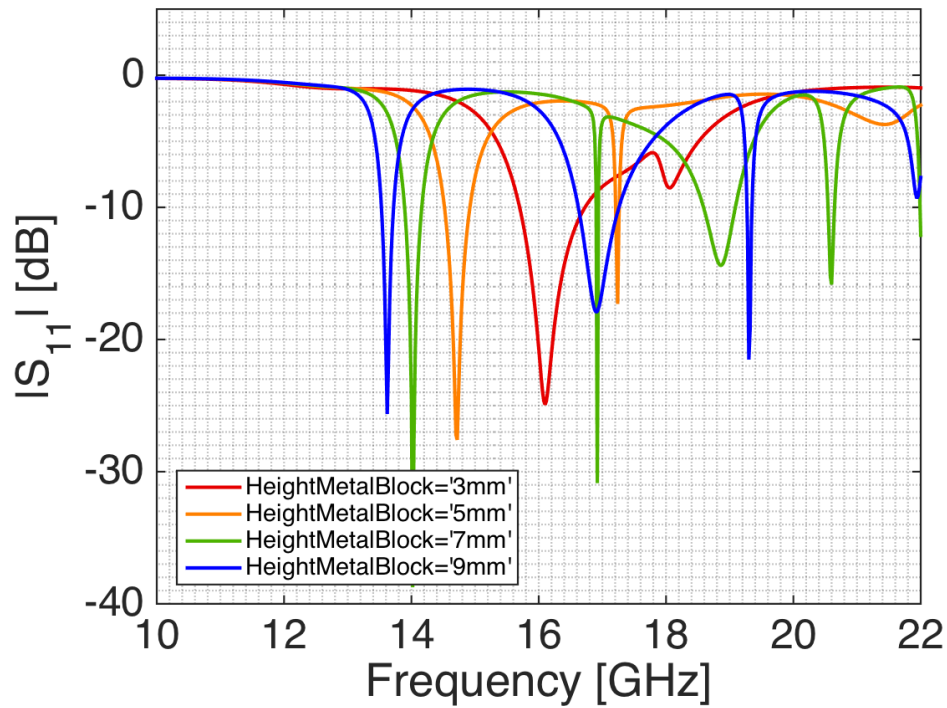


(a) $|S_{11}|$ in dB-scale for different radii of the waveguide. The other design parameters had the starting values listed in table 3.4.

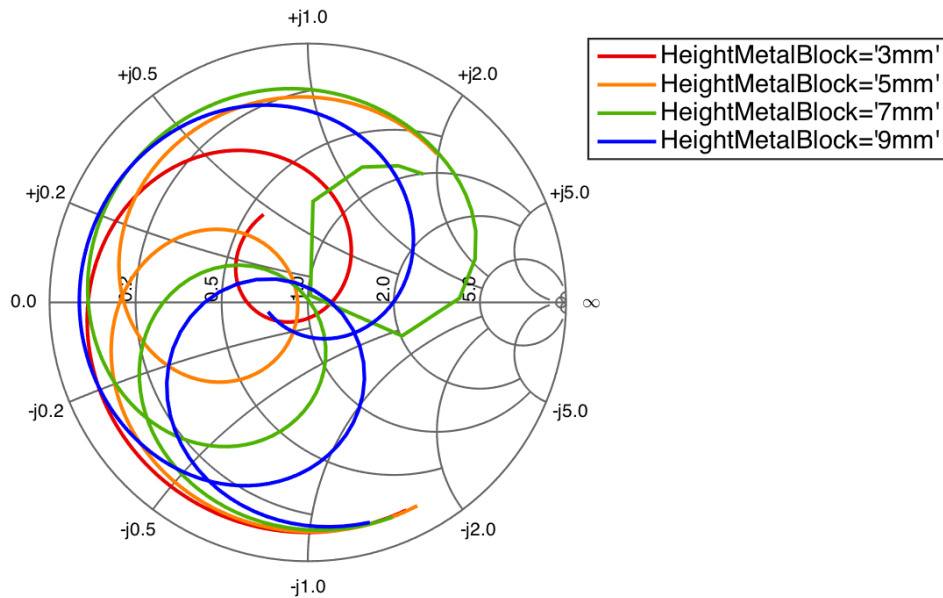


(b) Smith chart of S_{11} for different radii of the waveguide for frequencies between 13-17 GHz. The other design parameters had the starting values listed in table 3.4.

Figure 3.27: Parametric study of the waveguide radius. The other design parameters had the starting values listed in table 3.4.



(a) $|S_{11}|$ in dB-scale for different heights of the waveguide. The other design parameters had the starting values listed in table 3.4.



(b) Smith chart of S_{11} for different heights of the waveguide for frequencies between 13-17 GHz. The other design parameters had the starting values listed in table 3.4.

Figure 3.28: Parametric study of the waveguide height. The other design parameters had the starting values listed in table 3.4.

tion 3.2.2.4.8). In figure 3.29 the result of a design using the final parametric values as stated in table 3.4 is presented, where the wave port has been de-embedded 0.5 mm and the impedance is re-normalized to 110 Ω .

The de-embed function rotates the S-parameters according to the changed distance with respect to the port, in this case 0.5 mm. Through this, a better matching can be achieved and then the re-normalization and de-embedding can be implemented into the model. For example, the de-embedding can be implemented through a change of the size of the PCB and hardback (L_x , L_y).

The re-normalization of the port is harder to implement, e.g. changing Z_c from 50 Ω to 110 Ω . The main parameter which alters the resistance is the stripline width. Unfortunately, the PCB manufacturing limitations limits the minimum width of the stripline to 0.2 mm, which is not small enough to achieve the impedance change corresponding to the re-normalization of 110 Ω . Another solution would be to implement an impedance transformer between 50 and 110 Ω , e.g. a standard $\lambda/4$ -transformer. Unfortunately, this solution would have the same problem with the stripline width limitation. This idea was not investigated further since another promising design concept was found during the final simulations of the stripline excited design.

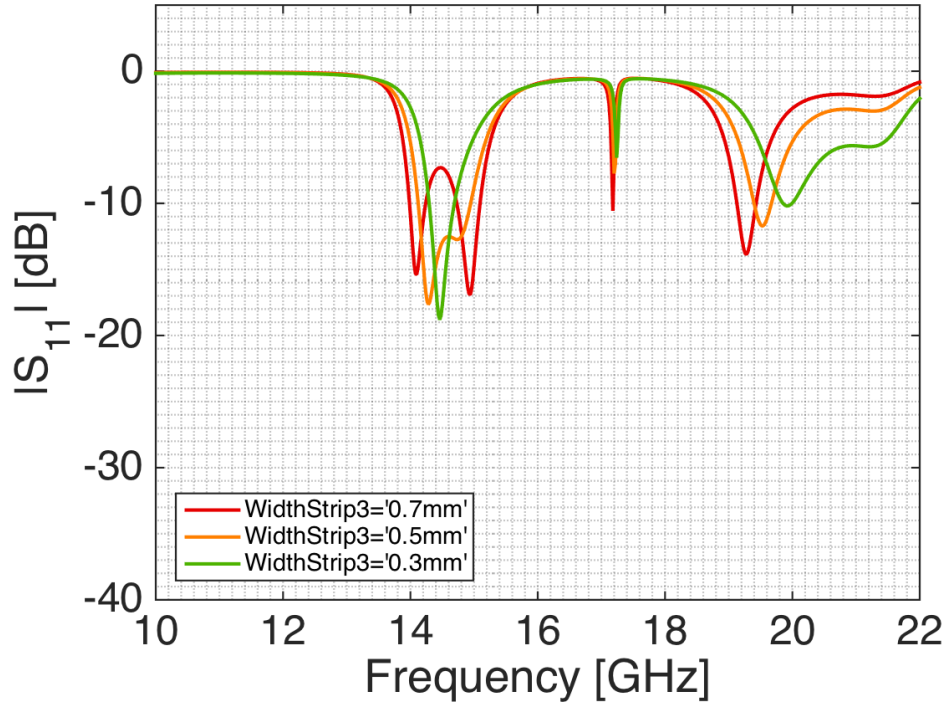
3.2.3 Slot Coupled Fed Dielectric Filled Waveguide

Since the design excited with the E-probes failed to achieve a good enough performance with regard to the bandwidth requirement, a second excitation method was investigated. This excitation used a cavity backed slot to excite the aperture, the cavity and slot being excited by a stripline. The element had several parameters used for impedance matching and optimization of the element, they can be seen in figures 3.30, 3.31. In figure 3.32 the design can be seen in a perspective view where the two ports are shown. A cross section of the stack up layers can be seen in figure 3.33. In figure 3.34 the coordinate system of the design is shown.

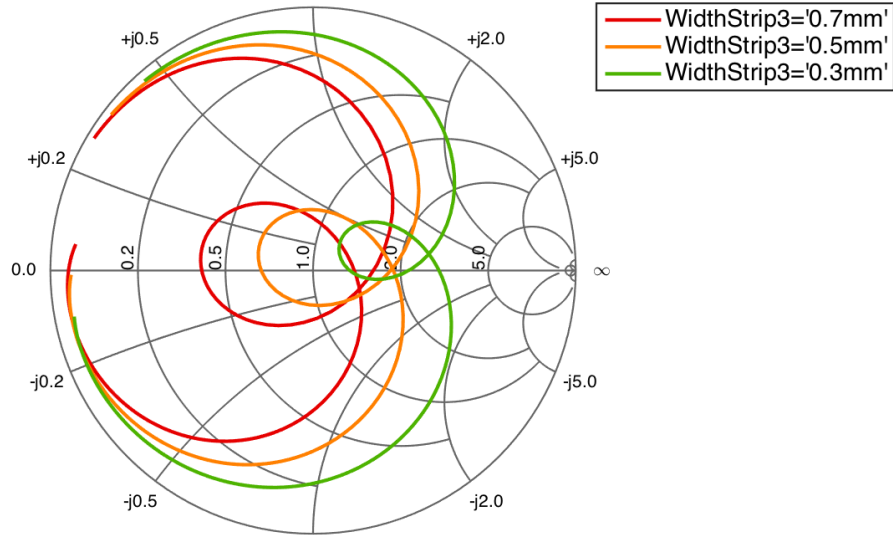
The main differences from the earlier design excited by a stripline are the addition of two substrate layers and a ground plane in the middle of the design where the slot is. The cavity layout is also changed and it now follows the slot shape, this change was made with regard to previous experience. Otherwise the design parameters remained the same as in the earlier design. The striplines were chosen to feed the slot in two different layers so the stripline length would not be limited by overlapping between the striplines.

3.2.3.1 Starting Parameters

The conclusions from the stripline fed design and its parametric studies were used to set the starting values of the parameters of the slot coupled design, where applicable. The previously used parameters and their starting point



(a) $|S_{11}|$ in dB-scale for different stripline widths and the wave port de-embedded 0.5 mm and re-normalized to 110 Ω . The other design parameters had the final values listed in table 3.4.



(b) Smith chart of S_{11} for different stripline widths and the wave port de-embedded 0.5 mm and re-normalized to 110 Ω for frequencies between 13-17 GHz. The other design parameters had the final values listed in table 3.4.

Figure 3.29: Tuning of the dielectric design excited by a stripline where the wave port has been de-embedded 0.5 mm and the re-normalization impedance has been changed from 50 Ω to 110 Ω . The design parameters had the final values listed in table 3.4.

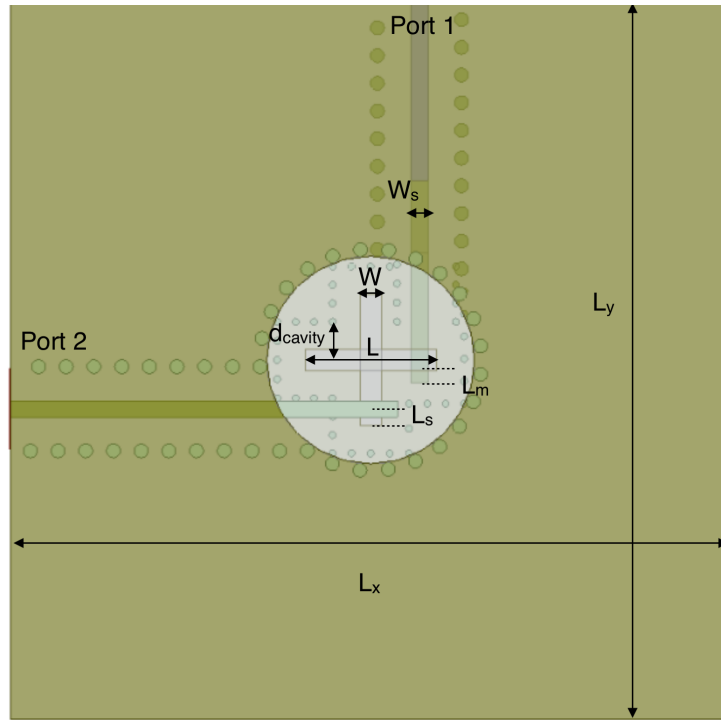


Figure 3.30: Top view of the design using a slot coupled feeding to excite the waveguide and the definition of the parameters studied.

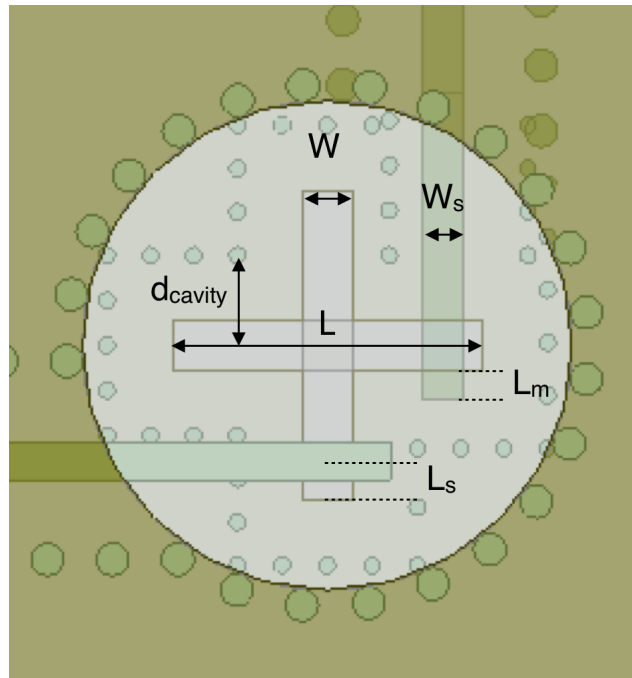


Figure 3.31: Close top view of the design using a slot coupled feeding to excite the waveguide and the definition of the parameters studied.

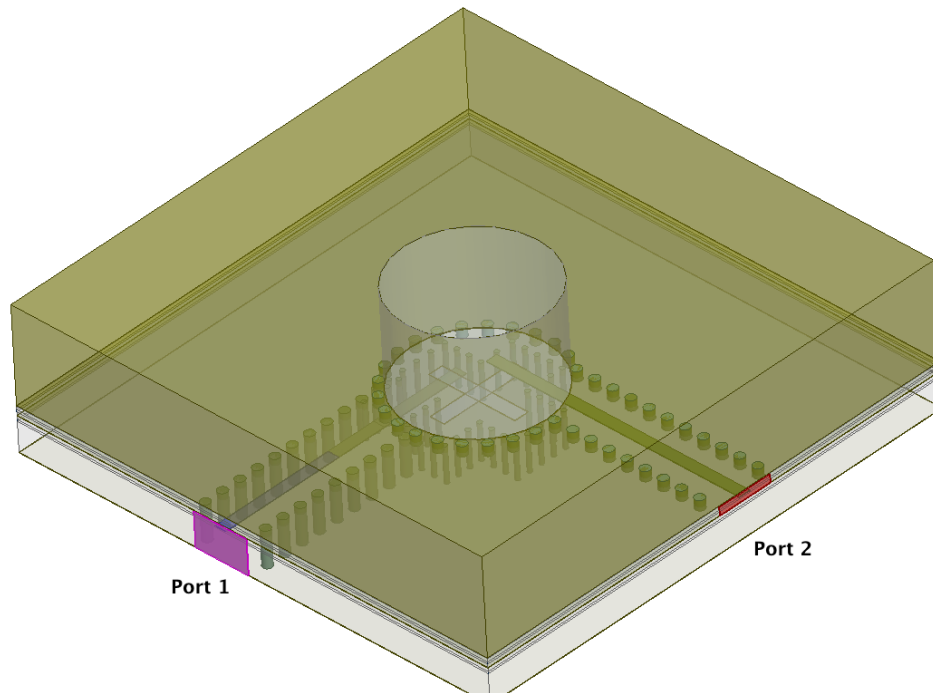


Figure 3.32: Perspective view of the design using a slot coupled feeding to excite the waveguide.

Metal Block: waveguide
Substrate 4
Stripline 2
Substrate 3
Ground Plane: slot
Substrate 2
Stripline 1
Substrate 1
Ground Plane

Figure 3.33: The stackup of the slot design, the heights are not to scale.

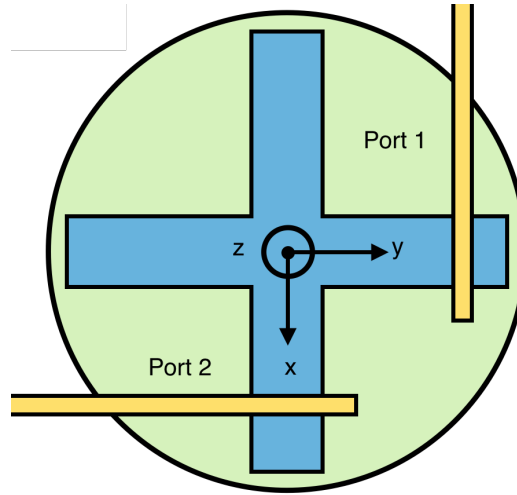


Figure 3.34: The coordinate system used in the design.

will therefore not be motivated since that is covered in section 3.2.2. The new parameters; the slot, cavity and substrates were chosen either according to theory from literature or manufacturing limitations. The parameters with their starting and end point values are listed in table 3.5 together with their parametric sweeps.

Table 3.5: Summary of the start, end and studied values of the parameters for the slot coupled dielectric filled waveguide.

	Start	Sweep	End
Waveguide Radius [mm]	3.5	3.5-3.7	3.7
Waveguide Length [mm]	5	0-10	5
Slot Length [mm]	5.23	3-5.23	4.75
Slot Width (% of slot length)	16	5-20	16
Stripline Length L_m [mm]	0.45	-0.3-0.9	0.45
Stripline Width [mm]	0.6	0.5-0.6	0.525
Stripline Position from slot edge [mm]	0.5	0.5-1	0.6
Substrate 1 [mm]	1.524	0.422-1.524	1.524
Substrate 2 [mm]	0.168	0.168-0.762	0.168
Substrate 3 [mm]	0.168	0.168-0.762	0.168
Substrate 4 [mm]	0.168	0.168-0.762	0.168
Cavity Size [mm]	1	0.3-1	0.9
Via Distance parts of λ_g	15	-	15

3.2.3.1.1 Slot Length: L The length of the slot was set to $\lambda_g/2$ which is the standard length of a resonant slot. [3] For a frequency of 15 GHz and a slot inserted between the substrates with $\epsilon_r = 3.66$ the starting length was $L = 5.23$ mm.

3.2.3.1.2 Slot Width: W The starting width of the slot was set to 16% of the slot length since it enables a high bandwidth. [43] This gave a slot width of $0.16L = 0.8368\text{mm}$.

3.2.3.1.3 Substrate Heights: h_1, h_2, h_3, h_4 The added substrates, because of the feeding in different layers (h_3 and h_4), were chosen to use the thinnest substrate thickness as a starting point. This choice was made with complexity, simulation time and manufacturing cost in mind.

3.2.3.1.4 Cavity Size: d_{cavity} The size of the cavity was set to 1 mm larger than the slot given previous experience from earlier work done by Ericsson AB.

3.2.3.1.5 Stripline Position and Stub: L_s, L_m The starting point of the stripline position from the edge of the slot to the center of the stripline, L_s , was set to 0.5 mm since the relationship of $L_s = 0.1L$ enables a large bandwidth. [43] The stub length was set to 0.45 mm by scaling the values used in [43] using the wavelength.

3.2.3.2 Parametric Study

The parameters shown in figures 3.30 and 3.32 were altered to see how they affected the antenna performance. This design employed two ports and their corresponding response were different for different parameters, hence both of the ports' responses were studied. There are several parameters that are similar to the previous design, see section 3.2.2.4, with the same response, for example the stripline widths and substrate heights. The overall behavior is presented here in Smith chart and $|S_{nn}|$ form. A more detailed presentation of the parametric study results can be found in Appendix C where the resistance and reactance of each parameter is shown.

3.2.3.2.1 Height of Substrate 1: h_1 The height of the lower substrate, the substrate labeled 1, was studied. The results can be seen in figures 3.35 and 3.36. The resonance and matching is very affected by this parameter, mostly for port 1. The reason behind this behavior is the substrate height's effect on the impedance of the stripline. For port 2 this parameter also affects the impedance but not to the same extent. Given the results, the lower substrate height is a critical parameter; and since the height of 1.524 mm is the only height to result in a resonance for port 1 this height was chosen.

3.2.3.2.2 Height of Substrate 2: h_2 The height of the substrate labeled 2 was studied. The results can be seen in figures 3.37 and 3.38. This parameter mainly alters the performance of the lower port, port number 1, since this substrate height affects the impedance of this stripline. Port 2 is fairly unaffected by a change of this parameter, the bandwidth of the resonant

frequencies increase slightly with a higher substrate. The reason is probably a higher cavity height which enables more frequencies to resonate inside the cavity. In figure 3.37 it is clearly seen that the best resonance and bandwidth is achieved with a low substrate 2 height. For higher heights the reactance is too high for port 1.

3.2.3.2.3 Height of Substrate 3: h_3 The height of substrate 3, the third substrate from the bottom, was studied. The results can be seen in figure 3.39 and 3.40. The impedance of port 2 is clearly seen to change with this parameter. This is expected since the substrate height affects the impedance of the stripline of port 2. In the Smith chart it is seen that the resistance is fairly stable whilst the reactance increases when the substrate height increases. A low substrate height seems to give a better performance.

3.2.3.2.4 Height of Substrate 4: h_4 The upper substrate height, substrate labeled 4, was also studied and the results are presented in figures 3.41 and 3.42. This parameter affects the responses in mainly the same way as the third substrate height which is to be expected since they affect the same stripline.

3.2.3.2.5 Slot Length: L The impact of the slot length was investigated and the results are presented in figures 3.43 and 3.44. A change in slot length affects the resonant bandwidth, the resistance and the reactance (with a larger change in reactance than resistance) which is seen in the Smith charts. As can be seen in the results, a slot length of $L = 4.75$ mm gives the best performance. A shorter slot length has a too small resonant frequency span and a longer slot length has a too large resonant bandwidth so the requirement of -13 dB can not be fulfilled.

3.2.3.2.6 Slot Width: W The slot width alters the impedance of both ports, which is seen in figures 3.45 and 3.46. The parameter 'Wconst' is defined as a constant times the slot length. Both ports are affected in the same way and the width of the slot also affects the bandwidth of the antenna. An increase of the width beyond 16% of the slot length does not give a significant increase in bandwidth. This corresponds to the theory of a dual resonant slot, see section 2.4.2.

3.2.3.2.7 Stripline Placement in Slot: L_s The stripline placement in the slot was defined as the distance between the middle of the stripline to the edge of the slot, see figure 3.31. The results of the parametric study are shown in figures 3.47 and 3.48 for the two ports.

As can be seen in figures 3.47 and 3.48, the main resonance at 15 GHz is rotated in the Smith chart, both the resistance and the reactance are affected by this parameter. The bandwidth is slightly affected by this parameter and thus it

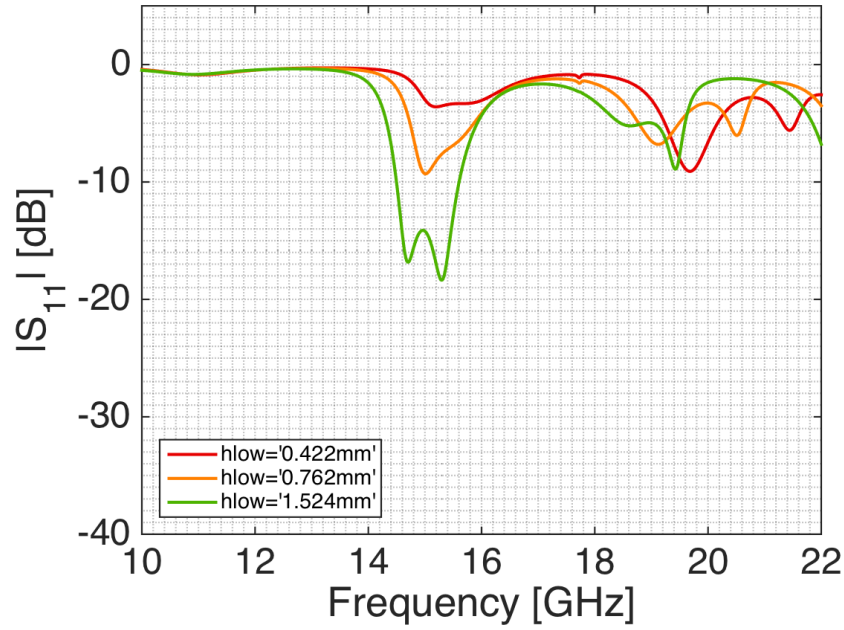
can be used to change the bandwidth if the other easily changed parameters fail to give the wanted performance.

3.2.3.2.8 Stripline Width: W_s The stripline width for both ports were studied. The results of the stripline width of port 1 are seen in figures 3.49 and 3.50 and the stripline width for port 2 in figures 3.51 and 3.52. As expected, the impact of the impedance of the port which stripline is not altered is negligible whilst the impedance for the port altered is affected. A wider stripline gives a lower resistance and reactance and this parameter can be used to for the final fine tuning. The same behavior is seen for both ports which is expected. The stripline widths studied are different for port 1 and port 2, which is the reason behind the different responses at first glance.

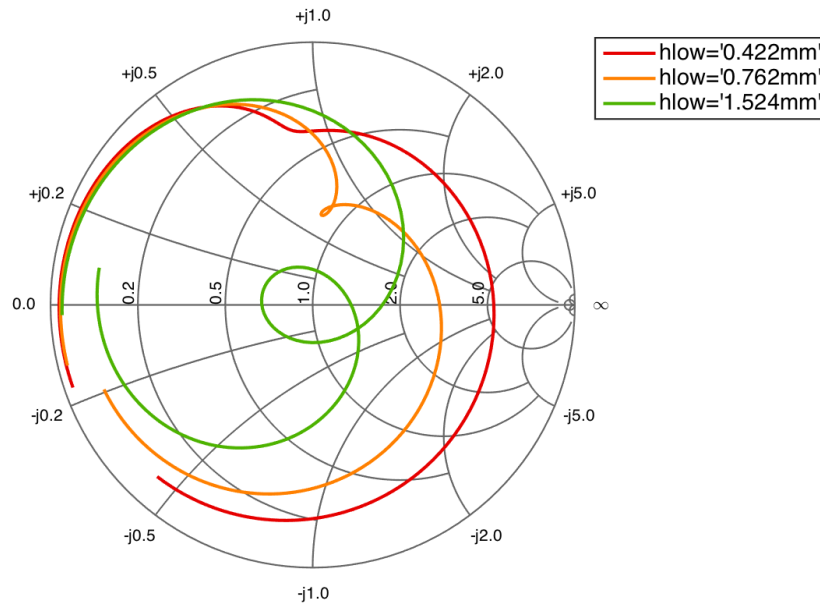
3.2.3.2.9 Stripline Stub Length: L_m The stripline length for both ports were studied. The results of the stripline length of port 1 is seen in figures 3.53 and 3.54 and the stripline length for port 2 in figures 3.55 and 3.56. As expected the impact on the port not altered is negligible. This parameter functions as a stub and alters the reactance: the resonance is rotated in the Smith chart. The bandwidth of the resonance is also affected since a longer stub results in a more narrow frequency response for which it is matched.

3.2.3.2.10 Cavity Size: d_{cavity} The cavity size and its effect on the response is presented in figures 3.57 and 3.58. This parameter is defined as the distance between the slot and the vias creating the cavity, see figure 3.31. The cavity size determines the resonance bandwidth, a smaller cavity gives a smaller bandwidth. The reactance is also slightly changed by this parameter. If a smaller bandwidth is needed this parameter could be used to create a better return loss by decreasing the resonant frequency span.

3.2.3.2.11 Waveguide Height The waveguide height parameter behaves similar as in the previous design, i.e. the design fed by the E-field probes. The frequency bandwidth is shifted and the response is rotated in the Smith chart which is expected. The waveguide height of 5 mm gives a resonance in the correct frequency range of 15 GHz and a bandwidth in the right sized order that gives a return loss below -13 dB and a bandwidth close to 6%.

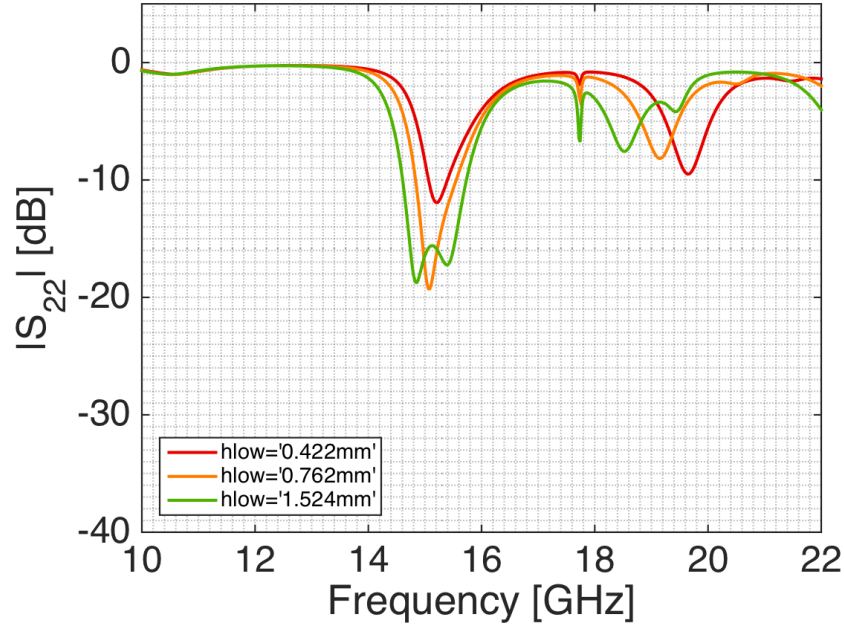


(a) $|S_{11}|$ in dB-scale for different heights of the lower substrate, h_1 . The other parameters were fixed and had the starting values as stated in table 3.5.

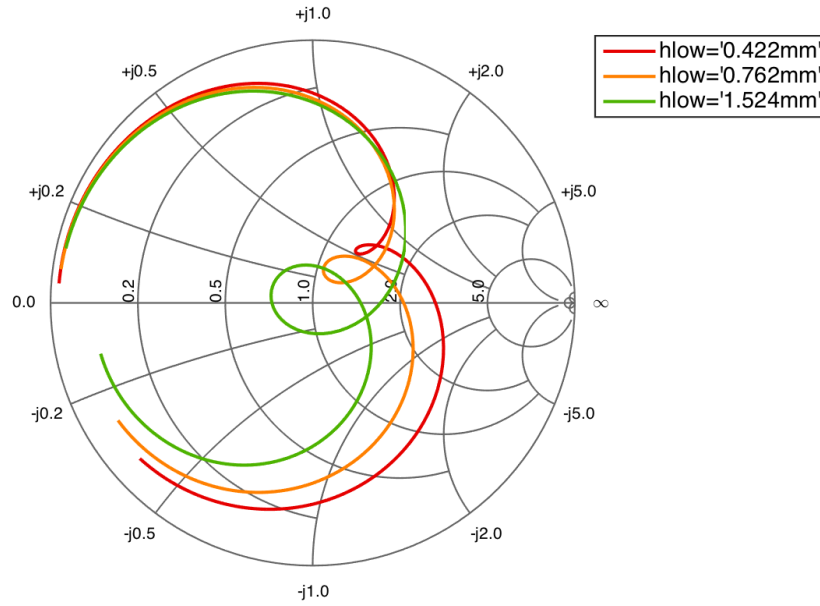


(b) Smith chart of S_{11} for different heights of the lower substrate, h_1 , for frequencies between 13-17 GHz. The other parameters were fixed and had the starting values as stated in table 3.5.

Figure 3.35: Parametric study of the lower substrate height, h_1 , for port 1. The other parameters were fixed and had the starting values as stated in table 3.5.

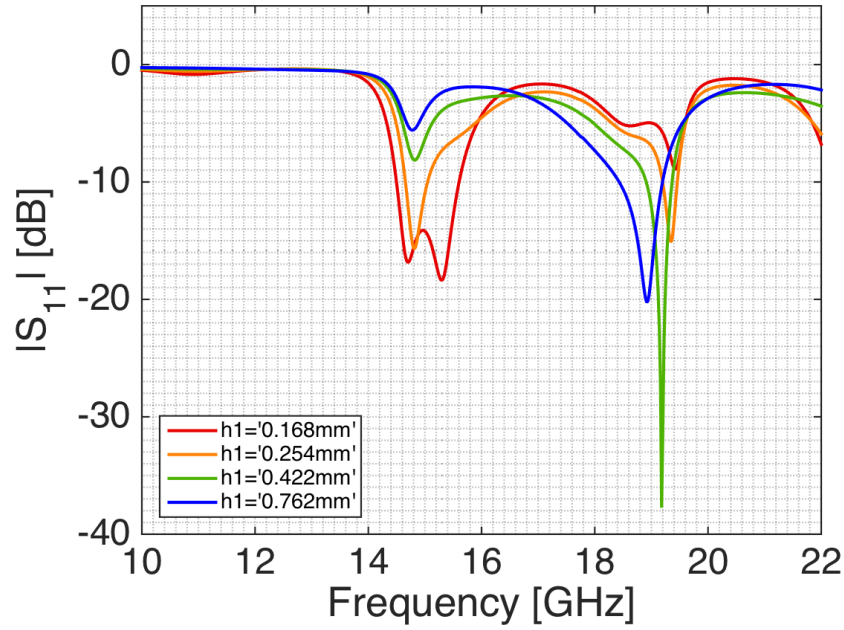


(a) $|S_{22}|$ in dB-scale for different heights of the lower substrate, h_1 . The other parameters were fixed and had the starting values as stated in table 3.5.

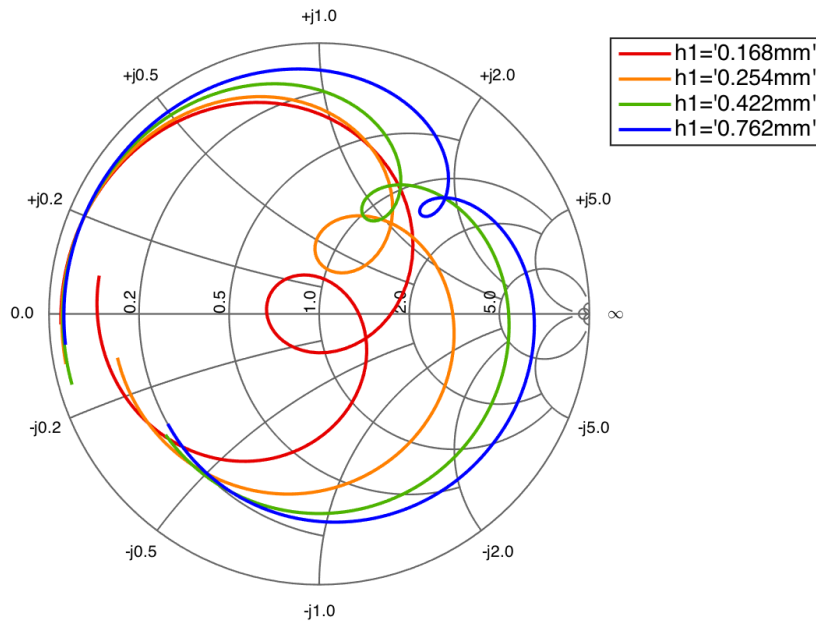


(b) Smith chart of S_{22} for different heights of the lower substrate, h_1 , for frequencies between 13-17 GHz. The other parameters were fixed and had the starting values as stated in table 3.5.

Figure 3.36: Parametric study of the lower substrate height, h_1 , for port 2. The other parameters were fixed and had the starting values as stated in table 3.5.

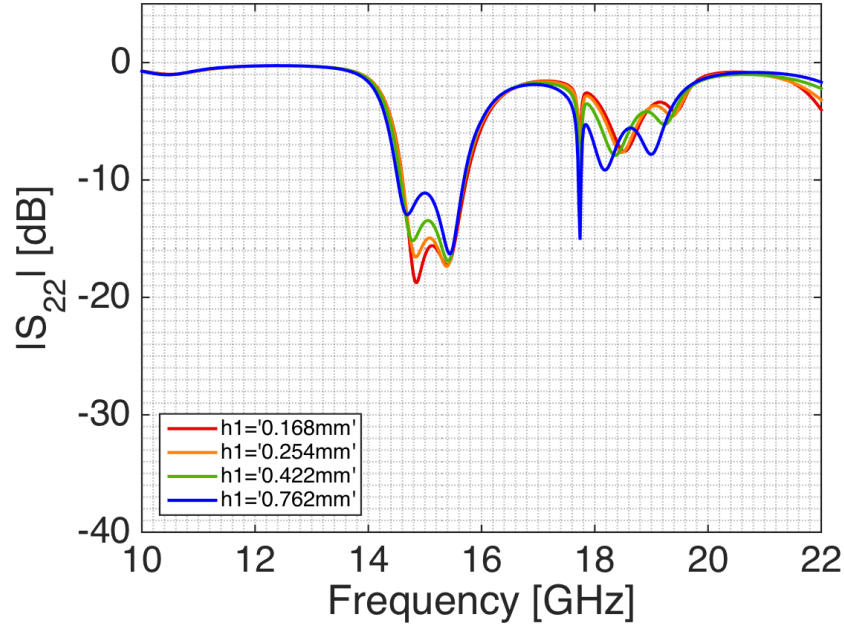


(a) $|S_{11}|$ in dB-scale for different heights of the second lower substrate, h_2 . The other parameters were fixed and had the starting values as stated in table 3.5.

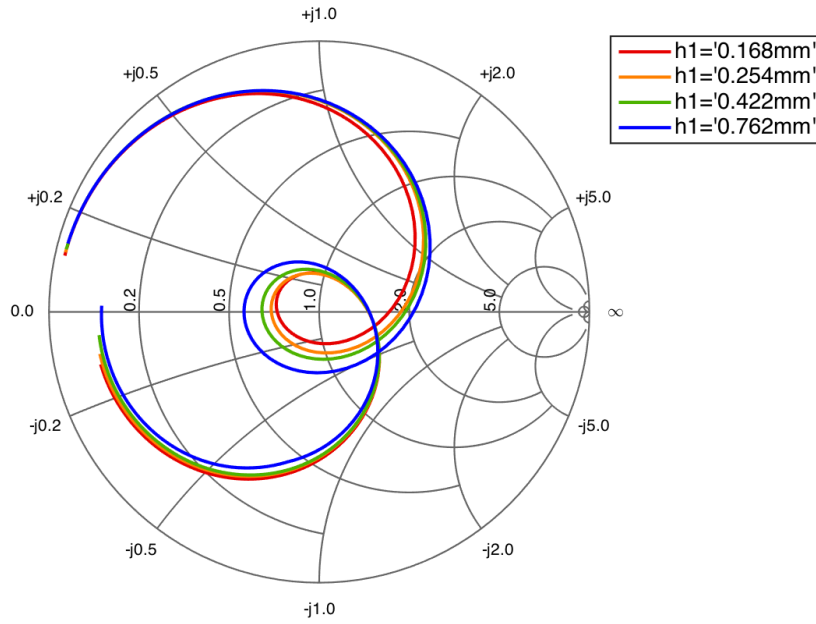


(b) Smith chart of S_{11} for different heights of the second lower substrate, h_2 , for frequencies between 13-17 GHz. The other parameters were fixed and had the starting values as stated in table 3.5.

Figure 3.37: Parametric study of S_{11} of the different heights of the second lower substrate, h_2 . The other parameters were fixed and had the starting values as stated in table 3.5.

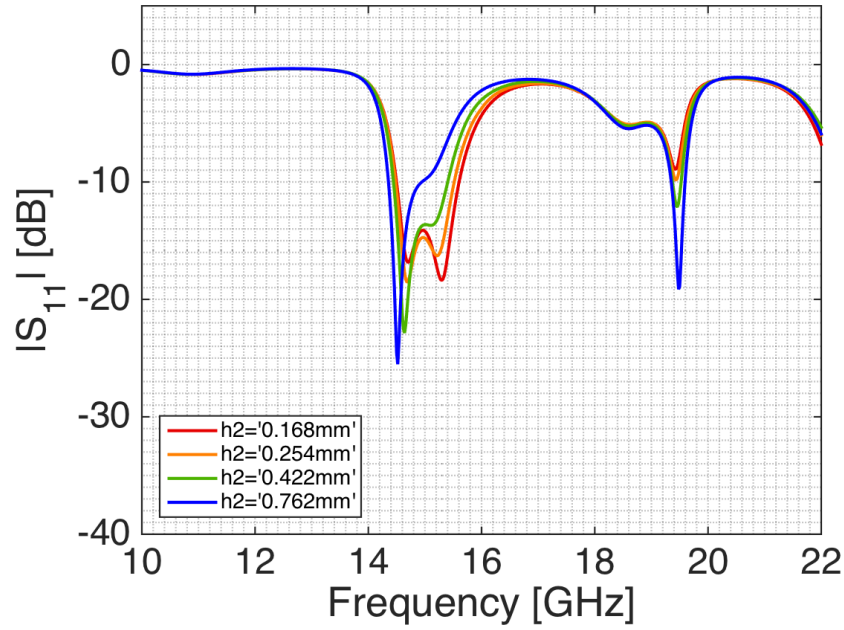


(a) $|S_{22}|$ in dB-scale for different heights of the second lower substrate, h_2 . The other parameters were fixed and had the starting values as stated in table 3.5.

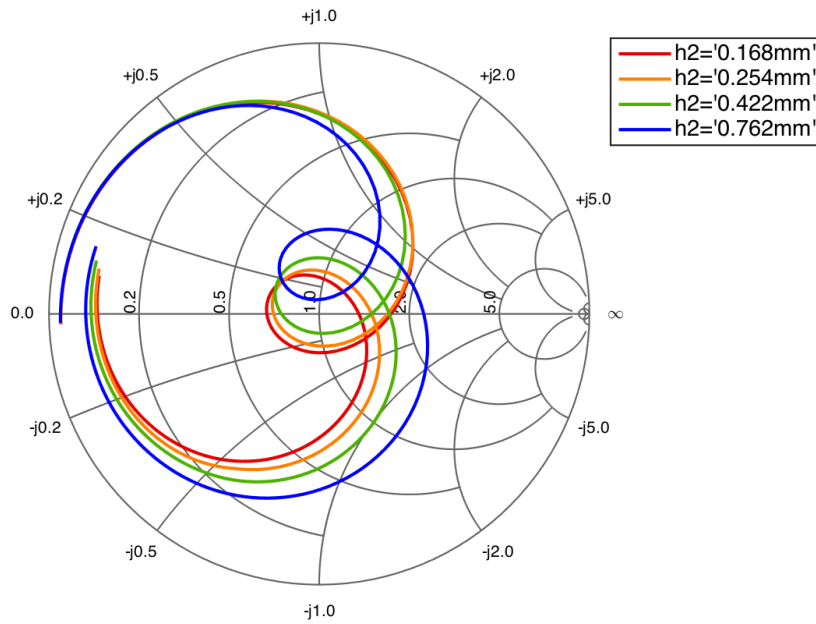


(b) Smith chart of S_{22} for different heights of the second lower substrate, h_2 , for frequencies between 13-17 GHz. The other parameters were fixed and had the starting values as stated in table 3.5.

Figure 3.38: Parametric study of S_{22} of the different heights of the second lower substrate, h_2 . The other parameters were fixed and had the starting values as stated in table 3.5.

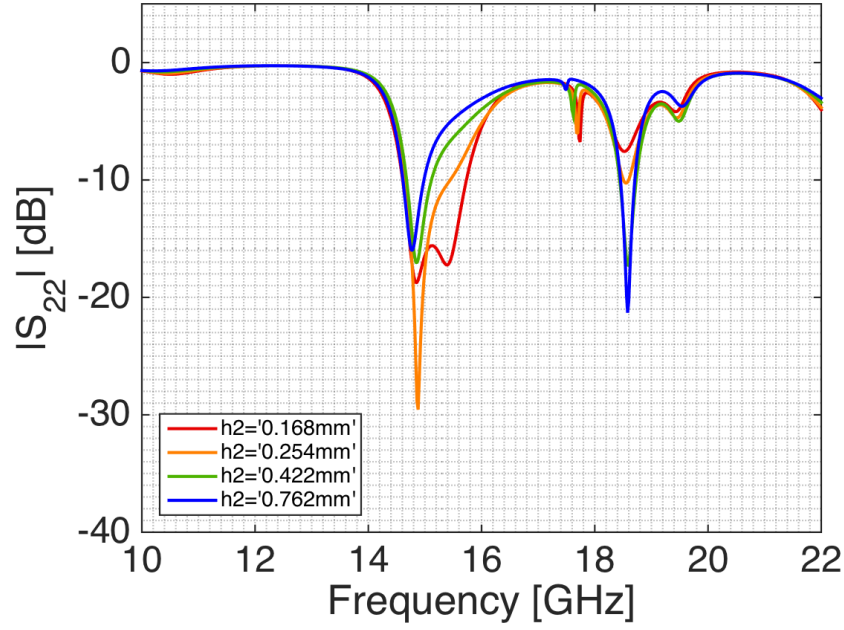


(a) $|S_{11}|$ in dB-scale for different heights of the second highest substrate, h_3 . The other parameters were fixed and had the starting values as stated in table 3.5.

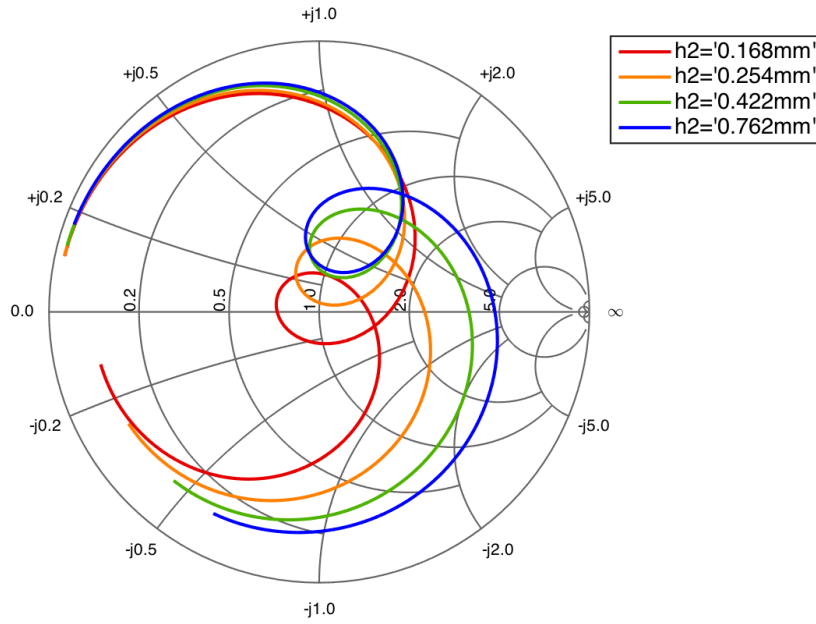


(b) Smith chart of S_{11} for different heights of the second highest substrate, h_3 , for frequencies between 13-17 GHz. The other parameters were fixed and had the starting values as stated in table 3.5.

Figure 3.39: Parametric study of S_{11} of the different heights of the second highest substrate, h_3 . The other parameters were fixed and had the starting values as stated in table 3.5.

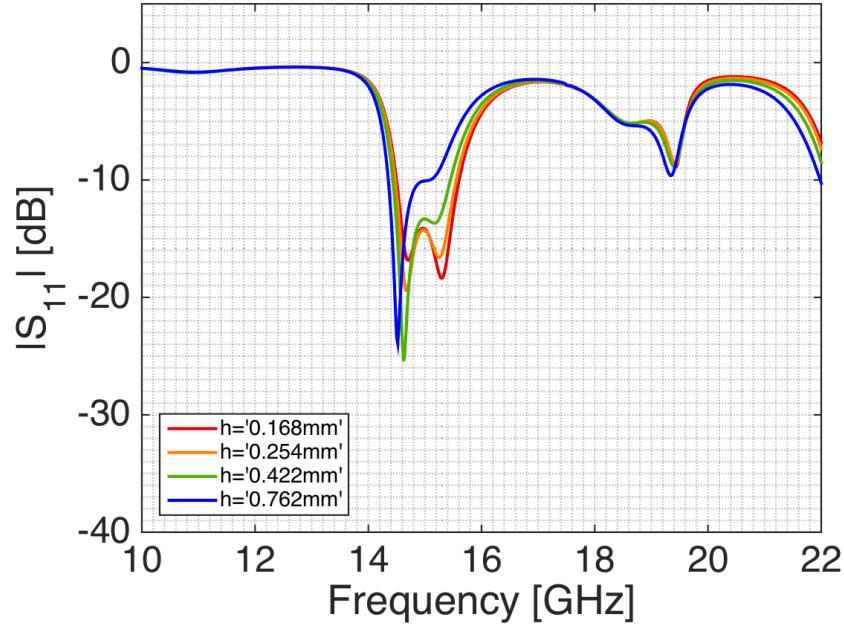


(a) $|S_{22}|$ in dB-scale for different heights of the second highest substrate, h_3 . The other parameters were fixed and had the starting values as stated in table 3.5.

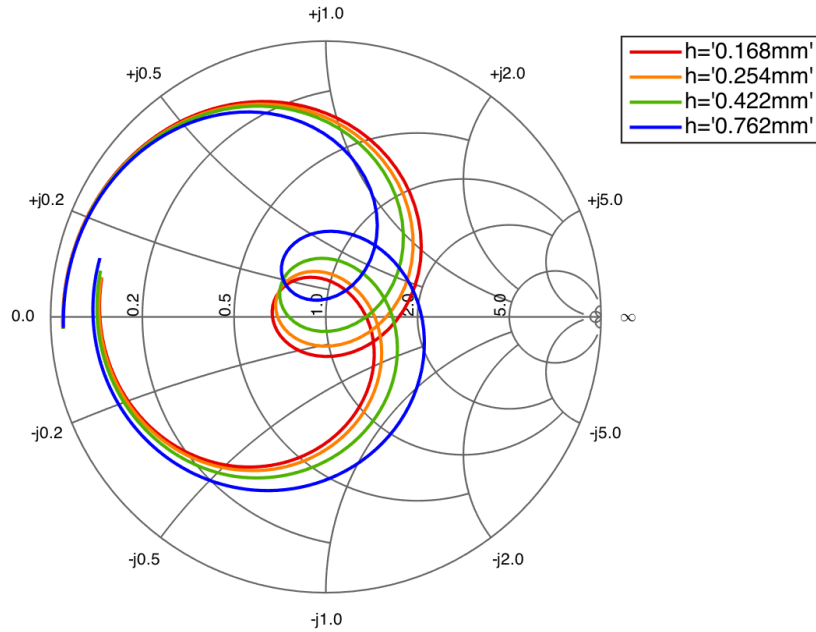


(b) Smith chart of S_{22} for different heights of the second highest substrate, h_3 , for frequencies between 13-17 GHz. The other parameters were fixed and had the starting values as stated in table 3.5.

Figure 3.40: Parametric study of S_{22} of the different heights of the second highest substrate, h_3 . The other parameters were fixed and had the starting values as stated in table 3.5.

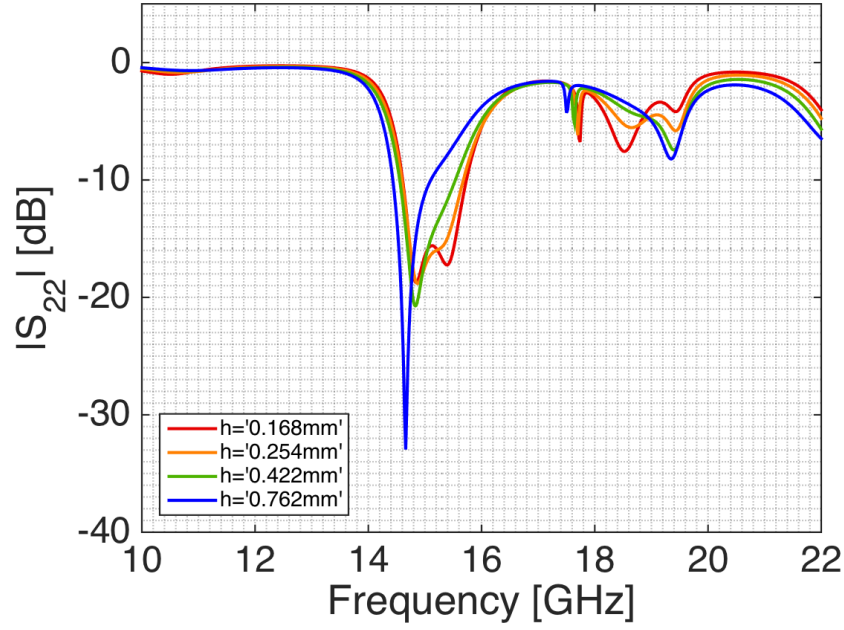


(a) $|S_{11}|$ in dB-scale for different heights of the uppermost substrate, h_4 . The other parameters were fixed and had the starting values as stated in table 3.5.

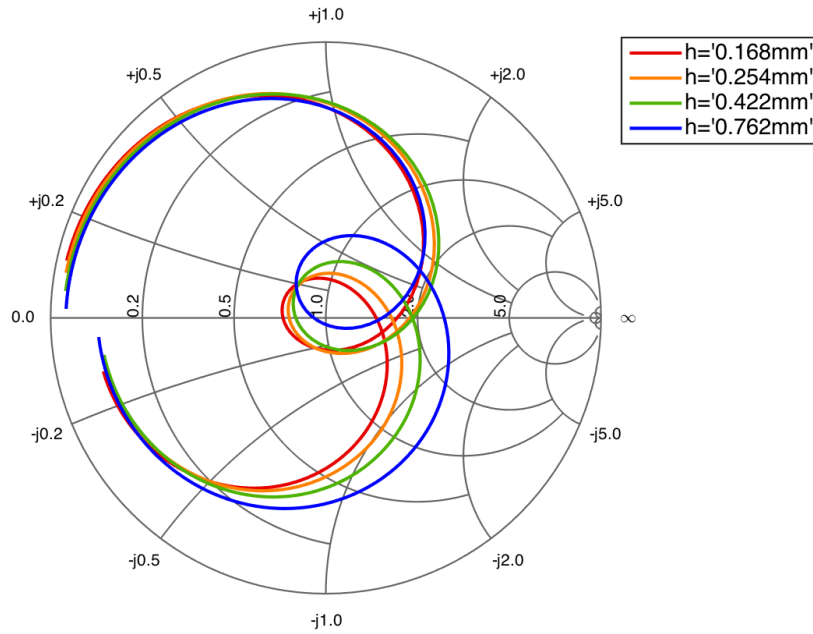


(b) Smith chart of S_{11} for different heights of the uppermost substrate, h_4 , for frequencies between 13-17 GHz. The other parameters were fixed and had the starting values as stated in table 3.5.

Figure 3.41: Parametric study of S_{11} of the different heights of the uppermost substrate, h_4 . The other parameters were fixed and had the starting values as stated in table 3.5.

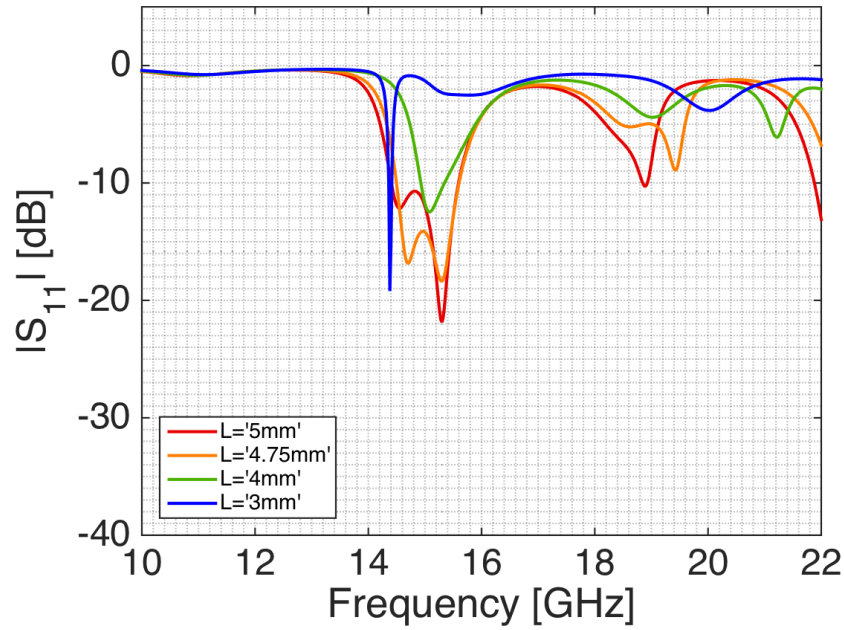


(a) $|S_{22}|$ in dB-scale for different heights of the uppermost substrate, h_4 . The other parameters were fixed and had the starting values as stated in table 3.5.

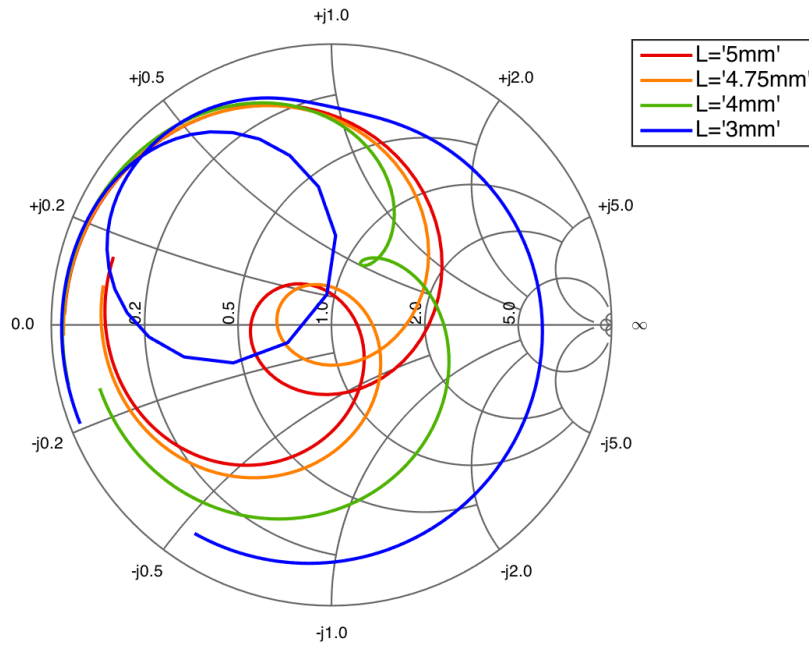


(b) Smith chart of S_{22} for different heights of the uppermost substrate, h_4 , for frequencies between 13-17 GHz. The other parameters were fixed and had the starting values as stated in table 3.5.

Figure 3.42: Parametric study of S_{22} of the different heights of the highest substrate, h_4 . The other parameters were fixed and had the starting values as stated in table 3.5.

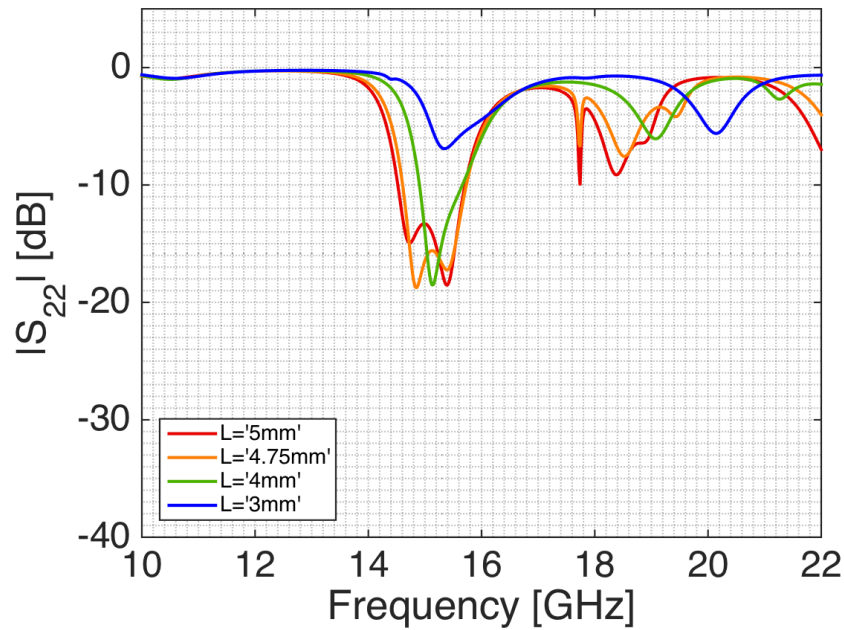


(a) $|S_{11}|$ in dB-scale for different lengths of the slot, L . The other parameters were fixed and had the starting values as stated in table 3.5.

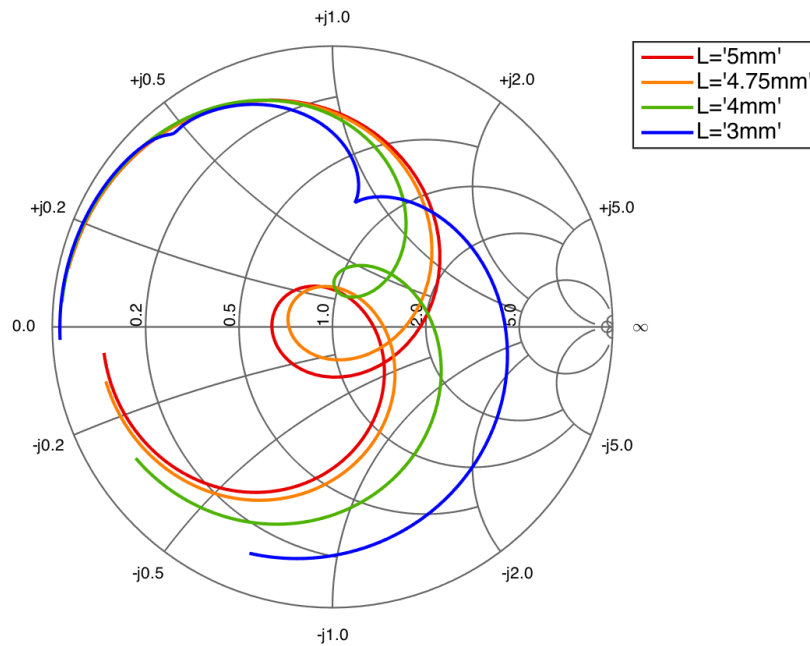


(b) Smith chart of S_{11} for different lengths of the slot, L , for frequencies between 13-17 GHz. The other parameters were fixed and had the starting values as stated in table 3.5.

Figure 3.43: Parametric study of S_{11} of different lengths of the slot, L . The other parameters were fixed and had the starting values as stated in table 3.5.

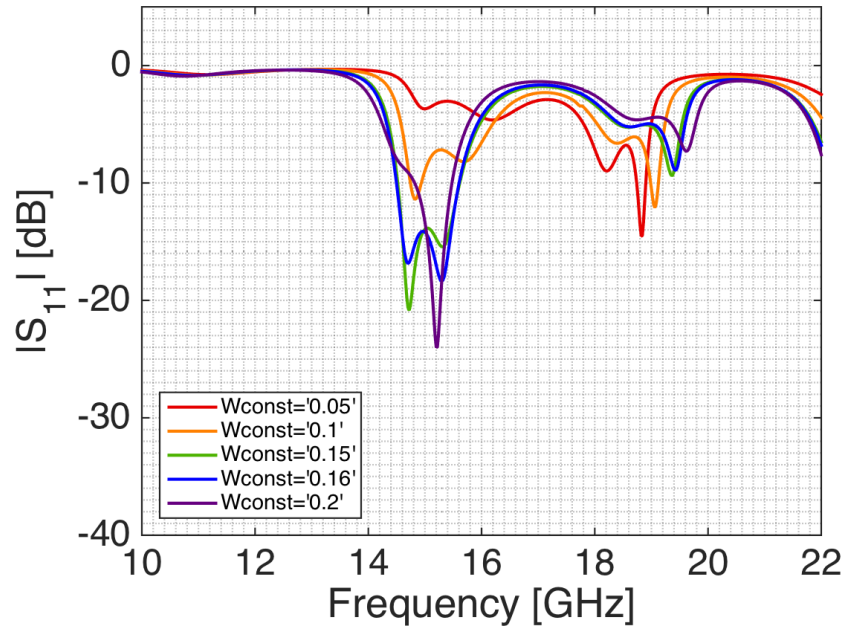


(a) $|S_{22}|$ in dB-scale for different lengths of the slot, L . The other parameters were fixed and had the starting values as stated in table 3.5.

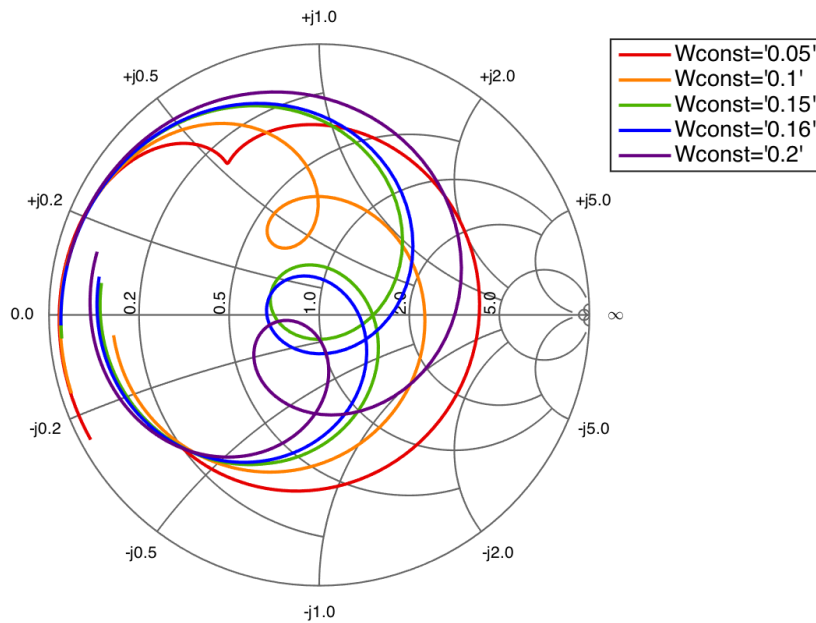


(b) Smith chart of S_{22} for different lengths of the slot, L , for frequencies between 13-17 GHz. The other parameters were fixed and had the starting values as stated in table 3.5.

Figure 3.44: Parametric study of S_{22} of different lengths of the slot, L . The other parameters were fixed and had the starting values as stated in table 3.5.

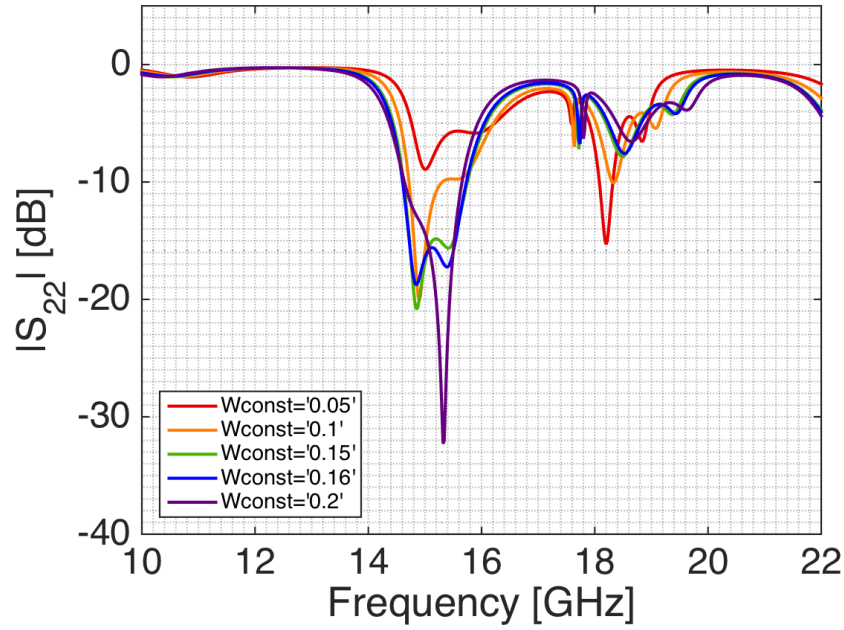


(a) $|S_{11}|$ in dB-scale for different widths of the slot, W , in parts of slot length. The other parameters were fixed and had the starting values as stated in table 3.5.

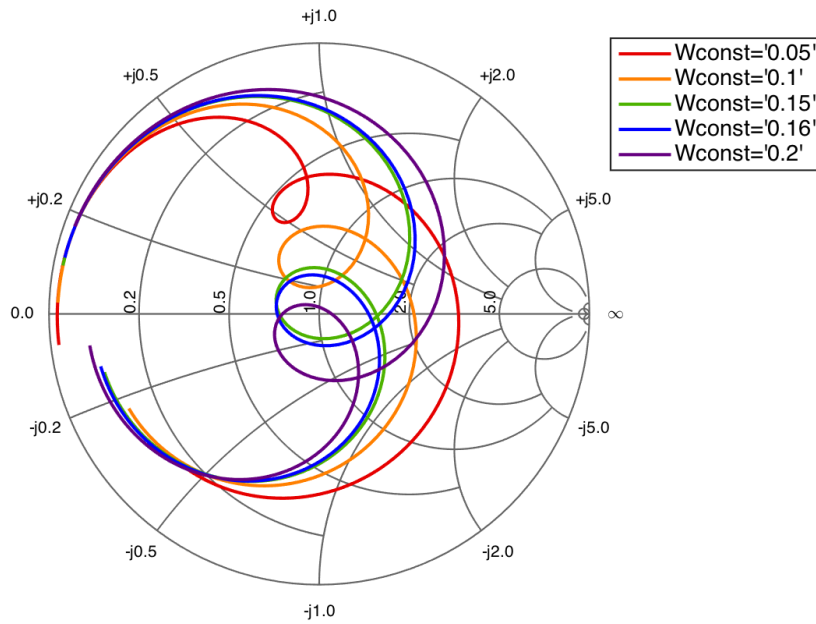


(b) Smith chart of S_{11} for different widths of the slot, W , in parts of slot length, for frequencies between 13-17 GHz. The other parameters were fixed and had the starting values as stated in table 3.5.

Figure 3.45: Parametric study of S_{11} of the different widths of the slot, W , in parts of slot length. The other parameters were fixed and had the starting values as stated in table 3.5.

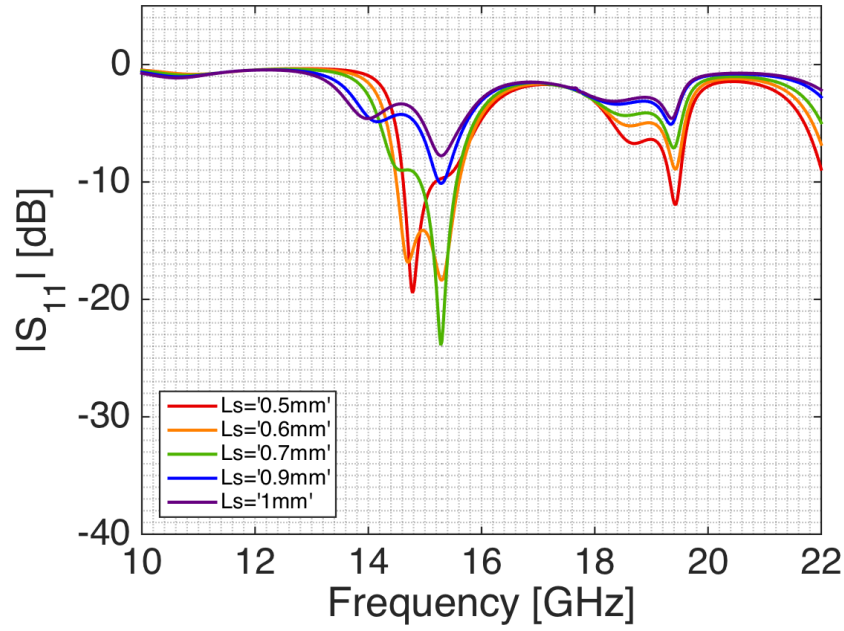


(a) $|S_{22}|$ in dB-scale for different widths of the slot, W , in parts of slot length. The other parameters were fixed and had the starting values as stated in table 3.5.

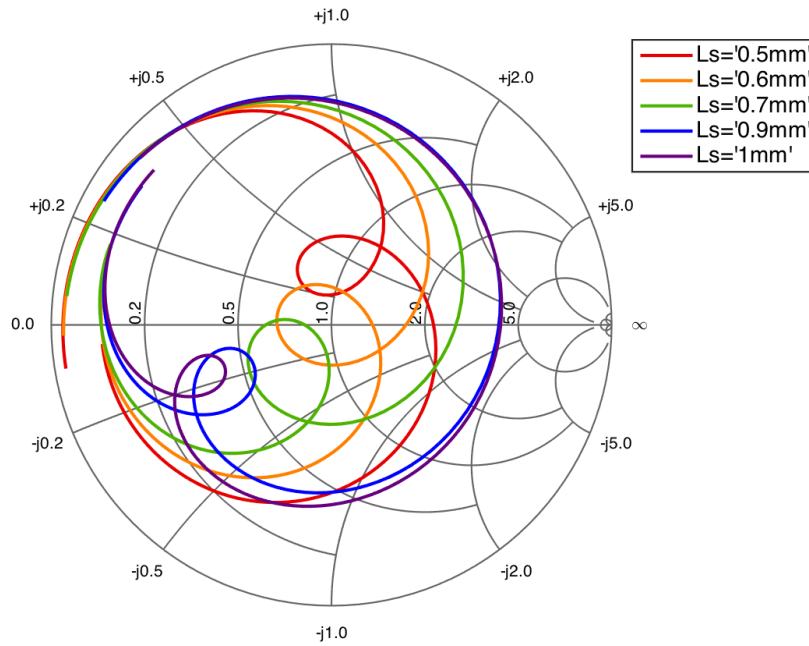


(b) Smith chart of S_{22} for different widths of the slot, W , in parts of slot length, for frequencies between 13-17 GHz. The other parameters were fixed and had the starting values as stated in table 3.5.

Figure 3.46: Parametric study of S_{22} of the different widths of the slot, W , in parts of slot length. The other parameters were fixed and had the starting values as stated in table 3.5.

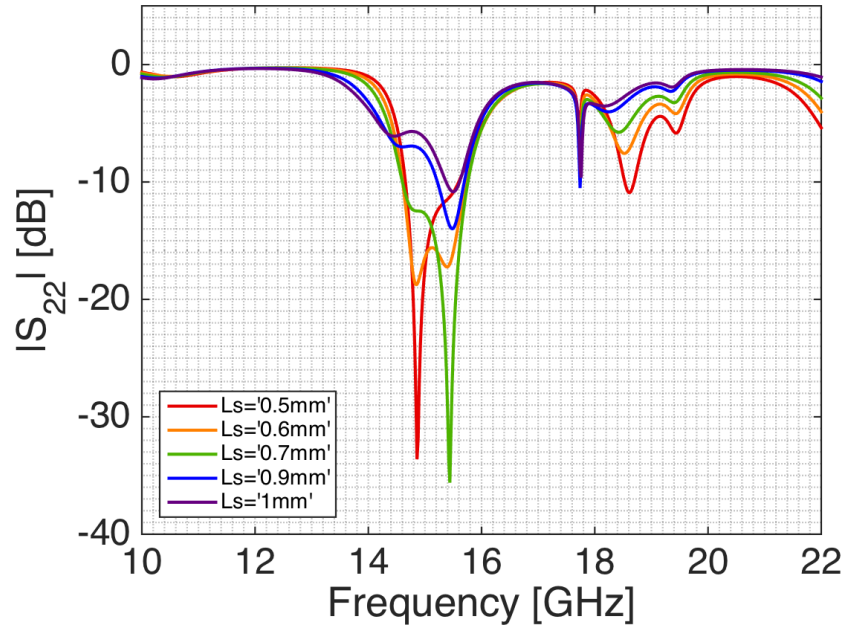


(a) $|S_{11}|$ in dB-scale for different placements of the striplines in the slot, distance L_s , defined as the distance between the middle of the stripline to the edge of the slot. The other parameters were fixed and had the starting values as stated in table 3.5.

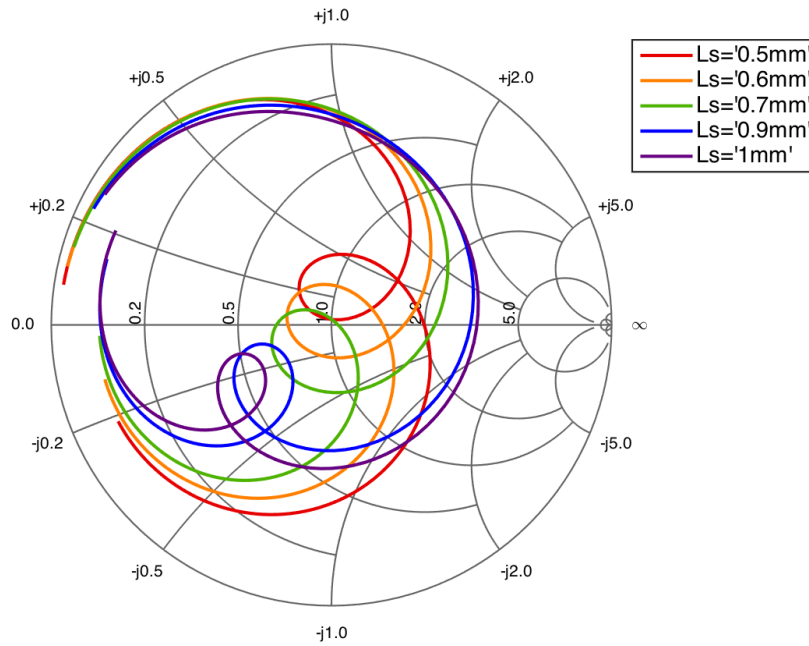


(b) Smith chart of S_{11} for different placements of the striplines in the slot, distance L_s , defined as the distance between the middle of the stripline to the edge of the slot, for frequencies between 13-17 GHz. The other parameters were fixed and had the starting values as stated in table 3.5.

Figure 3.47: Parametric study of S_{11} of the different placements of the striplines in the slot, distance L_s , defined as the distance between the middle of the stripline to the edge of the slot. The other parameters were fixed and had the starting values as stated in table 3.5.

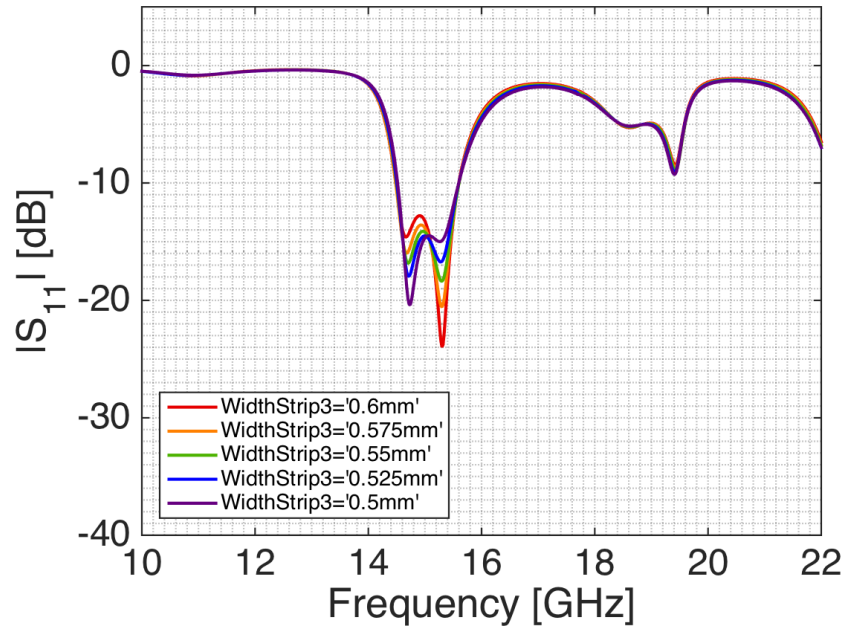


(a) $|S_{22}|$ in dB-scale for different placements of the striplines in the slot, distance L_s , defined as the distance between the middle of the stripline to the edge of the slot. The other parameters were fixed and had the starting values as stated in table 3.5.

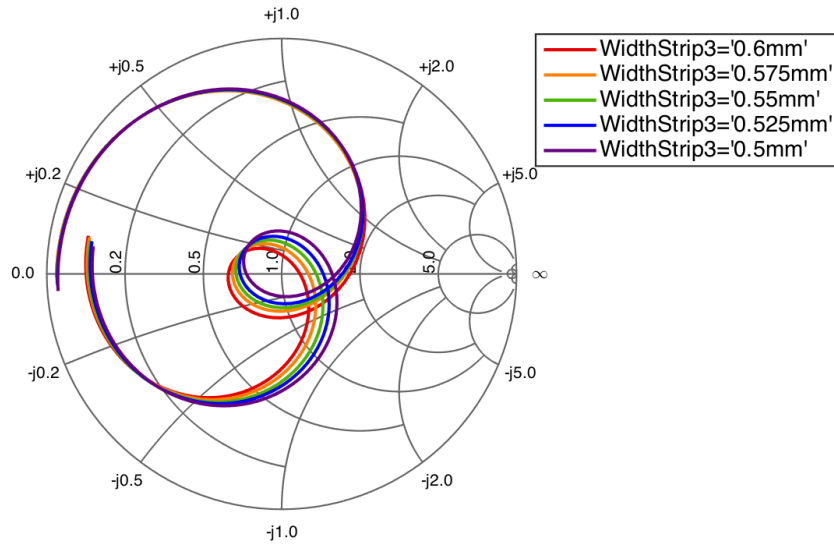


(b) Smith chart of S_{22} for different placements of the striplines in the slot, distance L_s , defined as the distance between the middle of the stripline to the edge of the slot, for frequencies between 13-17 GHz. The other parameters were fixed and had the starting values as stated in table 3.5.

Figure 3.48: Parametric study of S_{22} of the different placements of the striplines in the slot, distance L_s , defined as the distance between the middle of the stripline to the edge of the slot. The other parameters were fixed and had the starting values as stated in table 3.5.

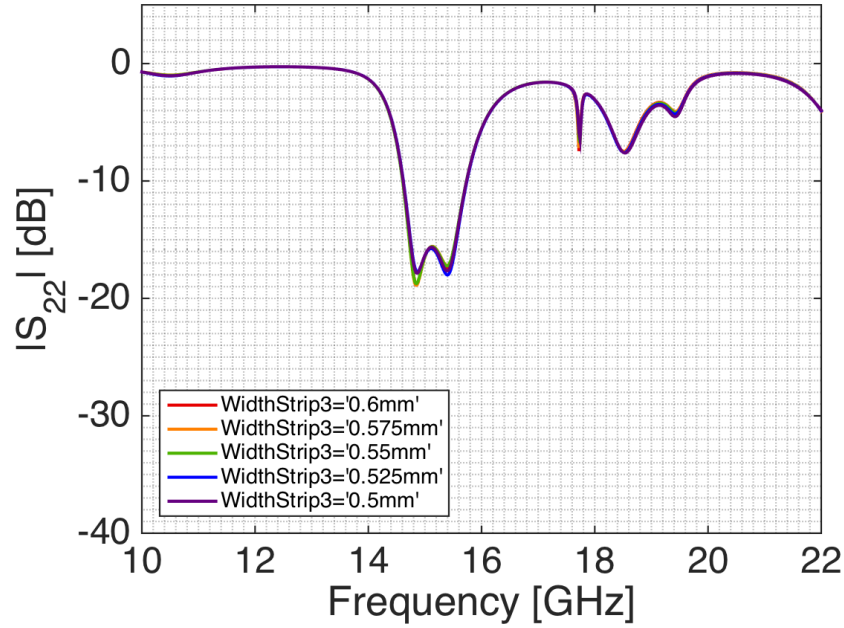


(a) $|S_{11}|$ in dB-scale for different stripline widths, W_s , for port 1. The other parameters were fixed and had the starting values as stated in table 3.5.

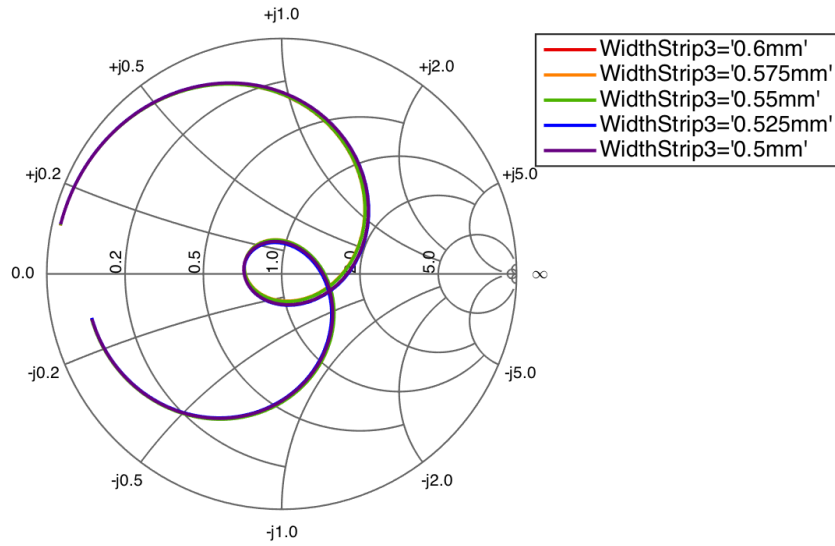


(b) Smith chart of S_{11} for different stripline widths, W_s , for port 1, for frequencies between 13-17 GHz. The other parameters were fixed and had the starting values as stated in table 3.5.

Figure 3.49: Parametric study of S_{11} of the different stripline widths, W_s , for port 1. The other parameters were fixed and had the starting values as stated in table 3.5.

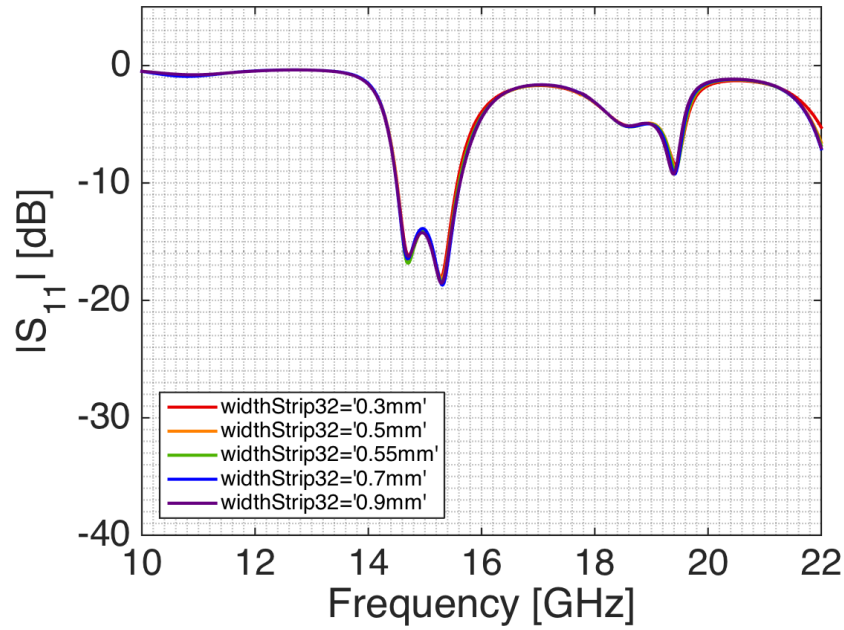


(a) $|S_{22}|$ in dB-scale for different stripline widths, W_s , for port 1. The other parameters were fixed and had the starting values as stated in table 3.5.

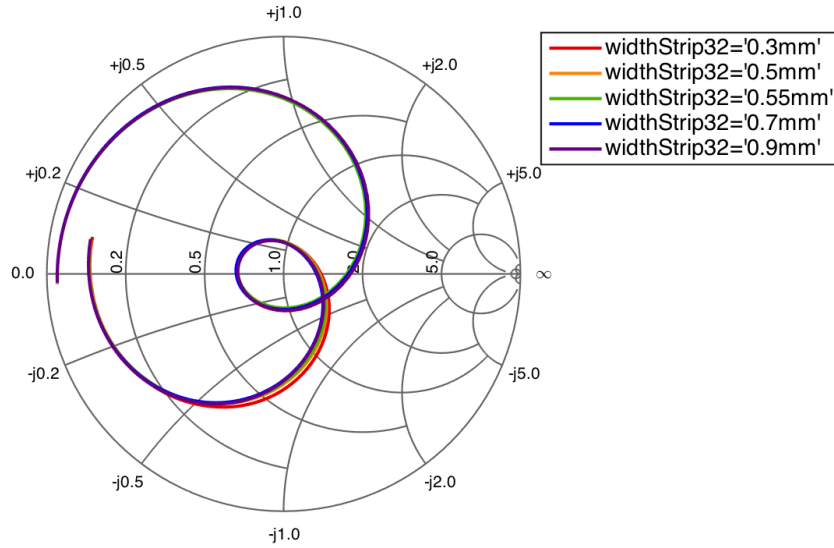


(b) Smith chart of S_{22} for different stripline widths, W_s , for port 1, for frequencies between 13-17 GHz. The other parameters were fixed and had the starting values as stated in table 3.5.

Figure 3.50: Parametric study of S_{22} of the different stripline widths, W_s , for port 1. The other parameters were fixed and had the starting values as stated in table 3.5.

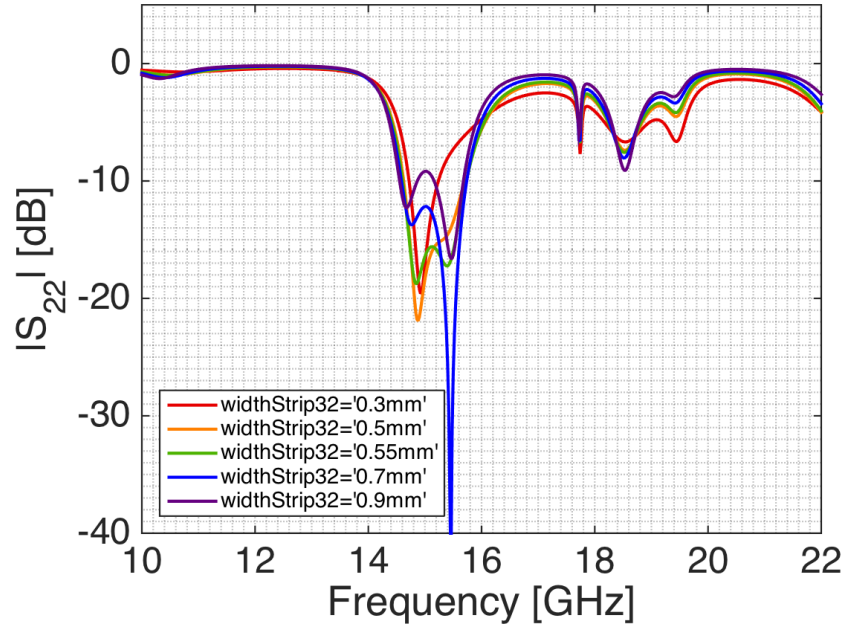


(a) $|S_{11}|$ in dB-scale for different stripline widths, W_s , for port 2. The other parameters were fixed and had the starting values as stated in table 3.5.

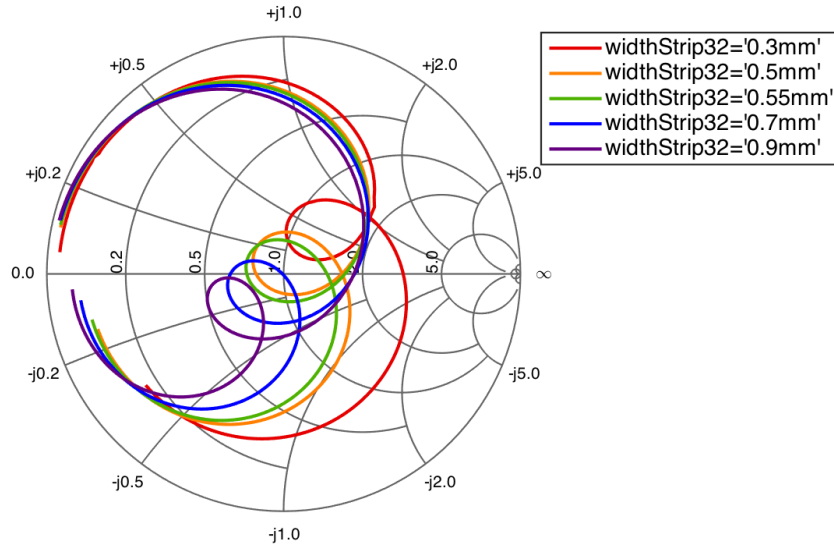


(b) Smith chart of S_{11} for different stripline widths, W_s , for port 2, for frequencies between 13-17 GHz. The other parameters were fixed and had the starting values as stated in table 3.5.

Figure 3.51: Parametric study of S_{11} of the different stripline widths, W_s , for port 2. The other parameters were fixed and had the starting values as stated in table 3.5.

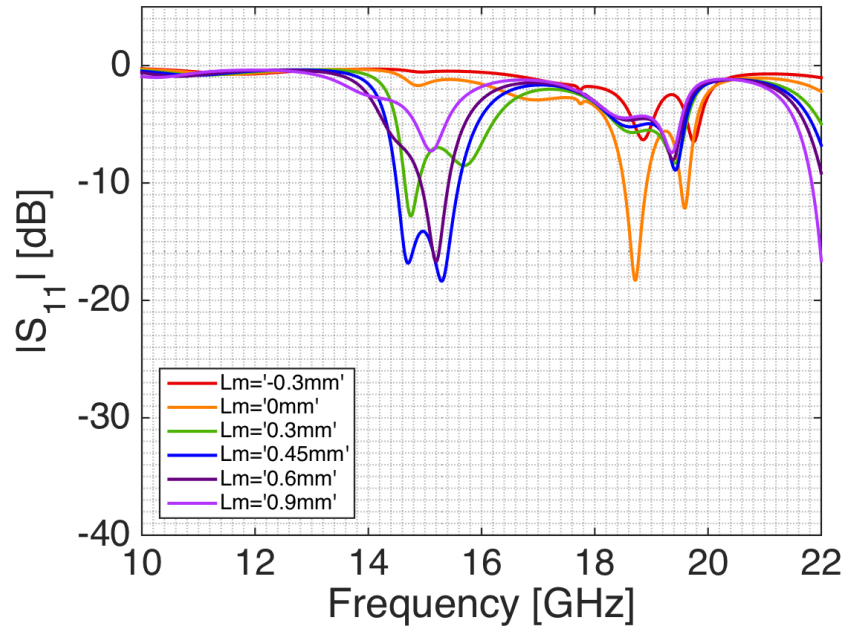


(a) $|S_{22}|$ in dB-scale for different stripline widths, W_s , for port 2. The other parameters were fixed and had the starting values as stated in table 3.5.

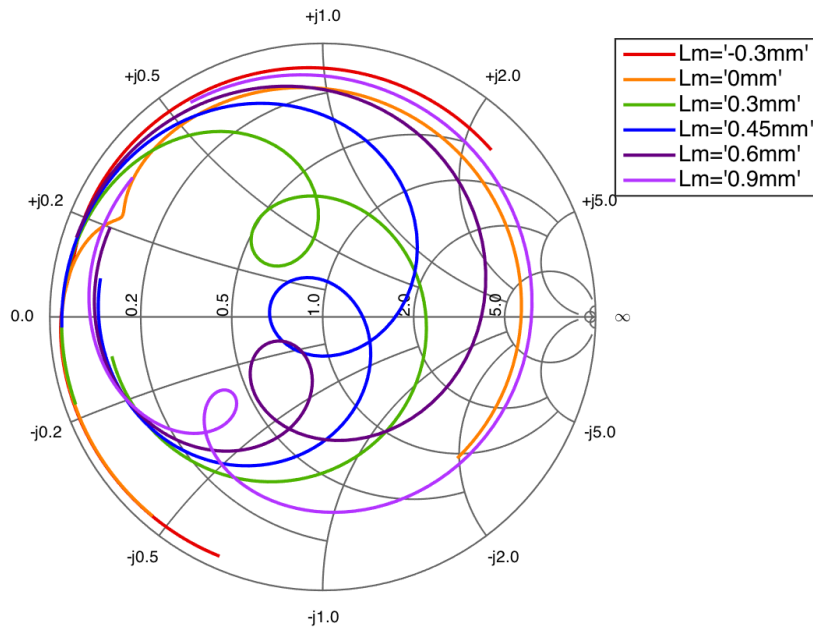


(b) Smith chart of S_{22} for different stripline widths, W_s , for port 2, for frequencies between 13-17 GHz. The other parameters were fixed and had the starting values as stated in table 3.5.

Figure 3.52: Parametric study of S_{22} of the different stripline widths, W_s , for port 2. The other parameters were fixed and had the starting values as stated in table 3.5.

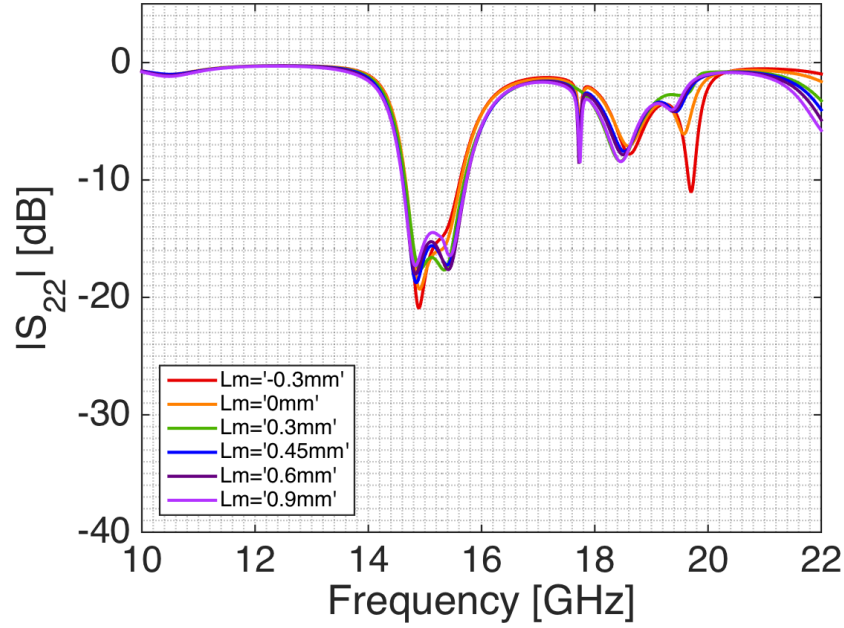


(a) $|S_{11}|$ in dB-scale for different stripline lengths, L_m , for port 1. The other parameters were fixed and had the starting values as stated in table 3.5.

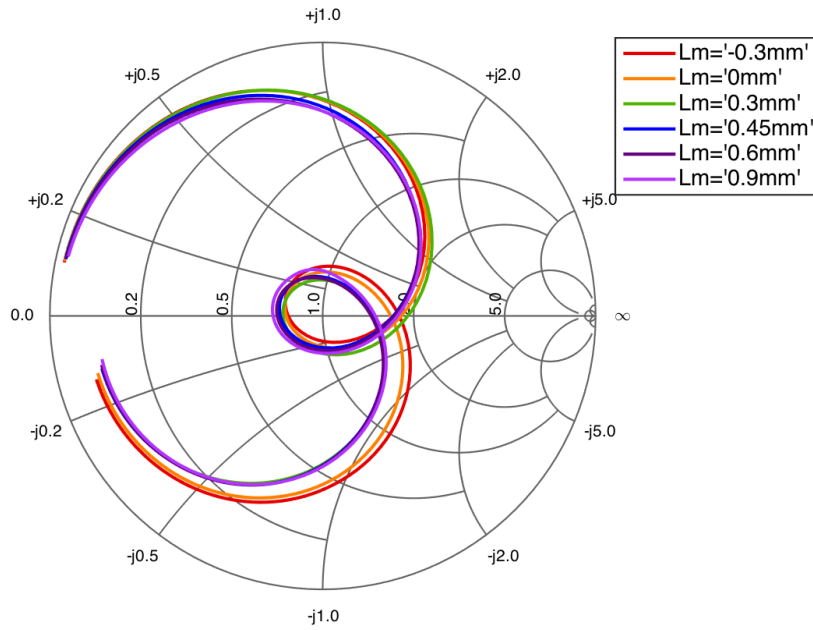


(b) Smith chart of S_{11} for different stripline lengths, L_m , for port 1, for frequencies between 13-17 GHz. The other parameters were fixed and had the starting values as stated in table 3.5.

Figure 3.53: Parametric study of S_{11} of the different stripline lengths, L_m , for port 1. The other parameters were fixed and had the starting values as stated in table 3.5.

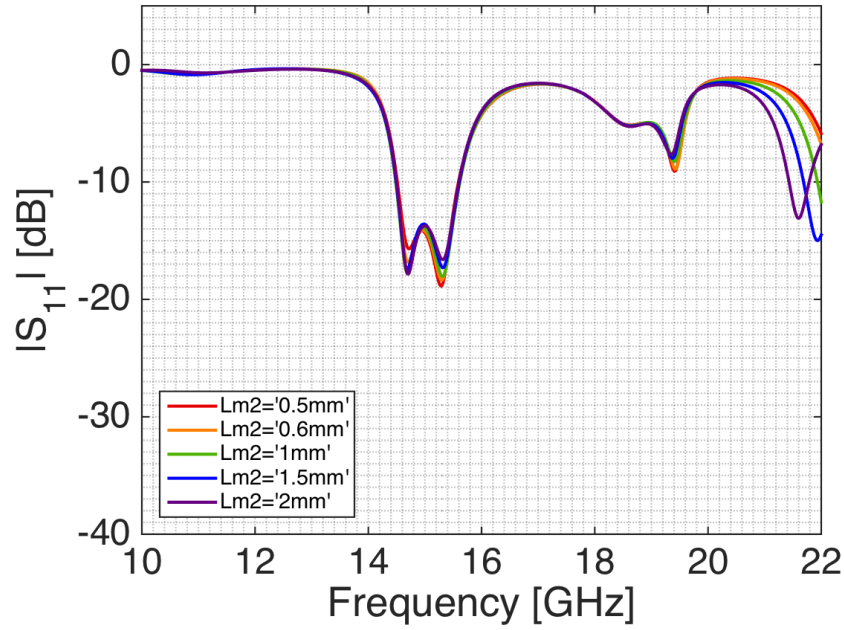


(a) $|S_{22}|$ in dB-scale for different stripline lengths, L_m , for port 1. The other parameters were fixed and had the starting values as stated in table 3.5.

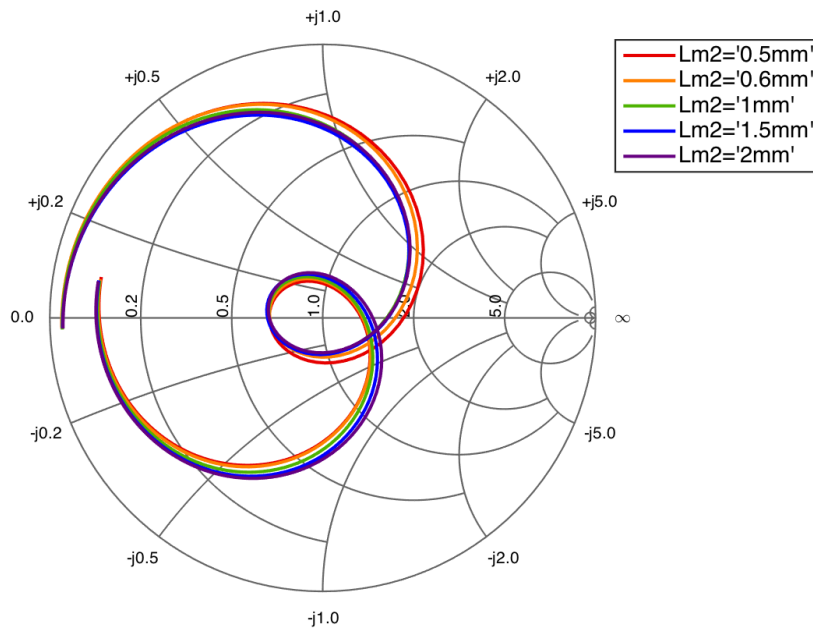


(b) Smith chart of S_{22} for different stripline lengths, L_m , for port 1, for frequencies between 13-17 GHz. The other parameters were fixed and had the starting values as stated in table 3.5.

Figure 3.54: Parametric study of S_{22} of the different stripline lengths, L_m , for port 1. The other parameters were fixed and had the starting values as stated in table 3.5.

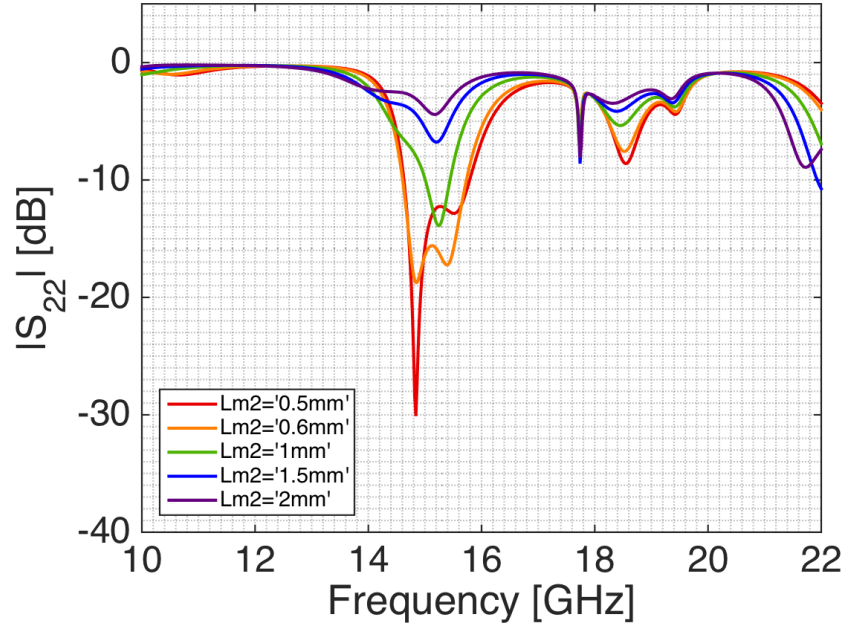


(a) $|S_{11}|$ in dB-scale for different stripline lengths, L_m , for port 2. The other parameters were fixed and had the starting values as stated in table 3.5.

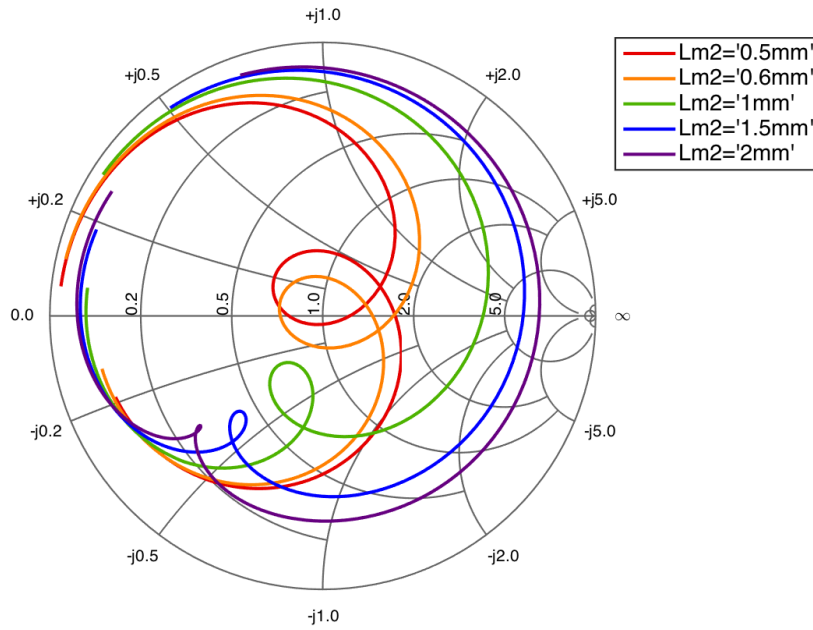


(b) Smith chart of S_{11} for different stripline lengths, L_m , for port 2, for frequencies between 13-17 GHz. The other parameters were fixed and had the starting values as stated in table 3.5.

Figure 3.55: Parametric study of S_{11} of the different stripline lengths, L_m , for port 2. The other parameters were fixed and had the starting values as stated in table 3.5.

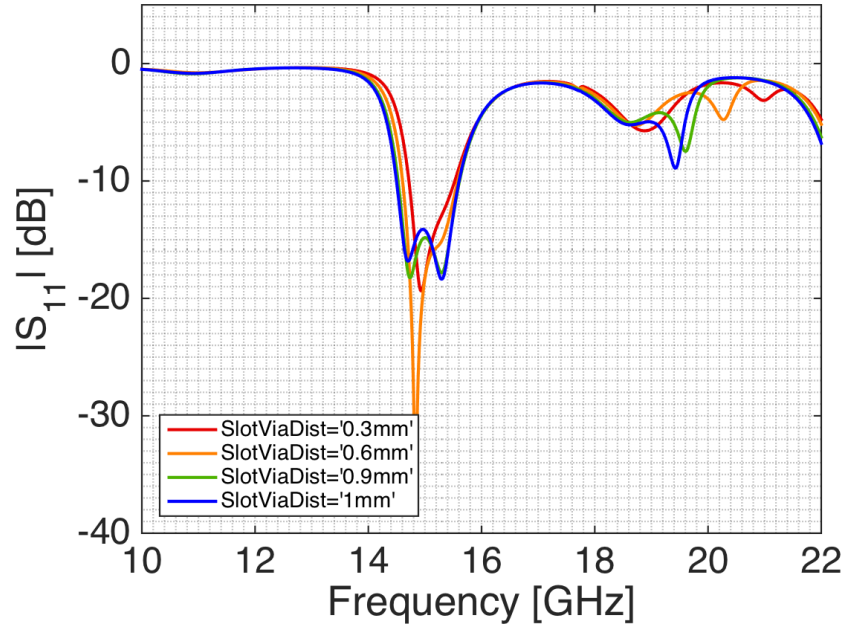


(a) $|S_{22}|$ in dB-scale for different stripline lengths, L_m , for port 2. The other parameters were fixed and had the starting values as stated in table 3.5.

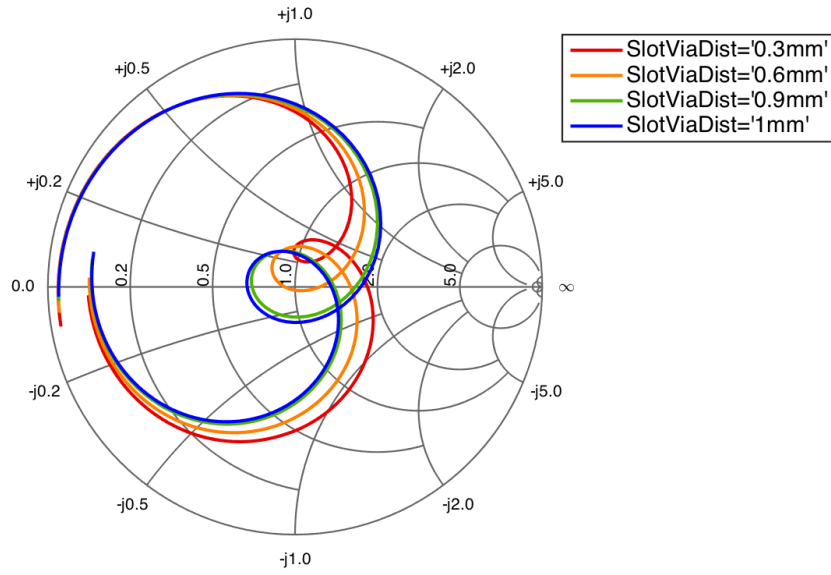


(b) Smith chart of S_{22} for different stripline lengths, L_m , for port 2, for frequencies between 13-17 GHz. The other parameters were fixed and had the starting values as stated in table 3.5.

Figure 3.56: Parametric study of S_{22} of the different stripline lengths, L_m , for port 2. The other parameters were fixed and had the starting values as stated in table 3.5.

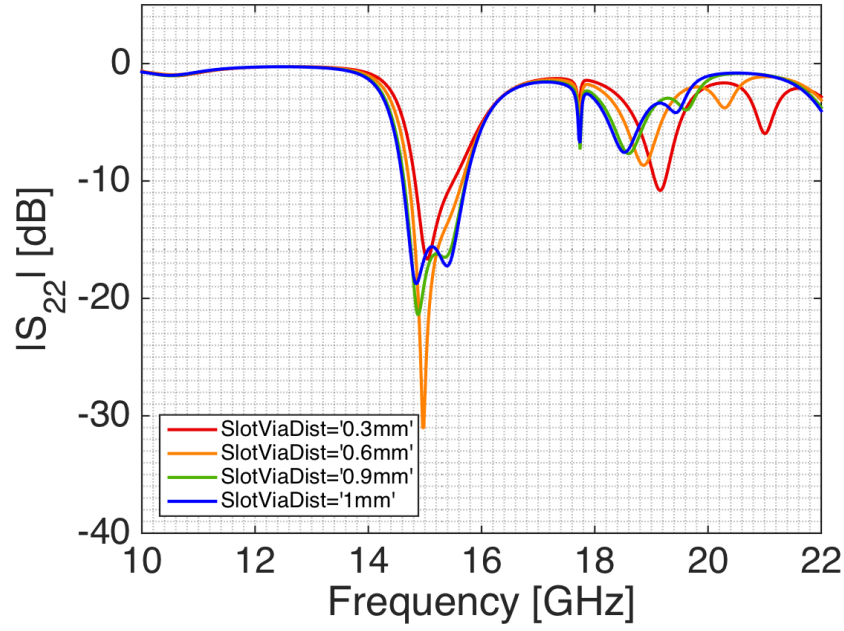


(a) $|S_{11}|$ in dB-scale for different sizes of the cavity, d_{cavity} . The other parameters were fixed and had the starting values as stated in table 3.5.

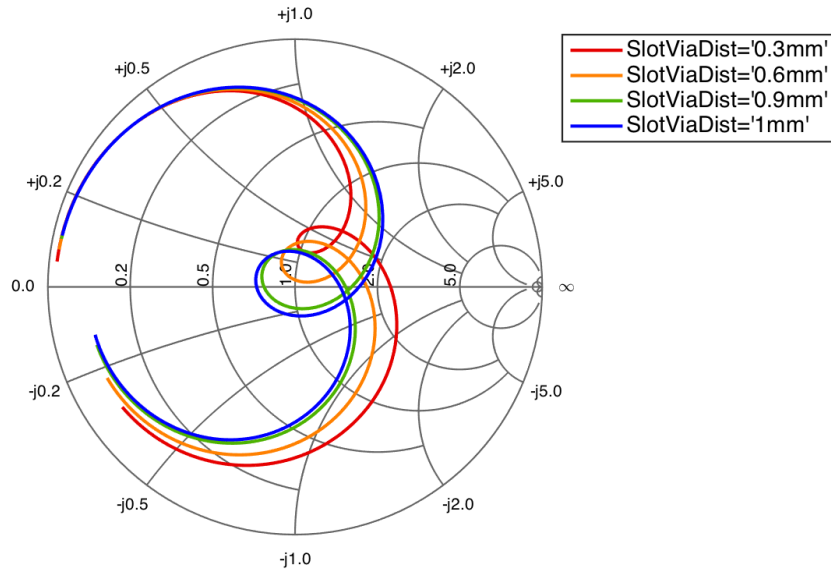


(b) Smith chart of S_{11} for different sizes of the cavity, d_{cavity} , for frequencies between 13-17 GHz. The other parameters were fixed and had the starting values as stated in table 3.5.

Figure 3.57: Parametric study of S_{11} of the different sizes of the cavity, d_{cavity} . The other parameters were fixed and had the starting values as stated in table 3.5.

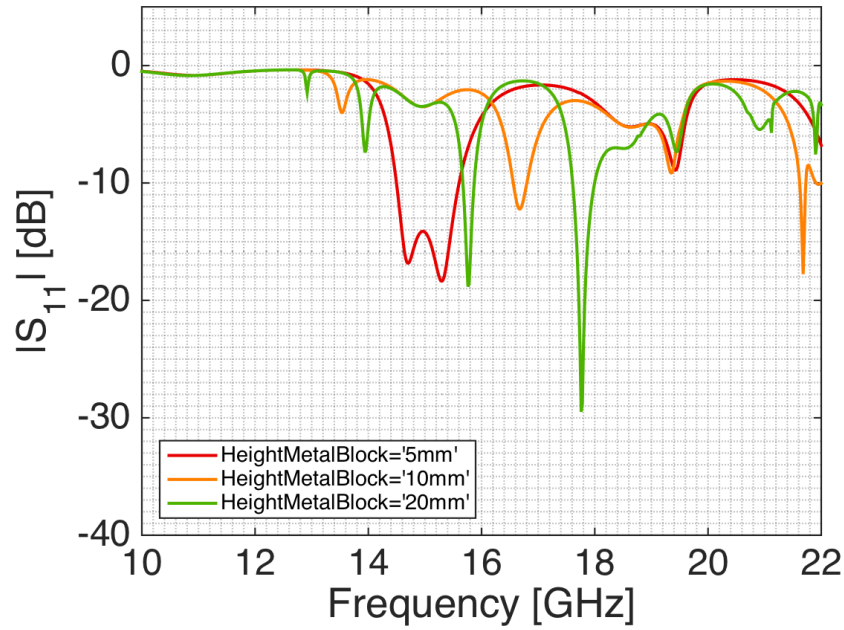


(a) $|S_{22}|$ in dB-scale for different sizes of the cavity, d_{cavity} . The other parameters were fixed and had the starting values as stated in table 3.5.

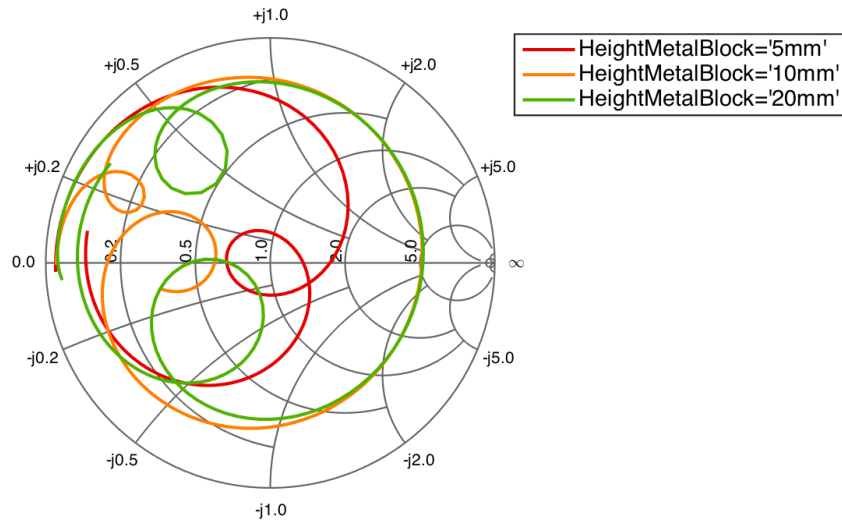


(b) Smith chart of S_{22} for different sizes of the cavity, d_{cavity} , for frequencies between 13-17 GHz. The other parameters were fixed and had the starting values as stated in table 3.5.

Figure 3.58: Parametric study of S_{22} of the different sizes of the cavity, d_{cavity} . The other parameters were fixed and had the starting values as stated in table 3.5.

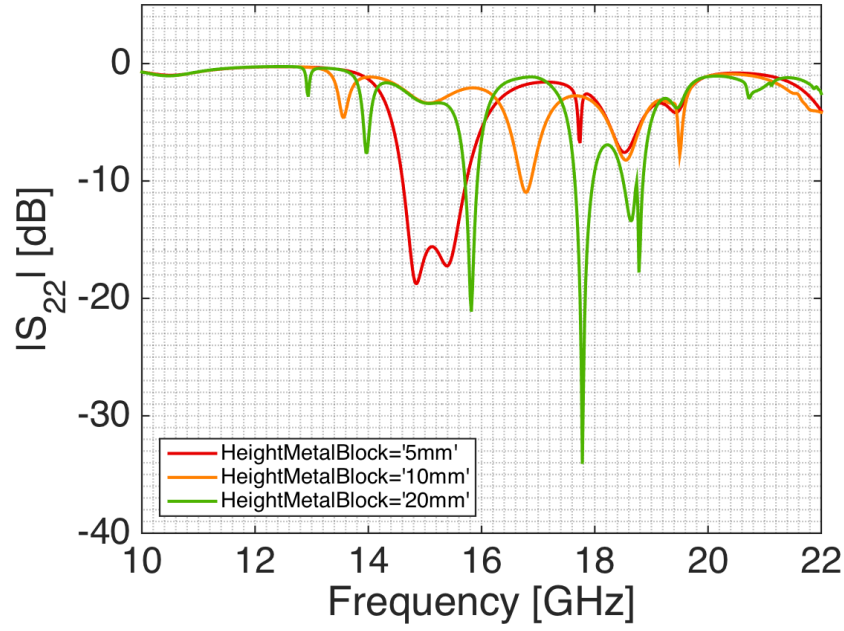


(a) $|S_{11}|$ in dB-scale for different waveguide heights, h_{metal} . The other parameters were fixed and had the starting values as stated in table 3.5.

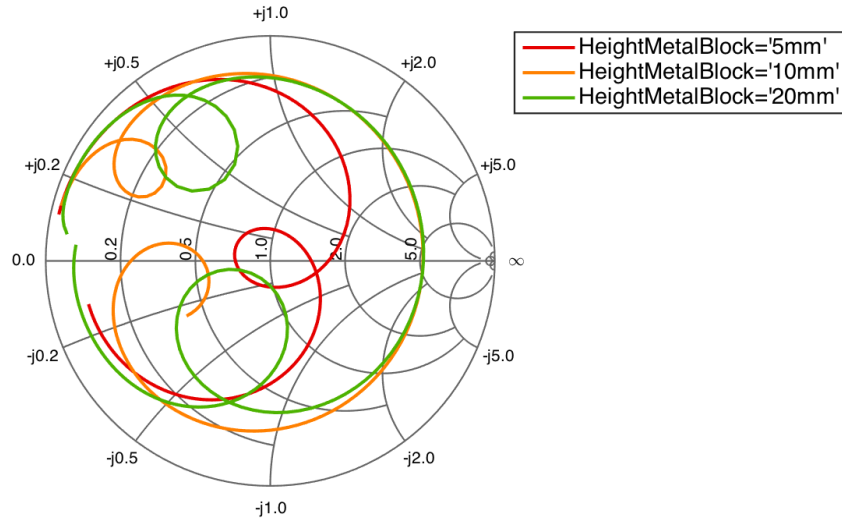


(b) Smith chart of S_{11} for different waveguide heights, h_{metal} , for frequencies between 13-17 GHz. The other parameters were fixed and had the starting values as stated in table 3.5.

Figure 3.59: Parametric study of S_{11} of the different waveguide heights, h_{metal} . The other parameters were fixed and had the starting values as stated in table 3.5.



(a) $|S_{22}|$ in dB-scale for different waveguide heights, h_{metal} . The other parameters were fixed and had the starting values as stated in table 3.5.



(b) Smith chart of S_{22} for different waveguide heights, h_{metal} , for frequencies between 13-17 GHz. The other parameters were fixed and had the starting values as stated in table 3.5.

Figure 3.60: Parametric study of S_{22} of the different waveguide heights, h_{metal} . The other parameters were fixed and had the starting values as stated in table 3.5.

3.2.3.2.12 Conclusions of Parametric Study The main challenge was to find a resonance close enough to the middle of the Smith chart with a resonance bandwidth where the return loss could be below -13 dB, according to the requirement. To achieve this, the substrates, cavity size and the slot's parameters had to be altered to find the best configuration. When a resonance had been found for the right frequency span (approximately 14.6 - 15.4 GHz) the final optimization could be done. This was mainly done with two parameters; the stripline width and the stub length of the stripline. Using these two parameters the element could be optimized by using the Smith chart as an aid. To change the resistance the stripline width was altered and the stripline length was altered to change the reactance. This is summarized below:

- Get correct bandwidth:
 - Slot
 - Substrates
 - Cavity size
- Fine tune resonance/impedance matching:
 - Stripline width for resistance
 - Stripline length for reactance

3.2.3.3 Evaluation of Slot Coupled Design

The design using a slot coupled feeding was found promising and the performance of the optimized element can be seen in figures 3.61 and 3.62. Port 1 has a bandwidth of $14.57 - 15.49 = 0.92$ GHz which corresponds to a bandwidth of 6.12%. Port 2 has a frequency span of $14.69 - 15.62 = 0.93$ GHz with a slightly shifted center frequency of 15.16 GHz. This corresponds to a bandwidth of 6.14%. The return loss requirement for the element was to be below -13 dB for a bandwidth of 6%, this requirement is fulfilled.

However, the coupling between the polarizations is too high which is clearly seen in figures 3.61 and 3.62. This problem had to be addressed, in order for the element to fulfill the requirements (i.e. isolation should be below -15 dB inband). Several design modifications were investigated, such as using extra vias in the cavity, displacement of one of the slots and changing the placement of the striplines in the slot (L_s).

Finally, the placement of the striplines, L_s , seemed to improve the isolation. When S_{12} was studied for the stripline placement it could be seen that an increased distance from the edge of the slot gave a rotation moving away from the center of the Smith chart. This can be seen in figure 3.63. Given this fact, the best isolation should be when the striplines are placed at the center of the slots. When the striplines were moved to this new location a re-optimization had to be done, using the stripline width and length.

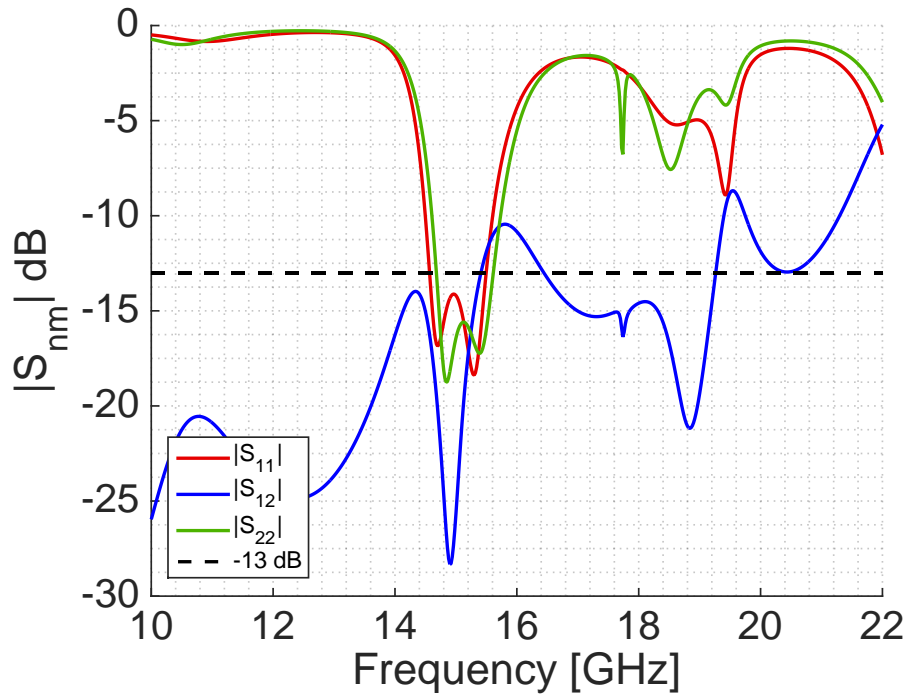


Figure 3.61: The S-parameters of the optimized slot coupled element design. The isolation between the two ports is too high and does not fulfill the requirement of being below -15 dB inband as is clearly seen. The bandwidth requirement of -13 dB is shown with the black dashed line. A closer view is shown in figure 3.62.

Another problem with the design was the difference between the E- and H-planes regarding gain. According to the specifications, the difference between the co-polar gain between the two polarizations in any plane should be below 3 dB. This difference is higher for this design, which can be seen in figure 3.64. According to the theory of circular apertures, see section 2.2.1.1, a larger aperture gives more similar radiation patterns between the two different planes. Therefore, the radius of the waveguide was also increased.

According to theory a radius of $0.22\lambda_0$ gives a difference of ~ 3 dB between the two polarizations. This radius is too large when the construction of a sub-array with a size of $0.53\lambda \cdot 1.06\lambda$ is taken into consideration, since the feeding network needs to be incorporated. A slight increase of the waveguide radius was made to improve the performance with regard to the ΔG_{co} -requirement without affecting the sub-array implementation too much.

3.2.3.4 Stripline in Middle of Slot

The design was changed to have the striplines inserted into the center of the slot, see figure 3.65, in order to improve the isolation. The change of the stripline placement necessitated a re-optimization of the element. This was done by modifying the width of the strip, W_s and the stub length, L_m , as earlier mentioned in paragraph 3.2.3.2.12. For this design, a new parametric

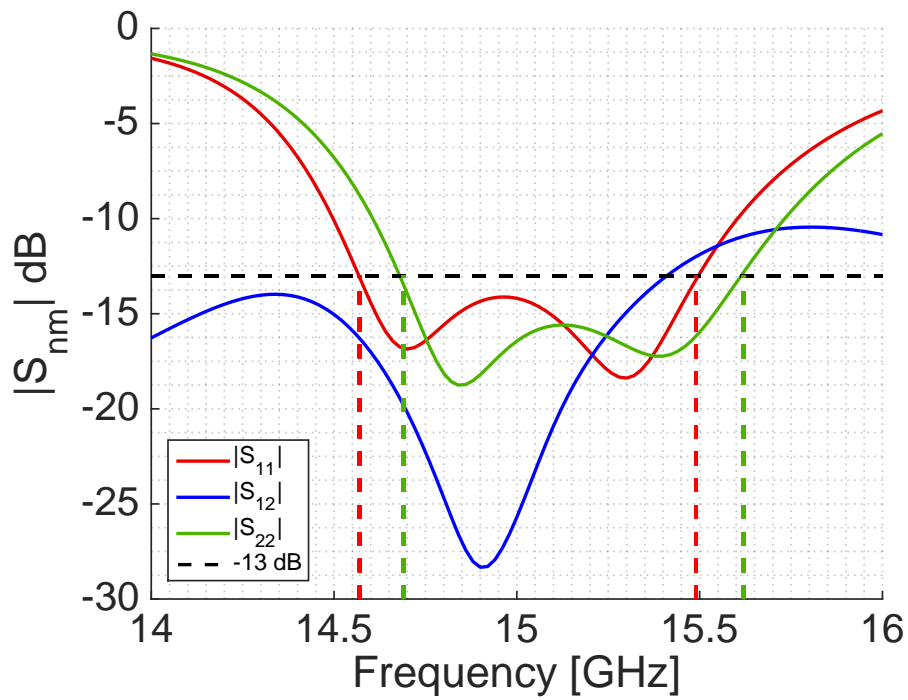
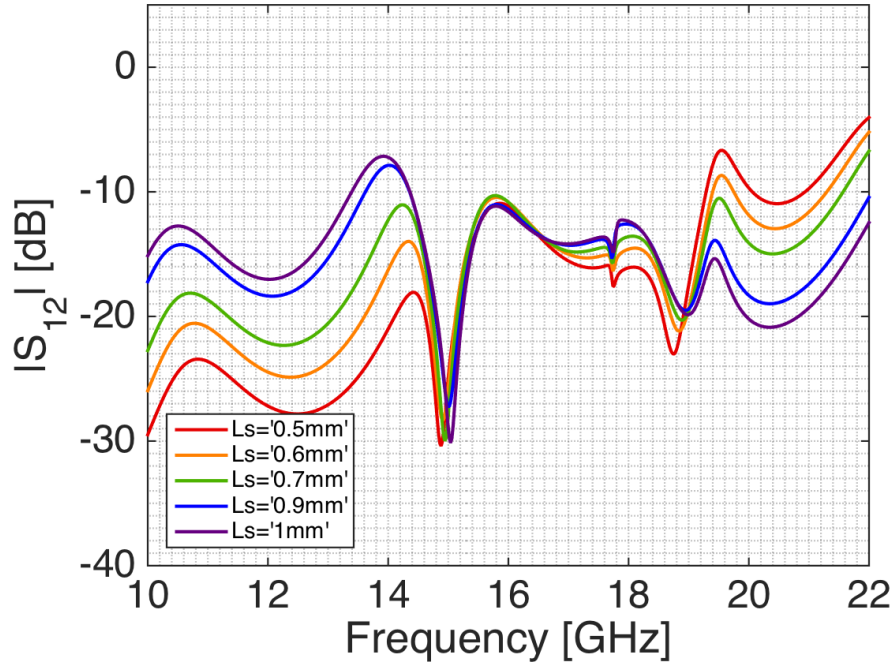
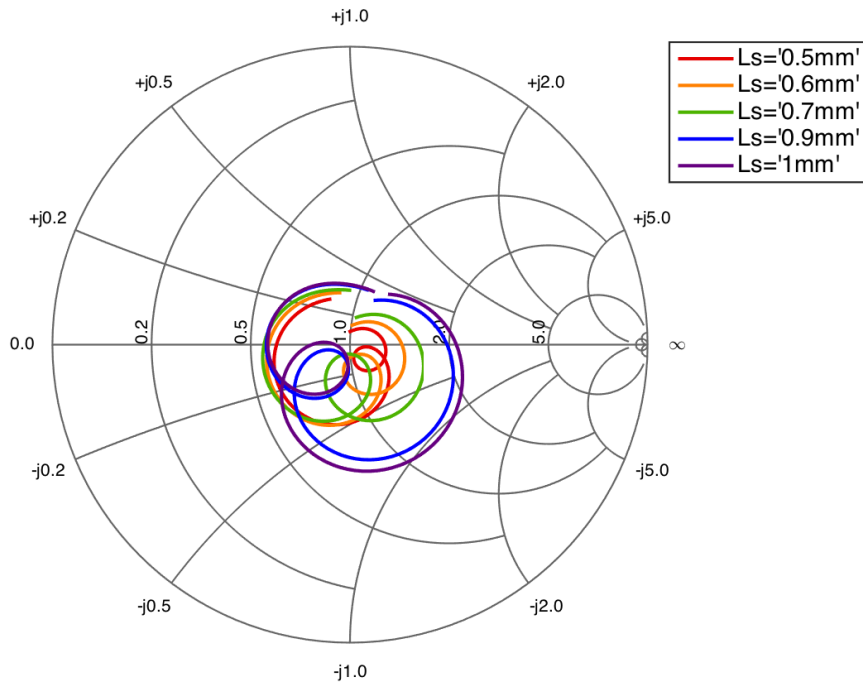


Figure 3.62: The S-parameters of the optimized slot coupled element design. Port 1 has a bandwidth of $14.57 - 15.49 = 0.92$ GHz which corresponds to a bandwidth of 6.12%. Port 2 has a bandwidth of $14.69 - 15.62 = 0.93$ GHz with a slightly shifted center frequency of 15.16 GHz. This corresponds to a bandwidth of 6.14%. However, the isolation fails to meet the requirement of being below -15 dB inband.



(a) $|S_{12}|$ in dB-scale for different placements of the striplines in the slot, distance L_s defined as distance between middle of stripline to edge of slot.



(b) Smith chart of S_{12} for different placements of the striplines in the slot, distance L_s defined as distance between middle of stripline to edge of slot, for frequencies between 18-20 GHz.

Figure 3.63: Parametric study of S_{12} the different placements of the striplines in the slot, distance L_s defined as distance between middle of stripline to edge of slot.

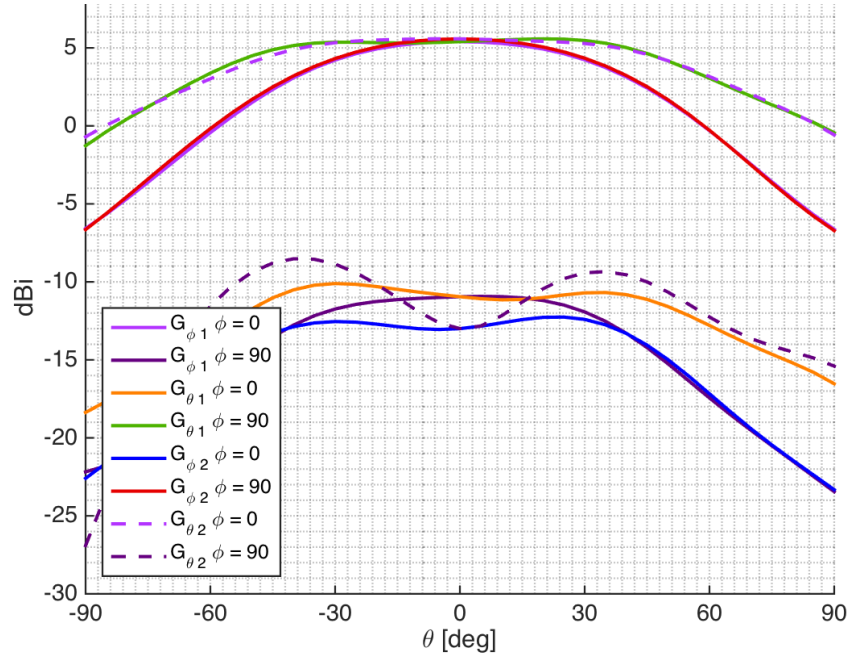


Figure 3.64: The gain of the design for both ports, the difference between G_{co1} and G_{co2} is at maximum 3.81 dB at $\theta = -60^\circ$ for $\phi = 90^\circ$ (port 1: E-plane and port 2: H-plane). This is more than the requirement of 3 dB.

study was not made, since its geometry and therefore parameters were the same as the previous design, see section 3.2.3.2.

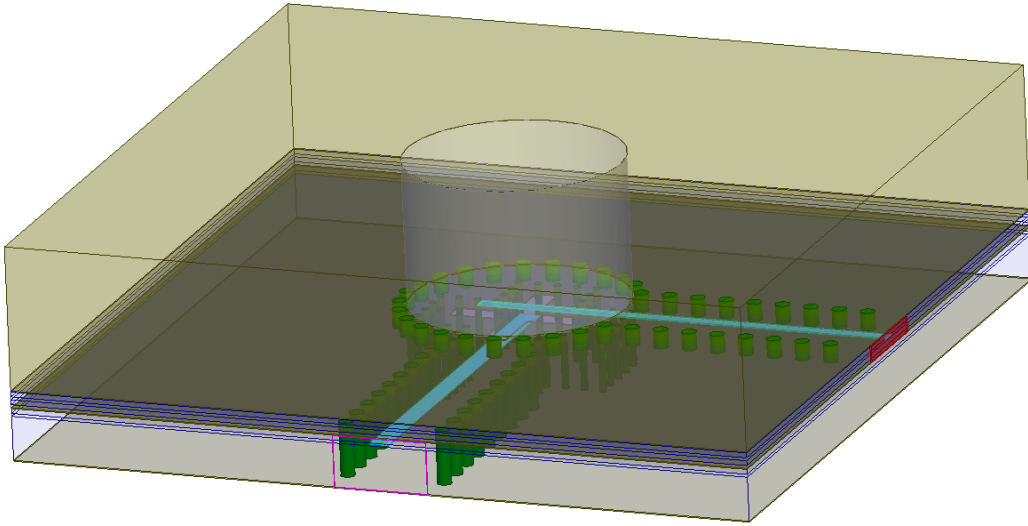


Figure 3.65: Perspective view of the design with the striplines in the middle of the slots.

3.2.3.4.1 Waveguide Radius The waveguide radius was changed to 3.75 mm to improve the ΔG_{co} performance, see sections 2.2.1.1 and 3.2.3.3. This resulted in a frequency shift of the resonance since the cutoff frequency was al-

tered due to the change of radius. The new center frequency was $f_{mid} = 14.5$ GHz, a summary of these changes are shown in table 3.6.

Table 3.6: The changed waveguide radius and its shift in frequency and size in λ_0 .

	Before	After
f_{mid} [GHz]	15	14.5
Waveguide radius [mm]	3.5	3.75
Waveguide radius [λ_0]	0.175	0.181

As can be seen in table 3.6, increasing the waveguide radius did not result in a much larger aperture size in wavelengths because of the frequency shift. Effectively the waveguide radius was increased by $0.006\lambda_0$. Thus, the waveguide radius change did not accomplish the wanted behavior.

Since the changed waveguide radius did not improve ΔG_{co} , both designs were optimized: the 3.5 and 3.75 mm waveguide radius. The 3.75 mm design proved easier to re-optimize and an impedance matching was realized quickly. Thus, this design was used for the final element design and the element's f_{mid} was shifted from 15 GHz to 14.5 GHz. The final parameters of this design are presented in table 3.7.

3.2.3.4.2 Unit Cell Design The unit cell should have an element size of $0.53\lambda_0$, as stated in the requirements, in order to create a phased array with an element spacing of $0.53\lambda_0$. Therefore, the ground plane size (parameters L_x and L_y in figure 3.30) was too large since it should be $0.53 \cdot 0.53\lambda_0$. A modified design was made with this ground plane size, it is shown in figure 3.66.

When the ground plane was changed, the impedance matching was degraded. This implies that the phase offset between the ports and the air interface is used as a tuning parameter, this can be seen in figure 3.67. This was earlier mentioned in the parametric study of the waveguide height of the first stripline fed dielectric design, see section 3.2.2.4.8. The phase offset is the length the wave needs to travel between the port and free space, the sum of the arrows in figure 3.67. When the ground plane size was changed the length of the arrow labeled 1 was changed.

The phase offset of the element was probably used to minimize the reflections of the inband frequencies. Therefore, a re-optimization was done of the unit cell using the stripline width and the stripline length. The final parameters of the unit cell are presented in table 3.7.

Another finding was that the radiation pattern showed a skewness, it was asymmetric which should not be the case for a circular aperture, see figure 3.68. This was investigated and the following hypotheses explaining the skewness and solutions for each hypothesis was made:

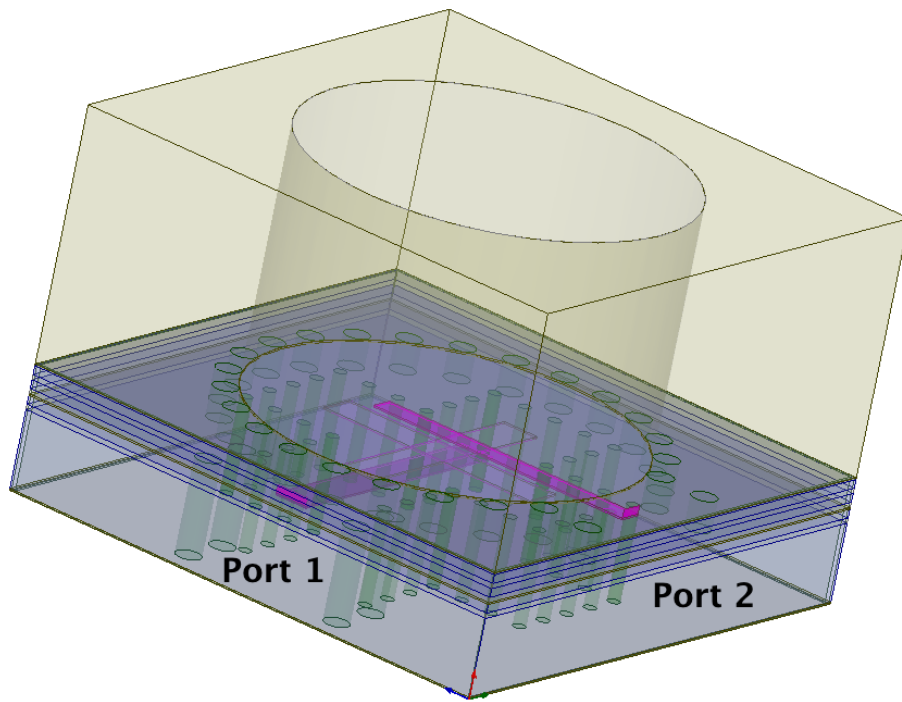


Figure 3.66: Perspective view of the unit cell.

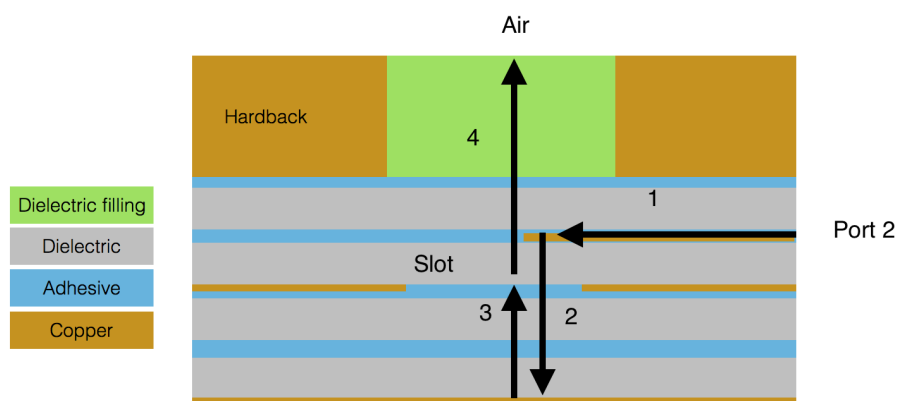


Figure 3.67: Schematic figure showing the phase offset as a sum of the arrows, where a change of the element size alters the phase offset since the arrow labeled 1 will change.

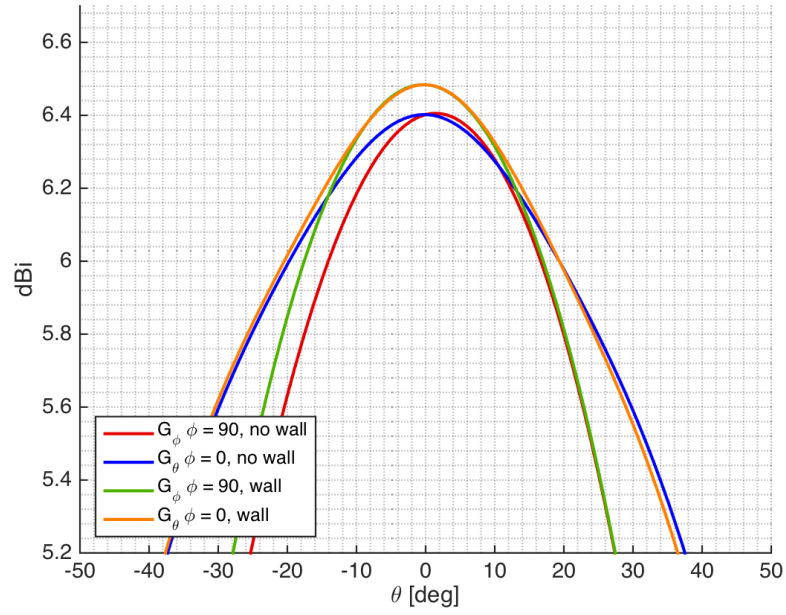
- Slot characteristics showing through (the slot's radiation pattern affecting the radiation pattern of the aperture)
 - Increase the waveguide length to attenuate the slot behavior
- Higher order modes in the waveguide which affect the radiation pattern
 - Increase the waveguide length to suppress the higher order modes
- Leakage of the E-field in the PCB affecting the radiation pattern
 - Decrease the distance between the vias to decrease the leakage

The metal block height could not be seen to alter the radiation pattern and thus the leakage hypotheses was tested. Metal walls were added to the design to see if the skewed radiation pattern was due to leakage, see figure 3.69. When metal walls were added to the PCB the radiation pattern became symmetric and it was concluded that the radiation pattern was, indeed, affected by leakage. The difference in the radiation patterns can be seen in figure 3.68, where the asymmetric behavior is more clearly observed for port 1. This implies that the leakage is related to port 1. Since troubleshooting the exact location and correct placement of the vias was deemed too time consuming, the addition of metal walls was instead made to the unit cell. A future investigation of the leakage should focus on the via placement for port 1.

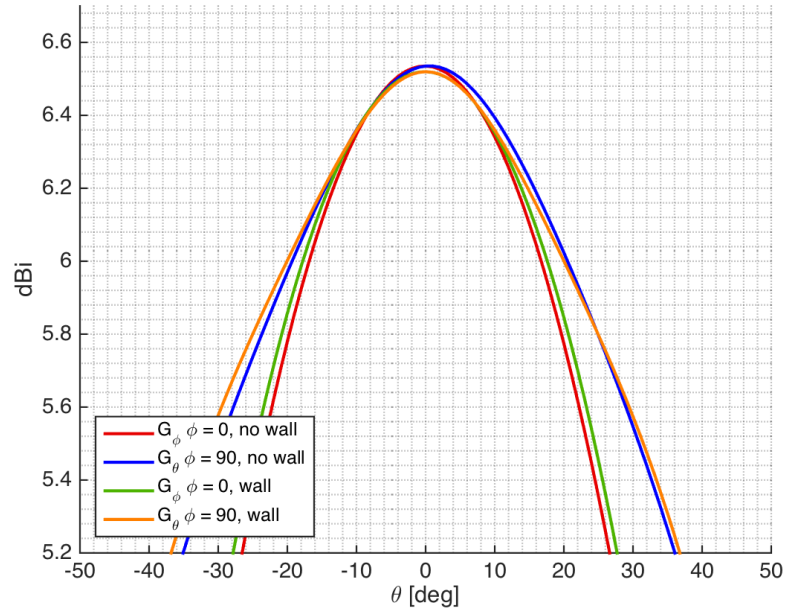
Furthermore, the use of wave ports at the side of the design is not compatible with array simulations in HFSS. The solution to this problem was to use another excitation model called *lumped ports* in HFSS, inside the PCB structure. A lumped port does not calculate the impedance of the wave as is the case for a *wave port*, instead an impedance is set before starting the simulation. The simulation is then done with this impedance at the port interface. As such, this impedance needs to be correct in order for the results to be valid.

An investigation was made of the correct setting, in order to get the same behavior for the unit cell as for the single element. For port 1 the impedance was set to $10\ \Omega$ and for port 2 it was set to $17\ \Omega$. The resulting S-parameters can be seen in figure 3.70. The impedance setting for port 1 could be improved further but given the timeframe further optimization was left as a possible future improvement.

3.2.3.4.3 Final Parameters In order to summarize the different set ups generating designs fulfilling or close to fulfilling the requirements, the final parameters for both the single element, unit cell and the design with a stripline offset in the slot are presented in table 3.7. The main differences are the stripline parameters and the waveguide radius.



(a) Directivity pattern for two designs with and without metal walls, as shown in figure 3.69, for port 1. In the H-plane ($\phi = 90^\circ$) it is clearly seen that the design without the walls has an asymmetric pattern. There is also an amplitude difference between the designs, implying that the metal walls remove leakage.



(b) Directivity for two designs with and without metal walls for port 2, as shown in figure 3.69.

Figure 3.68: Directivity for two designs with and without metal walls for both ports, as shown in figure 3.69. In the H-plane for port 1 it is clearly seen that the design without the walls has an asymmetric pattern.

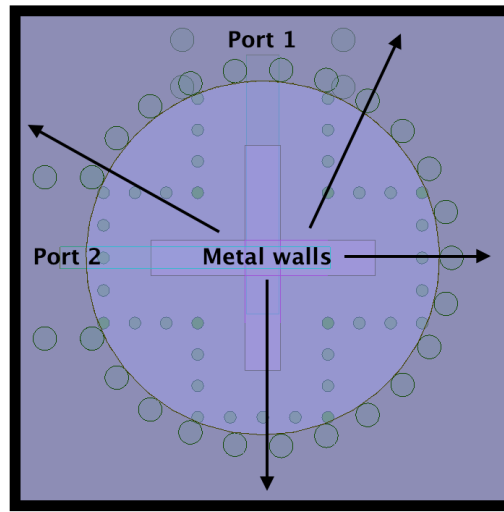


Figure 3.69: Top view of the unit cell where the addition of metal walls were made in order to prevent leakage.

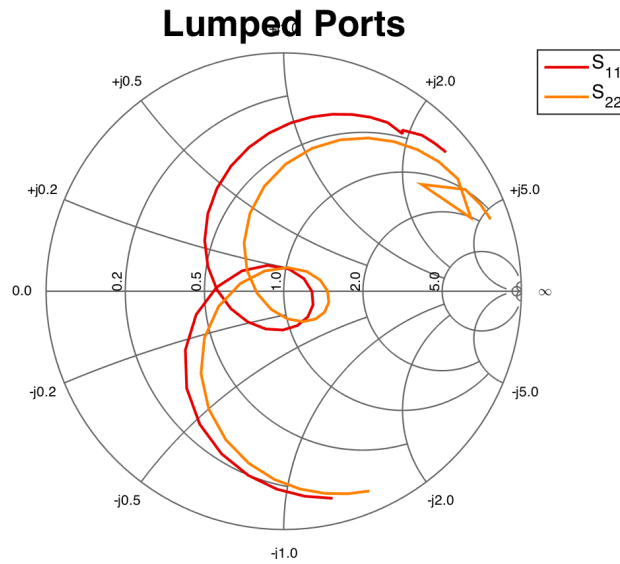


Figure 3.70: Smith chart showing S_{nn} for the unit cell design using the HFSS *lumped port* excitation method in order to enable array simulations. The impedance of the lumped ports were set to $10\ \Omega$ for port 1 and $17\ \Omega$ for port 2. The performance of port 1 can be improved further and moved closer to the middle of the Smith chart but given the timeframe this was left as a future improvement.

Table 3.7: Summary of the values of the final parameters for the different final designs.

Parameter	Slot in Middle		
	Slot Offset	Single Element	Unit Cell
$L_x [\lambda_0]$	1.3	1.3	0.53
$L_y [\lambda_0]$	1.3	1.3	0.53
Waveguide Radius [mm]	3.5	3.75	3.75
Waveguide Length [mm]	5	5	5
Slot Length [mm]	4.75	4.75	4.75
Slot Width [% of slot length]	16	16	16
Stripline Stub port 1 [mm]	0.45	0.45	0.8
Stripline Stub port 2 [mm]	0.6	1.05	1.05
Stripline Width port 1 [mm]	0.5	0.7	0.7
Stripline Width port 2 [mm]	0.5	0.46	0.46
Substrate 1 [mm]	1.524	1.524	1.524
Substrate 2 [mm]	0.168	0.168	0.168
Substrate 3 [mm]	0.168	0.168	0.168
Substrate 4 [mm]	0.168	0.168	0.168
Distance via - slot [mm]	-	1	1
Via Distance [parts of λ_g]	15	15	15

4

Results and Discussion

This chapter presents the performance of the final design; both for a single element and the element in an array environment. The focus is mainly how the final design performs with regard to the requirements, a summary can be seen in table 4.1.

Table 4.1: Summary of the performance of the final element compared to the requirements of the sub-array design.

Requirement	Final design
Sub-array implementation	Possible
Dual Polarized	Fulfilled
Reflection Coefficient $S_{nn} < -13$ dB	Fulfilled
Bandwidth $> 6\%$	Fulfilled ¹
Gain > 2 dBi at $\pm 60^\circ$ in azimuth (sub-array)	Fulfilled
Polarization Isolation < -15 dB	Fulfilled
Losses < 1 dB	Possible
$\Delta G_{co} < 3$ dB	Not fulfilled
Coupling < 13 dB	Fulfilled
XPD > 20 dB	Not fulfilled

4.1 Single Element Performance

4.1.1 Sub-array

One of the requirements was the possibility of implementation of the element into a vertical sub-array. A sub-array implementation is shown in figure 4.1. The sub-array is $0.53\lambda_0$ in the horizontal dimension and $2 \cdot 0.53\lambda_0$ in the vertical dimension. As can be seen in the figure, there is enough space in the sub-array cell to implement the feeding network between the two elements. Thus, it is evident that it is possible to implement the model into a vertical sub-array. The performance of the sub-array was not investigated, as the design of the feeding network would have been too time consuming.

¹When the ports are evaluated individually.

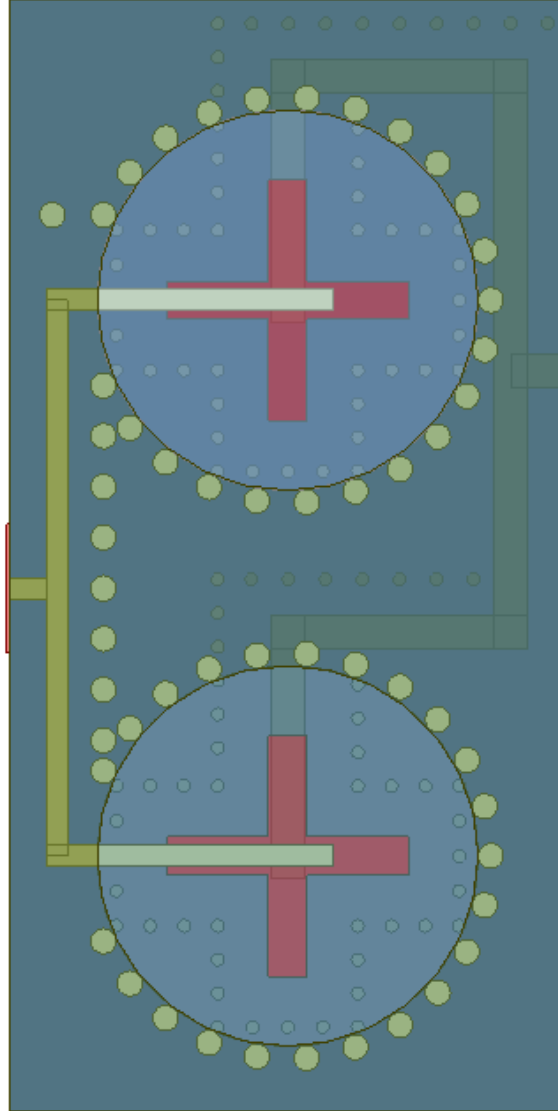


Figure 4.1: Figure showing the possibility of implementing the final design into a vertical sub-array where it is shown that there is enough space to realize a feeding network. The dimensions of the sub-array is $0.53\lambda_0 \times 2 \cdot 0.53\lambda_0$.

4.1.2 S-parameters

The S-parameters of the final design are shown in figure 4.2 and a close up of the area of interest is seen in figure 4.3. A readout of the values from the graph is presented in table 4.2. The bandwidth and reflection coefficient requirements are fulfilled for both ports where port 1 has a bandwidth of 6.71% and port 2 has a bandwidth of 7.01% when they are evaluated individually.

However, there is a frequency shift between the ports. Efforts were made to make the ports cover the same frequency band, but due to time limitations it could not be accomplished. If the bandwidth that is shared between the ports is evaluated the bandwidth requirement is not fulfilled, which is presented in table 4.2 under 'Port 1 & 2'. In figure 4.3 the isolation is clearly below the requirement of -15 where the maximum value is -24.12 dB inband.

Table 4.2: Summary of the performance of the final single element with the values as presented in figure 4.3. When the ports are evaluated individually they fulfill the requirements. However, due to a frequency shift between the ports, they do not fulfill the requirements if the common bandwidth is evaluated, see 'Port 1 & 2'.

	$S_{nn} < -13$ dB				$S_{nn} < -10$ dB			
	f_l	f_h	f_{mid}	Bandwidth	f_l	f_h	f_{mid}	Bandwidth
Port 1	13.98	14.95	14.47	6.71 %	13.9	15.07	14.49	8.08 %
Port 2	14.17	15.2	14.69	7.01 %	14.07	15.31	14.69	8.44 %
Port 1 & 2	14.17	14.95	14.56	5.36 %	14.07	15.07	14.57	6.86 %

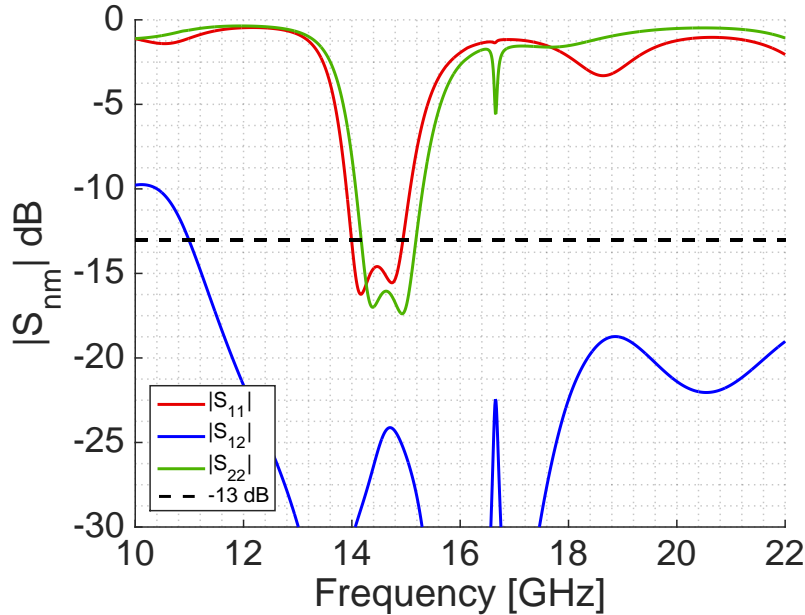


Figure 4.2: S-parameters of the final design where the bandwidth and isolation is shown. For a closer view of the performance, see figure 4.3.

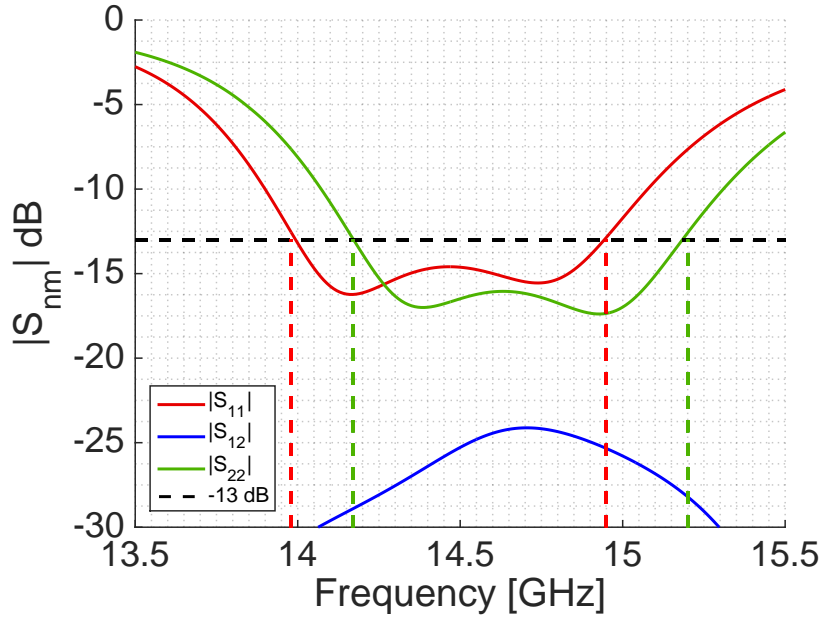


Figure 4.3: S-parameters of the final design where the bandwidth and isolation is shown. The maximum value of the isolation is -24.12 dB inband which is below the requirement of -15 dB. The specific values of the two orthogonal polarizations are presented in table 4.2. In summary, the bandwidth of port 1 is 6.71% and port 2 has a bandwidth of 7.01%.

4.1.3 Radiation Patterns

The radiation patterns of the final single element design are presented in figures 4.4 and 4.5. The patterns are for a single element and thus the requirement of -1 dBi is the requirement evaluated. Both ports fulfill this requirement and the specific values are presented in table 4.3.

Table 4.3: Summary of the performance of the final single element with the values as presented in figure 4.3. Both polarizations fulfill the gain requirement of $G_{co,\pm 60^\circ} > -1$ dBi.

[dBi]	Port 1 (V-pol)		Port 2 (H-pol)	
	$\theta = -60^\circ$	$\theta = 60^\circ$	$\theta = -60^\circ$	$\theta = 60^\circ$
$G_\phi(\phi = 0^\circ)$	-25.82	-23.73	-0.32	0.16
$G_\phi(\phi = 90^\circ)$	-0.20	-0.213	-26.61	-23.74
$G_\theta(\phi = 0^\circ)$	2.92	2.95	-21.00	-24.69
$G_\theta(\phi = 90^\circ)$	-19.64	-24.15	2.86	2.88

Another requirement is that the difference in G_{co} between the polarizations in any plane should be below 3 dB. Using the values from table 4.3 the following result is obtained at the edges of the operating area:

ϕ, θ	$G_{co \text{ E-plane, port n}} - G_{co \text{ H-plane, port m}}$
$\phi = 0^\circ, \theta = -60^\circ$	$G_{\theta 1} - G_{\phi 2} = 2.92 - (-0.32) = 3.24 \text{ dB}$
$\phi = 0^\circ, \theta = +60^\circ$	$G_{\theta 1} - G_{\phi 2} = 2.95 - (+0.16) = 2.79 \text{ dB}$
$\phi = 90^\circ, \theta = -60^\circ$	$G_{\theta 2} - G_{\phi 1} = 2.86 - (-0.20) = 3.06 \text{ dB}$
$\phi = 90^\circ, \theta = +60^\circ$	$G_{\theta 2} - G_{\phi 1} = 2.88 - (-0.21) = 3.09 \text{ dB}$

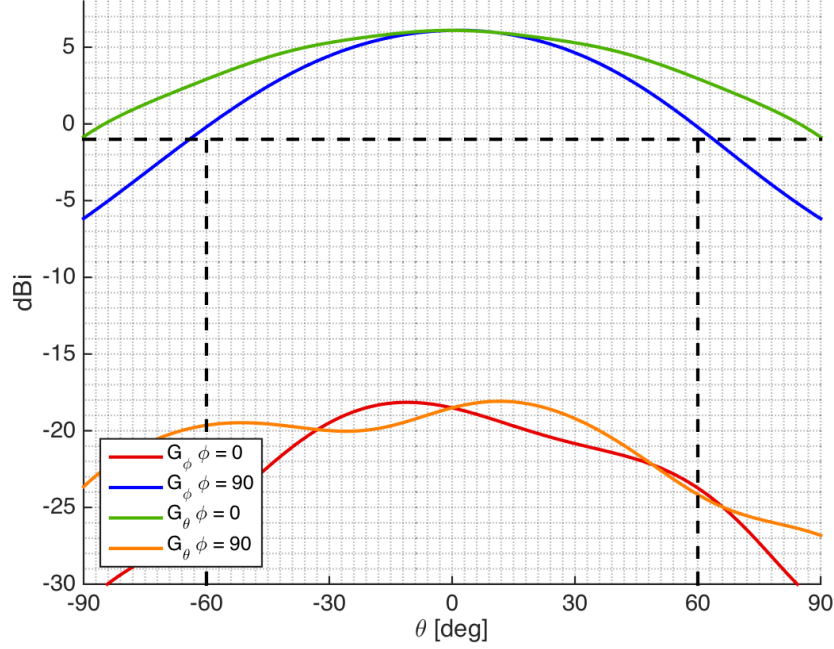


Figure 4.4: Gain of the final single element design, co-polar and cross-polar for 14.5 GHz, when port 1 (vertical polarization) is excited. The 2 dBi requirement at $\pm 60^\circ$ for a sub-array is likely fulfilled since the single element gain requirement is fulfilled ($G_{co, \pm 60^\circ} > -1 \text{ dBi}$).

As can be seen the requirement is not fulfilled, the maximum deviation is a 0.24 dB difference between the two co-polar patterns. Other planes than the two principal planes were not tested since the requirement was not fulfilled.

The result of the XPD investigation is presented in figures 4.6 and 4.7 where the difference between the co-polar and cross-polar gain is shown for both ports. The H-plane patterns were chosen since the difference between the co-polar and cross-polar gain was smaller than the E-plane and thus were more prone to fail to fulfill the requirement. The requirement is not fulfilled for port 1, since the XPD is 19.5 dB, 0.5 dB below the requirement of 20 dB.

Before setting up the single element in an array environment a simulation of the element with a large ground plane was made. The ground plane was $8 \cdot 8 \text{ cm}$ and the element was put in the corner of this large ground plane, 0.8 cm from the closest edges. The resulting directivity patterns are seen in figures 4.8 and 4.9. It is clearly seen that the ground plane creates a more ripply pattern as expected. The requirement of -1 dBi over the operating area is fulfilled.

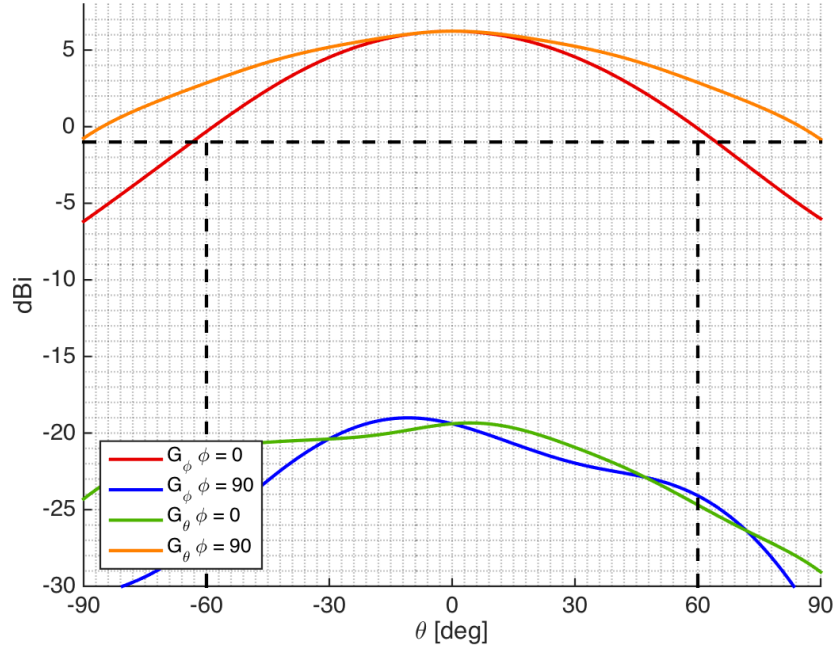


Figure 4.5: Gain of the final single element design, co-polar and cross-polar for 14.5 GHz, when port 2 (horizontal polarization) is excited. The 2 dBi requirement at $\pm 60^\circ$ for a sub-array is likely fulfilled, since the single element gain requirement is fulfilled ($G_{co,\pm 60^\circ} > -1$ dBi).

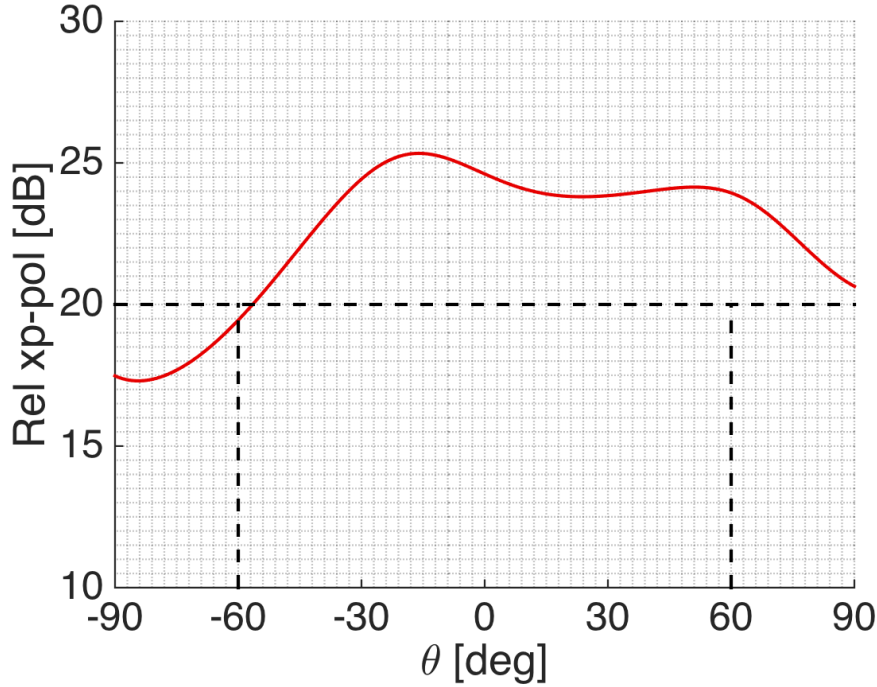


Figure 4.6: The cross-polar decoupling of port 1, i.e. the difference defined by $G_\phi(\phi = 90^\circ) - G_\theta(\phi = 90^\circ) = XPD_1$. The requirement is to have the relative cross-polarization level above 20 dB, this requirement is almost fulfilled inside the operating area.

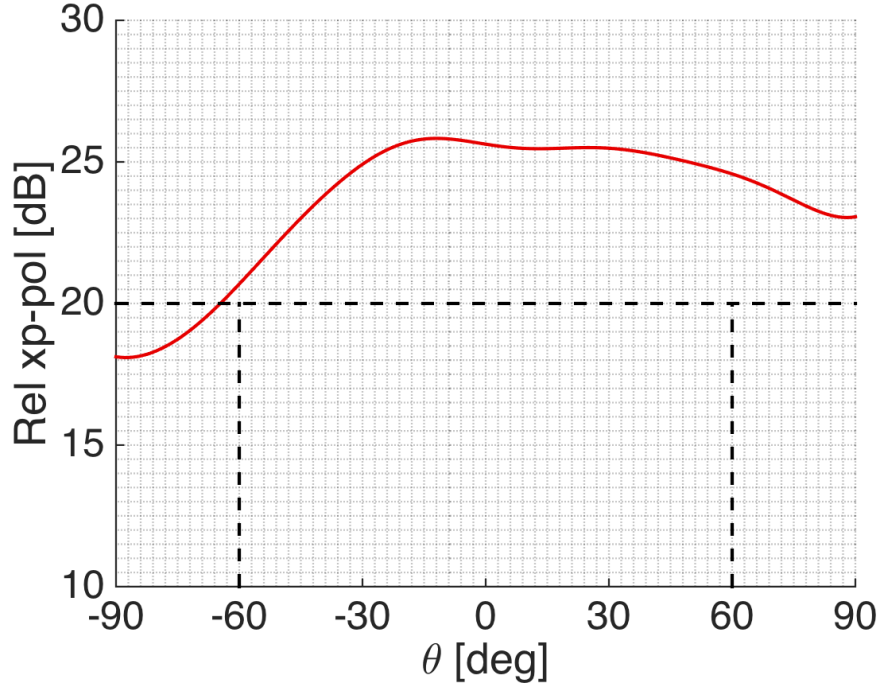


Figure 4.7: The cross-polar decoupling of port 2, i.e. the difference defined by $G_\phi(\phi = 0^\circ) - G_\theta(\phi = 0^\circ) = XPD_2$. The requirement is to have the relative cross-polarization level above 20 dB, this requirement is fulfilled inside the operating area.

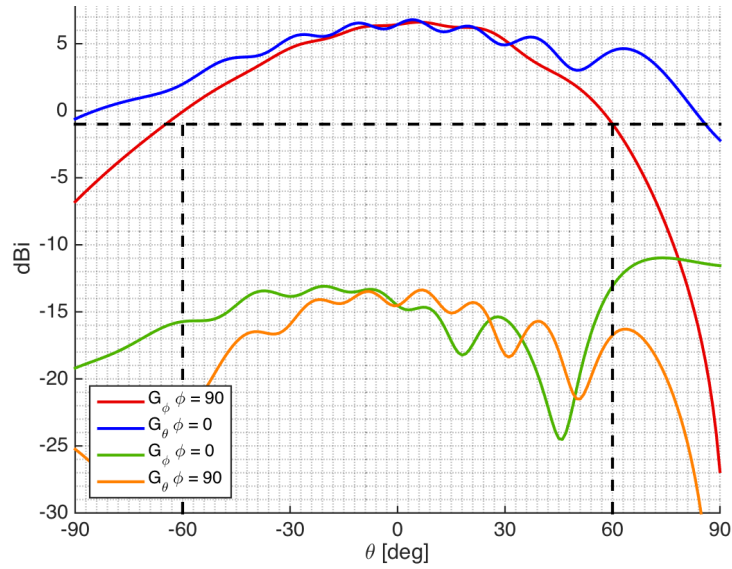


Figure 4.8: Directivity of the final single element design on a large ground plane ($8 \cdot 8$ cm, element placed 0.8 cm from edge), co-polar and cross-polar for 15 GHz, when port 1 is excited.

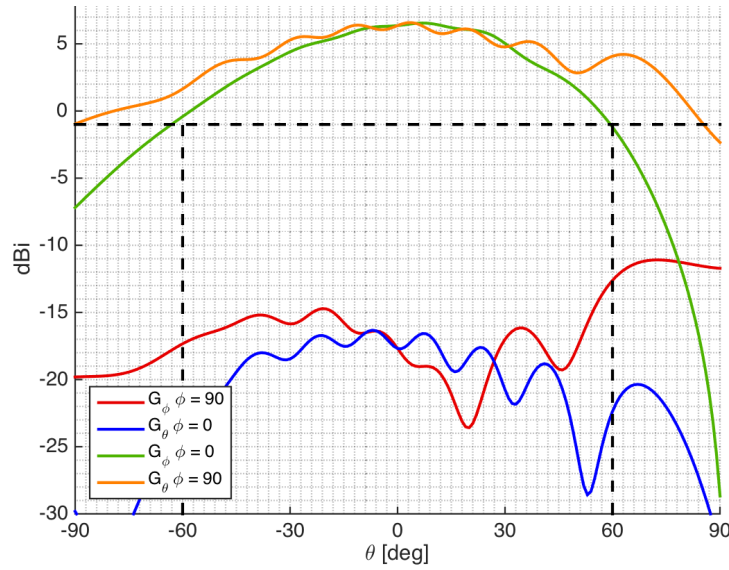


Figure 4.9: Directivity of the final single element design on a large ground plane (8·8 cm, element placed 0.8 cm from edge), co-polar and cross-polar for 15 GHz, when port 2 is excited.

4.1.4 Losses

The losses of the sub-array should be below 1 dB according to requirement 8. This can be validated by analyzing the difference between the directivity and the gain. Since the sub-array was not implemented, the single element design was analyzed instead and this should be taken into account when the fulfillment of the requirement is evaluated. In figures 4.10 and 4.11 both the directivity and the gain of port 1 and port 2 in the E- and H-plane are shown, divided into co- and cross-polar parts. The differences are

$$D_1 - G_1 = 0.3537 \text{ dB} \quad D_2 - G_2 = 0.3411 \text{ dB} \quad (4.1)$$

for both ports respectively where the subindex denotes the port.

This leaves approximately 0.65 dB as a margin for losses when a sub-array is considered. The sub-array will have a more complex and longer feeding network which will introduce more losses. Therefore it is hard to determine whether or not the requirement will be fulfilled for a sub-array, since the performance will depend on the sub-array implementation. With the available data the requirement could or could not be fulfilled, thus a definitive answer can not be given until a sub-array implementation has been made, which is recommended for a future study.

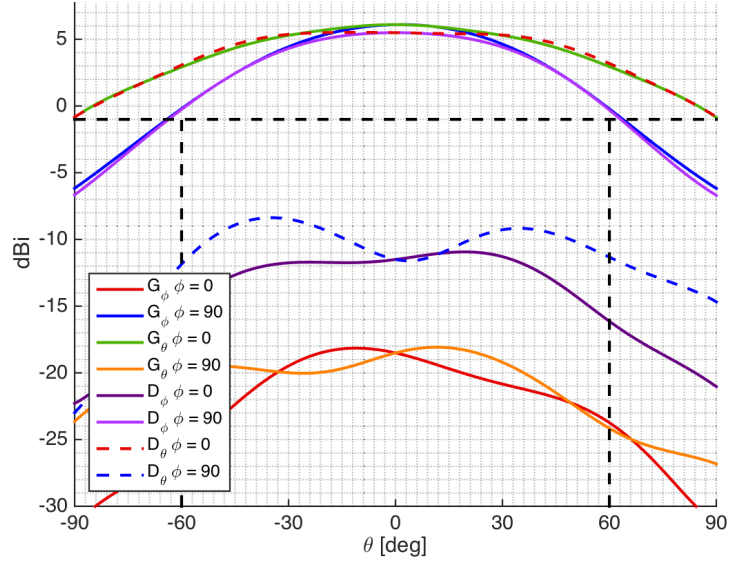


Figure 4.10: Gain and directivity for port 1 at 15 GHz, the co- and cross-polar patterns are shown for the E- and H-plane respectively. The maximum difference between the directivity and the gain is $D_1 - G_1 = 0.3537$ dB.

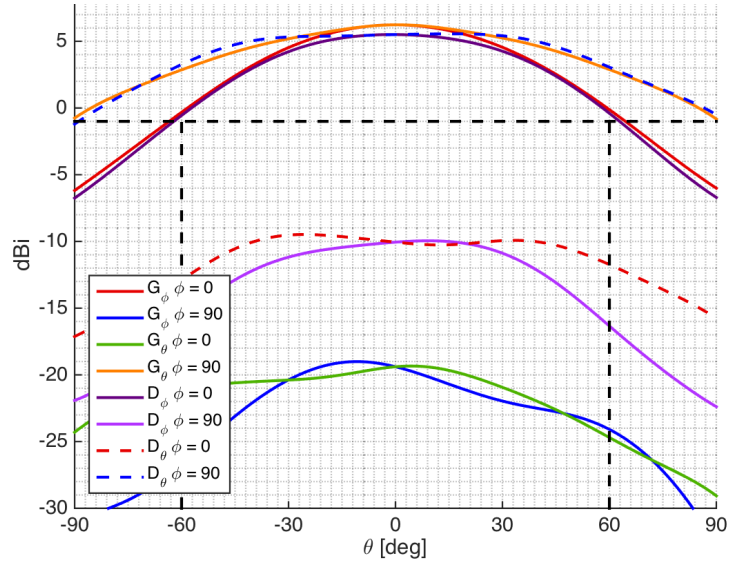


Figure 4.11: Gain and directivity for port 2 at 15 GHz, the co- and cross-polar patterns are shown for the E- and H-plane respectively. The maximum difference between the directivity and the gain is $D_2 - G_2 = 0.3411$ dB.

4.2 Array Performance

A finite square array consisting of 64 elements ($8 \cdot 8$) was simulated at three frequency points; 14, 14.5 and 15 GHz corresponding to the start, center and end frequency points of the bandwidth. To help with the visualization of the elements' behavior depending on their placement, the chart seen in figure 4.12 was used to map the elements. Each color corresponds to a row and each column has one element of each color.

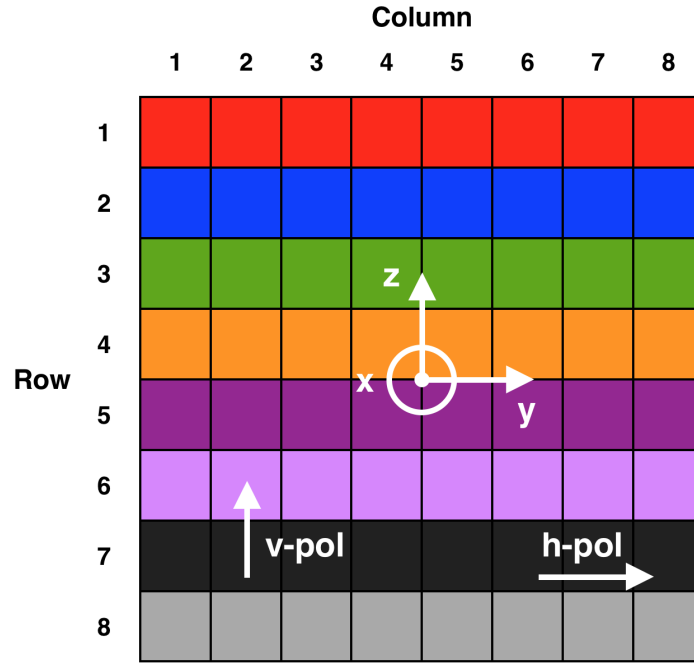


Figure 4.12: Schematic array layout where the color coding shown will be used when presenting the results where the element placement is of interest. The coordinate system of the array is also shown together with the polarization directions of the E-plane.

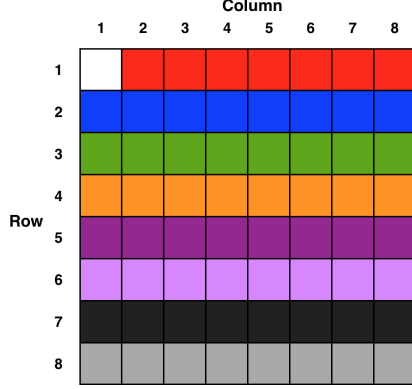
The coordinate system used for the array is also shown where the propagation axis is the x-axis. The directions of the two polarizations are also shown, where the horizontal polarization has its E-plane in the xy-plane and the E-plane of the vertical polarization in the xz-plane. This can be translated to a spherical coordinate system according to

$$\begin{aligned}
 \text{xy-plane} : \phi &= [-90^\circ, 90^\circ], \theta = 90^\circ && (\text{E-plane, H-pol}) \\
 \text{xz-plane} : \phi &= 0^\circ, \theta = [0^\circ, 180^\circ] && (\text{E-plane, V-pol}).
 \end{aligned} \tag{4.2}$$

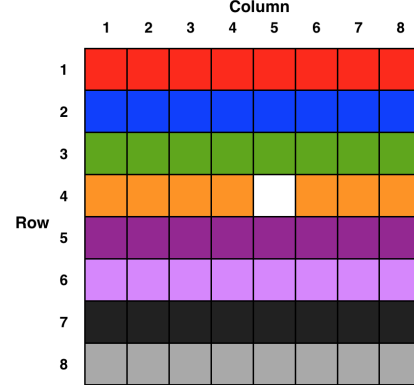
4.2.1 Mutual Coupling

The requirement of the mutual coupling between the elements in the array was to have the coupling coefficients ($S_{nm}, n \neq m$) below -13 dB. The coupling requirement is fulfilled for both polarizations at all three simulated frequency

points. Two samples are shown for a corner element in figures 4.14 and 4.15 and for an element in the middle of the array in figures 4.16 and 4.17 for both polarizations. The colors correspond to the array layout shown in figure 4.13 where the blank element is the one investigated. The only element whose coupling parameter is above the requirement is the self coupling (S_{nn}) which is not covered in the requirement and it can therefore be neglected.



(a) Visualization of the element placement in the array whose coupling is shown in figures 4.14 and 4.15.



(b) Visualization of the element placement in the array whose coupling is shown in figures 4.16 and 4.17.

Figure 4.13: Figure presenting the color coded array where the element whose coupling is presented is blank.

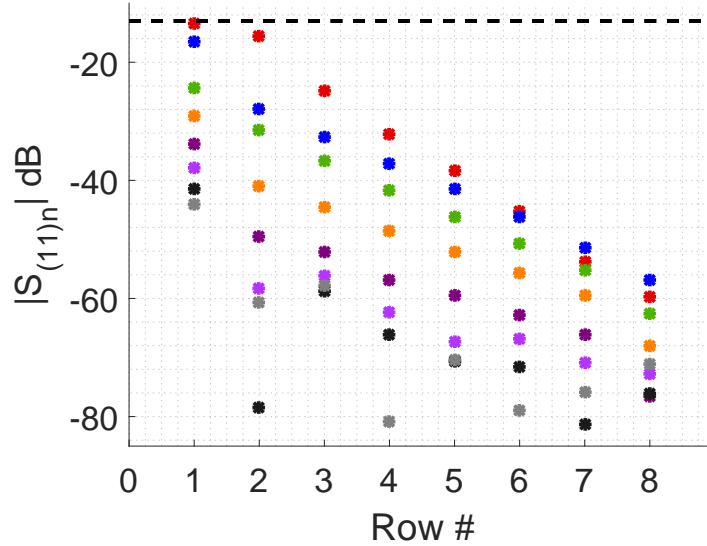


Figure 4.14: The coupling between a corner element and the rest of the elements in the array for vertical polarization (port 1) at 14.5 GHz. The coupling requirement is fulfilled, the point above the dashed requirement line is the self coupling and as such it is not included in the requirement. See figure 4.13a for a visualization of which element the coupling is shown for.

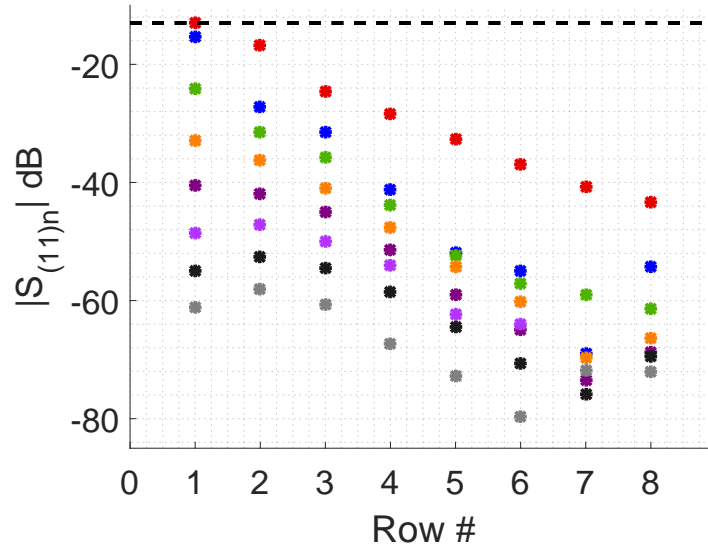


Figure 4.15: The coupling between a corner element and the rest of the elements in the array for horizontal polarization (port 2) at 14.5 GHz. The coupling requirement is fulfilled, the point above the dashed requirement line is the self coupling and as such it is not included in the requirement. See figure 4.13a for a visualization of which element the coupling is shown for.

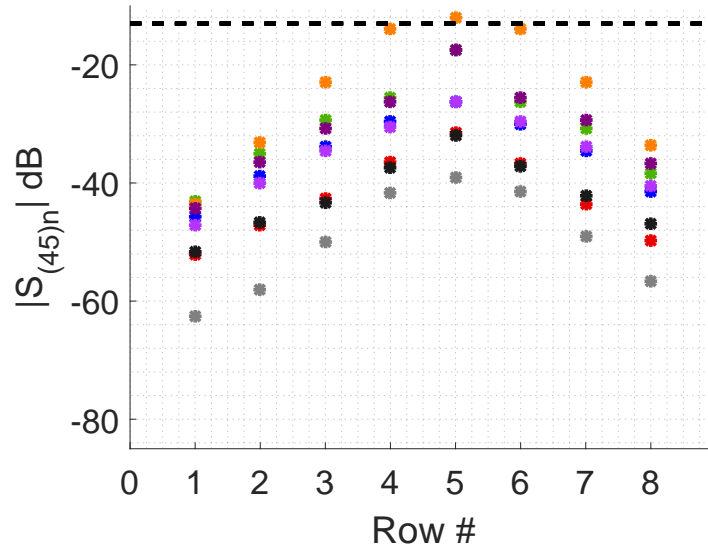


Figure 4.16: The coupling between an element in the middle and the rest of the elements in the array for vertical polarization (port 1) at 14.5 GHz. The coupling requirement is fulfilled, the point above the dashed requirement line is the self coupling and as such it is not included in the requirement. See figure 4.13b for a visualization of which element the coupling is shown for.

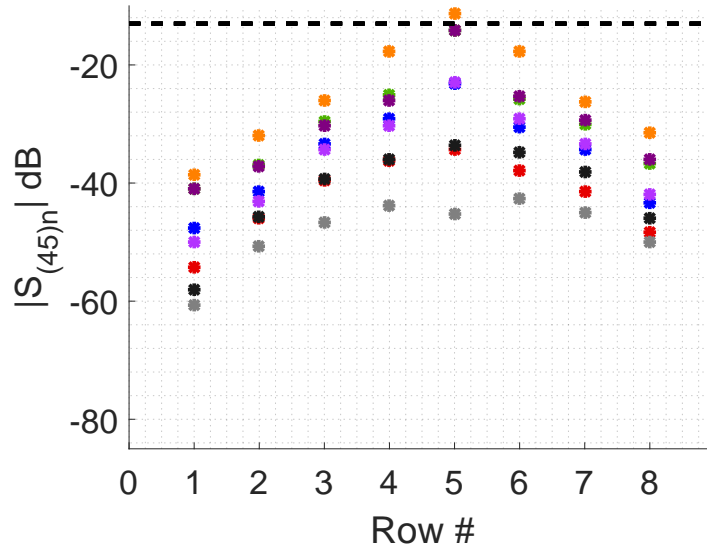


Figure 4.17: The coupling between an element in the middle and the rest of the elements in the array for horizontal polarization (port 2) at 14.5 GHz. The coupling requirement is fulfilled, the point above the dashed requirement line is the self coupling and as such it is not included in the requirement. See figure 4.13b for a visualization of which element the coupling is shown for.

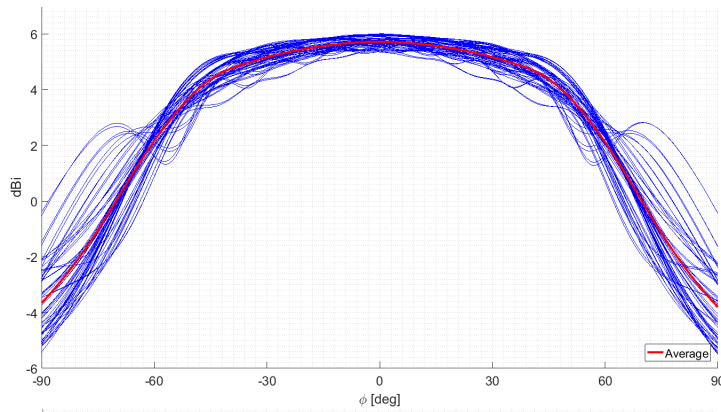
4.2.2 Embedded Patterns

The single element patterns in the E- and H-plane for both polarizations are shown in figures 4.18 and 4.19 together with the average. A more detailed study of the effect the placement in the array has on the embedded element pattern can be seen in figures 4.20 to 4.27 where the colors correspond to the array layout color mapping in figure 4.12.

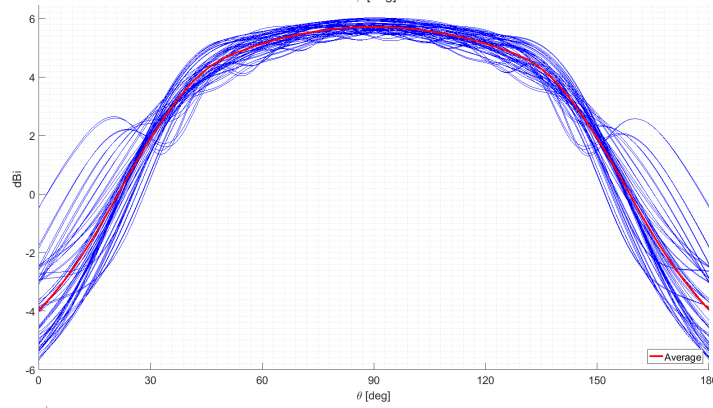
As can be seen the edge elements have more ripples in their embedded patterns than elements with a more central placement. The two polarizations show similar behavior when their relation to the orientation and E- and H-plane is the same, e.g. a column for the horizontal polarization in the E-plane (figure 4.20) is similar to a row for the vertical polarization in the E-plane (figure 4.25). As such, the color coding for the columns can be used to understand the figures with the rows.

4.2.3 Beam Steering

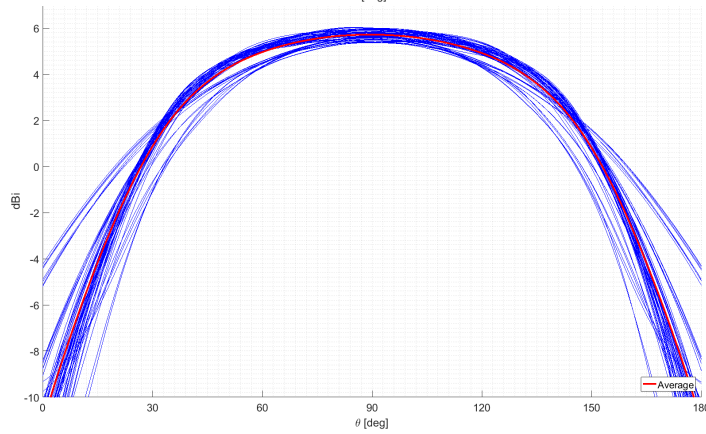
The performance of the array when the beam was steered was also simulated by exporting the data from HFSS and using Matlab to post-process it. When the beam is steered to the edge of the operating area the peak power of the main beam decreases since an increase in sidelobes and grating lobes affects the performance. This can be seen in figures 4.28a and 4.28b where the maximum peak value is plotted for each integer angle position when the beam is steered



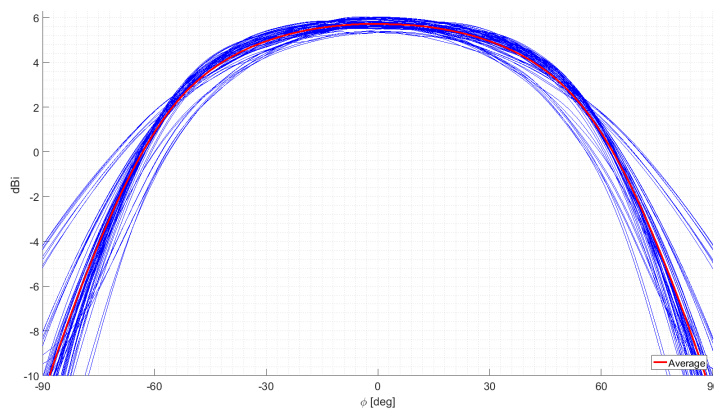
(a) Co-polar directivity of embedded elements in E-plane for the horizontal polarization.



(b) Co-polar directivity of embedded elements in E-plane for the vertical polarization.

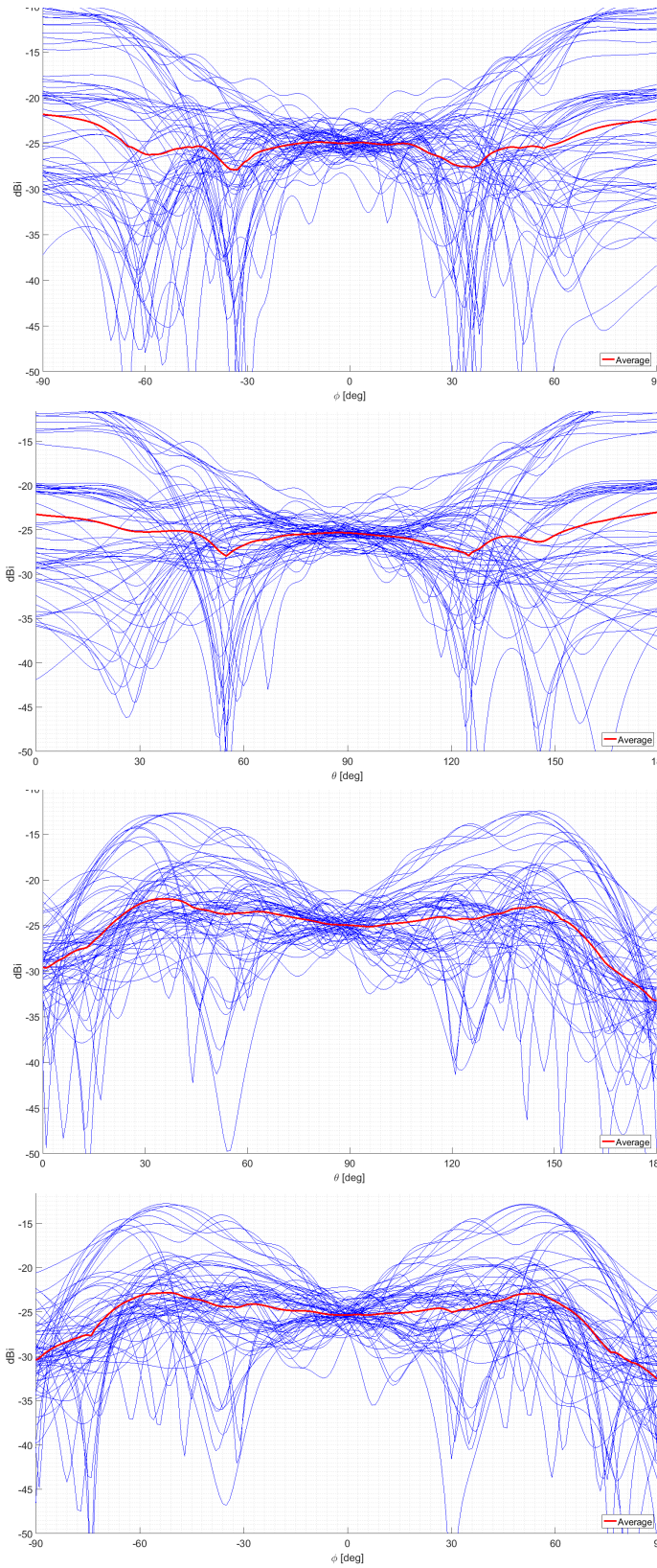


(c) Co-polar directivity of embedded elements in H-plane for the horizontal polarization.



(d) Co-polar directivity of embedded elements in H-plane for the vertical polarization.

Figure 4.18: Embedded co-polar directivity patterns for both polarizations in the E- and H-planes.



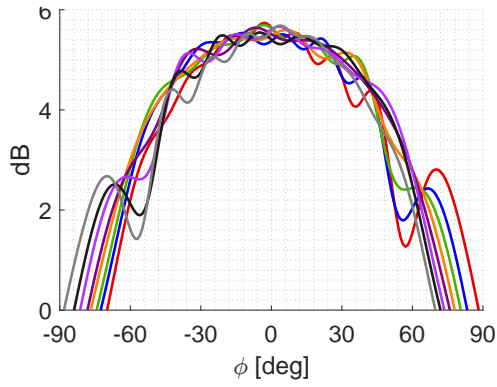
(a) Xp-polar directivity of embedded elements in H-plane for the horizontal polarization.

(b) Xp-polar directivity of embedded elements in H-plane for the vertical polarization.

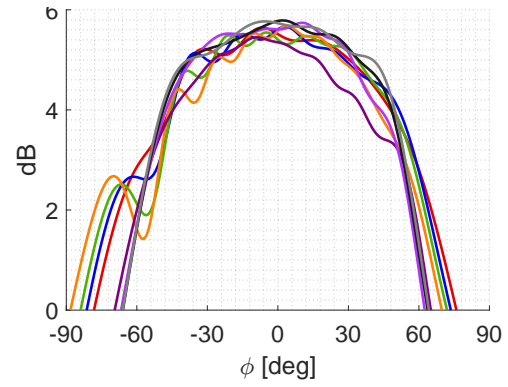
(c) Xp-polar directivity of embedded elements in H-plane for the horizontal polarization.

(d) Xp-polar directivity of embedded elements in H-plane for the vertical polarization.

Figure 4.19: Embedded cross-polar directivity patterns for both polarizations in the E- and H-planes.

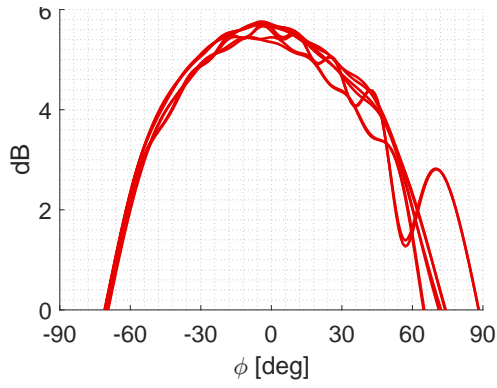


(a) Embedded patterns of column 1, the E-plane cut of the horizontal polarization.

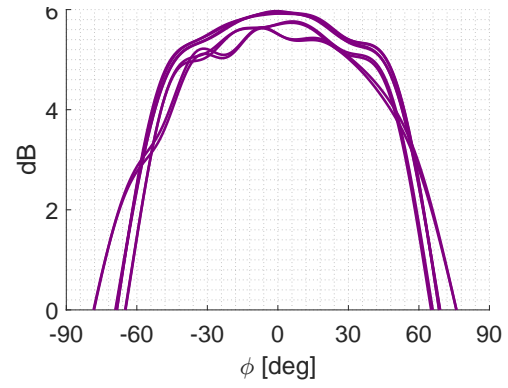


(b) Embedded patterns of column 5, the E-plane cut of the horizontal polarization.

Figure 4.20: Embedded directivity patterns of the E-plane cut of the horizontal polarization for different columns.

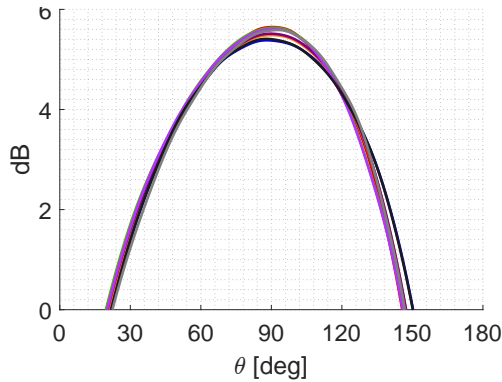


(a) Embedded patterns of row 1, the E-plane cut of the horizontal polarization.

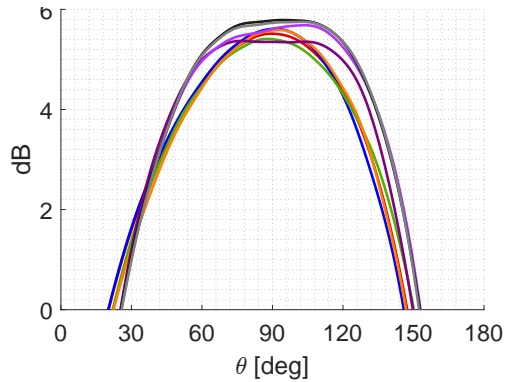


(b) Embedded patterns of row 5, the E-plane cut of the horizontal polarization.

Figure 4.21: Embedded directivity patterns of the E-plane cut of the horizontal polarization for different rows.

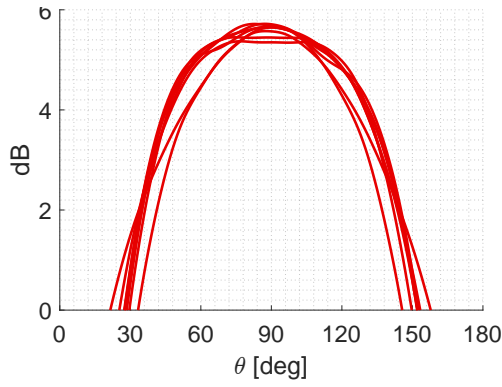


(a) Embedded patterns of column 1, the H-plane cut of the horizontal polarization.

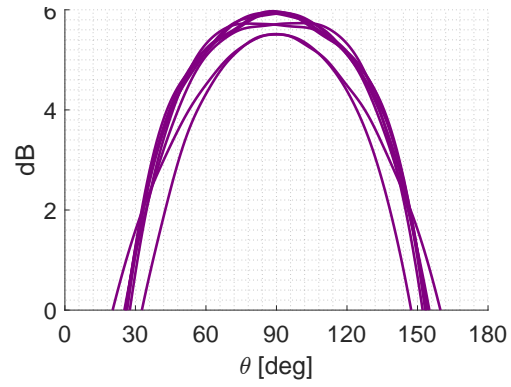


(b) Embedded patterns of column 5, the H-plane cut of the horizontal polarization.

Figure 4.22: Embedded directivity patterns of the H-plane cut of the horizontal polarization for different columns.

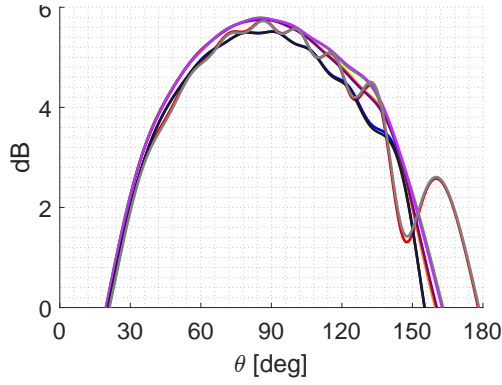


(a) Embedded patterns of row 1, the H-plane cut of the horizontal polarization.

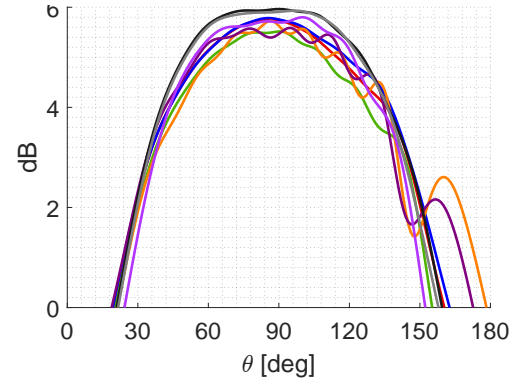


(b) Embedded patterns of row 5, the H-plane cut of the horizontal polarization.

Figure 4.23: Embedded directivity patterns of the H-plane cut of the horizontal polarization for different rows.

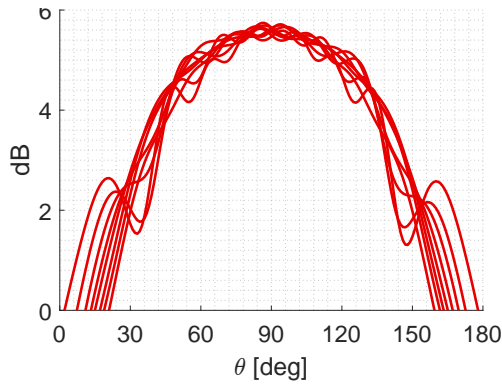


(a) Embedded patterns of column 1, the E-plane cut of the vertical polarization.

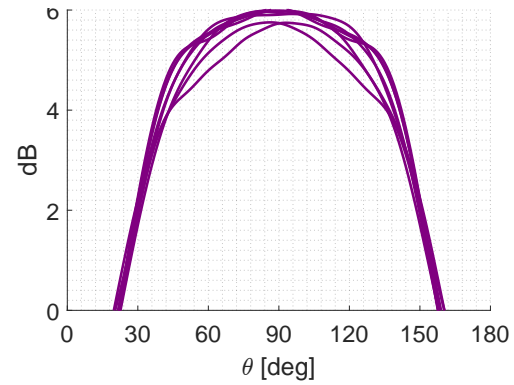


(b) Embedded patterns of column 5, the E-plane cut of the vertical polarization.

Figure 4.24: Embedded directivity patterns of the E-plane cut of the vertical polarization for different columns.

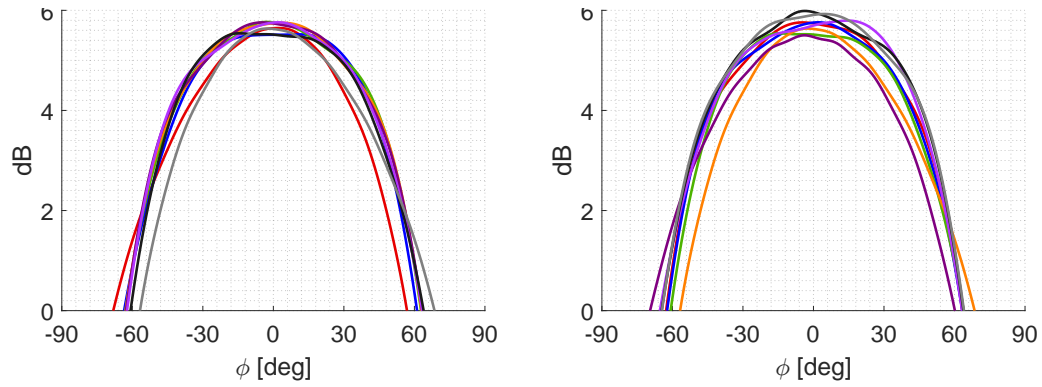


(a) Embedded patterns of row 1, the E-plane cut of the vertical polarization.



(b) Embedded patterns of row 5, the E-plane cut of the vertical polarization.

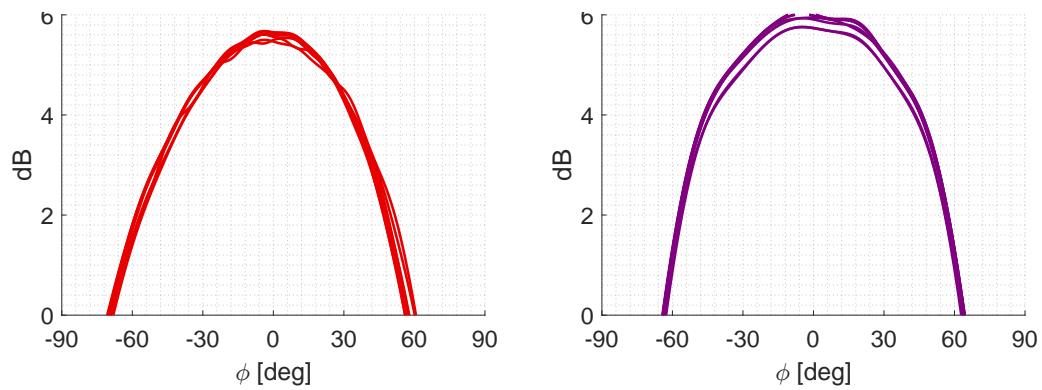
Figure 4.25: Embedded directivity patterns of the E-plane cut of the vertical polarization for different rows.



(a) Embedded patterns of column 1, the H-plane cut of the vertical polarization.

(b) Embedded patterns of column 5, the H-plane cut of the vertical polarization.

Figure 4.26: Embedded directivity patterns of the H-plane cut of the vertical polarization for different columns.

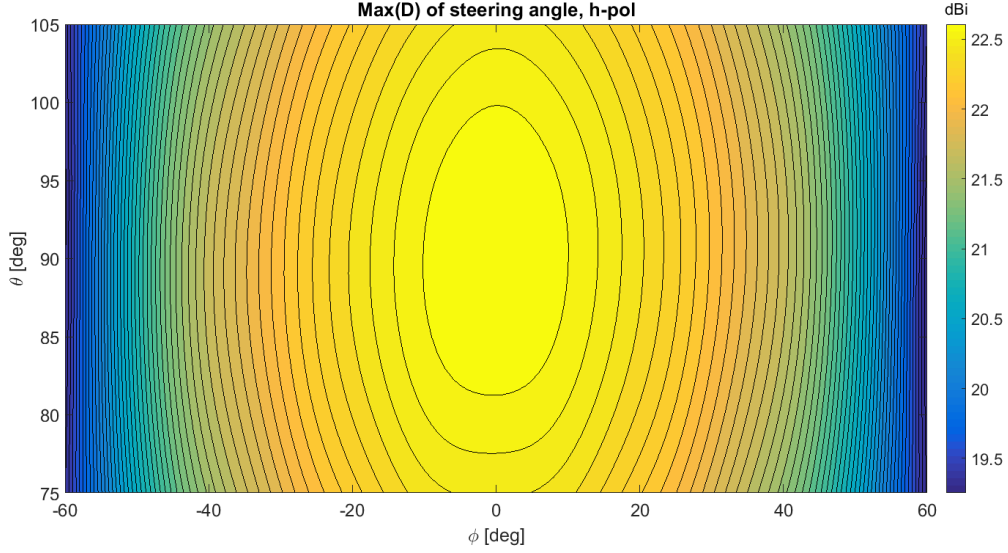


(a) Embedded patterns of row 1, the H-plane cut of the vertical polarization.

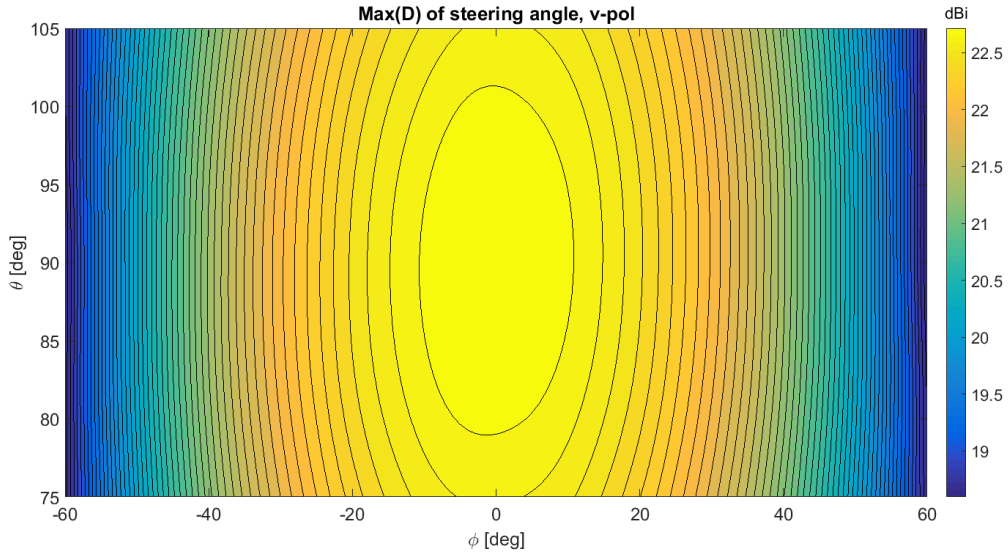
(b) Embedded patterns of row 5, the H-plane cut of the vertical polarization.

Figure 4.27: Embedded directivity patterns of the H-plane cut of the vertical polarization for different rows.

in that direction. As expected, further away from broadside the directivity is lower.



(a) Peak directivity as a function of steering angle for the horizontal polarization.



(b) Peak directivity as a function of steering angle for the vertical polarization.

Figure 4.28: The array was steered to each integer angle position and the peak directivity for a beam steered to that position is presented here for both polarization at 14.5 GHz. It is clearly seen that the maximum directivity decrease further away from broadside.

In figures 4.29 to 4.36 the co- and cross-polar directivity for the two polarizations at different steered beam positions are shown. Their maximum directivity and the maximum side lobe level are presented in table 4.4. There it is seen that a steered beam decreases the directivity of the main beam due to more side lobes.

Table 4.4: The maximum directivity of the main beam and the maximum side lobe level for a beam steered in different directions.

Beam direction	H-pol		V-pol	
	max(main)	max(side)	max(main)	max(side)
$\phi = 0^\circ, \theta = 90^\circ$	22.67	9.50	22.79	9.67
$\phi = 0^\circ, \theta = 105^\circ$	22.50	9.34	22.65	9.94
$\phi = 60^\circ, \theta = 90^\circ$	19.26	9.05	18.59	9.53
$\phi = 60^\circ, \theta = 105^\circ$	19.35	9.05	18.35	9.37

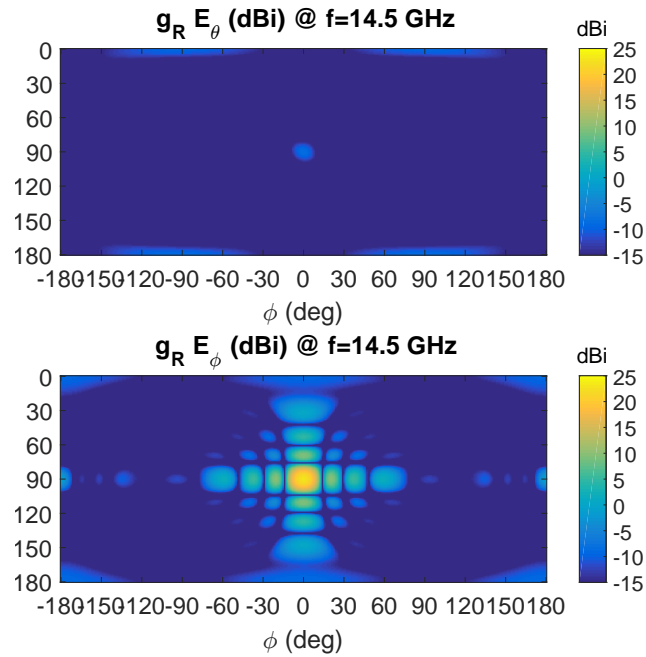


Figure 4.29: Directivity for the horizontal polarization in the broadside direction, $\phi = 0^\circ, \theta = 90^\circ$.

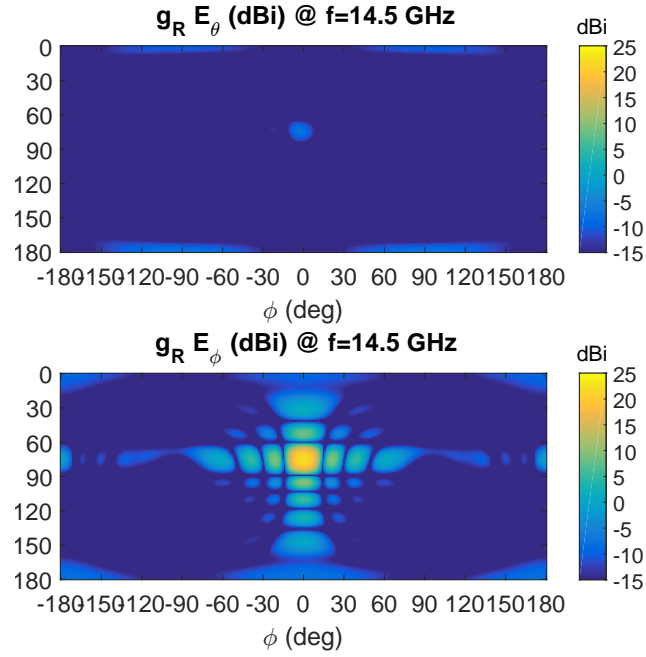


Figure 4.30: Directivity for the horizontal polarization steered to $\phi = 0^\circ, \theta = 105^\circ$.

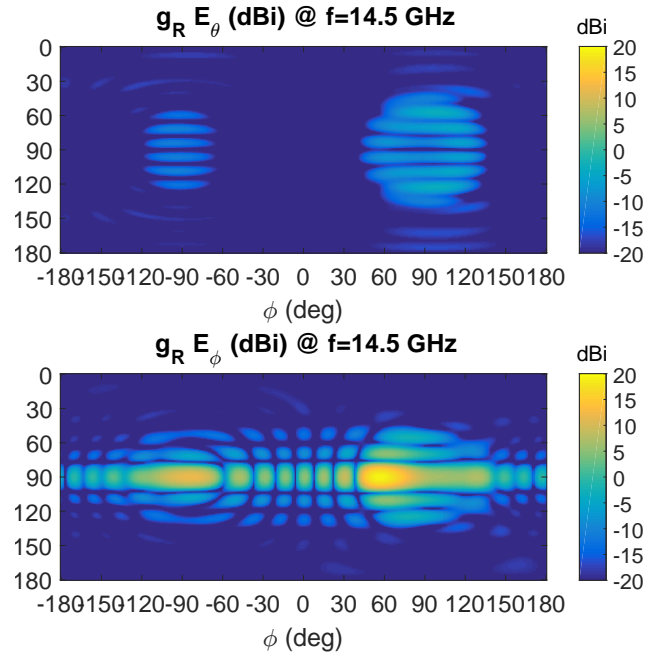


Figure 4.31: Directivity for the horizontal polarization steered to $\phi = 60^\circ, \theta = 90^\circ$.

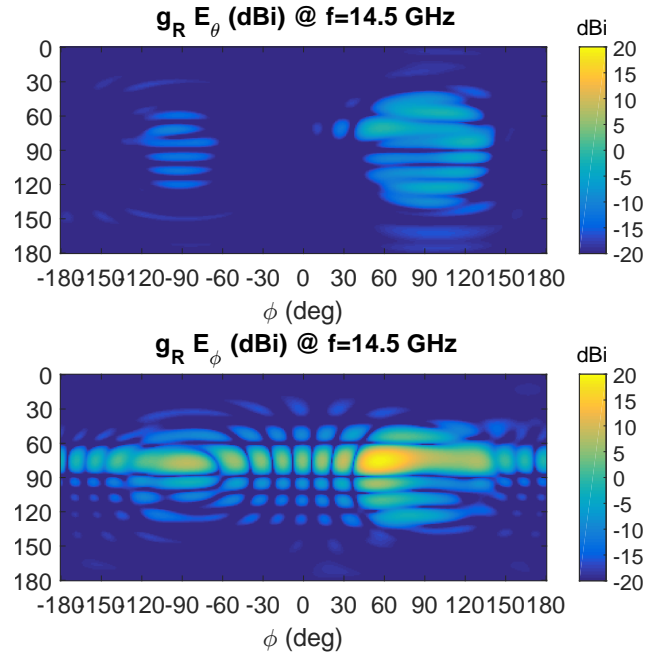


Figure 4.32: Directivity for the horizontal polarization steered to $\phi = 60^\circ, \theta = 105^\circ$.

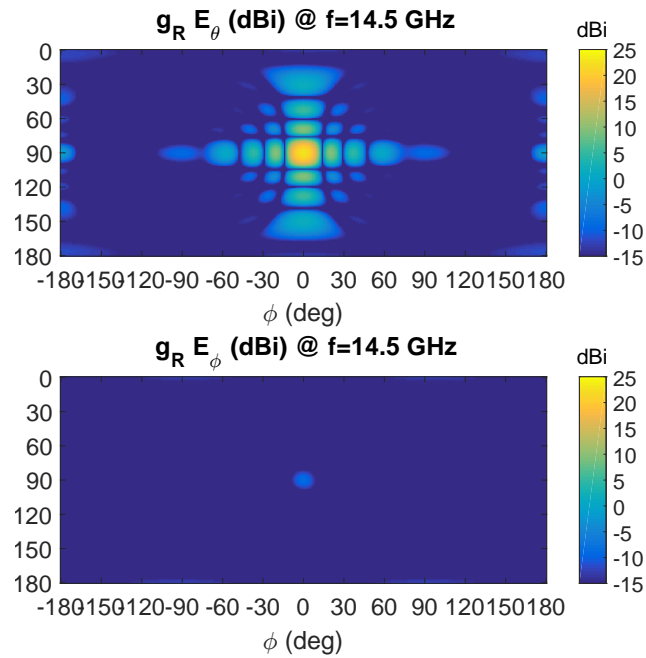


Figure 4.33: Directivity for the vertical polarization in the broadside direction, $\phi = 0^\circ, \theta = 90^\circ$.

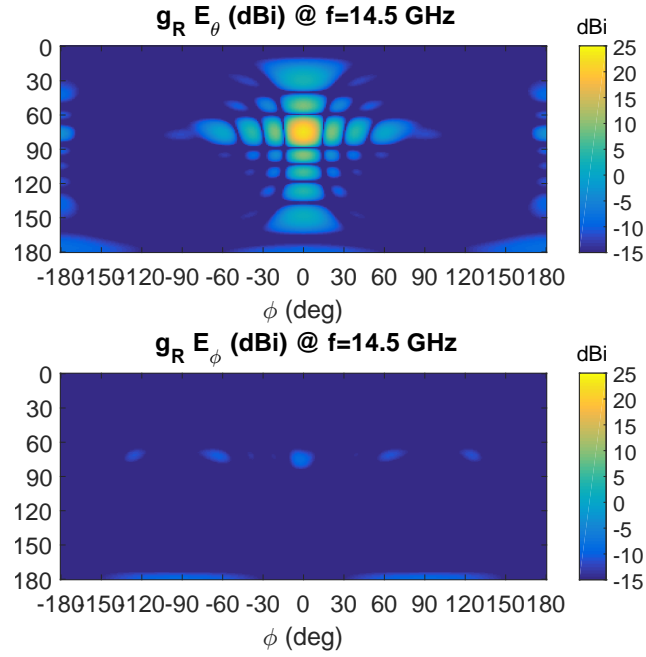


Figure 4.34: Directivity for the vertical polarization steered to $\phi = 0^\circ, \theta = 105^\circ$.

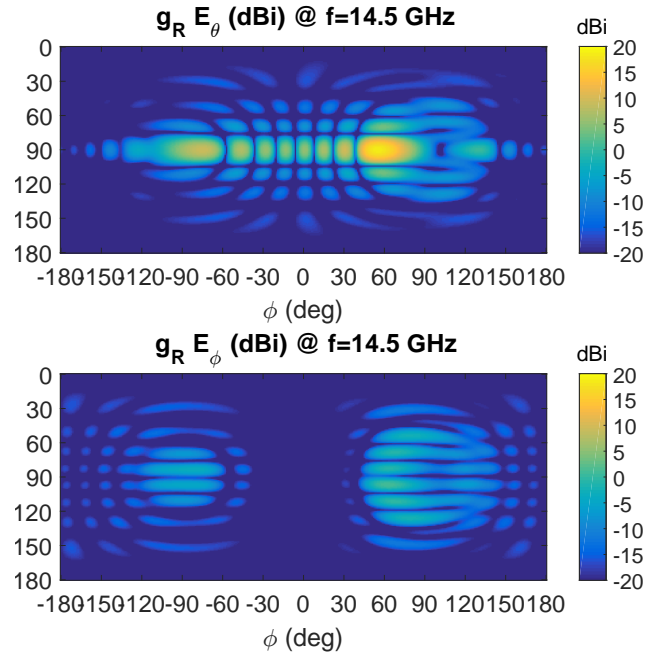


Figure 4.35: Directivity for the vertical polarization steered to $\phi = 60^\circ, \theta = 90^\circ$.

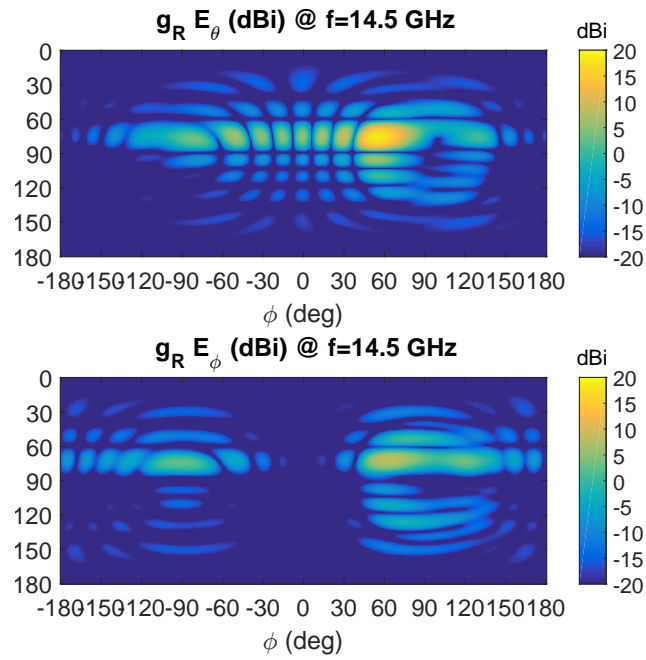


Figure 4.36: Directivity for the vertical polarization steered to $\phi = 60^\circ, \theta = 105^\circ$.

5

Conclusions and Recommendations for Future Work

This master thesis has investigated the possibility of using a PCB hardback to create a radiating aperture, which seems possible with regard to the simulation results. In order to create a circular aperture with a diameter smaller than 0.53λ the element needs to be loaded using either ridges or dielectric filling. The stated requirements seem possible to fulfill with some further optimization of the final element design.

5.1 Ridged Element Design

A circular aperture loaded with ridges has the disadvantage of the second mode having a cutoff frequency too close to the fundamental mode, limiting the bandwidth. The drilled ridged design idea is simple with regard to the manufacturing process and if the second mode is successfully suppressed it could potentially fulfill the requirements. However, optimization and a proper analysis of the circular ridged geometry is advised in order to set the parameters correctly.

5.2 Dielectric Filled Design

The final dielectrically filled aperture with a slot coupled feeding was the most promising design and was close to fulfilling all of the requirements. One problem with the simulation model was leakage somewhere in the PCB which made the radiation patterns asymmetric. This should be investigated properly in order to identify the location of the leakage so more vias can be added.

The design could also be further optimized to get a better performance. One future improvement should be a frequency shift of one of the ports to get a larger common bandwidth for both of the polarizations. Some suggestions to achieve this is to change the stripline parameters in combination with one sub-

strate height or to change the length of one of the slots.

The requirements regarding the difference between G_{co} of the two polarizations (requirement 7) and the XPD (requirement 10) were not fulfilled. To improve the similarity between the co-polar gain in the E- and H-plane a $\lambda/4$ -choke could be added on the outside of the waveguide [21, pp. 185-192]. This may be hard to implement with the chosen manufacturing technique but a variation of the choke may be possible to realize. Olver, [21], also mentions that the choke could lower the cross-polar levels and it is therefore possible that the XPD would improve as well.

One conclusion from the parametric study of the slot coupled element was the impact of the stripline placement with regard to the slot. The isolation between the ports was improved the closer to the middle of the slot the stripline was placed. In the final design the stripline placement was therefore in the middle of the slot. This affects the bandwidth of the design as the slot impedance is highest in the middle of the slot, and large impedance variations lowers the available bandwidth. Furthermore, the placement of the stripline in the middle of the slot excludes the possibility of using the double resonance as described in section 2.4.2. It could be that a balanced feeding, e.g. two striplines with a 180° phase shift exciting the slot for each polarization, could enable a double resonant slot feeding without a degraded isolation. This would then improve the bandwidth of the design.

The plausibility of the manufacturing technique should also be investigated in reality, e.g. the element should be manufactured. Before manufacturing, the element should be fully optimized and also implemented into a sub-array. The sub-array needs to have a functioning feeding network together with real connectors, e.g. SMA-connectors. Before manufacturing a tolerance study should also be made to verify that the element can be manufactured without too much decreased performance.

Bibliography

- [1] J. Rodriguez, *Fundamentals of 5G Mobile Networks*. John Wiley & Sons, 2015.
- [2] F. Boccardi, R. W. Heath, A. Lozano, T. L. Marzetta, and P. Popovski, “Five disruptive technology directions for 5G,” *IEEE Communications Magazine*, vol. 52, no. 2, pp. 74–80, 2014.
- [3] P.-S. Kildal, *Foundations of Antenna Engineering: A Unified Approach for Line-of-sight and Multipath*. Artech House, 2015.
- [4] R. Maaskant, D. J. Bekers, M. J. Arts, W. A. van Cappellen, and M. V. Ivashina, “Evaluation of the radiation efficiency and the noise temperature of low-loss antennas,” *IEEE Antennas and Wireless Propagation Letters*, vol. 8, pp. 1166–1170, 2009.
- [5] L. B. S. Kavitha and I. J. Raglend, “A wide-scan phased array antenna for a small active electronically scanned array: a review,” in *Circuits, Power and Computing Technologies (ICCPCT), 2013 International Conference on*. IEEE, 2013, pp. 1008–1016.
- [6] “Metal core & metal back,” CiREXX, March 2017. [Online]. Available: <https://www.cirexx.com/metal-core-metal-back/>
- [7] “IMS/metal-back PCBs,” elvia Printed Circuit Boards Groupe, March 2017. [Online]. Available: <http://www.pcb-elvia.com/thermal-management/ims/>
- [8] “Pre-bond metal PCB and IMS,” BoardTek Electronics Corp, March 2017. [Online]. Available: http://www.boardtek.com.tw/EG/product_1_5.html
- [9] “Post-bonding metal PCB,” BoardTek Electronics Corp, March 2017. [Online]. Available: http://www.boardtek.com.tw/EG/product_1_6.html
- [10] “Thermal clad & metal backed printed circuit boards,” epec, March 2017. [Online]. Available: <http://www.epectec.com/pcb/thermal-clad.html>
- [11] “Aluminum PCB,” AMITRON, March 2017. [Online]. Available: <http://www.amitroncorp.com/printed-circuit-boards/aluminum.html>
- [12] “High heat circuits - PCB design for high-temperature applications,” San Francisco Circuits, March 2017. [Online]. Available: <https://www.sfcircuits.com/pcb-school/high-heat-circuits>
- [13] Y. N. Vasilenko, A. Il’inskii, and Y. Y. Kharlanov, “Cross-shaped and four-ridge waveguide—horn radiators: Internal and external character-

- istics,” *Journal of Communications Technology and Electronics*, vol. 51, no. 1, pp. 2–19, 2006.
- [14] A. Ellgardt, “Study of rectangular waveguide elements for planar wide-angle scanning phased array antennas,” in *Antennas and Propagation Society International Symposium, 2005 IEEE*, vol. 1. IEEE, 2005, pp. 815–818.
- [15] G. Tsandoulas and G. Knittel, “The analysis and design of dual-polarization square-waveguide phased arrays,” *IEEE Transactions on Antennas and Propagation*, vol. 21, no. 6, pp. 796–808, 1973.
- [16] A. H. Akgiray, “New technologies driving decade-bandwidth radio astronomy: quad-ridged flared horn and compound-semiconductor InAs,” Ph.D. dissertation, California Institute of Technology, 2013.
- [17] K. S. Packard, “The origin of waveguides: A case of multiple rediscovery,” *IEEE Transactions on Microwave Theory and Techniques*, vol. 32, no. 9, pp. 961–969, 1984.
- [18] “Ports and lumped ports for wave electromagnetics problems,” COMSOL Multiphysics, December 2016. [Online]. Available: <https://www.comsol.com/blogs/ports-and-lumped-ports-for-wave-electromagnetics-problems/>
- [19] D. M. Pozar, *Microwave engineering*. John Wiley & Sons, 2009.
- [20] C. C. Chen, N. Wong, and R. Tang, “Ultra-wideband phased arrays,” DTIC Document, Tech. Rep., 1973.
- [21] A. D. Olver, P. J. Clarricoats, A. A. Kishk, and L. Shafai, *Microwave horns and feeds*, ser. Electromagnetic Waves. IET, 1994, vol. 39.
- [22] C. A. Balanis, *Antenna theory: analysis and design*. John Wiley & Sons, 2005.
- [23] C.-C. Chen, “Wideband wide-angle impedance matching and polarization characteristics of circular waveguide phased arrays,” *IEEE Transactions on Antennas and Propagation*, vol. 22, no. 3, pp. 414–418, 1974.
- [24] W. Sun and C. A. Balanis, “Analysis and design of quadruple-ridged waveguides,” *IEEE Transactions on microwave theory and techniques*, vol. 42, no. 12, pp. 2201–2207, 1994.
- [25] W. Sun and C. Balanis, “Analysis of double-or quadruple-ridged waveguides by a magnetic surface integral equation approach,” in *Antennas and Propagation Society International Symposium, 1993. AP-S. Digest. IEEE*, 1993, pp. 181–184.
- [26] N. Amitay and V. Galindo, “The analysis of circular waveguide phased arrays,” *Bell System Technical Journal*, vol. 47, no. 9, pp. 1903–1932, 1968.
- [27] —, “Characteristics of dielectric loaded and covered circular waveguide phased arrays,” *IEEE Transactions on Antennas and Propagation*, vol. 17, no. 6, pp. 722–729, 1969.
- [28] L. Lewis, L. Kaplan, and J. Hanfling, “Synthesis of a waveguide phased array element,” *IEEE Transactions on Antennas and Propagation*, vol. 22, no. 4, pp. 536–540, 1974.

- [29] E. Magill and H. Wheeler, "Wide-angle impedance matching of a planar array antenna by a dielectric sheet," *IEEE Transactions on Antennas and Propagation*, vol. 14, no. 1, pp. 49–53, 1966.
- [30] R. G. Schmier and M. J. Buckley, "Broadband circular waveguide radiating element for use in phased array antennas," in *Antennas and Propagation Society International Symposium, 1994. AP-S. Digest*, vol. 2. IEEE, 1994, pp. 1236–1239.
- [31] A. J. Sangster and J. Grant, "Mode degeneracy in circular cylindrical ridge waveguides," *Progress In Electromagnetics Research Letters*, vol. 9, pp. 75–83, 2009.
- [32] M. Chen and G. Tsandoulas, "Bandwidth properties of quadruple-ridged circular and square waveguide radiators," in *1973 Antennas and Propagation Society International Symposium*, vol. 11. IEEE, 1973, pp. 391–394.
- [33] M. Chen, G. Tsandoulas, and F. Willwerth, "Modal characteristics of quadruple-ridged circular and square waveguides (short papers)," *IEEE Transactions on Microwave Theory and Techniques*, vol. 22, no. 8, pp. 801–804, 1974.
- [34] A. Sangster and J. Grant, "Dual-mode quadruple ridge waveguide feed for broadband satellite communications," *International Journal of Electronics*, vol. 100, no. 6, pp. 793–802, 2013.
- [35] P. DALY, "Cut-off frequencies of quad-ridged waveguides used in the design of microwave circular-polarisers," *COMPEL-The international journal for computation and mathematics in electrical and electronic engineering*, vol. 4, no. 1, pp. 43–53, 1985.
- [36] A. Ellgardt, "Wide-angle scanning wide-band phased array antennas," Ph.D. dissertation, KTH, 2009.
- [37] J. Montgomery, "Ridged waveguide phased array elements," *IEEE Transactions on Antennas and Propagation*, vol. 24, no. 1, pp. 46–53, 1976.
- [38] Y. Rong and K. A. Zaki, "Characteristics of generalized rectangular and circular ridge waveguides," *IEEE Transactions on Microwave Theory and Techniques*, vol. 48, no. 2, pp. 258–265, 2000.
- [39] J. Lee and R.-S. Chu, "Aperture matching of a dielectric loaded circular waveguide element array," *IEEE transactions on antennas and propagation*, vol. 37, no. 3, pp. 395–399, 1989.
- [40] R. E. Collin, *Foundations for microwave engineering*. John Wiley & Sons, 2007.
- [41] B. C. Wadell, *Transmission line design handbook*. Artech House, 1991.
- [42] N. Behdad and K. Sarabandi, "A novel approach for bandwidth enhancement of slot antennas," DTIC Document, Tech. Rep., 2003.
- [43] —, "A wide-band slot antenna design employing a fictitious short circuit concept," *IEEE Transactions on antennas and Propagation*, vol. 53, no. 1, pp. 475–482, 2005.
- [44] R. Paryani, "Design of a wideband dual-polarized cavity backed slot antenna," University of Central Florida, Tech. Rep., 2010.

- [45] R. C. Paryani, P. F. Wahid, and N. Behdad, "A wideband, dual-polarized, substrate-integrated cavity-backed slot antenna," *IEEE Antennas and Wireless Propagation Letters*, vol. 9, pp. 645–648, 2010.
- [46] R. J. Mailloux, *Phased array antenna handbook*. Artech House Boston, 2005, vol. 2.
- [47] M. Ivashina and C. v. Klooster, "Focal fields in reflector antennas and associated array feed synthesis for high efficiency multi-beam performances," *TIJDSCHRIFT-NERG*, vol. 68, no. 1, pp. 11–19, 2003.
- [48] M. V. Ivashina, O. Iupikov, R. Maaskant, W. A. van Cappellen, and T. Oosterloo, "An optimal beamforming strategy for wide-field surveys with phased-array-fed reflector antennas," *IEEE Transactions on Antennas and Propagation*, vol. 59, no. 6, pp. 1864–1875, 2011.
- [49] C. Bencivenni, M. Ivashina, R. Maaskant, and J. Wettergren, "Synthesis of maximally sparse arrays using compressive sensing and full-wave analysis for global earth coverage applications," *IEEE Transactions on Antennas and Propagation*, vol. 64, no. 11, pp. 4872–4877, 2016.
- [50] A. Ellgardt and M. Norgren, "A study of edge effects in triangular grid tapered-slot arrays using coupling coefficients," *Radio Science*, vol. 45, no. 2, 2010.
- [51] K. Wu, D. Deslandes, and Y. Cassivi, "The substrate integrated circuits—a new concept for high-frequency electronics and optoelectronics," in *Telecommunications in Modern Satellite, Cable and Broadcasting Service, 2003. TELSIKS 2003. 6th International Conference on*, vol. 1. IEEE, 2003, pp. P–III.
- [52] *RO4000® Series High Frequency Circuit Materials datasheet*, Rogers Corporation, March 2012.
- [53] *RO4400™ Series Bondply Data Sheet*, Rogers Corporation, November 1997.
- [54] H. Kellerer, U. Pferschy, and D. Pisinger, "Knapsack problems. 2004."

A

Knapsack Problem: Matlab code

```
1  %%%%%%%%%% CONSTANTS %%%%%%%%%%
2
3  mu0 = (pi)/(2500000); %permeability
4  eps0 = (625000)/(22468879468420441*pi); %permittivity
5  c0 = 1 / sqrt(mu0*eps0);
6  f0 = 15*10^9;
7  lambda0 = c0/f0;
8  eps_rel = 3.66;
9  lambda_g = lambda0./sqrt(eps_rel);
10 Goal = lambda_g./4 * 10^(3);
11
12 Thickness = [0.168, 0.254, 0.338, 0.422, 0.508,
               0.762, 1.524];
13 glue = 0.101;
14 GlueAndThickness = Thickness + glue;
15
16 %%%%%%%%%% INITIATE VARIABLES %%%%%%%%%%
17
18 n = [0,0,0,0,0,0,0,0];
19 best = [];
20 best(1) = Goal - dot(GlueAndThickness,[0 0 0 0 0 0 3
    0] );
21 nBest = [];
22 nBest(1,:) = [0 0 0 0 0 0 3 0];
23
24 %% CHECK DIFFERENT CONFIGURATIONS
25 index = 1;
26 for n1 = 0:4
27     for n2 = 0:4
28         for n3 = 0:4
29             for n4 = 0:4
30                 for n5 = 0:4
31                     for n6 = 0:4
32                         for n7 = 0:2
```

```
33         n = [n1 n2 n3 n4 n5 n6 n7
34              ];
35         test = Goal - dot(n,
36                          GlueAndThickness);
37         if abs(test) < abs(best
38             (1))
39             if sum(n) <= 4
40                 index = index +1;
41                 nBest(index,:) =
42                     n;
43                 best(index) =
44                     test;
45             end
46         end
47     end
48 end
```

B

Parametric Study of Stripline Fed Dielectric Element: Impedance

The impedance variations of the parameters from the parametric study of the stripline fed waveguide filled with dielectric material.

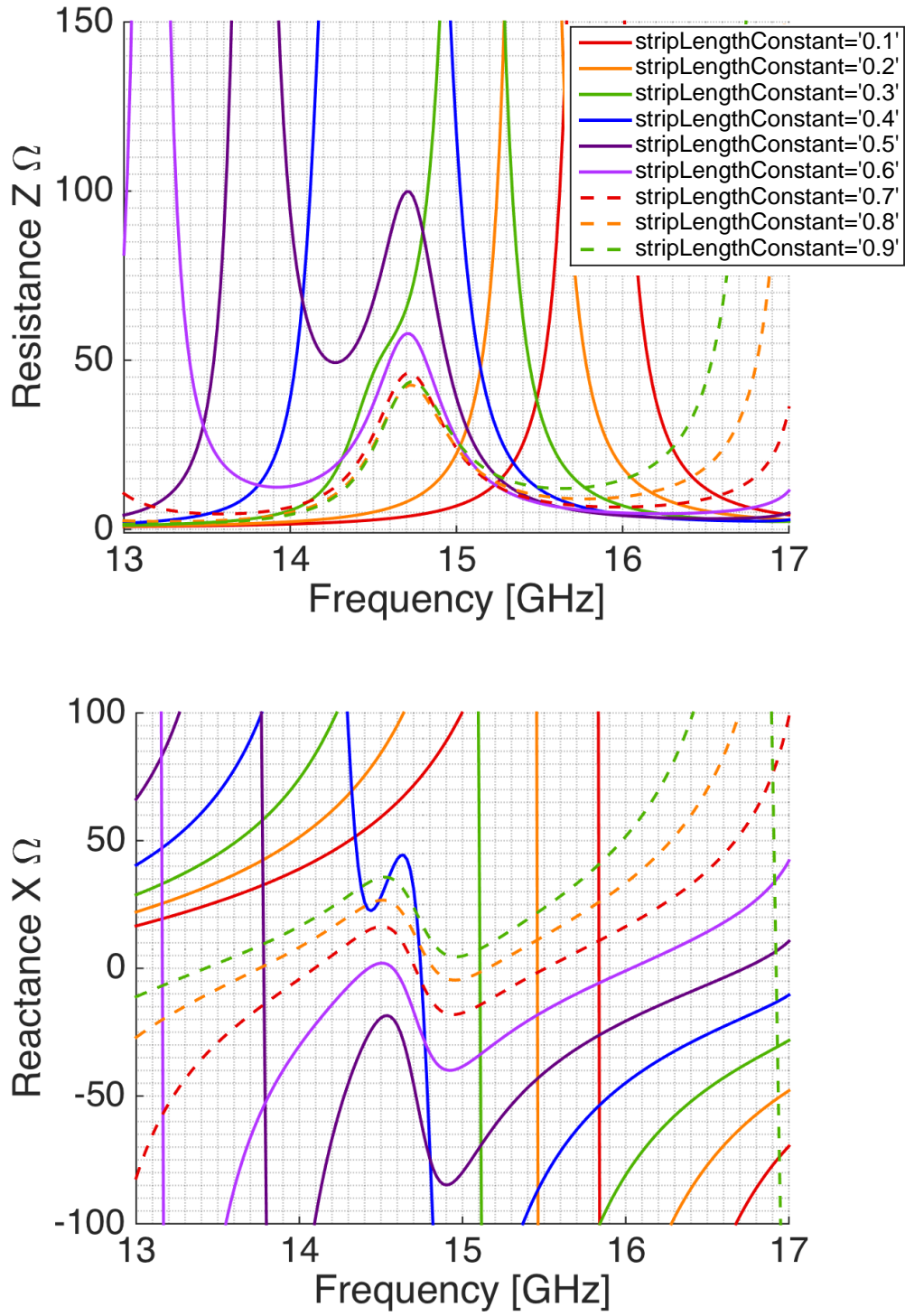


Figure B.1: Impedance variations from the parametric study of different stripline lengths in parts of the waveguide radius for the waveguide filled with dielectric material and excited by a stripline. The other design parameters had the starting values listed in table 3.4.

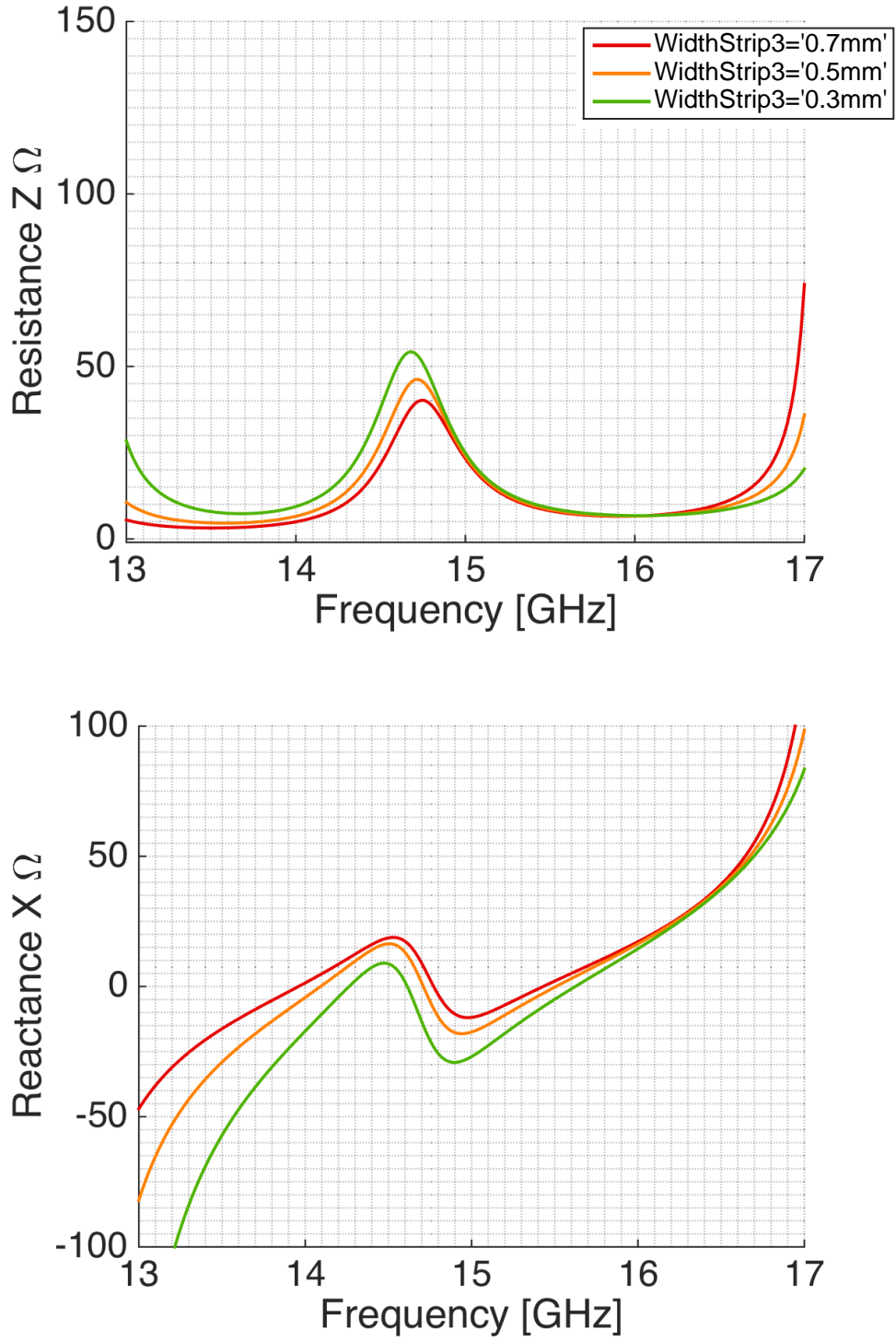


Figure B.2: Impedance variations from the parametric study of different stripline widths for the waveguide filled with dielectric material and excited by a stripline. The other design parameters had the starting values listed in table 3.4.

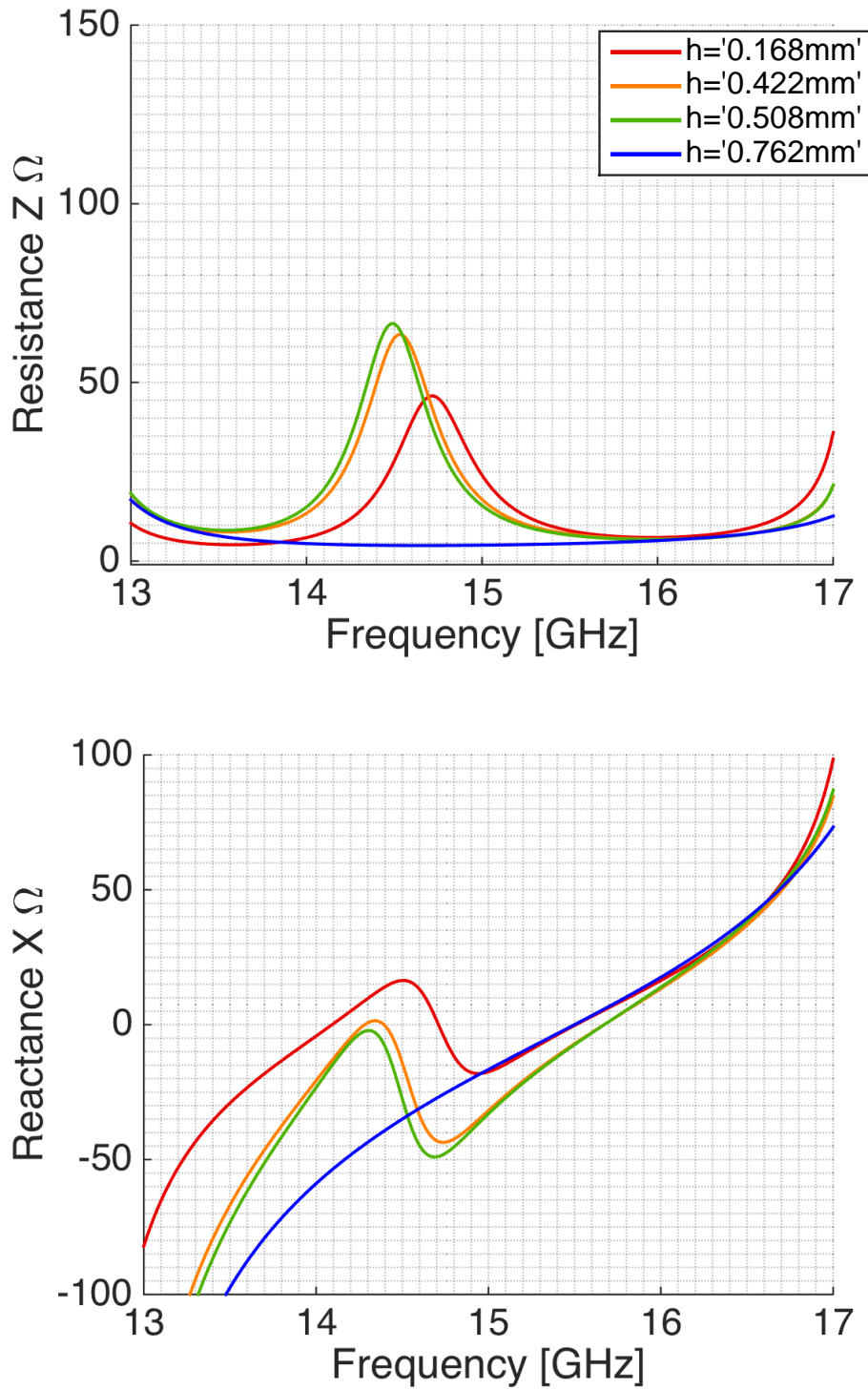


Figure B.3: Impedance variations from the parametric study of different upper substrate heights h_2 for the waveguide filled with dielectric material and excited by a stripline. The other design parameters had the starting values listed in table 3.4.

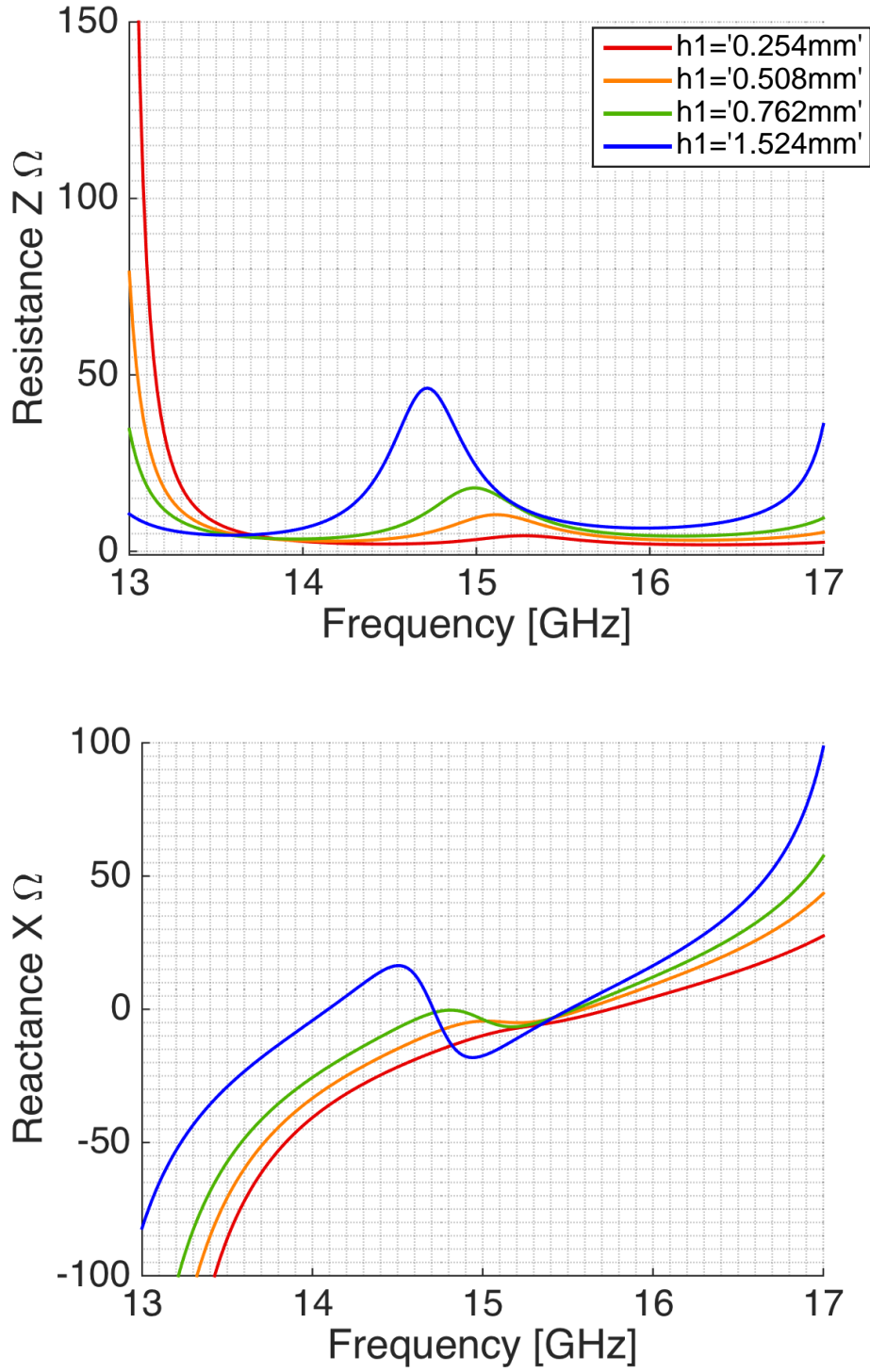


Figure B.4: Impedance variations from the parametric study of different lower substrate heights h_1 for the waveguide filled with dielectric material and excited by a stripline. The other design parameters had the starting values listed in table 3.4.

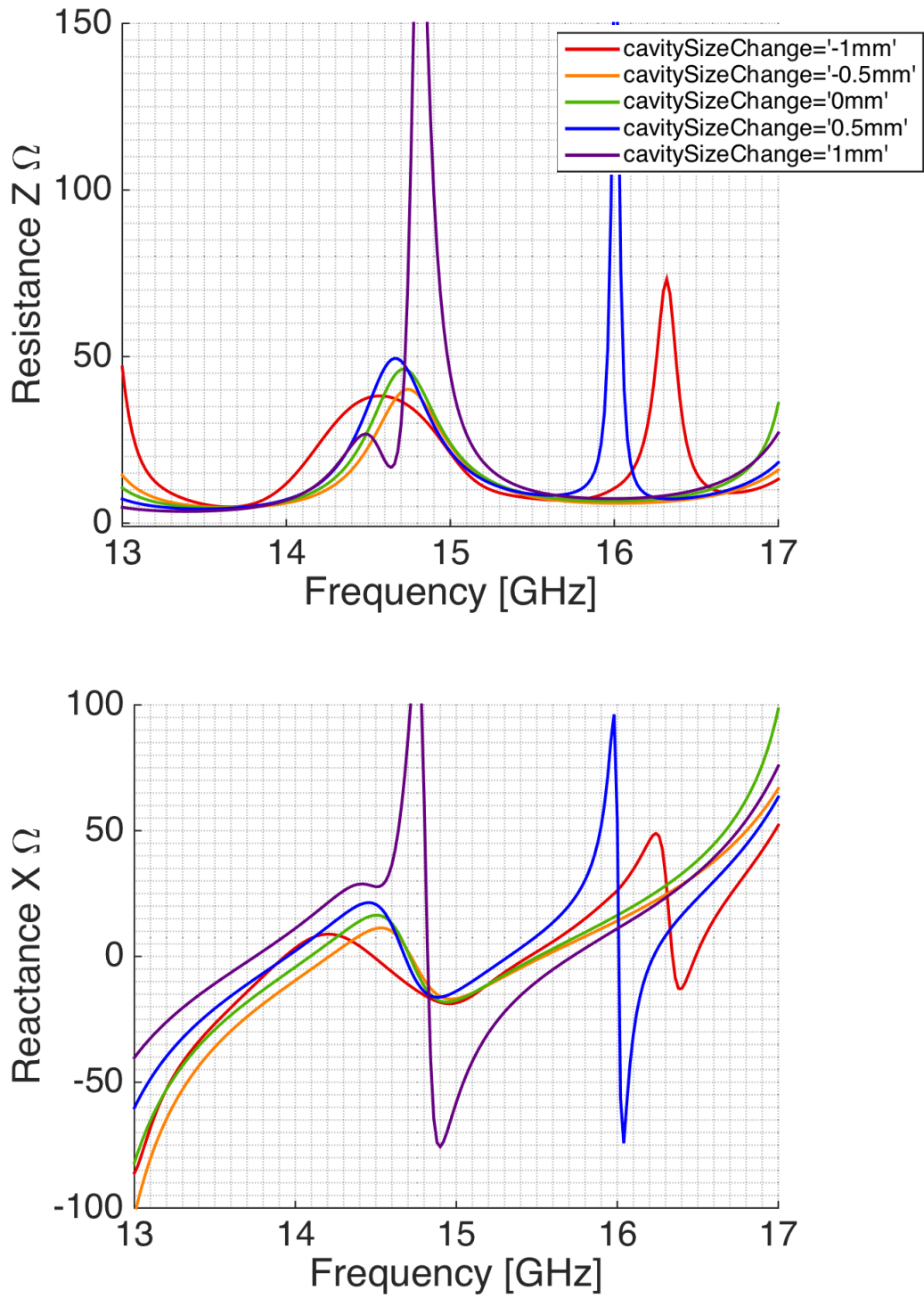


Figure B.5: Impedance variations from the parametric study of different sizes of the cavity (size change from waveguide radius) for the waveguide filled with dielectric material and excited by a stripline. The other design parameters had the starting values listed in table 3.4.

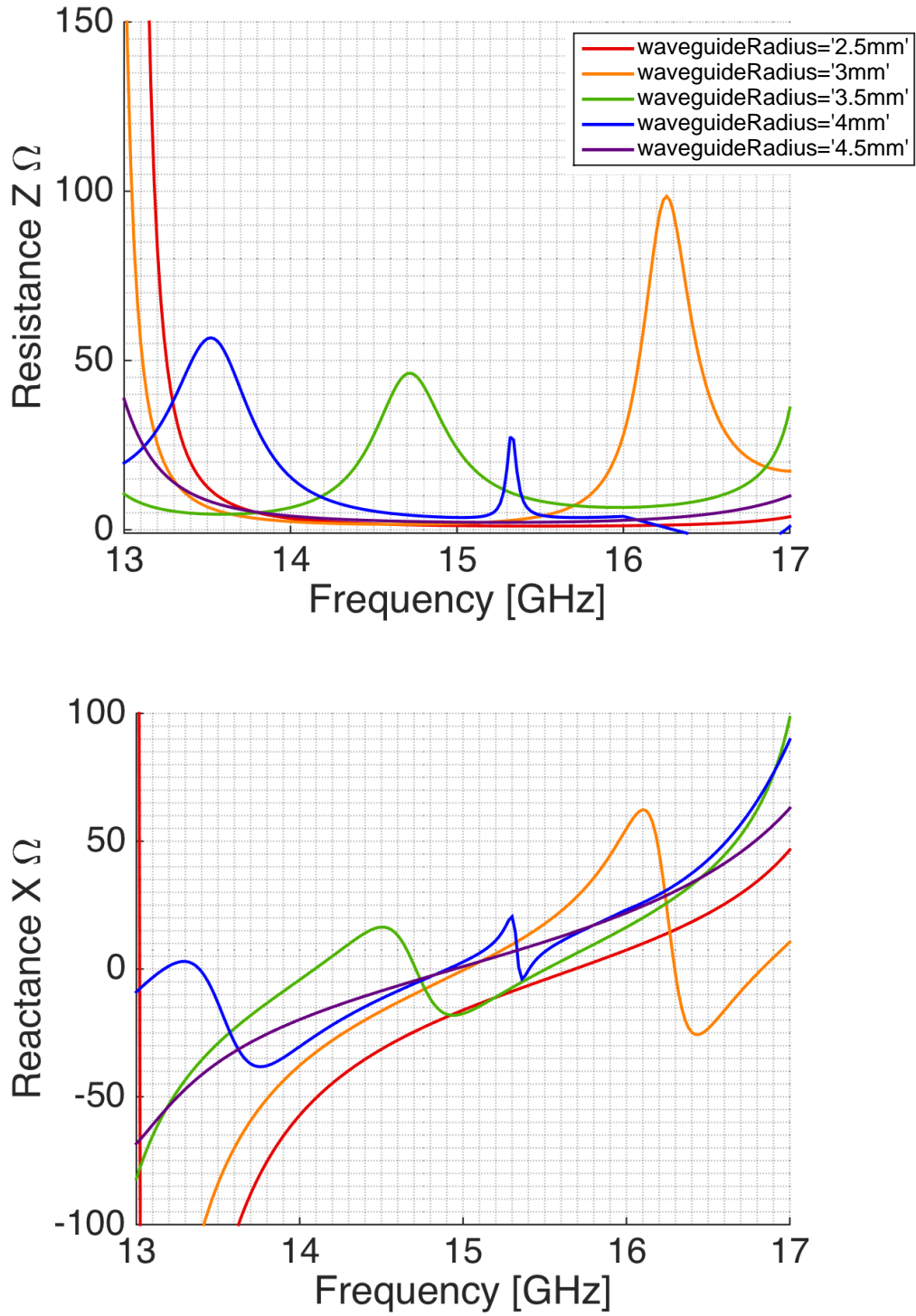


Figure B.6: Impedance variations from the parametric study of different radii of the waveguide for the waveguide filled with dielectric material and excited by a stripline. The other design parameters had the starting values listed in table 3.4.

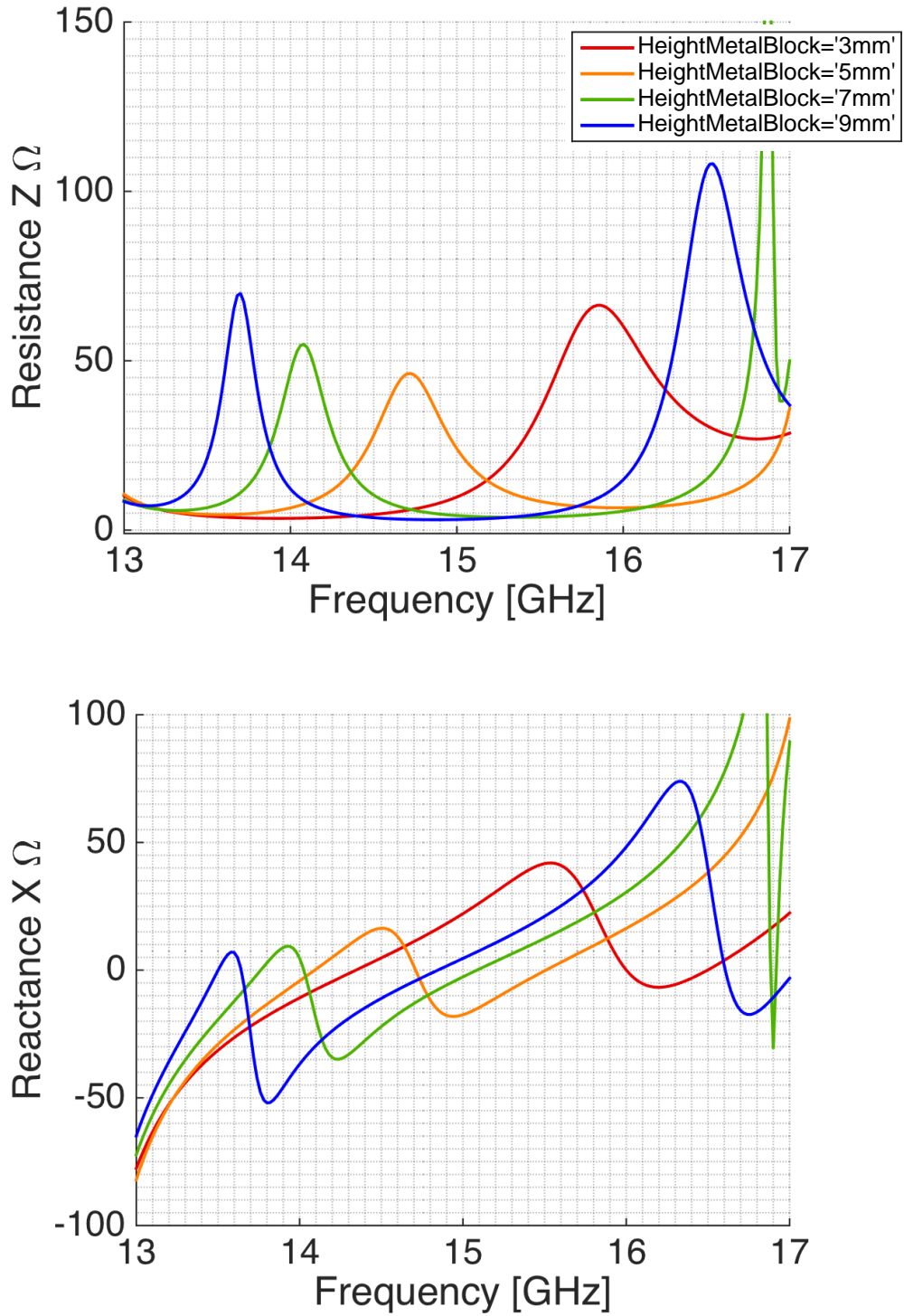


Figure B.7: Impedance variations from the parametric study of different heights of the waveguide h_{metal} for the waveguide filled with dielectric material and excited by a stripline. The other design parameters had the starting values listed in table 3.4.

C

Parametric Study of Slot Coupled Dielectric Element: Impedance

The impedance variations of the parameters from the parametric study of the slot coupled fed waveguide filled with dielectric material.

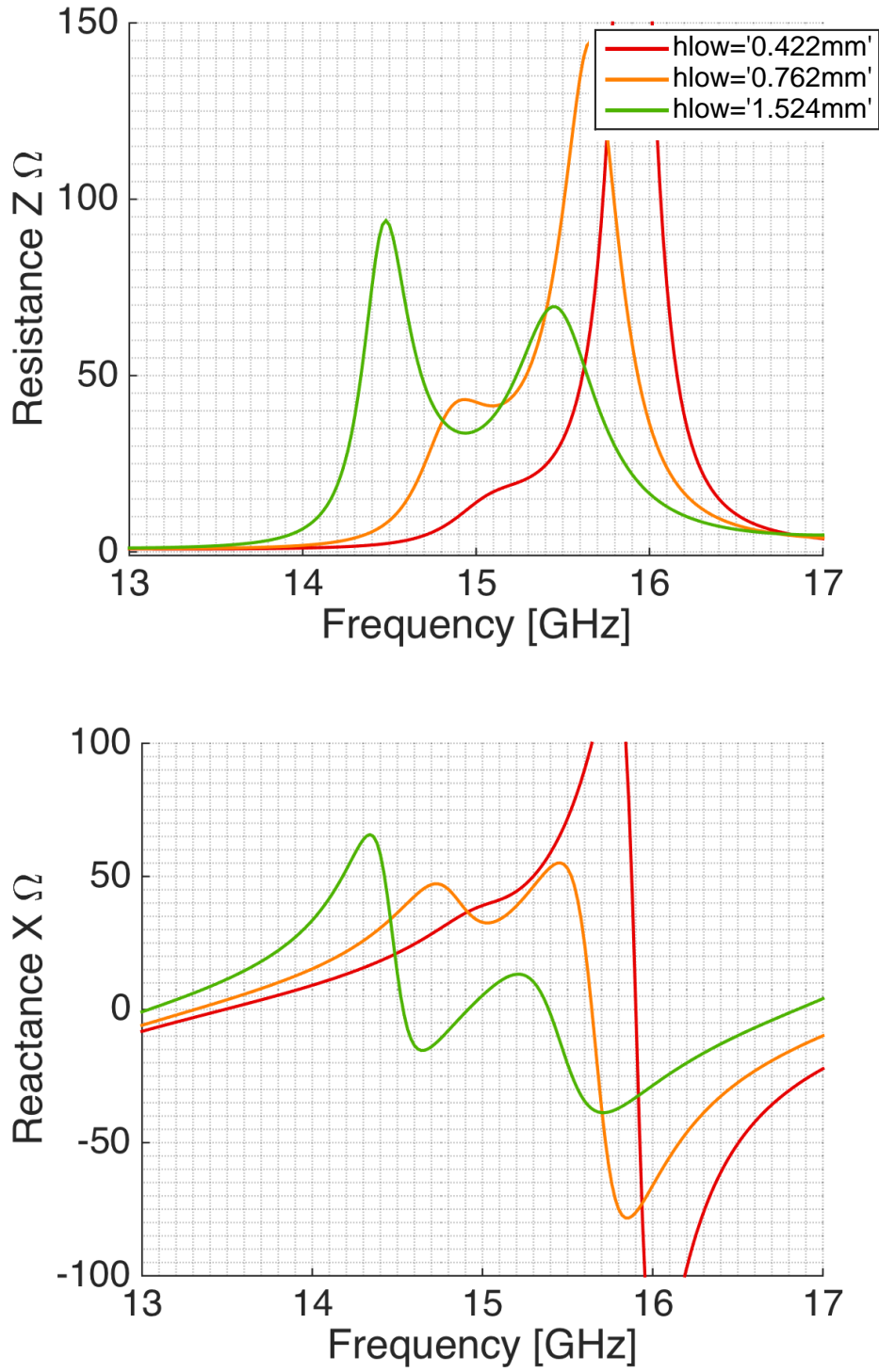


Figure C.1: Impedance variations from the parametric study of different heights of the lower substrate h_1 for port 1 for the waveguide filled with dielectric material and excited by a slot. The other design parameters had the starting values listed in table 3.5.

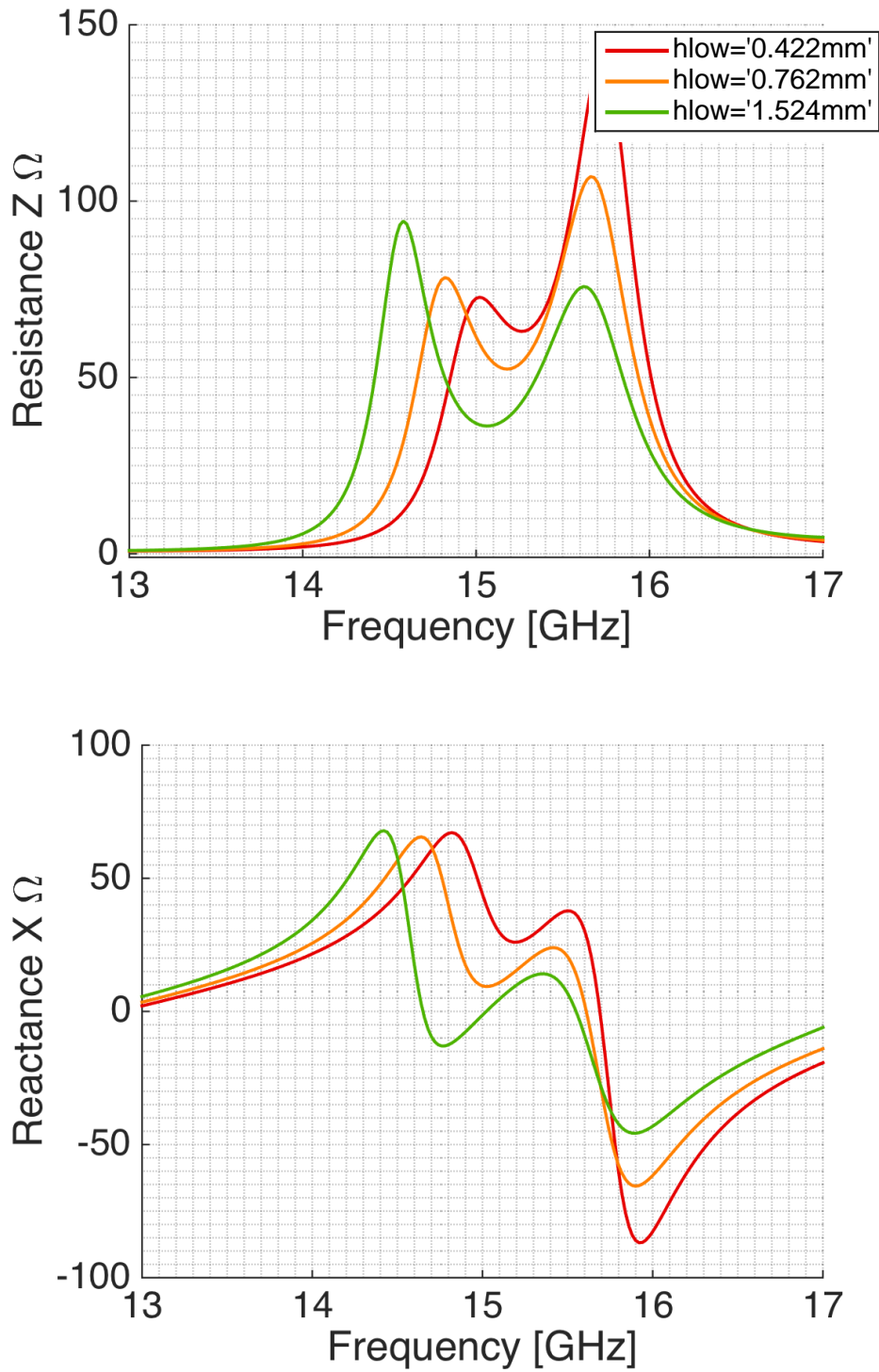


Figure C.2: Impedance variations from the parametric study of different heights of the lower substrate h_1 for port 2 for the waveguide filled with dielectric material and excited by a slot. The other design parameters had the starting values listed in table 3.5.

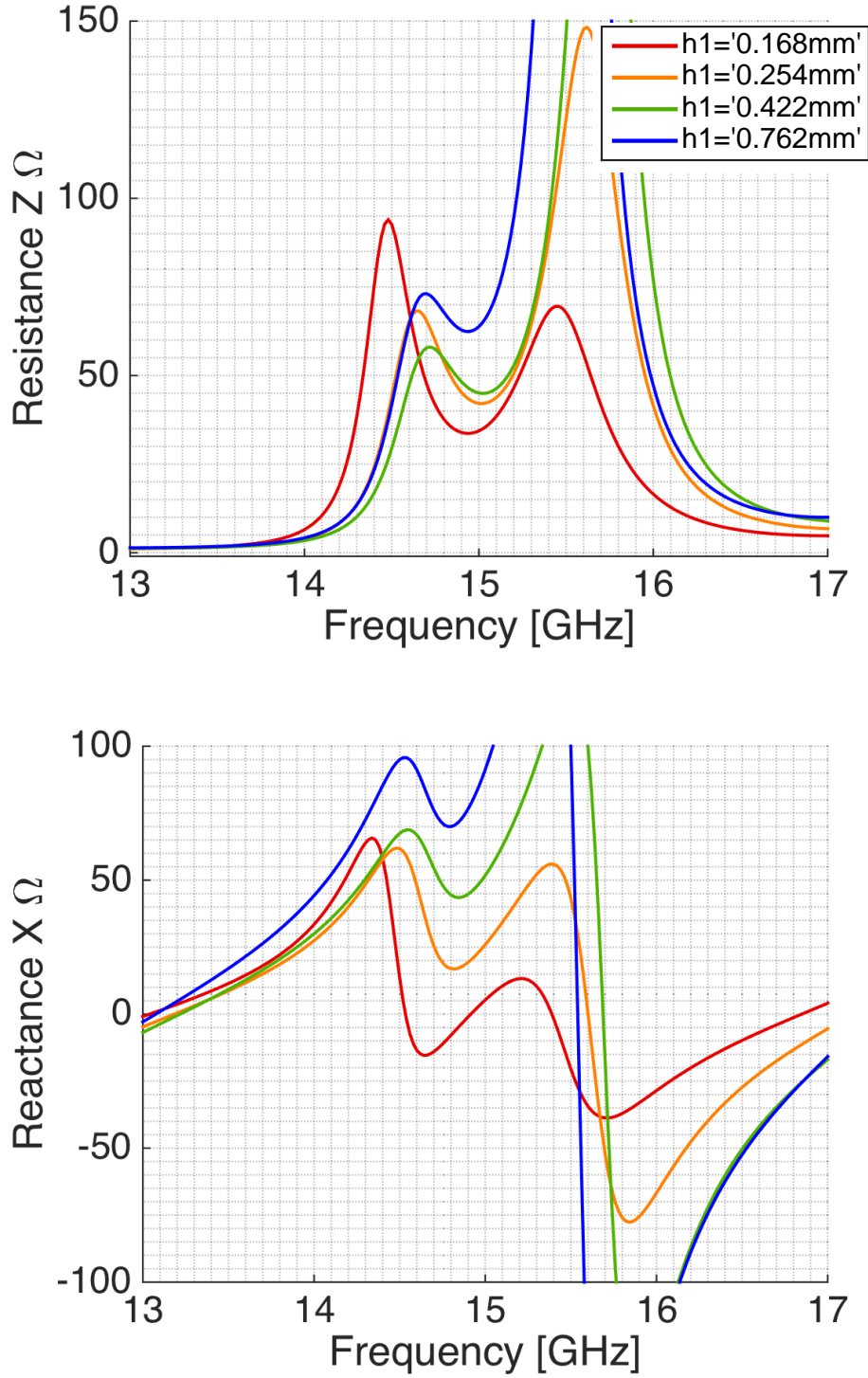


Figure C.3: Impedance variations from the parametric study of different heights of the lower substrate h_2 for port 1 for the waveguide filled with dielectric material and excited by a slot. The other design parameters had the starting values listed in table 3.5.

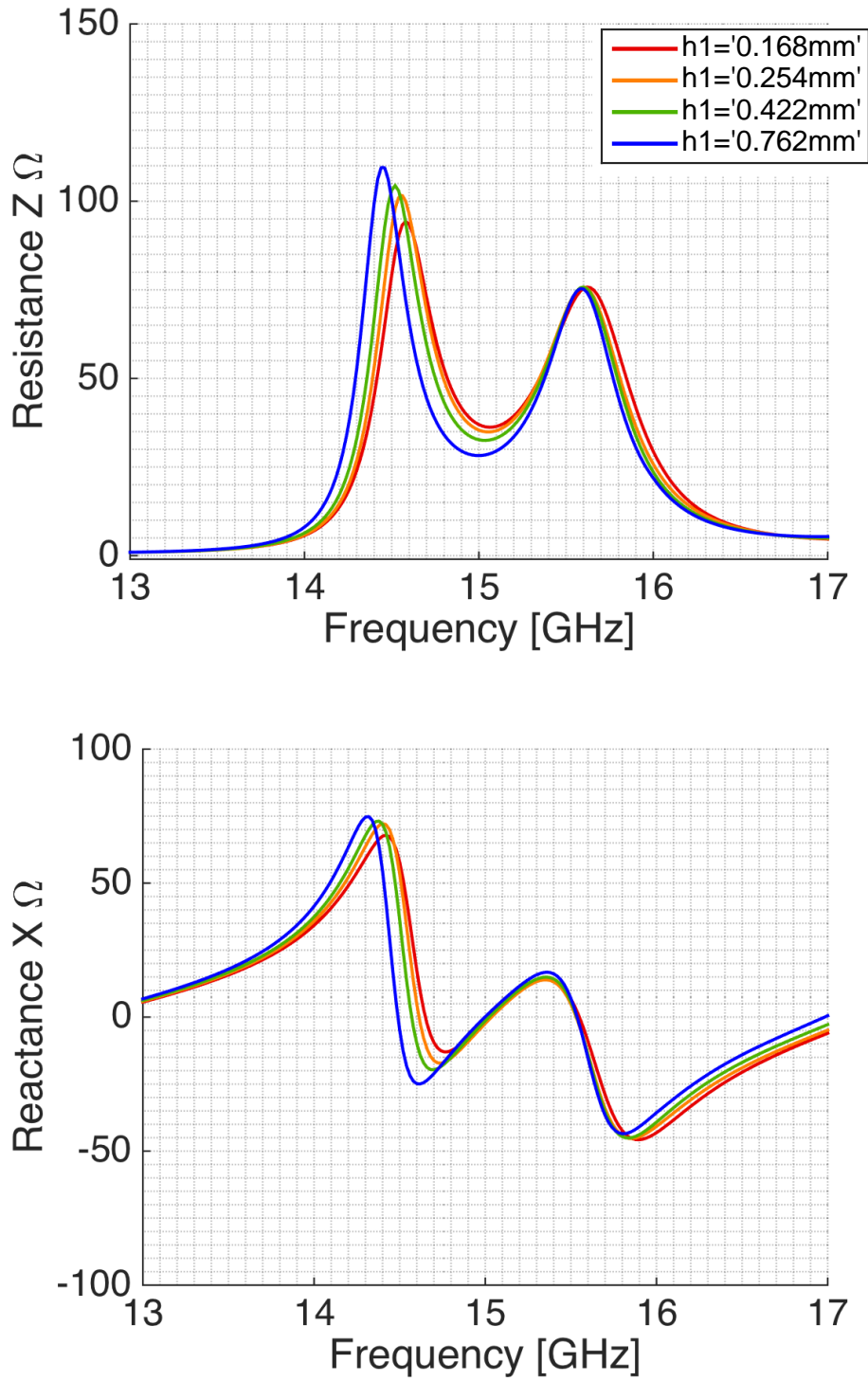


Figure C.4: Impedance variations from the parametric study of different heights of the lower substrate h_2 for port 2 for the waveguide filled with dielectric material and excited by a slot. The other design parameters had the starting values listed in table 3.5.

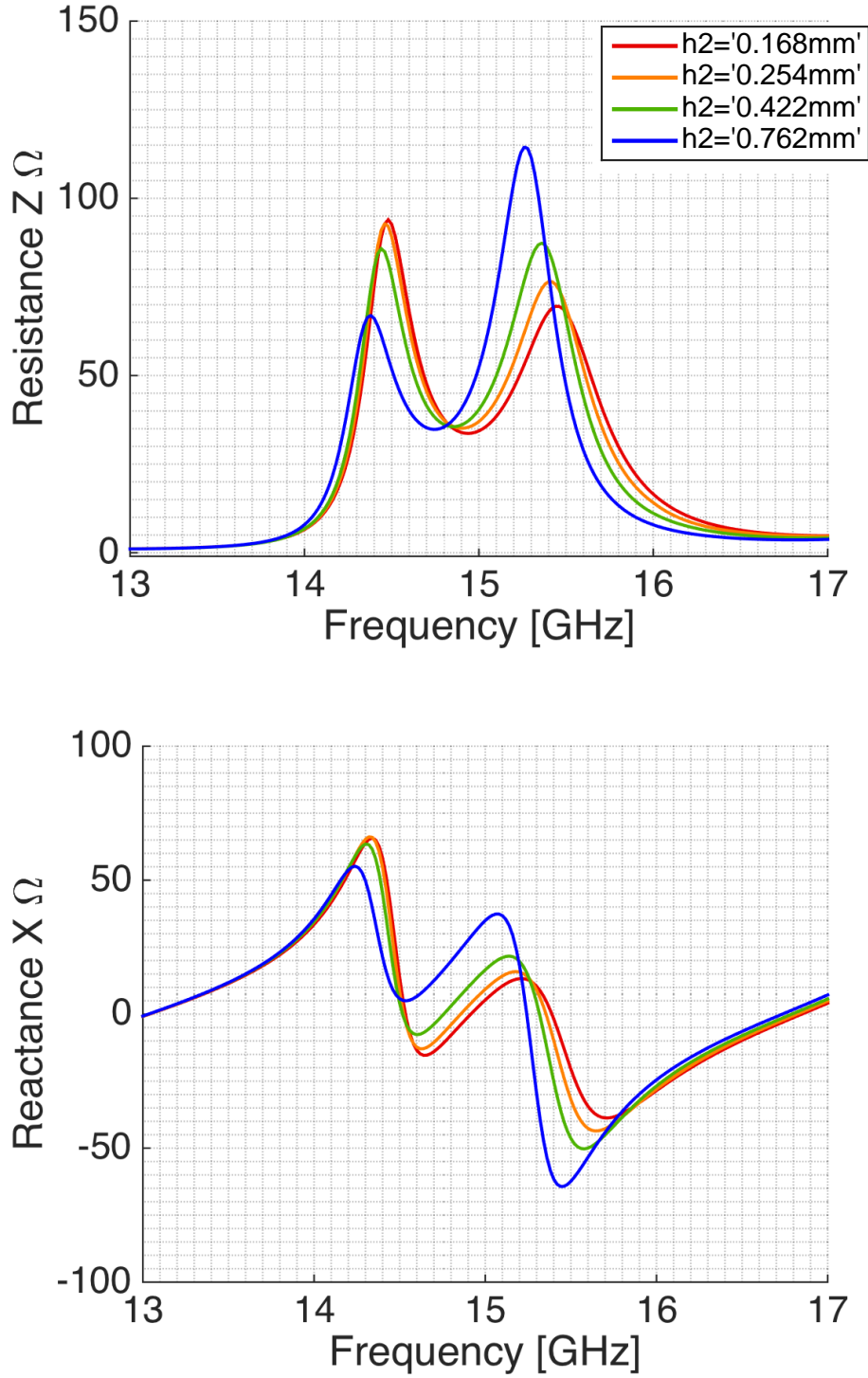


Figure C.5: Impedance variations from the parametric study of different heights of the lower substrate h_3 for port 1 for the waveguide filled with dielectric material and excited by a slot. The other design parameters had the starting values listed in table 3.5.

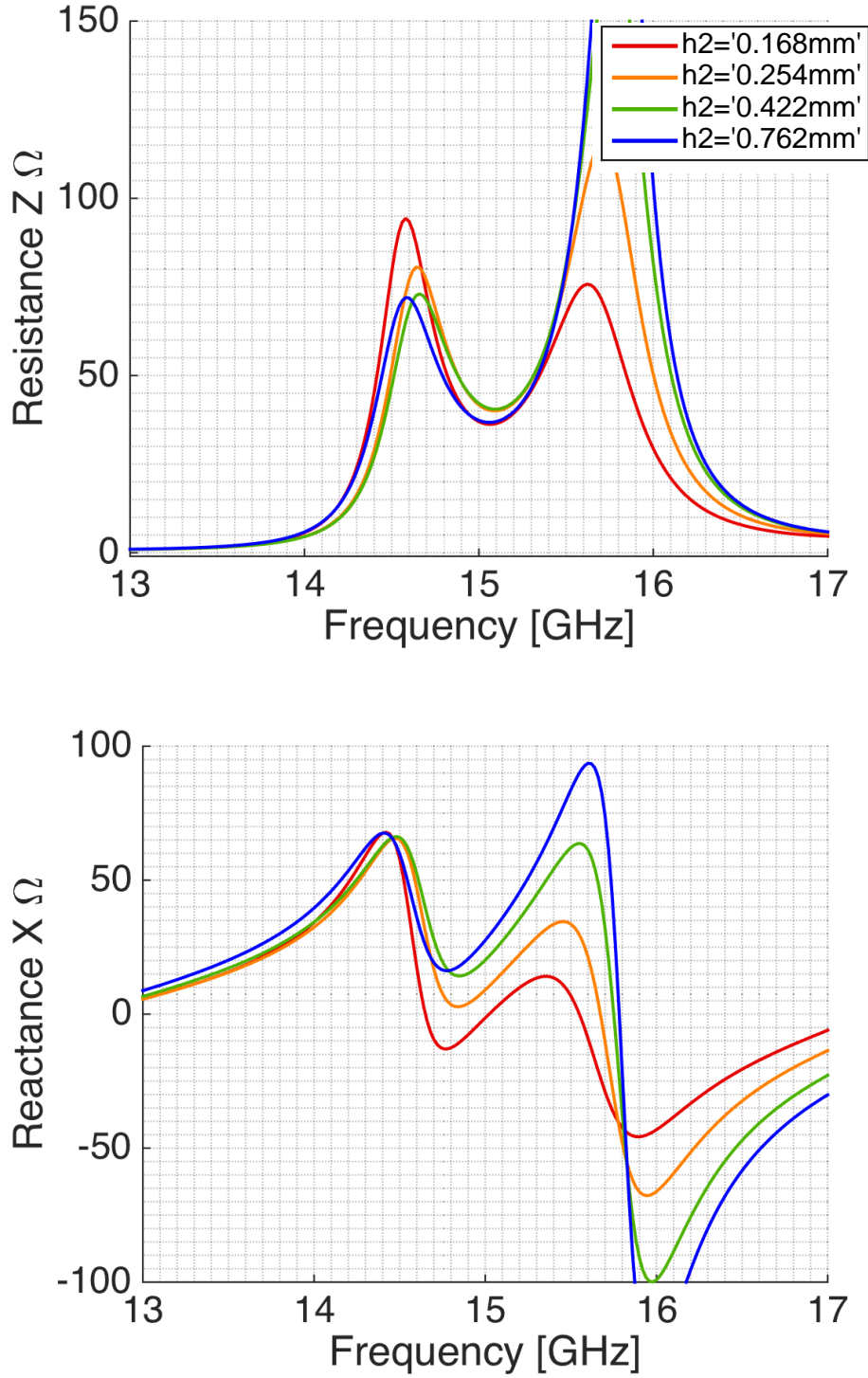


Figure C.6: Impedance variations from the parametric study of different heights of the lower substrate h_3 for port 2 for the waveguide filled with dielectric material and excited by a slot. The other design parameters had the starting values listed in table 3.5.

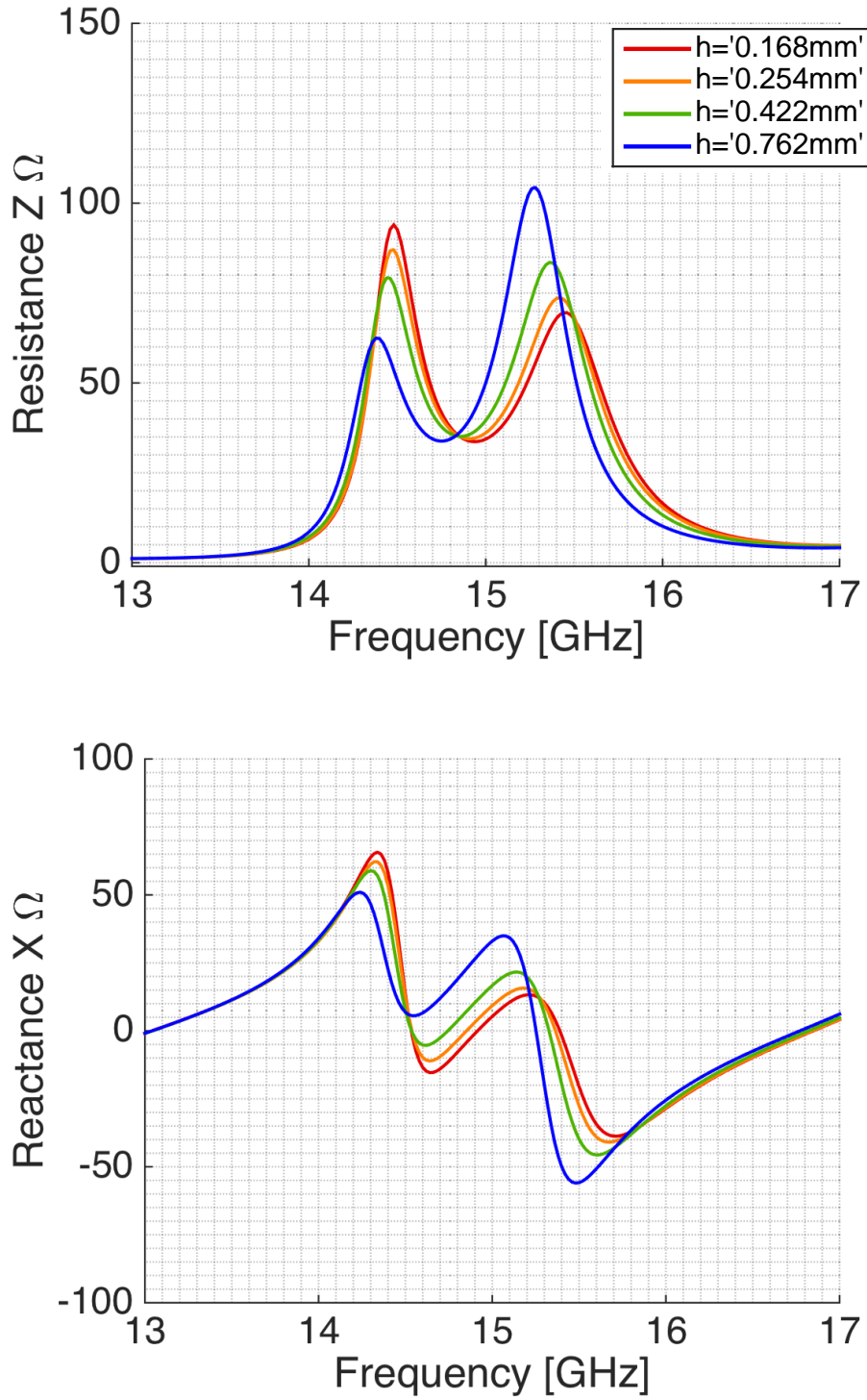


Figure C.7: Impedance variations from the parametric study of different heights of the lower substrate h_4 for port 1 for the waveguide filled with dielectric material and excited by a slot. The other design parameters had the starting values listed in table 3.5.

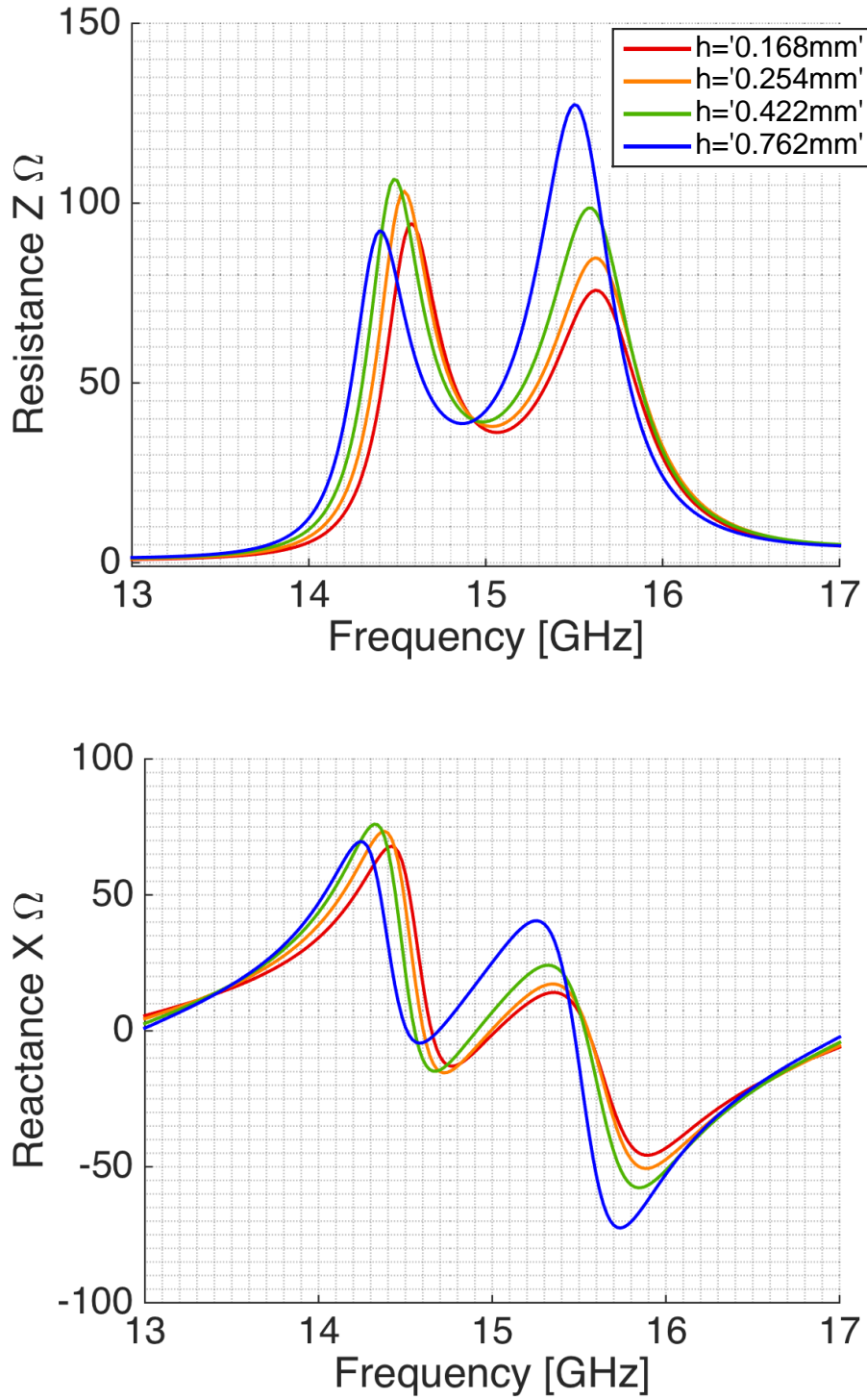


Figure C.8: Impedance variations from the parametric study of different heights of the lower substrate h_4 for port 2 for the waveguide filled with dielectric material and excited by a slot. The other design parameters had the starting values listed in table 3.5.

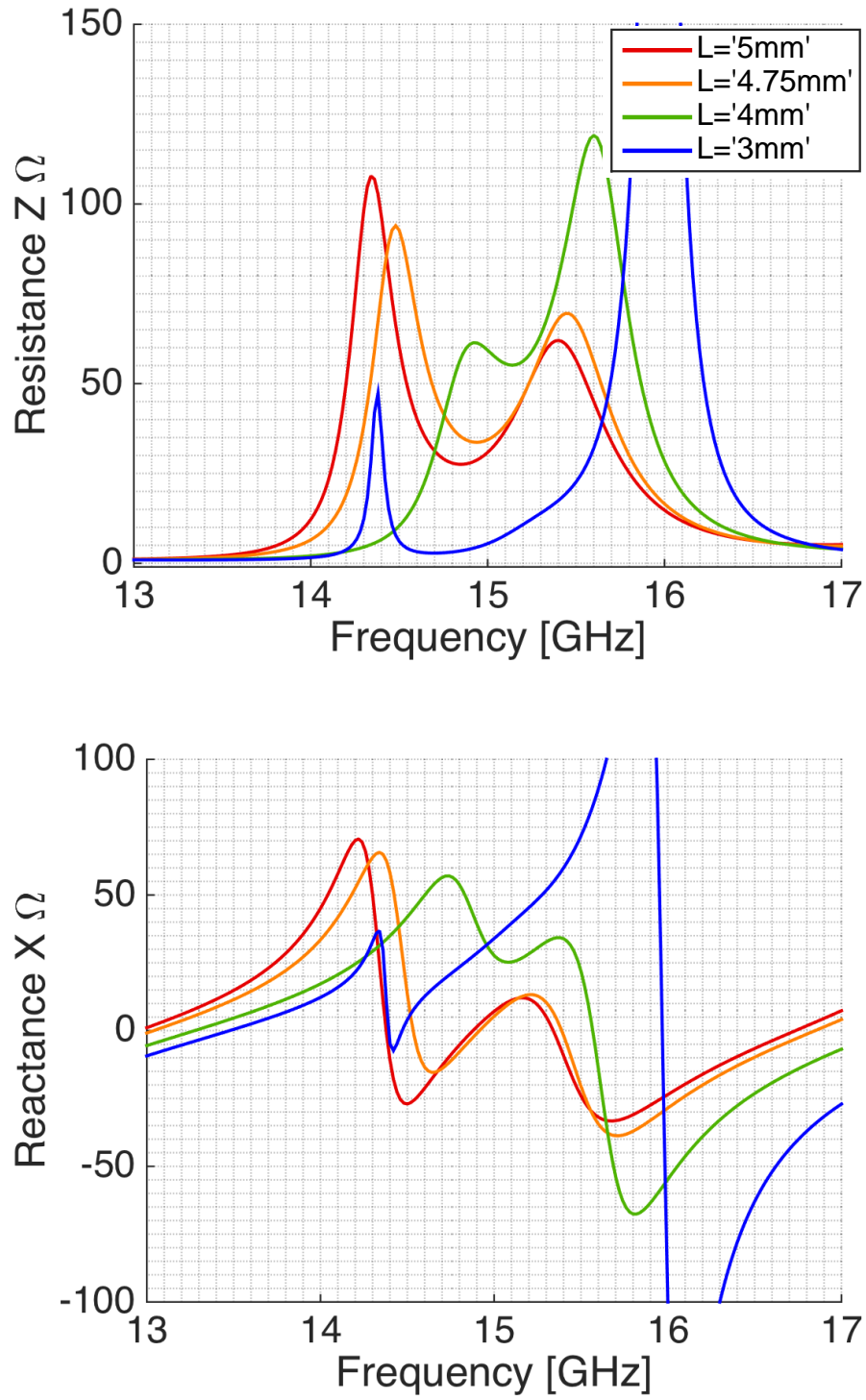


Figure C.9: Impedance variations from the parametric study of different slot lengths L for port 1 for the waveguide filled with dielectric material and excited by a slot. The other design parameters had the starting values listed in table 3.5.

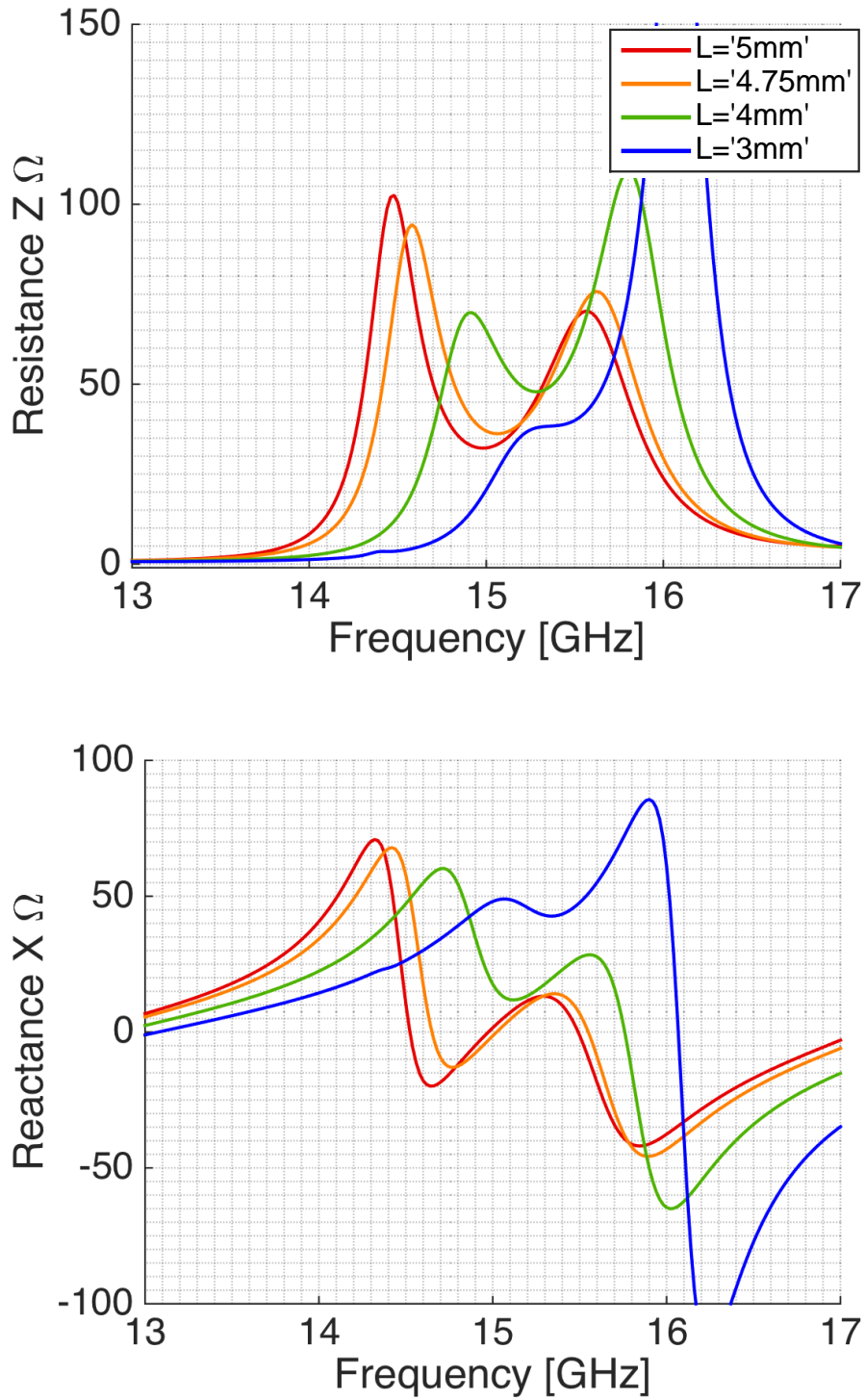


Figure C.10: Impedance variations from the parametric study of different slot lengths L for port 2 for the waveguide filled with dielectric material and excited by a slot. The other design parameters had the starting values listed in table 3.5.

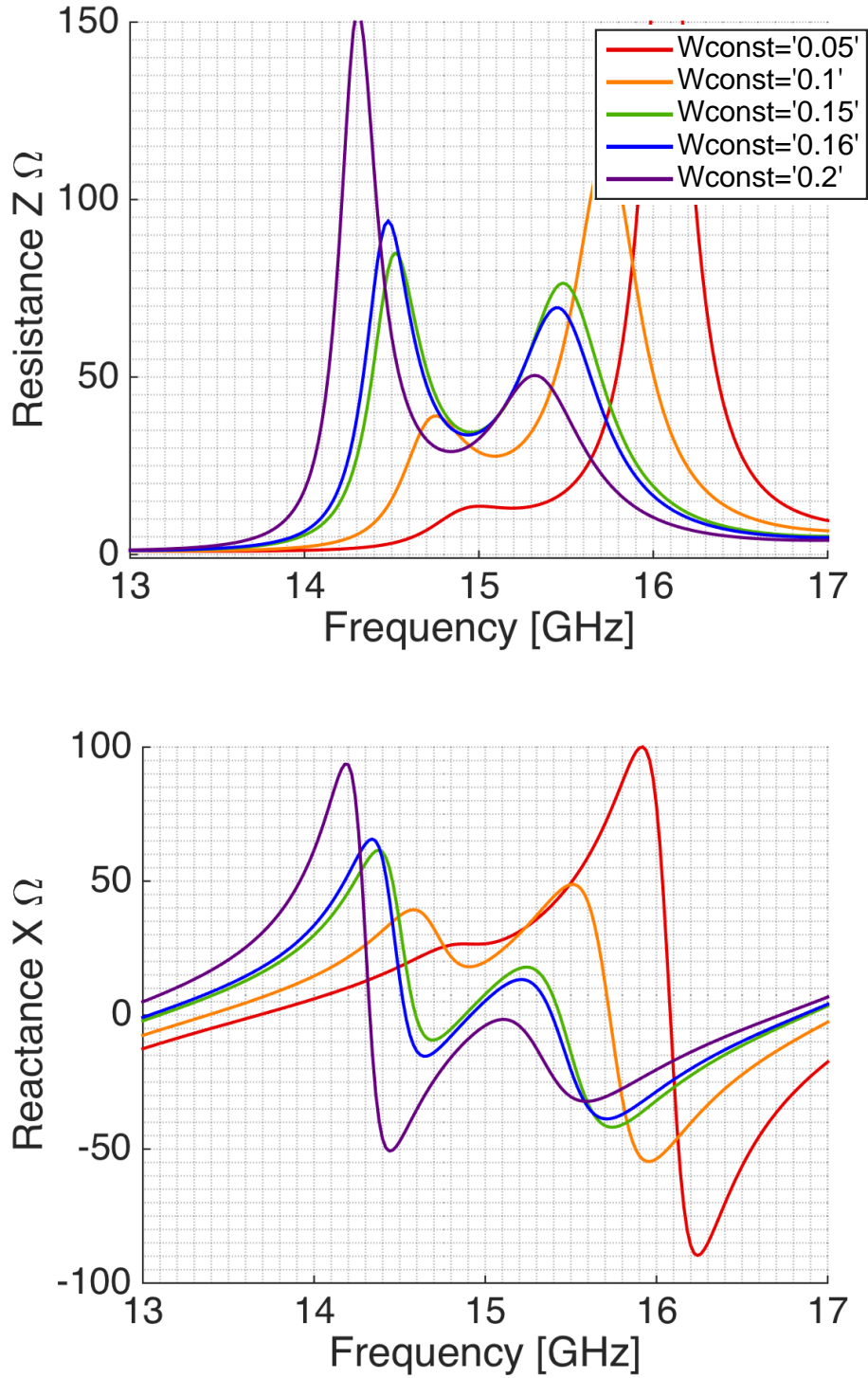


Figure C.11: Impedance variations from the parametric study of different slot widths W for port 1 (port 2 shows the same behavior) for the waveguide filled with dielectric material and excited by a slot. The other design parameters had the starting values listed in table 3.5.

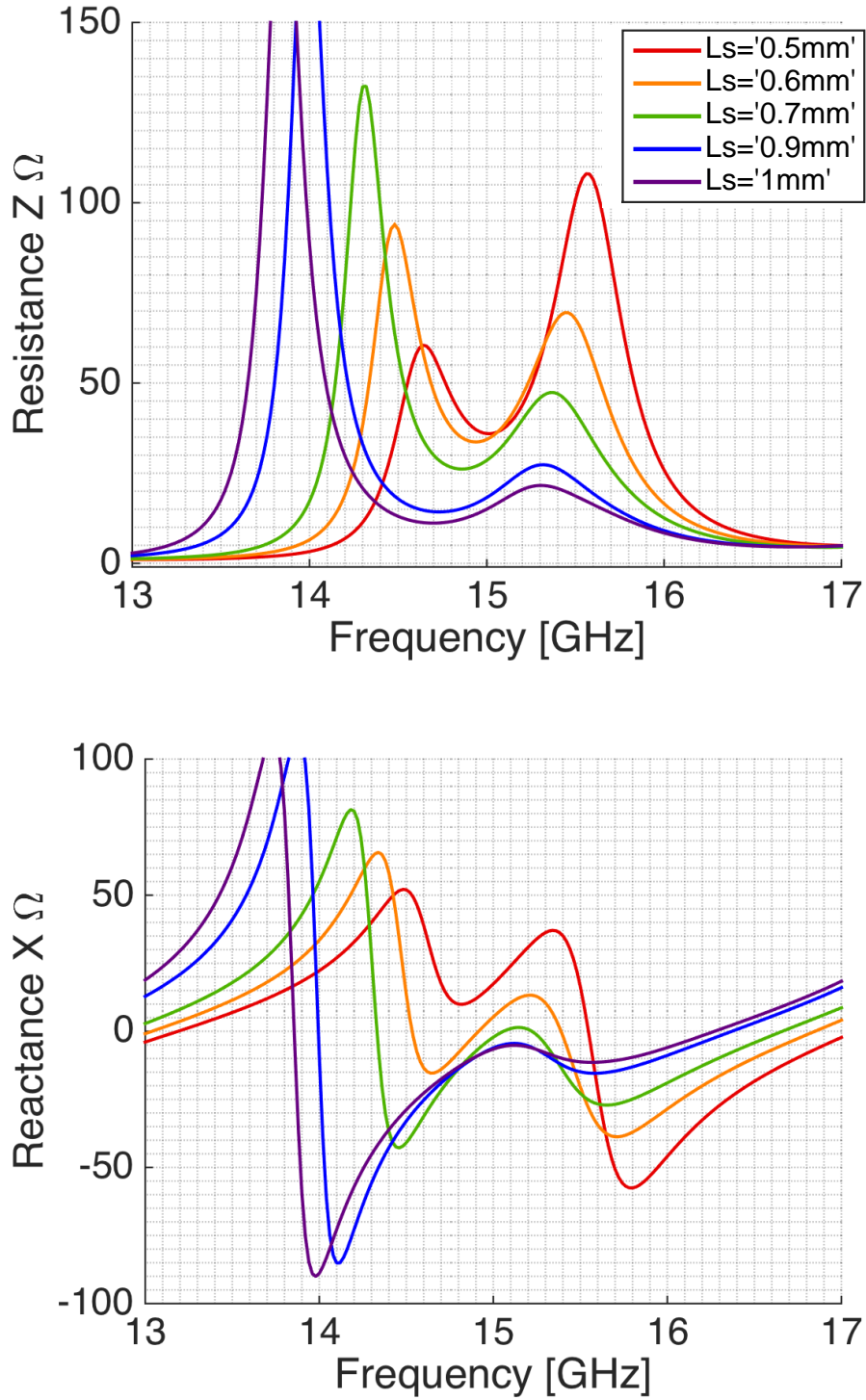


Figure C.12: Impedance variations from the parametric study of different stripline placements L_s for port 1 (port 2 shows the same behavior) for the waveguide filled with dielectric material and excited by a slot. The other design parameters had the starting values listed in table 3.5.

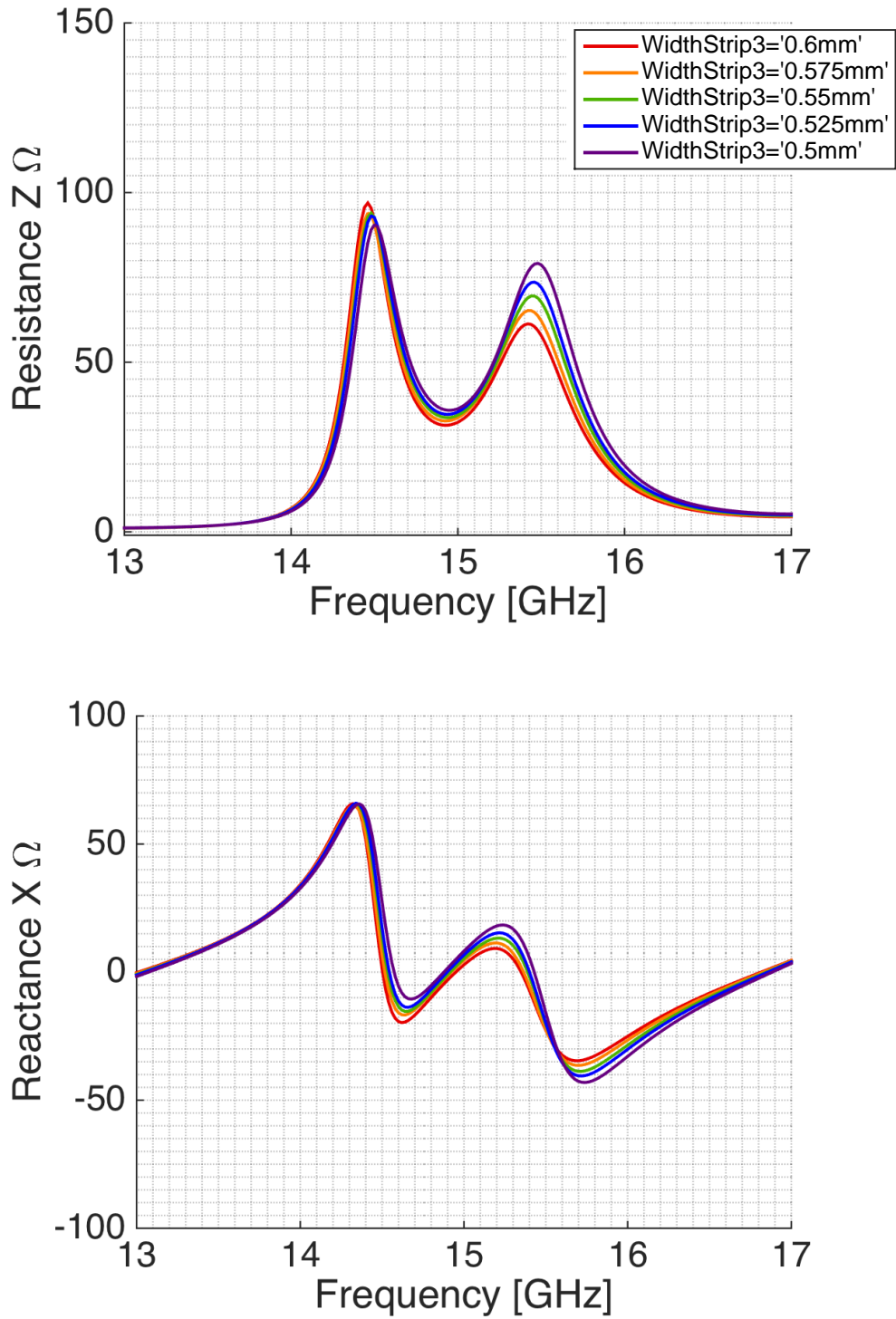


Figure C.13: Impedance variations from the parametric study of different stripline widths of the stripline in port 1 W_{s1} for port 1 for the waveguide filled with dielectric material and excited by a slot. The other design parameters had the starting values listed in table 3.5.

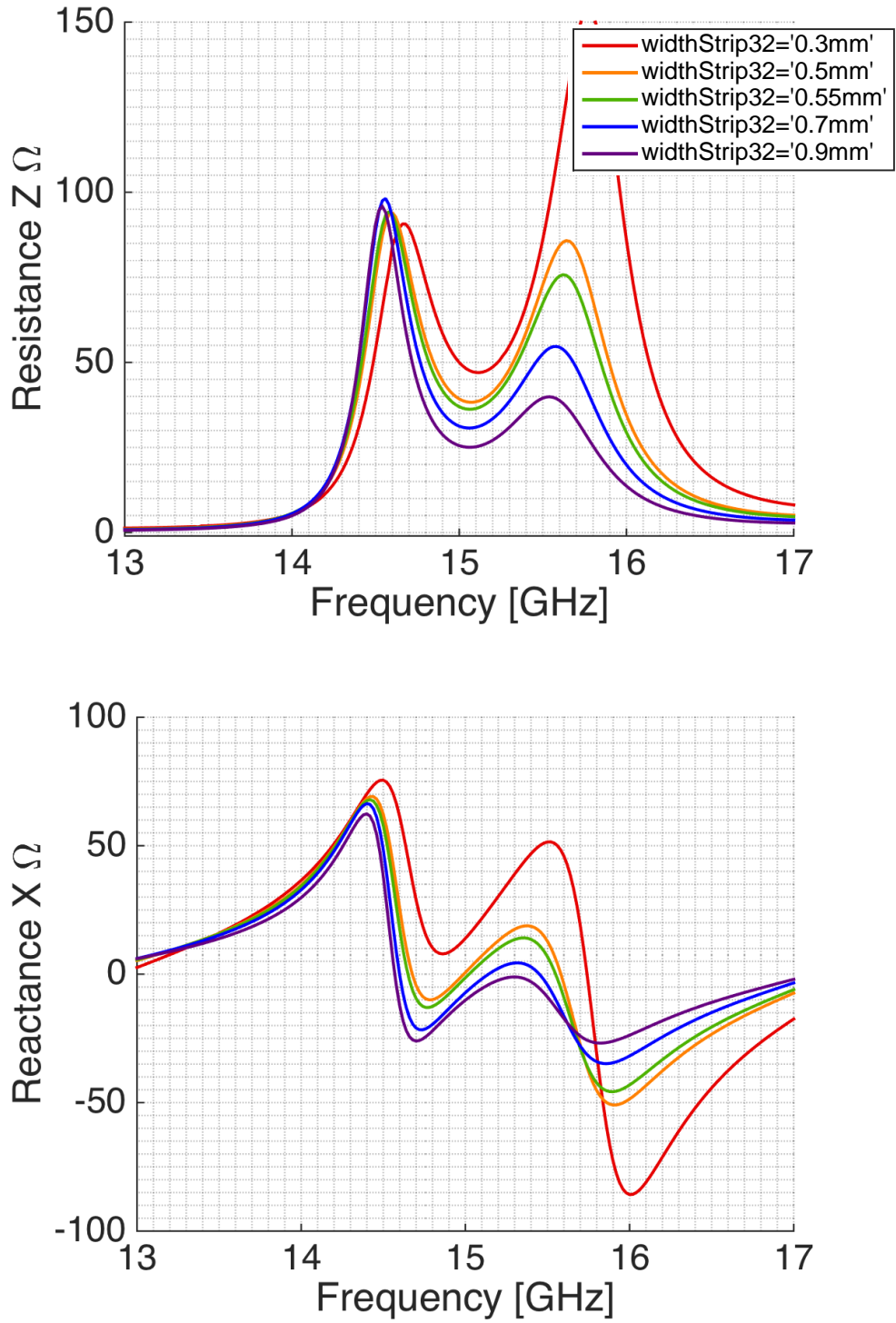


Figure C.14: Impedance variations from the parametric study of different stripline widths of the stripline in port 2 W_{s2} for port 2 for the waveguide filled with dielectric material and excited by a slot. The other design parameters had the starting values listed in table 3.5.

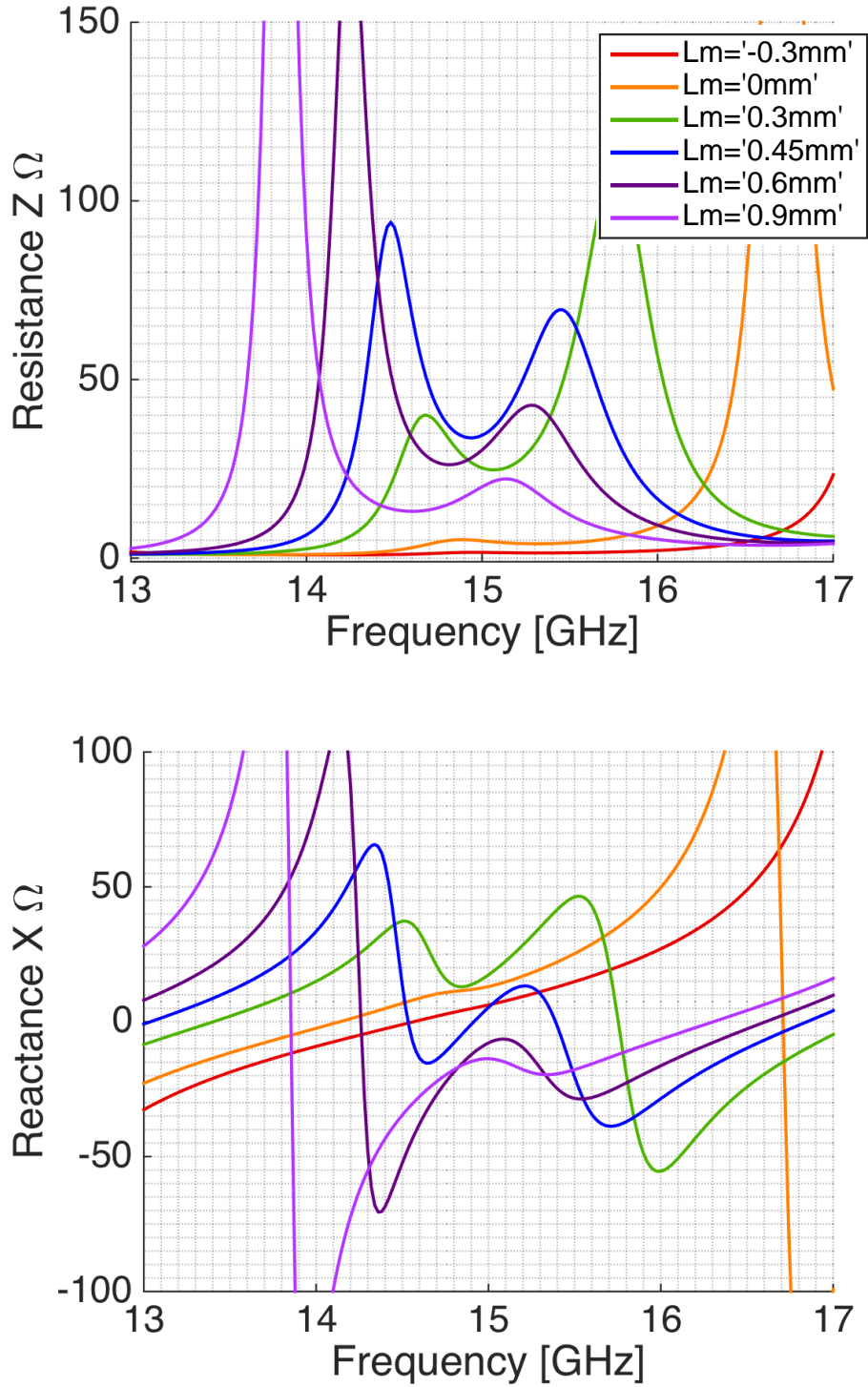


Figure C.15: Impedance variations from the parametric study of different stripline stub lengths of the stripline in port 1 L_{m1} for port 1 (the behavior is similar for the stub length of port 2) for the waveguide filled with dielectric material and excited by a slot. The other design parameters had the starting values listed in table 3.5.

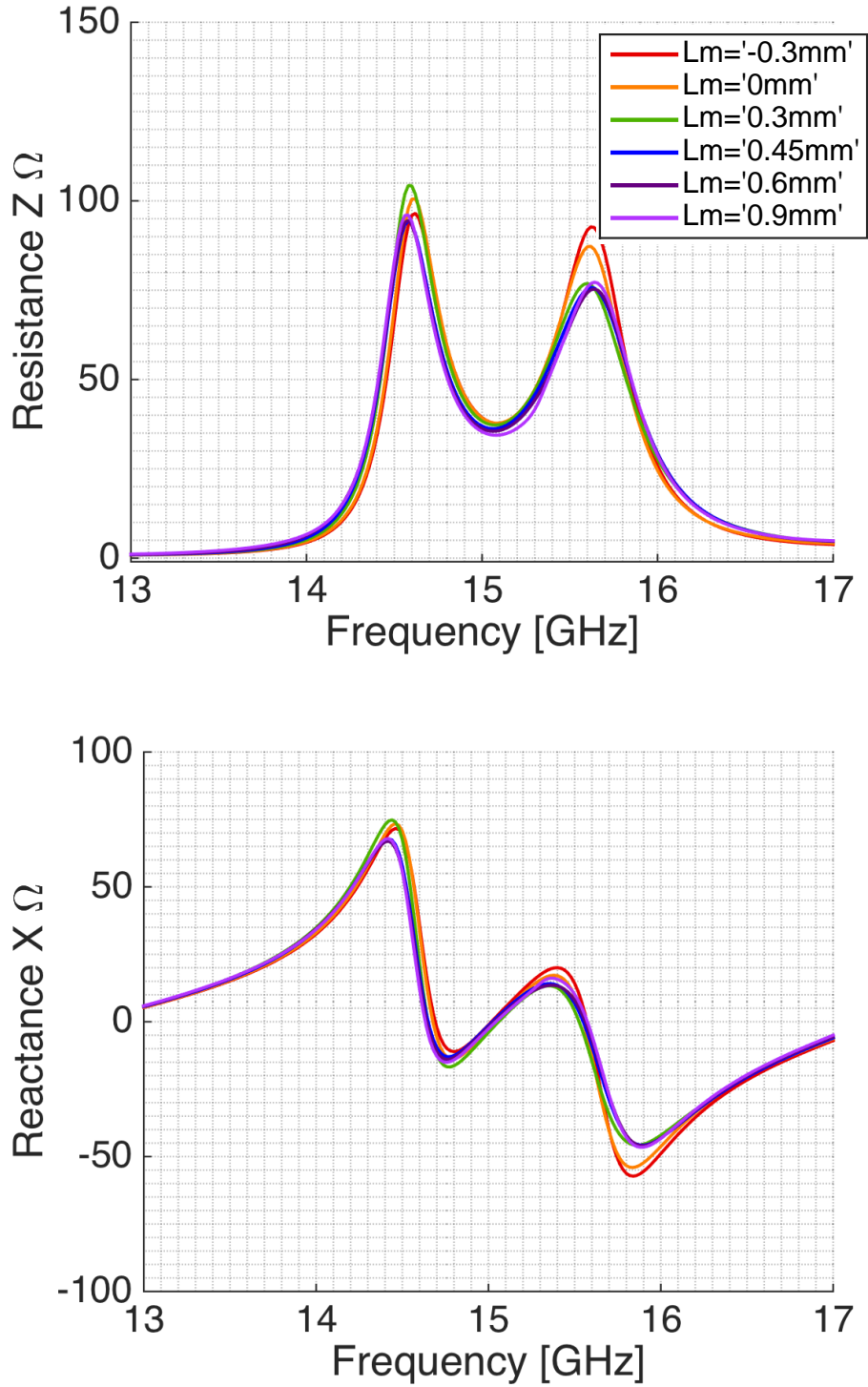


Figure C.16: Impedance variations from the parametric study of different stripline stub lengths of the stripline in port 1 L_{m1} for port 2 (the behavior is similar for the stub length of port 2) for the waveguide filled with dielectric material and excited by a slot. The other design parameters had the starting values listed in table 3.5.

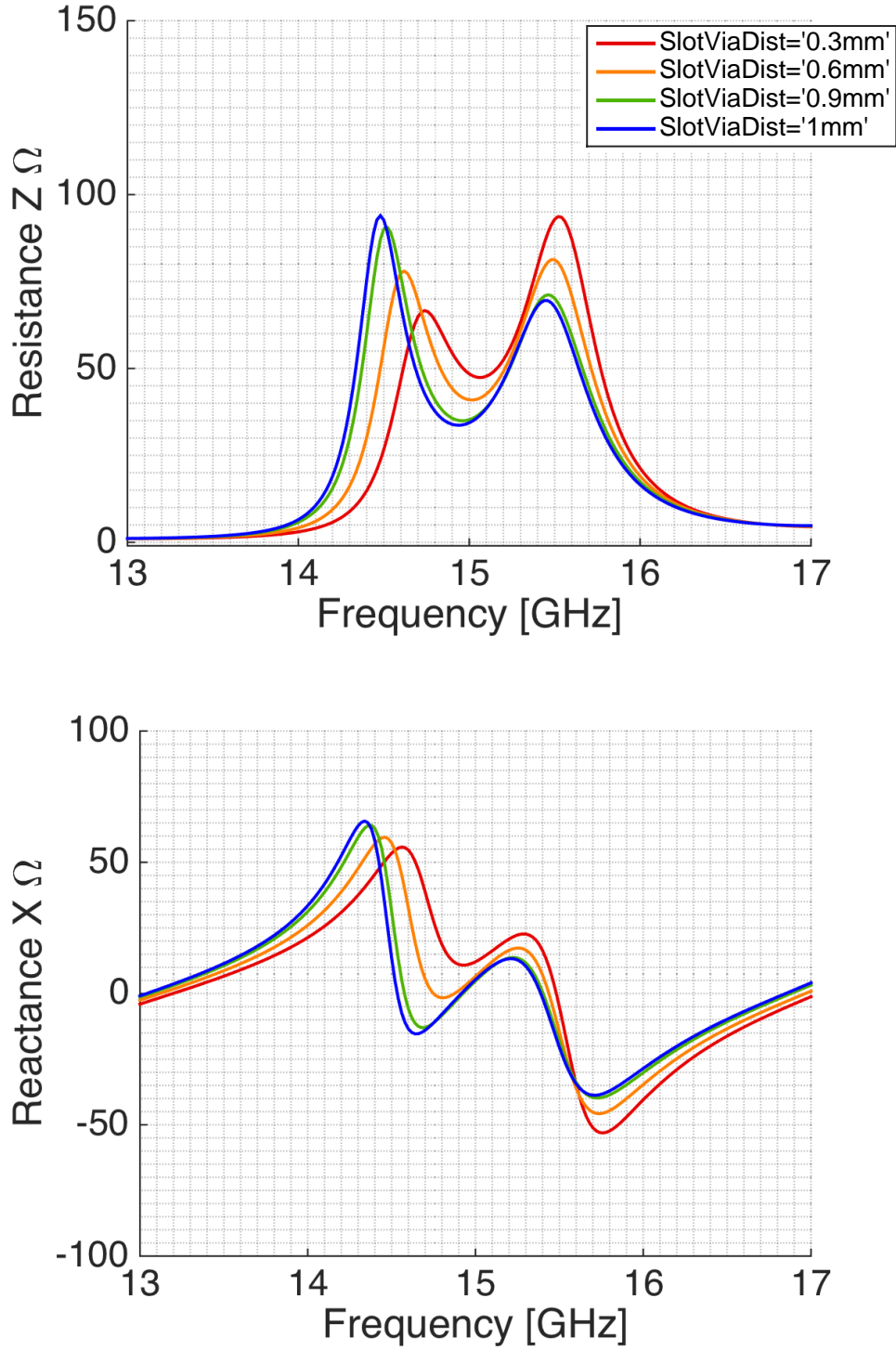


Figure C.17: Impedance variations from the parametric study of different cavity sizes d_{cavity} for port 1 (port 2 shows the same behavior) for the waveguide filled with dielectric material and excited by a slot. The other design parameters had the starting values listed in table 3.5.

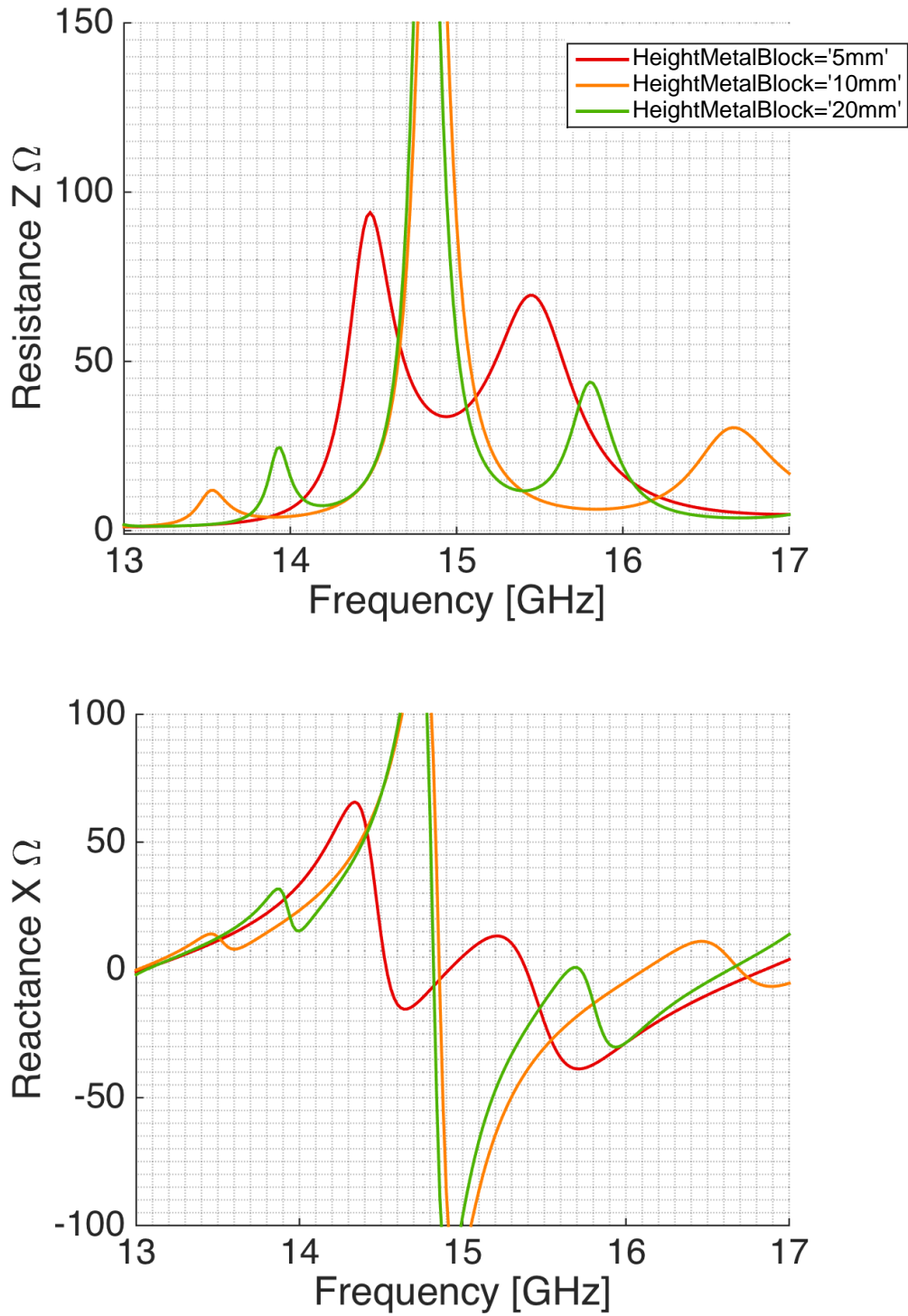


Figure C.18: Impedance variations from the parametric study of different waveguide heights for port 1 (port 2 shows the same behavior) for the waveguide filled with dielectric material and excited by a slot. The other design parameters had the starting values listed in table 3.5.